

**STUDIES TOWARDS AN ENHANCED UNDERSTANDING OF
ELECTRON BEAMS AND THEIR DIAGNOSTICS**



UNIVERSITY OF
LIVERPOOL

Thesis submitted in accordance with the requirements of the University of
Liverpool for the degree of Doctor of Philosophy

By
Lee James Devlin

March 2016

Abstract.

A large part of current research and innovation capacity depends on high quality electron beams. Electron accelerators are found in many applications from cancer therapy, cargo scanners, high energy particle colliders, synchrotron light sources to free electron lasers. Electron beams also offer exciting opportunities for developments at the cutting edge of science, for example on novel accelerating schemes which promise accelerating gradients several orders of magnitude higher than what can be realised with conventional radiofrequency accelerators.

Whilst R&D into the optimisation of electron accelerators has been performed over many decades, further improvements are still required so their potential can be fully exploited. This includes studies into advanced instrumentation to yield more precise information about the beam itself, novel simulation tools that model the physics of emission and interaction processes, as well as improved beam generation and shaping schemes to enhance the achievable beam brightness.

In the frame of this PhD work, different areas of electron beams and associated technologies have been studied whilst still pertaining to the same question: How can we better understand the generation, control and use of electron beams? The thesis is split into three main sections: After a general introduction to the subject, studies into electron emission and initial beam shaping are covered in chapter 2, before the results from investigations into novel beam loss detection techniques are presented in chapter 3.

In any accelerator based light source, maintaining the beam quality is crucial. The electron source itself is a key element that determines the achievable beam quality. A variety of source materials are currently under test across many institutes to better understand emission characteristics and to identify the best materials and optimum preparation methods. Here, one experimental set-up at the Cockcroft Institute has been considered. The Transverse Energy Spread Spectrometer (TESS) apparatus uses electrostatic elements to measure both the transverse and longitudinal energy properties of electron beams generated from photocathodes. This then provides detailed information about the electron emission process and allows optimisation of beam generation schemes. To enhance the understanding of the experimental data, a dedicated particle tracking code has been developed which uses accurate maps obtained from simulation or experiment to represent all electromagnetic fields of the set-up. This code has then been used to study two different techniques to measure the longitudinal energy spread of electrons emitted from gallium arsenide. The first technique was to use a wire mesh as an energy

filter which the electrons must pass through, the second was to generate a potential difference between the cathode source and detector system. Experimental results are presented for both techniques and the analysis is supplemented with simulations. Monte Carlo results are in good agreement with experimental data, however, through this analysis it is found that using the meshes as a wire filter may not be an efficient method of measuring the longitudinal energy distribution curve as a result of the potential distribution surrounding the wire meshes. The second method is sufficient to the task however the resolution of the technique may be affected by focusing effects around the meshes.

Measurement and detection of beam loss is important for any accelerator as unwanted losses yield reduced beam transmission and cause higher background noise. It is crucial in high energy accelerators where unwanted loss particles could easily damage parts of the accelerator and the experiments. Currently used techniques, however, are often limited in their dynamic range, spatial and time resolution, radiation hardness and can be expensive. A detector based on optical fibres with photodetector readout has been studied as part of this work as a detector for a future electron-positron collider. It can cover large distances at the expense of many smaller localised detectors. The ultimate performance of this detector is strongly affected by the light sensor at the fibre end. This in turn limits the performance to locate beam loss intensity and position and hence ultimately limits the understanding of beam losses along an accelerator. To this end Silicon Photomultipliers have been studied as an advanced light sensor that shows great promise for beam loss applications. Preliminary models are compared to experimental data and it is shown that the detector performance in this application is limited by the finite number of pixels available to fire along with pixel recovery/dead time. Measurements carried out at the CLIC Test Facility at CERN using an optical fibre systems are presented and used to assess the system's performance to specific beam structures. Several techniques are used to analyse signals recorded by multiple detectors however it is found that the layout of optical fibres, which could not be changed, limited full understanding, however, these results are the basis of later experiments which fully measure the effect of a fibre optic beam loss monitor to different beam structures and additional changes to the set-up, which may aid further tests, are covered.

Contents

List of Constants	10
List of Abbreviations	11
1 Introduction	12
1.1 The First Particle Accelerator	12
1.2 Linear Accelerator Development	14
1.3 Linear Electron Accelerators	14
1.4 Accelerating Structures	16
1.5 Focusing Elements	18
1.6 Beam Dynamics	19
1.6.1 Transverse Beam Dynamics	19
1.6.2 Longitudinal Beam Dynamics	22
1.7 Applications	23
1.7.1 Light Sources	23
1.7.1.1 FEL Beam Requirements	27
1.7.2 Future Linear Collider	28
1.7.2.1 Compact Linear Collider	29
1.7.2.2 Diagnostic Requirements	31
1.8 Chapter Summary	31
2 Investigations into the Longitudinal Energy Distribution of Emitted Electrons	33
2.1 Electron Sources	34
2.1.1 Field Emission Sources	35
2.1.2 Thermionic Sources	35
2.1.3 Photoemission Sources	37
2.1.3.1 Three Step Model	38
2.1.3.2 Band Structures	39

2.1.3.3	Theoretical Thermal Emittance	40
2.1.3.4	Typical Photocathode Properties	41
2.1.3.5	Gallium Arsenide.....	43
2.2	The TESS Experiment.....	43
2.2.1	Photocathode Preparation.....	45
2.2.2	TESS Set-up	47
2.2.3	Transverse Experiments	50
2.3	Longitudinal Experimental Technique.....	53
2.4	Modelling Fields Around an Electrostatic Wire Mesh.....	55
2.4.1	Analytical Solution.....	55
2.4.1.1	Thin Wire Mesh Solution	55
2.4.1.2	Applicability of the Analytical Solution.....	63
2.4.2	Finite Element Method Comsol Model	64
2.4.2.1	Numerical Methods	66
2.4.2.2	Wire Thickness Study.....	67
2.4.2.3	Finite Element Mesh Convergence Study	68
2.4.2.4	Cell Convergence Study	69
2.4.2.5	Cell Size Study	72
2.4.2.6	Introducing Deformations.....	72
2.4.2.7	Benchmarking With Opera.....	74
2.5	Development of a Low Energy Tracking Code for Mesh Systems	76
2.5.1	Code Structure.....	76
2.5.2	Operation of the Code	77
2.5.3	Initial Parameters.....	81
2.6	Method one: Filter Mesh Technique	84
2.6.1	Experimental Results.....	84
2.6.2	Simulation of the Filter Mesh Technique.....	88
2.6.2.1	Potential Surrounding the Mesh	88
2.6.2.2	Electron Motion in the Filter Mesh Technique.....	88
2.6.2.3	Simulation Results using Realistic Initial Conditions	93
2.6.3	Comparison Between Simulation and Experimental Results.....	95
2.6.4	Review of the Filter Mesh Technique	97

2.7	Method two: MCP/Cathode Gap Technique.....	98
2.7.1	Experimental Results	99
2.7.2	Simulation.....	101
2.7.2.1	Electron Motion in the MCP/Cathode Gap Technique	101
2.7.2.2	Potential Limitations of the Technique	102
2.7.3	Summary of the MCP/Cathode Gap Technique	106
2.8	Chapter Summary	106
3	Chapter 3 Beam Loss Monitoring study for the Compact Linear Collider	109
3.1	Machine Protection for Particle Accelerators	110
3.1.1	Beam Loss Monitoring	110
3.1.2	Parameters for Discussing BLMs	111
3.1.2.1	Charged Particle Interaction with Matter	112
3.1.2.2	Photon Interaction with Matter.....	114
3.2	Classical Beam Loss Monitoring Technology	115
3.2.1	Short Ionisation Chambers.....	115
3.2.2	PIN Diodes.....	116
3.2.3	Long Ionisation Chambers.....	117
3.2.4	Scintillating Screens	118
3.2.5	Secondary Emission Monitors	120
3.2.6	Diamond Detectors	120
3.2.7	Neutron Detector Beam Loss Monitors	121
3.2.8	Choice of BLM Detector	121
3.3	CLIC BLM Study	122
3.4	Fibre Optics for Beam Loss Monitors.....	124
3.4.1	Optical Fibres.....	125
3.4.2	Multi-Mode Fibres	126
3.4.2.1	Refractive Index Profile	127
3.4.2.2	Intermodal Dispersion	128
3.4.2.3	Chromatic Dispersion.....	128
3.4.3	Single Mode Fibres	129
3.4.4	Attenuation.....	129

3.4.5	Radiation Damage to Fibres	131
3.4.6	Cherenkov Radiation.....	133
3.4.7	Signal Generation in Fibres.....	134
3.4.8	Current State of Fibre BLMs.....	135
3.5	Photodetector for Fibre Readout	136
3.5.1	The Silicon Photomultiplier	136
3.5.1.1	SiPM Structure and Properties.....	136
3.5.1.2	Dark Noise, Afterpulsing and Crosstalk.....	140
3.5.2	Experimental Characterisation	141
3.5.2.1	SER Finding Algorithm.....	142
3.5.2.2	Experimental Characterisation Set-up	144
3.5.2.3	Dark Noise Measurement	145
3.5.2.4	Spectrum Measurement	146
3.5.2.5	Time Resolution measurement	148
3.5.3	SiPM application to optical fibre BLM.....	149
3.5.3.1	SiPM Response Under a High Load.....	151
3.5.3.1.1	Experimental Results.....	151
3.5.3.1.2	Analytical Model of Initial Response to High Intensities..	157
3.5.3.2	SiPM Response to Double Pulses.....	159
3.6	Measurements at CTF3	161
3.6.1	CTF3	161
3.6.2	Simulations of Losses.....	163
3.6.3	Detector Layout.....	164
3.6.3.1	Fibre Layout.....	165
3.6.3.2	Silicon Photomultipliers	165
3.6.3.3	Localised Detectors	166
3.6.4	Measurements	169
3.6.5	Dose Calculations.....	171
3.6.6	Signal Deconvolution.....	173
3.6.6.1	SiPM Single Electron Response Deconvolution	173
3.6.6.2	Localised Detector Deconvolution	176
3.6.7	Further Experiments.....	177

3.7 Chapter Summary	178
4 Conclusions and Outlook	181
4.1 Electron Beam Generation	181
4.2 Beam Loss Detection	184
Appendix A.....	188
Appendix B.....	190
List of Figures	194
List of Tables	198
Bibliography	199
Acknowledgments.....	215

List of Constants

The following constants are used throughout this body of work and to avoid redefining them each time they are globally declared here. Many more parameters and variables will be used, however, they are often specific to the concept being discussed and are defined at the point they first appear. Values and units using standard notation are given also and can be assumed to take the values presented here unless explicitly stated otherwise.

Name	Symbol	Value	Unit
Electron Rest Mass	m_e	9.10938×10^{-31}	Kg
Electron Charge	q_e	1.60218×10^{-19}	C
Speed of Light	c	299,792,458	ms^{-1}
Permittivity of Free Space	ϵ_0	8.85419×10^{-12}	Fm^{-1}
Permeability of Free Space	μ_0	$4\pi \times 10^{-7}$	TmA^{-1}
Planck's Constant	h	6.62607×10^{-34}	Js
Planck's Reduced Constant	\hbar	1.05457×10^{-34}	Js
Boltzmann's Constant	K_B	1.38065×10^{-23}	JK^{-1}
Classical Electron Radius	r_e	2.81794×10^{-15}	m
Avagadros Number	N_A	6.02214×10^{23}	mol^{-1}

List of Abbreviations

ACEM	Aluminium Cathode Electron Multiplier
APD	Avalanche PhotoDiode
BLM	Beam Loss Monitor
CLIC	Compact Linear Collider
CTF3	CLIC Test Facility 3
DB	Drive Beam
FEL	Free Electron Laser
LEDC	Longitudinal Energy Distribution Curve
LHC	Large Hadron Collider
LION	Long IONisation chamber
MB	Main Beam
MCP	Multi Channel Plate
MIP	Minimum Ionising Particle
NA	Numerical Aperture
PDE	Photon Detection Efficiency
PETS	Power Extraction and Transfer Structures
PMT	PhotoMultiplier Tube
PPF	Photocathode Preparation Facility
QE	Quantum Efficiency
RF	Radio Frequency
RIA	Radiation Induced Attenuation
SEM	Secondary Emission Monitor
SER	Single Electron Response
SIPM	Single PhotonMultiplier
TESS	Transverse Energy Spread Spectrometer

Chapter 1:

Introduction

The purpose of this chapter is to introduce general aspects of electron accelerators. This includes a historical context in which the technology has been developed, as well as the terms for describing a beam and also the applications for which they are used. The chapter serves to introduce concepts and motivations which will be addressed further in later chapters.

The chapter starts with a mention of the world's first particle accelerator before moving historically through circular and linear accelerator development and addressing the difference between the two. The chapter then proceeds by discussing beam physics by highlighting basic parameters which describe a particle beam. The chapter ends with two advanced applications of linear electron beams, electron-positron colliders and free electron laser light sources. These two examples will serve as a basis to highlight current R&D requirements in this area of science.

1.1 The First Particle Accelerator

The first particle accelerator, the use of which John Cockcroft and Ernest Walton were awarded the Nobel Prize, was built out of a desire to probe the building blocks of the universe. Their accelerator worked on the principle of electrostatics, in which a charged particle is accelerated across a potential difference.

The Cockcroft-Walton accelerator works as a voltage multiplier composed of capacitors and diodes in a ladder formation [1], figure 1.1. The capacitors are charged in turn at each polarity shift of an alternating power supply. The voltage at the end of the capacitor chain is the sum of the potentials across each capacitive component in the ladder, thus a relatively low voltage

supply can be stepped up to a much higher one. Using this technique, Cockcroft and Walton were able to produce a high accelerating potential, 800 kV, which was used to accelerate protons to bombard and split lithium. This technique of accelerating particles with a large potential drop is still a popular technique today with variations such as the Van de Graff generator and tandem accelerator used for the production of x-rays, material analysis and ion implantation [2].



Figure 1.1: Cockcroft-Walton voltage multiplier located at the Cockcroft Institute.

Electrostatic accelerators are limited in their operation by electrical sparking, which makes them difficult to control at higher voltages. Over the past century the field of accelerator physics has grown to such an extent that they are now tools for many physical sciences. Modern accelerators can be broadly split into two categories, circular accelerators and linear accelerators. Though acceleration is the principle aim for both technologies the physics of their operation and performance require different considerations.

1.2 Linear Accelerator Development

When made to follow a circular path, charged particles emit radiation called synchrotron radiation. The power, P , of synchrotron radiation is given by [3]:

$$P = \frac{2}{3} \cdot \frac{q_e^2 c}{4\pi\epsilon_0} \cdot \frac{\beta^4 \gamma^4}{\rho^2} \quad (1.1)$$

Where β is the ratio between the particle velocity and the speed of light, γ is the relativistic Lorentz factor, ρ is the bending radius which the particles are made to follow and B is the magnetic field strength. The problem arises with the γ^4 term. Since γ is related to mass and energy by $E = \gamma m_e c^2$ this means the synchrotron radiation power scales as m_e^{-4} . The mass ratio between an electron and a positron is approximately 2000, therefore, the power lost through synchrotron radiation is 10^{13} times higher for an electron than a proton of the same energy. For this reason it is inefficient to run high energy electron/positron circulator accelerators, as not only does energy need to be supplied to the particles for acceleration but also to compensate the energy that is lost due to synchrotron radiation losses. Linear accelerators on the other hand, do not suffer from these energy losses.

Linear accelerators, often shortened to linac, began as an idea from Gustav Ising in 1924 who proposed a method of accelerating ions through multiple small steps between drift tubes which the ions travel though accelerated through a potential difference generated by a spark gap generator [4]. In 1927 the young Norwegian PhD student Rolf Widerøe working in Germany, developed and built a multi-stage linear accelerator, figure 1.2 [5]. In this scheme ions were accelerated through copper tubes housed in a glass vacuum vessel. Widerøe's linac consisted of two copper tubes and using a 1 MW oscillator potassium ions were accelerated up to 50 keV.

1.3 Linear Electron Accelerators

Electron linacs were not feasible to begin with because they become relativistic much sooner than heavier particles. To run a linac at higher velocities requires a high frequency source to keep the copper drift tubes an appropriate length. Higher frequency sources did not exist at this point and since they can only reach limited energies in a finite space it meant there was little interest in their development and for the time being circular accelerators dominated.

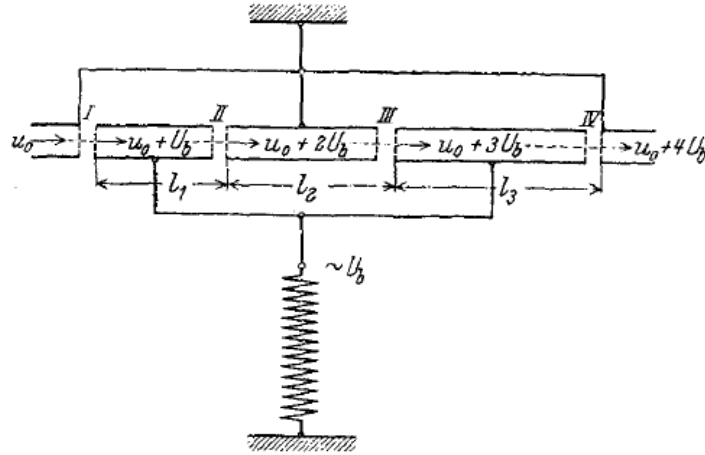


Figure 1.2: Initial idea of a linear accelerator based on an accelerating field generated by an oscillator as it appeared in Widerøe's 1928 paper [5]. The tubes stop ions seeing the incorrect polarity whilst they are inside and are of increasing length to account for the increase in velocity.

During the Second World War, high powered microwave sources were developed for radar technology [6]. This included the klystron and also the magnetron which were initially developed in the years preceding the war [7] [8]. Both technologies use velocity modulation of a DC electron beam to generate waves with microwave frequencies and can also amplify the waves to higher amplitudes. The technology developed for the war time effort was well suited for linac technology and it meant once again that linear structures were considered with the first electron linac being developed in the late 1940s [9].

The next advancement in linac technology occurred in 1946 with the work of Luis Walter Alvarez and his group in California [10]. Alvarez' linac worked on a different design to Widerøe's linac though on the same basic principle. The glass casing was replaced with a metal cylindrical cavity. Instead of energising each individual electrode the entire cylinder is energised. In Alvarez' case, it was at a frequency of 200 MHz. In this set-up a standing wave is produced in the cavity so that at any point in time the electric field points in the same direction. As with the Widerøe drift tube linac, the drift tube shields the particles from the electric field when the field is pointing in the wrong direction and the field is concentrated between the drift tubes.

The Alvarez drift tube linac was a major step forward in linac design and is still common today. However one change that was made was the removal of drift tube protecting elements, it became

clear that they were not strictly necessary and that protecting particles from decelerating fields is simply a matter of correct timing of the RF pulse so they only see an accelerating potential in the cavity. Modern designs of linac structures use cavities, hollow structures, which are excited with RF power [11].

1.4 Accelerating Structures

To understand how accelerating fields can be generated in a cavity it is necessary to start with Maxwell's equations, which are the underpinning of electromagnetism [12]:

$$\nabla \cdot \vec{D} = \rho \quad (1.2)$$

$$\nabla \cdot \vec{B} = 0 \quad (1.3)$$

$$\nabla \times \vec{E} = -\frac{\delta \vec{B}}{\delta t} \quad (1.4)$$

$$\nabla \times \vec{H} = \vec{j} + \frac{\delta \vec{D}}{\delta t} \quad (1.5)$$

Where ρ is the electric charge density and J is the current density. Maxwell's equations link the electric type vectors \vec{E} and \vec{D} with the magnetic type vectors \vec{B} and \vec{H} which are related to each other by the relative material permittivity and permeability, μ_r and ϵ_r , and the universal constants μ_0 and ϵ_0 which are related to the universal speed of light by $c = 1/\sqrt{\epsilon_0\mu_0}$.

$$\vec{D} = \epsilon_r \epsilon_0 \vec{E} \quad (1.6)$$

$$\vec{B} = \mu_r \mu_0 \vec{H} \quad (1.7)$$

In a cavity, i.e. in the absence of charges, Maxwell's equations can be written as:

$$\nabla \cdot \vec{D} = 0 \quad (1.8)$$

$$\nabla \cdot \vec{B} = 0 \quad (1.9)$$

$$\nabla \times \vec{E} = -\frac{\delta \vec{B}}{\delta t} \quad (1.10)$$

$$\nabla \times \vec{B} = \frac{1}{c^2} \frac{\delta \vec{E}}{\delta t} \quad (1.11)$$

Application of basic vector calculus, i.e. $\nabla \times (\nabla \times V) = \nabla(\nabla \cdot V) - \nabla^2 V$, shows that both \vec{B} and \vec{E} satisfy the wave equation which for \vec{E} can be written:

$$\nabla^2 \vec{E} = \frac{1}{c^2} \frac{\delta^2 \vec{E}}{\delta t^2} \quad (1.12)$$

Which, taking one spatial direction only, has a solution:

$$\vec{E}(x, t) = E_0 e^{i(kx - \omega t)} \quad (1.13)$$

Where E_0 is a constant, k is the wavevector which points in the direction of wave propagation and ω is the angular frequency. The magnetic field follows the same form and the two are perpendicular to each other. The wavevector and angular frequency are not independent values but are related to the phase velocity of the wave:

$$v_p = \frac{\omega}{|k|} \quad (1.14)$$

The wavevector describes each mode that is excited in a cavity. Boundary conditions dictate that electric fields at the boundary of the cavity must go to zero. This condition means that in a waveguide the values of k can take multiple discrete values such that the boundary conditions are satisfied.

The value of k dictates the mode number for a particular allowed wave in a cavity. Ideally the lowest mode, with the highest amplitude is used to accelerate particles. However, higher order modes are usually unavoidable. Practically, cavities in accelerators are designed so that either the electric or magnetic field in the longitudinal direction is zero. These are called TE, transverse electric, and TM, transverse magnetic, modes. The most commonly used is the TM_{01} mode which is the lowest TM mode.

Cavities can take many shapes such as rectangular, cylindrical and pillbox to name a few.

Figure 1.3 shows some different modes supported for a circular waveguide in a cross sectional and a longitudinal view of the cavity.

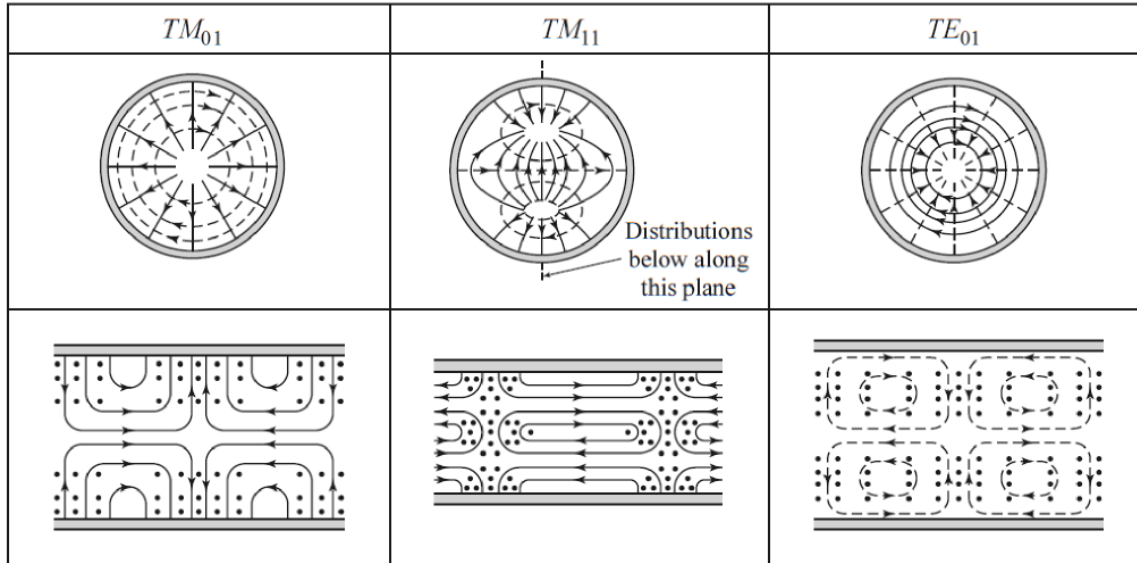


Figure 1.3: Lowest modes for a circular cavity, adapted from [13]. The top row shows a cross sectional view of the cavity and the bottom row shows a longitudinal view. Solid lines are electric field lines and dashed lines and dots are magnetic field lines.

1.5 Focusing Elements

A travelling beam will slowly diverge, similar to a ray of light in optics. A particle beam can be focused, or defocused, using quadrupole magnets. A quadrupole, figure 1.4, is an arrangement of four poles with a field strength increasing from the centre with zero field directly at the centre.

An important property of quadrupoles is that the horizontal force depends on the horizontal particle position and similarly for the vertical force. This means that horizontal and vertical motions are decoupled. This is only true when they are perfectly aligned and not skewed relative to each other. Furthermore a quadrupole which focuses in the vertical plane will be defocusing in the horizontal plane and similarly for the converse situation. An overall focusing, strong, effect can be achieved by periodic focusing and defocusing. A typical arrangement is the FODO lattice which is a series of focusing magnets, drift spaces and defocusing magnets.

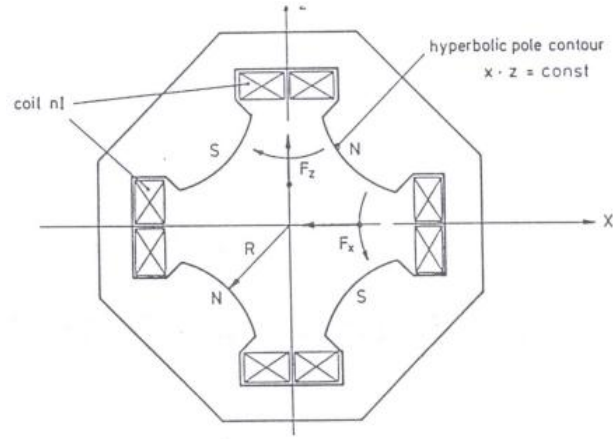


Figure 1.4: Quadrupole magnet [10].

1.6 Beam Dynamics

A particle travelling through an accelerator will experience forces from the accelerating structures as well as the focusing elements. To understand dynamics in an accelerator, motion is usually split into transverse beam dynamics and longitudinal beam dynamics.

1.6.1 Transverse Beam Dynamics

Transverse particle motion can be described using Hill's equation, a second order linear ordinary differential equation, which when incorporating only quadrupoles may be written in terms of the transverse position x and longitudinal path length s [10]:

$$\frac{d^2x}{ds^2} + k(s)x = 0 \quad (1.15)$$

Where k here refers to the gradient of the magnetic field generated by quadrupoles and other magnets along a beam line. The solution to this equation is a harmonic function and is sometimes called the phase-amplitude form and can be written as [10]:

$$x(s) = \sqrt{\epsilon\beta(s)} \cos(\phi(s) + \phi_1) \quad (1.16)$$

The functions ϵ and ϕ_1 are constants defined by the initial conditions whilst $\beta(s)$ and $\phi(s)$ are

called the amplitude and phase functions however $\beta(s)$ is sometimes simply called the β function. The parameter ϵ is called the emittance and will be discussed further shortly. The β function varies along the beam line and is a measure of how much the beam is focused along a beam line. The parameters β and ϵ along with two others, α and γ , make up what are known as the TWISS parameters which are used to describe transverse characteristics of a particle in an accelerator. The TWISS parameters can be written as an equation in phase space with axis x and x' which represent particle position and transverse momentum. This equation takes the form of an ellipse and is written as [14]:

$$\gamma x^2 + 2\alpha x x' + \beta x'^2 = \epsilon \quad (1.17)$$

The phase space ellipse is shown in figure 1.5. The emittance is directly related to the area of the ellipse by $A = \pi\epsilon$. A particle will traverse the blue line of the phase space ellipse as it travels along an accelerator.

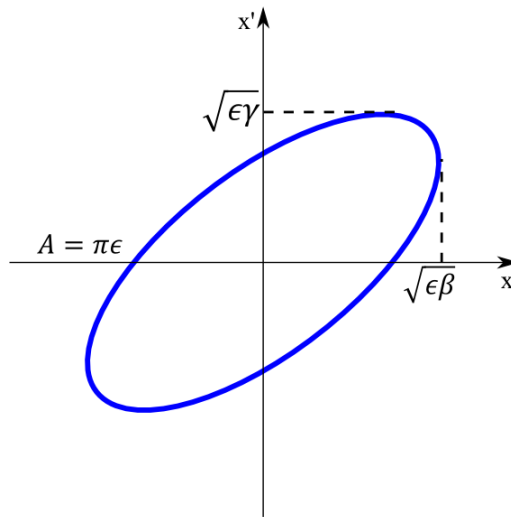


Figure 1.5: Phase space ellipse which describes transverse motion in an accelerator.

A particle beam is comprised of many particles however they may also be described by TWISS parameters where root mean square values (rms) are often quoted. The beam size $\sqrt{\beta\epsilon}$ needs to be smaller than the mechanical aperture of the accelerator otherwise it will collide with the walls; this will result in particles being lost from the beam. Since the β function changes most around

quadrupoles, it is here that particle losses are expected to occur.

From equation 1.17 it can be seen that ϵ is a constant of motion. This is an important concept in accelerator design and is down to Liouville's theorem [15] which states that the area of a shape in phase space, such as figure 1.5, will stay constant as long as only conservative forces are acting on it. In figure 1.5 this means that the area of this ellipse will stay constant as long as only conservative forces act upon the particle. When the beam is accelerated the emittance increases, however, the normalised emittance is and is calculated by taking into account the velocity v and relativistic factor γ [15] and is given by:

$$\epsilon_n = \frac{\gamma v}{c} \epsilon \quad (1.18)$$

So far emittance has only been discussed in terms of a perfect system. In reality, non-linear forces exist which can blow up beam emittance. One such contribution which can lead to emittance growth is due to space charge, which is the Coulomb interaction of a multi-particle beam. Space charge effects are stronger at low velocities as a result of electric fields being radial in all directions. Further non-conservative effects which lead to emittance blow up are [16] intrabeam scattering, scattering with instrumentation such as scrapers and thin foils, scattering off residual gas and wakefield effects which occur due to the beam inducing image charges in the cavity. A beam with large emittance is a poor quality beam and many applications require very small emittances for the beam to be useful. Emittance reduction can occur but this occurs in special configurations, for example by means of emittance transfer from transverse to longitudinal [17] or dedicated beam cooling schemes. Some large scale linear accelerators use circular elements at lower energy to reduce the emittance in so-called damping rings before using linacs to accelerate the beam further. For most linear accelerator based machines, however, this is not an option and emittance is usually limited to emittance at the source.

Transverse emittance is often quoted in units of mm·mrad. A rms value of the emittance is often given as a statistical definition to describe a measurable beam and is defined by [18]:

$$\epsilon_{rms} = \sqrt{\langle x \rangle \langle x'^2 \rangle - \langle x x' \rangle^2} \quad (1.19)$$

For a purely linear accelerator the emittance of an electron beam is ultimately limited to the

emittance at the source since the emittance will only grow from this value. A linear electron accelerator that can deliver a beam with small transverse velocities is one that has a small emittance from the electron source and is able to preserve it through the accelerator. The emittance of an electron beam from a source due to the fundamental emittance as well as emittance growth terms is given by [19]:

$$\epsilon = \sqrt{\epsilon_{thermal}^2 + \epsilon_{RF}^2 + \epsilon_{SC}^2 + \dots} \quad (1.20)$$

The fundamental emittance, $\epsilon_{thermal}$, delivered by an electron source is called the thermal emittance which represents the lowest emittance that is achieved. Many effects can increase the emittance at the low energy scale such as space charge ϵ_{SC} , RF effects ϵ_{RF} and magnetic components. Emittance compensation solenoids are used to focus the beam at small energies with a bucking coil [20]. This technique aims to reduce emittance growth from space charge effects. However, misalignment of the solenoid can leave a non-zero magnetic field on the cathode face which increases emittance. There has been growing interest in the pursuit of three dimensional elliptical bunch generation, as the space forces are completely linear and may be completely compensated [21]. RF induced emittance growth occurs when the electrons leave the injector cavity and experience a transverse kick [22].

1.6.2 Longitudinal Beam Dynamics

A particle is accelerated if it sees the correct phase of the RF wave. The electric field inside a cavity is sinusoidal so a particle sees different field strengths depending on its phase relative to the wave. It is important to catch electrons at the correct phase of the RF pulse doing so will allow electrons to reach peak acceleration. Particles injected at a phase off peak will be decelerated and be lost from the bunch [23]. For this reason sources should ideally inject electrons with small energy spreads so the largest number of electrons possible are caught by the RF field and experience maximum acceleration.

1.7 Applications

Electron beams are used for many reasons including medical applications [24], lithography [25], physical vapour deposition [26] and electron diffraction [27] to name a few. Two advanced applications will now be described. These two examples are intended to highlight where exactly electron accelerators can be improved upon. The two applications that will be discussed are:

1. Light sources
2. Future electron colliders

1.7.1 Light Sources

Electron beams can be used to generate intense sources of light which can be used to study surface and bulk properties of materials. Applications can cover areas such as medical x-rays [28] and probing viral structures [29].

Light sources are often discussed in terms of generations [30], with each progression generating more photons. The first generation of light sources were not dedicated machines. Pre-existing synchrotrons for nuclear particle physics experiments were used to benefit from the synchrotron radiation that was generated in the bending magnets. When their usefulness became apparent, second generation light sources were built as dedicated storage rings. An example of a second generation light source was the SRS at Daresbury Laboratory, UK. Third generation light sources use insertion devices, discussed shortly, placed along straight sections of an accelerator lattice to increase the intensity of light generated in these circular accelerators. An example of a third generation light source is Diamond based in Oxfordshire, UK.

Generations one and two use bending magnets to generate radiation and generation three achieves this with insertion devices. In all three generations magnets are used to produce radiation. The origin of the radiation is a result of the distortion of near and far observed field lines around the electron when it is being accelerated. In the longitudinal direction, acceleration at relativistic velocities is small as it is asymptotic towards the speed of light. In the transverse plane, however, acceleration is larger thus when passing through magnetic fields particles are deflected transversely and emit radiation. The spectrum of light from a synchrotron is a broadband from infrared to hard and soft x-rays and reaches up to the critical photon energy

given by [14]:

$$\epsilon_c = \frac{3 \hbar c}{2 \rho} \gamma^3 \quad (1.21)$$

Bending magnets serve two purposes, the first is to direct the beam around the design orbit and secondly to generate radiation. This put limitations on accelerator design as both requirements need to be met. One way around this is to find other ways to generate light along the accelerator. Insertion devices are commonly used to do this and are inserted along straight parts of accelerator beam lines and comprise of an arrangement of magnets of alternating polarity. Such an array means electrons will oscillate as they travel down the beam line emitting synchrotron radiation. Insertion devices are broadly split into two categories, wigglers and undulators. The difference between the two comes down to their magnetic field strength. A parameter K is used when discussing insertion devices and is proportional to the magnetic field strength B [31]:

$$K \approx 0.934 \cdot B[T] \cdot L[cm] \quad (1.21)$$

Where L is the length of the insertion device. For a wiggler $K \gg 1$ and for an undulator $K \leq 1$ [32]. A good review of the differences between undulators and wigglers may be found in [32]. As a result of having stronger magnetic fields, wigglers have shorter oscillation periods compared to undulators. The wavelength of the emitted light can be written as [14]:

$$\lambda_L = \frac{\lambda_u}{2\gamma^2} (1 + K^2) \quad (1.22)$$

Where λ_u is the undulator period, i.e. the distance between same polarity magnets. As a result of larger amplitudes, wiggler radiation occurs in short bursts which can be delivered into experiments. The spectral distribution from wigglers is similar to that of bending magnets however since there are many oscillations a greater number of photons are produced. Undulator radiation as a result of its longer period leads to optical interference between emitted waveforms which mean narrow band spikes are delivered to experiments from waveforms which constructively interfere. This is summarised in figure 1.6 for bending magnets, wigglers and undulators [33].

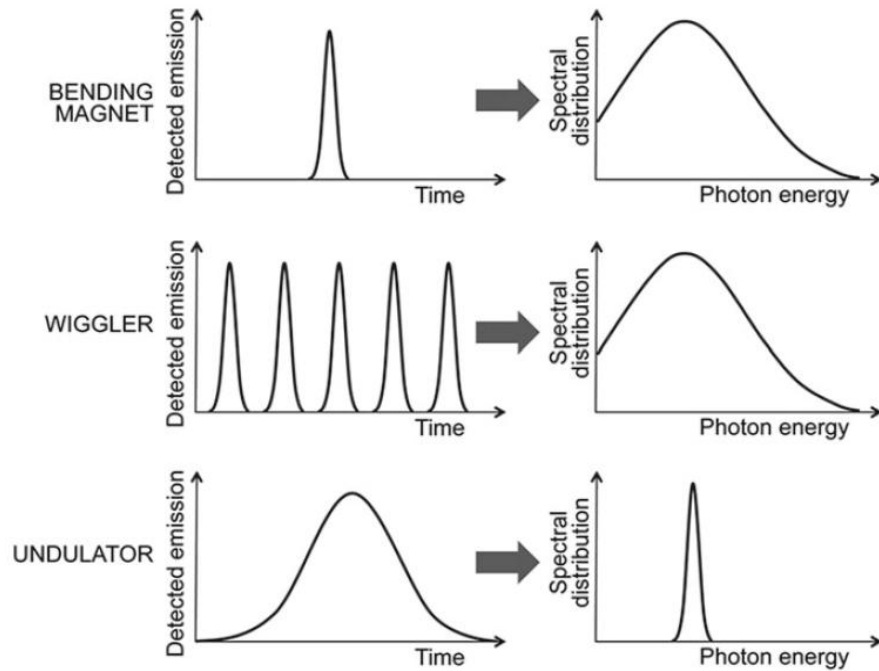


Figure 1.6 Profile of radiation produced by bending magnets, wigglers and undulator [33].

Fourth generation light sources are also referred to as free electron lasers (FELs). Examples of this generation light sources include the accelerator FLASH in Hamburg and machines such as the European XFEL, also based in Hamburg, and SwissFEL currently being commissioned at PSI in Switzerland. FELs also use insertion devices; however, their operation is slightly different to third generation light sources which use emitted light directly from insertion devices, FELs use the light generated in [33] insertion devices to condition the beam to generate even more photons.

The principle of operating an oscillator type FEL is shown in figure 1.7. The photons generated by an electron beam passing through an undulator are reflected back by mirrors in an optical cavity. The interaction between the reflected photons and the electron beam leads to a process called microbunching in which electrons move towards the nodes of the optical field within the cavity. This occurs due to a Lorentz force produced from the interaction of the transverse B field of the optical wave and transverse motion of the electron beam. This leads to some electrons losing energy to the optical field and others gaining energy from the field. Since microbunching occurs at the nodes the separation between bunches is one optical wavelength. The energy of the beam when this happens is called the resonant energy condition, γ_r . Typically in an undulator

the electrons emit incoherent light, however, due to microbunching coherence is achieved. This allows a high number of coherent photons to be produced frequencies below extreme ultraviolet.

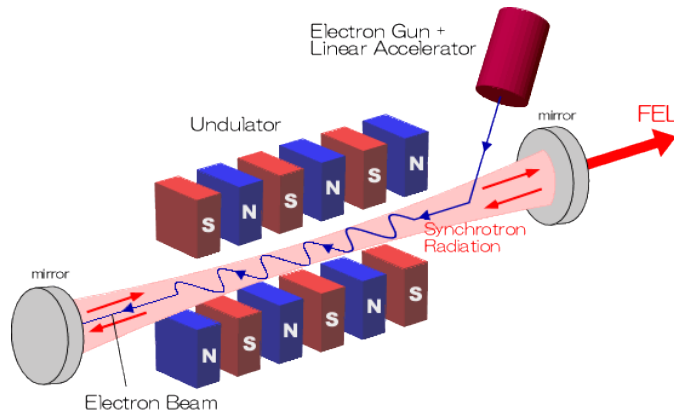


Figure 1.7: Operating principle of an oscillator type free electron laser [34].

At higher photon energies it is not possible to use mirrors due to material damage at these energies. To achieve X-ray FELs it is necessary to use self-amplified spontaneous emission (SASE) in which the mirrors are removed and long length undulators are used instead. In this scheme photons emitted in an undulator interact with electrons in front of the source electron [35]. Bunching is achieved from light produced further back and continues as the electron bunches travel further along the accelerator. The SASE concept lacks initial coherence and is noisy which can be avoided by external seeding with a laser [35]. This type of scheme is called an amplifier FEL and requires a long undulator and the high optical intensity is achieved in a single pass unlike the oscillator FEL.

By using a FEL it is possible to generate a high intensity laser with a narrow wavelength spectrum. Furthermore, the wavelength is tunable in that the energy of the beam can control the wavelength of light. FELs can be used to generate optical fields from infrared to hard x-rays.

A parameter often used when discussing light sources is the brilliance which is a measure of photon concentration and is given by the number of photons produced per second per angular divergence per electron beam cross section per photons within a bandwidth of 0.1% of the central photon wavelength. A high brilliance means a higher number of photons available to be used. Figure 1.8 shows the evolution in brightness achieved from each generation. An increase in brightness is clear. Dedicated accelerator facilities allowed beams to be designed for generating higher intensity light sources. This was then followed by insertion devices which

allowed even more photons to be produced. Finally FEL development has led to amplified emission of insertion device allowing even more photons to be produced.

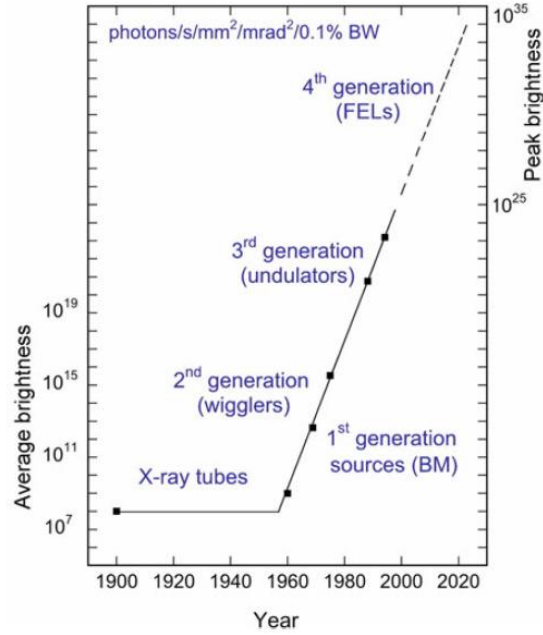


Figure 1.8: Increase in brilliance across four generations [33].

1.7.1.1 FEL Beam Requirements

To operate an FEL at a high efficiency it is necessary to optimise the electron beam in terms of energy, energy spread, emittance and current [36]. Although there is no exact upper limit on energy spread an accepted condition on energy spread is given by [36]:

$$\left| \frac{\Delta\gamma}{\gamma} \right| \ll \frac{2\gamma_r^2 \lambda_L}{1 + \frac{1}{2}K^2} \quad (1.23)$$

Furthermore, the emittance of the electron beam also needs to be small. Small emittances mean the beam is small in size. This ensures that the electron beam and optical beam overlap so there is full interaction between the two and the photons emitted from the electrons are coherent. This is described quantitatively as [36]:

$$\epsilon_n < \frac{\gamma\lambda_L}{\pi} \left(\frac{r_0}{w_0}\right)^2 \quad (1.24)$$

Where w_0 and r_0 are the beam waist and focus, respectively. From this relation it is clear to see the importance of transverse emittance for an FEL, it is possible to run an FEL at a lower energy with a smaller emittance. A review of current and future x-ray FEL developments are given in [37] which shows that for modern FELs emittance values of typically $< 1 \text{ mm}\cdot\text{mrad}$ are required. There has been a great push in recent years to improve the emittance of electron beams for this reason. Improvement to transverse emittance means less acceleration is required and so FELs can be shorter more readily available structures. Recalling back to Liouville's theorem, it is possible to see the importance of conserving beam quality along the accelerator from the source. For this reason a great deal of research and development has been focussed on electron sources with small emittances [38] both in the transverse and longitudinal planes. One such experiment is the transverse energy spread spectrometer (TESS) experiment based at Daresbury Laboratory. The next chapter will explore the concepts of electron sources and the TESS experiment will be described. Work will then be focussed in the subsequent chapters on the modelling of the TESS experiment, so its operation can be understood which in turn will give a better understanding of the emission process and therefore contribute to building better performing and shorter FELs allowing them to be used by a greater audience.

1.7.2 Future Linear Colliders

The standard model of physics describes the interaction of particles and forces which govern the basic building blocks of the universe. Particle accelerators are used to search for new particles either predicted by the standard model, look for new particles which may not be expected and to probe the fundamental forces which govern the standard model.

In terms of accelerator performance, two parameters are of interest in this field for particle physicists. The first is the energy of the colliding particles, the other is the luminosity which is related to the total number of collisions. The reason why the energy of the particles is important should be clear as it represents the energy required to make high mass particles. Due to a limited accelerating gradient, to achieve higher energies requires larger machines to be built.

Proton-proton collisions involve acceleration to the highest possible energy and searching

amongst the debris for particular interesting decays which lie within the data. Proton-proton collisions are messy and require a high amount of statistics to claim a discovery due to the large amount of background data. Electron-positron collisions are far cleaner and are usually performed once it is known where interesting physics occurs. The electrons are accelerated to energies where the interesting decays/particles are known to be found so more of these are created and more precise measurements of their properties can be taken. Research and development is already well under way into a future electron-positron collider to provide precision measurements of future discoveries. Since it is inefficient to reach high energies using circular accelerators due to synchrotron radiation a linear collider is the logical option.

1.7.2.1 Compact Linear Collider

A proposed accelerator is the Compact Linear Collider (CLIC) [39], figure 1.9. CLIC will not use superconducting cavities for acceleration but a novel acceleration method called ‘two beam acceleration’. In this method the main beam (MB) which is to be accelerated for collision is accelerated by another beam called the drive beam (DB) which is accelerated and decelerated. Energy is transferred to the MB through power extraction and transfer structures (PETS). A list of parameters of a full scale CLIC machine is given in table 1.1.

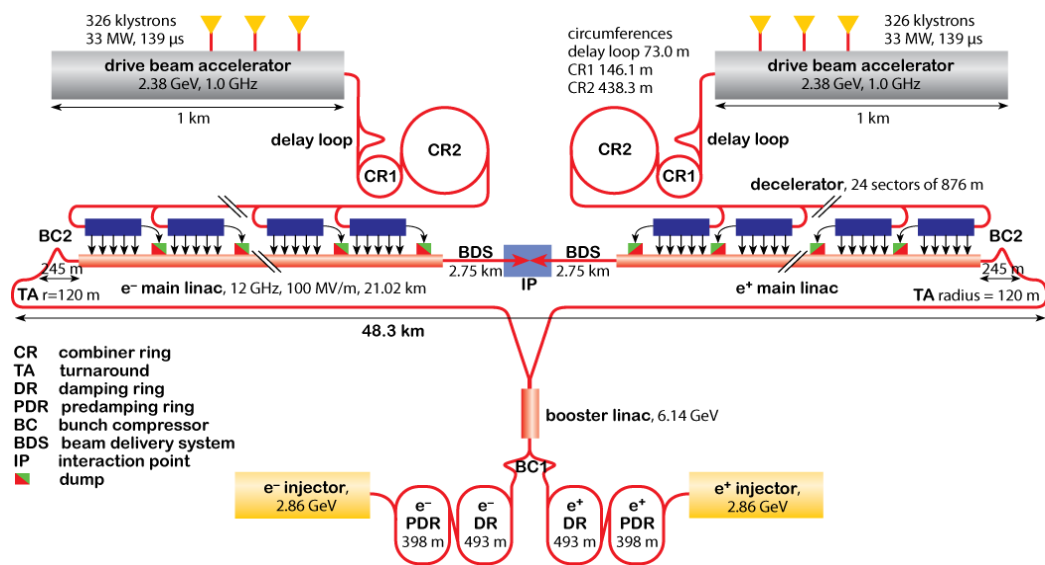


Figure 1.9: Overview of the CLIC 3 TeV layout [39].

Superconducting RF cavities are limited in the maximum accelerating gradient they can deliver, this means that to reach TeV energy scales would require large infrastructure. CLIC offers the opportunity to build a multi-TeV accelerator at an approximately similar scale to a competing project, the international linear collider, which uses superconducting technology at a lower centre of mass energy collisions. The novel acceleration scheme in CLIC is what makes it so unique. A beam going through an RF structure will excite an RF field within the structure and by doing this the beam loses kinetic energy. The beam generates a travelling wave within the PETS which is coupled at the end with a waveguide to the MB.

Table 1.1: Sample of CLIC parameters [39].

Parameter	Value
Centre of mass energy	3 TeV
Main beam frequency	11.944 GHz
Time between bunches	0.5 ns
Bunch train length	156 ns
Luminosity	$10^{35} \text{ cm}^{-2}\text{s}^{-1}$
Beam Power	14 MW

Each PET is designed so it extracts 136 MW peak power and generates 12 GHz of RF power to feed two accelerating structures. At CLIC the DB will have an initial energy of 2.38 GeV and will lose on average 144 MeV in each PET so after all PETS the beam has lost 84% of its power and is decelerated to a minimum of 239 MeV, 90% extraction [39]. To maintain acceleration the PET structures must remain operational. To achieve this, the CLIC design team aims for a breakdown rate of less than 10^{-7} /pulse/m which has been achieved in recent experiments [40].

The CLIC Test Facility 3 (CTF3) is a dedicated facility where the two beam acceleration concept has successfully been proven [41]. Recent work being done includes decreasing the breakdown rate of PETS. If too many PETS break down then further acceleration is not possible. It needs to be proven that this acceleration method is stable for continuous operation.

1.7.2.2 Diagnostic Requirements

Breakdown rates are critical for CLIC but there are many other issues which need to be addressed. To operate CLIC effectively it is necessary to understand the beam as it is accelerated. For example, as a result of the deceleration from the DB, large energy spreads can occur [42] in the MB which need to be understood. Also, the small beam size of a CLIC beam means better resolution is needed to observe the transverse profile of a beam in adequate detail. To this end diagnostics are required to understand the beam. Some of the devices intended to be used were never designed or untested to operate at parameters CLIC is aiming for. Furthermore, the energy of CLIC is unprecedented for a lepton collider and mishandling a beam of such intensity could have devastating consequences if it were lost from the beamline or if diagnostics were not designed to work at such a high intensity.

CLIC has been under design now for many years and the diagnostics being considered have either had to be conceived to measure this type of beam or adapted from old technology to perform the task. Non-invasive beam diagnostics are often sought after as they detect the beam with minimal disturbance to the beam itself. Along with the performance of a diagnostic device its location for installation is also a factor that needs to be considered as it is not possible to place detectors immediately next to the beam line as there are restrictions such as EM fields and vacuum systems. In the past few years [43] diagnostic development for CLIC has been targeted on: cavity beam position monitors [44], longitudinal beam profile monitors using electro-optical [45] and coherent diffraction [46] techniques and transverse profile monitors including laser wires [47], optical transition radiation [48] and gas jet based profile monitors [49]. Another area of diagnostics which has been highlighted in the CLIC conceptual design report as an important area is machine protection. If the high intensity beam were lost from the accelerator it could cause a lot of damage and halt operation of the accelerator. Beam diagnostic devices designed to monitor losses in an accelerator are called beam loss monitors (BLMs). The development of a CLIC beam loss monitor based on optical fibres is addressed in the third chapter of this work.

1.8 Chapter Summary

The purpose of this chapter was to introduce some key concepts with which an electron beam may be described, depict how an accelerator operates and to highlight areas which require development. The chapter is not a comprehensive introduction to electron accelerators, which

can be found in many textbooks, but rather aims to give a basis to particular concepts and to highlight the motivations behind later chapters. The next two chapters will have their own introductions which will further lay the foundations of results that will be presented.

It was seen that the beam emittance of an electron bunch is fundamentally limited by the emittance at the source. This has an importance consequence when trying to operate high brilliance free electron lasers. Chapter 2 will pick up the topic of electron sources and present studies into measuring the longitudinal energy distribution of photoemitted electrons.

It was also noted in this chapter that if a particle beam is poorly controlled then the beam size can become larger than the beam pipe which it travels through. If this were to occur then particles will collide with the walls and be lost from the beam. This will be addressed further in chapter 3 when detectors for measuring beam loss will be discussed. This will be in relation to the CLIC project and why it was necessary to present the background of that particular accelerator.

Chapter 2: Investigations into the Longitudinal Energy Distribution of Emitted Electrons

In chapter 1 the importance of beam quality was discussed in relation to operating state of the art free electron lasers. For these devices, good beam quality at the start of the accelerator is critical for operation. In this chapter the physics and technology of electron beam generation is presented along with work underdone to further improve the understand the longitudinal velocity component of emitted electrons. This is done using an experimental set up designed to measure basic properties of photocathodes which are a common source of electrons at current accelerator facilities. This work includes the development of a low energy tracking code which uses accurate field data to model the experiment to aid in the understanding of experimentally acquired data.

The chapter begins with an overview of electron sources and their current applicability at accelerators. Photocathodes are the most common electron source for fundamental research accelerators. The process in which electrons are emitted from photocathodes is covered as well as the specifics for choosing certain cathode materials over others, particular focus is placed on gallium arsenide as it is the photocathode material used in experiments and also holds several interesting properties. Techniques which are used to measure the beam properties of these cathodes at other facilities are then discussed.

The chapter then moves onto the Transverse Energy Spread Spectrometer which is an experiment built at Daresbury laboratory designed to measure the basic properties of photocathode materials. The design and operation of the set-up is presented along with an overview of previous experiments which were conducted to measure the transverse energy

distribution.

The main focus of this chapter is to assess the applicability of using TESS to measure the longitudinal energy distribution curve (LEDC). Two methods are discussed in which TESS may do this.

To understand the two methods proposed it was necessary to develop a tool set in which the experiments can be simulated. The first step was to understand the electric potential and fields generated around an electrostatic mesh. This is especially crucial when using one of the meshes as a retarding potential. At first an analytical solution of the electrostatic problem was sought after. As it will be shown the analytical approximation is not exact enough to be used, especially close to the mesh wires, however, it does offer some insight into the general far field solution. The next step was to find the potential and field values based on computer based methods using the finite element method.. Finally, to complete the simulation tool set, a tracking code for low energy electron transport has been developed in Matlab-Simulink. This allowed the computed field data to be used to track the particles through a realistic electrostatic field and to define different initial position and velocity distributions.

The chapter then closes with experiments undertaken to measure the LEDC using TESS and simulations performed to understand the results which are obtained and to understand the limitation of each technique. The merits and drawbacks of each technique are then described and improvements to the techniques based on simulation analysis are suggested and tested.

2.1 Electron Sources

The methods in which electrons can be prompted from a material can be classed into three possible types: photoemission, thermionic emission and field emission. In each case the electrons must overcome the energy required to move an electron from a material to the vacuum. The minimum energy to do this is called the work function, ψ . Each emission mechanism will now be discussed in turn with a particular attention on photoemission and to a lesser extent thermionic emission as they are both used in many types of light sources. Field emission sources are not used in large scale accelerator facilities due to manufacturing complications though research suggests that may be applicable in certain situations.

2.1.1 Field Emission Sources

Field emission occurs as a result of a quantum effect in which an electron is able to tunnel through the Coulomb barrier due to a reduction in the work function, from a high potential. The current density, J_{field} , from a field emission source is found from the rate of electrons moving towards the surface and the tunnelling probability to travel through the potential barrier (developed by Fowler and Nordheim) where there is an electric field F at the tip, leading to the equation [50]:

$$J_{field} = \frac{q_e^2}{8\pi h \psi} F^2 \exp\left(\frac{-4\sqrt{8\pi^2 m_e} \cdot (q_e \psi)^{3/2}}{3h q_e F}\right) \quad (2.1)$$

Field emission is an important property to understand in accelerator physics for detrimental effects such as multipacting in cavities [51]. In terms of use as an electron source they are being considered for future light source injectors. They are considered a true cold source of electrons as thermionic and photoelectric cathodes require energy to be given to the electrons to extract them whilst field assisted electrons are not given energy to overcome the barrier and so should have much smaller energy spread. Current research is focused on double gated arrays of small metallic tips, field emitter arrays (FEA). A single tip will emit 1 mA from an area as small as 30 nm [52]. This current is too small for most applications so $10^4/10^6$ tips are arranged in an array to produce high currents [53]. A first metallic gate provides the extracting potential whilst a second gate focuses each individual beamlet to produce a parallel beam. Energy spread in this arrangement of tips comes from: the energy spread due to tunnelling, space charge effects, energy spread introduced by the radial emission from the tip and potential variations between tips [53]. Further limitations come from fabrication tolerances, impurities and erosion due to back sputtering from residual gases. For these reasons the technology is not yet mature enough to be used in any user facility but there are plans for this source to be installed in a future SwissFEL upgrade [54].

2.1.2 Thermionic Sources

Electrons are emitted from a cathode when they are given sufficient thermal energy to overcome

the work function. The outermost valence electrons in a metallic bond are nearly free and held to the positive nucleus by the Coulomb force. At low temperatures electrons around a nucleus are ordered by Fermi-Dirac statistics up to the Fermi energy E_f , however at higher temperatures the Fermi-Dirac distribution can be replaced by the Maxwell-Boltzmann distribution because electrons have enough energy to occupy many different energy states so electrons are not forced into different states as a result of the exclusion principle. The current density of electrons from a thermionic cathode is found as the integral of all possible velocities that the electrons can have from the Maxwell-Boltzmann distribution multiplied by the total number of electrons and the charge of the electron. Performing these integrations the total current, J_D , as a function of temperature, T , is described by the Dushman equation [55]:

$$J_D = \frac{-q_e m_e}{2\pi^2 \hbar^3} T^2 e^{-\frac{\psi}{k_B T}} \quad (2.2)$$

Sometimes a factor of $(1-r)$, where r accounts for the reflectivity off the surface, is included in front of the exponential term. After escaping the metal, electrons are accelerated away by an electric field, V_A , applied to the surface by an anode located at distance b away from the cathode surface. The field reduces the work function by a factor $\Delta\psi$ where $\Delta\psi = \sqrt{V_A q_e^3 / 4\pi\epsilon_0}$ and increases the thermionic emission current. This is commonly referred to as the Schottky effect and is valid up to fields where field emission effects are no longer negligible. The maximum current output from a thermionic cathode is limited by space charge effects between emitted electrons and those in the metal which makes it difficult to extract more electrons to the vacuum. The result is known as the Child-Langmuir limit, J_{C-L} , which is given by [55]:

$$J_{C-L} = \frac{4\epsilon_0}{9b} \cdot \sqrt{\frac{2q_e}{m_e} \cdot V_A^2} \cdot V_A^{\frac{3}{2}} \quad (2.3)$$

The thermal emittance of a thermionic cathode is found from equation 1.19. In which the spatial co-ordinate is defined by the cathode size and the divergence is related to the velocity of the emitted electrons. The rms beam size, $\sigma_{cathode}$, is half of the cathode radius R and the rms divergence is found by: $\sigma' = \sqrt{\langle v^2 \rangle} / \beta\gamma c$ [15] where γ and β are the relativistic Lorentz factor

and fraction of the speed of light respectively. The mean squared transverse velocity for a Maxwell distribution is calculated to be $\langle v^2 \rangle = K_B T / c$. The thermionic emittance, $\epsilon_{Thermionic}$, of a thermionic cathode is given by [55]:

$$\epsilon_{Thermionic} = \sigma_{cathode} \sqrt{\frac{K_B T}{m_e c^2}} \quad (2.4)$$

The two most common thermionic materials used in accelerators are lanthanum hexaboride, LaB₆, and cerium hexaboride, CeB₆ [56] which both have high electron emissivity with work functions around 2.5 eV and are robust to poisoning. The thermal emittance reported for CeB₆ is around 0.6 π mm·mrad at $T = 1400$ K with a cathode diameter of 3 mm which is close to the value predicted from theory, 0.4 π mm·mrad [57].

Thermionic sources are preferred electron sources for DC beams as they can generate high currents, good values of emittance and are straightforward to maintain. Their downfall comes when pulsed beams, mandatory for FEL operation, are required as bunching cavities are needed and so photocathodes are preferred in this case.

2.1.3 Photoemission Sources

Photoemission of electrons from metals with ultraviolet light was initially explained by Einstein in 1905 [58]. In this process electrons are emitted from a material when irradiated with electromagnetic radiation above a threshold energy related to the work function. Radiation below the threshold raises orbital electrons to a higher state before falling to a lower state resulting in which a photon with an energy equal to the difference between the two orbital states being emitted. The energy of a photon can be written in terms of the wavelength λ or in terms of the angular frequency ω . The kinetic energy, E_k , of the emitted electrons which overcome a work function of the material is given by the well known equation:

$$E_k = \frac{hc}{\lambda} - \psi \quad (2.5)$$

2.1.3.1 Three Step Model

In 1964 Spicer put forward a 3 step process in which to explain photoemission, figure 2.1, in summary these three steps are [59].

- 1) Absorption of a photon and excitation of an electron
- 2) Transport of the excited electron to the bulk surface
- 3) Overcoming the surface potential and escape to the vacuum

In order to understand the quality of a beam produced from a photocathode it is necessary to understand each step.

Step 1 deal with the absorption of the energy of a photon. It was initially thought that photoemission was a surface effect [60]; however photons travel a short distance inside the material before being absorbed. It is entirely possible that an electron can absorb two photons however the cross section for this interaction is small.

Step 2 describes the process in which electrons migrate to the surface. Not all of the electrons excited in the first step necessarily make it to the surface. Collisions may occur, leading to energy loss, which could mean electrons have insufficient energy to continue. In metal photocathodes, such as copper and aluminium, electron-electron collisions are more likely due to the abundance of free electrons in the structure. Such a collision is non-elastic and as the photon energy is usually less than two times the work function collisions between two electrons will mean neither electron can escape. For this reason metal photocathodes have poor efficiencies because only electrons that have avoided any collision in the bulk are able to escape the barrier at the surface. In semiconductor photocathodes, such as gallium arsenide (GaAs) and caesium telluride (Ce_2Te) electron-electron scattering is uncommon, only becoming negligible when the photon energy is 2-3 times the band gap energy [59], however, electron-phonon scattering is more prevalent in these materials. Electron-phonon scattering is a quasi-elastic process, meaning energy transfer is small, so the scattering process is not enough to prevent emission due to energy loss.

Step 3 concludes with the emission of an electron to the vacuum. To improve the yield of electrons in this step, two methods can be implemented. The first is to apply a potential to the surface of the cathode, again the Schottky effect. This is standard in electron guns because it is ideal to accelerate the electrons away from the cathode to stop emittance blow up due to space

charge. The second method involves chemically treating the surface to reduce the electron affinity at the surface. This process is known as band bending. The three steps are shown in figure 2.1 in a band structure diagram.

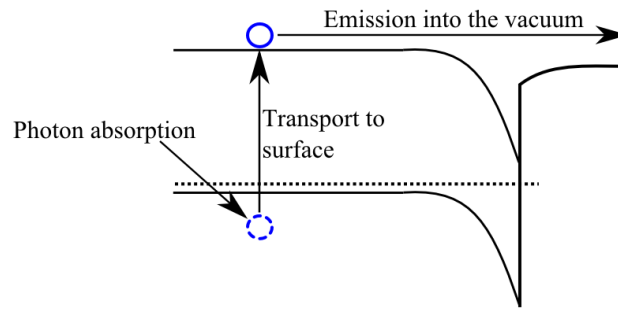


Figure 2.1: The Spicer 3 step model of photoemission in this case for a semiconductor photocathode. Photoemission can be explained over three stages. 1) Absorption of a photon 2) Transports to the surface 3) Escape to the vacuum.

By splitting the aspects up in this manner the physical interactions can be broken down and explained simply before combining them to describe the process as a whole. A more accurate model in which the whole process is explained in one step does exist [61]. In this formalism photoemission is described as the transmission of an electron between two quantum states due to an electromagnetic perturbation, i.e. a laser. However the model is less intuitive and is only used in specialised circumstances [62].

2.1.3.2 Band Structures

The emission of electrons from materials can be explained numerically by considering their band structures which are shown in figure 2.2 for metals and semiconductors.

The work function is defined for metal cathodes, figure 2.2 left, as the energy difference between the Fermi level E_f and the vacuum level E_v .

For semiconductors, figure 2.2 centre and right, the workfunction is defined as the energy difference between the valence band maximum E_{VBM} and the vacuum level. A further distinction can be made for semiconductors based on the position of the vacuum level with respect to the conduction band minimum E_{CBM} . They are split into positive electron affinity (PEA) and

negative electron affinity (NEA) photocathode. The vacuum level in NEA cathodes, figure 2.2 centre, is below E_{CBM} whilst for PEA, figure 2.2 right, it is above E_{CBM} . An NEA cathode is produced by coating the surface of the cathode with a p-doped, electron acceptor, material which forms a strong dipole at the surface lowering the vacuum level. To keep a continuous link between the conduction/valence band and the vacuum level they must bend downwards whilst the Fermi level is unaffected. A good example of this is GaAs doped with oxygen or fluorine. GaAs is intrinsically a PEA cathode however upon doping an NEA band structure can be achieved.

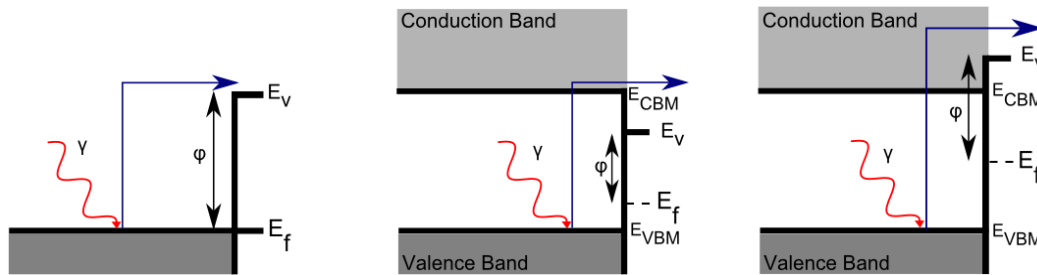


Figure 2.2: Band structures of different types of photocathodes. Left) Metal photocathode. Middle) Negative electron affinity photocathode. Right) Positive electron affinity photocathode.

For PEA cathodes it is energetically impossible for an electron at the CBM to escape to the vacuum. In NEA cathodes electrons can scatter with phonons before being emitted. This means they are thermalised and reach the ambient temperature before escaping. This offers a way of generating electrons with small thermal emittances. This does mean, however, that the emission is delayed by several picoseconds, whilst it is scattering in the band bending region. In this case the thermal emittance of a cathode is the same as in equation 2.4. The thermalisation of electrons in NEA cathodes from the conduction band to the vacuum level can mean that electrons are emitted with small transverse energies. This is only true for small incident photon energies. For higher energies, the emitted electrons will be a mixture of prompt and delayed electrons.

2.1.3.3 Theoretical Thermal Emittance

An approximation of the theoretical normalised transverse emittance can be defined for a metal photocathode in terms of the rms laser spot size on the cathode, σ_{RMS} , the laser energy $\hbar\omega$ and

the effective wavefunction ψ_{eff} [63]:

$$\frac{\epsilon_n}{\sigma_{RMS}} = \sqrt{\frac{\hbar\omega - \psi_{eff}}{3m_e c^2}} \quad (2.6)$$

Where the effective work function takes into account the material work function and the reduction of the work function due to the Schottky effect when a field E is applied to the surface:

$$\psi_{eff} = \psi - q_e \sqrt{\frac{q_e E}{4\pi\epsilon_0}} \quad (2.7)$$

For a semiconductor cathode the thermal emittance is defined in terms of the band gap energy E_G and the electron affinity E_A [64]:

$$\frac{\epsilon_n}{\sigma_{RMS}} = \sqrt{\frac{\hbar\omega - E_G - E_A}{3m_e c^2}} \quad (2.8)$$

Experimentally it is usual to quote transverse electron emission properties in terms of mean transverse energy (MTE). This is related to the accelerator emittance unit, i.e. in terms of mm·mrad by [65]:

$$\epsilon_n (mm \cdot mrad) = \sigma_{RMS} \cdot \sqrt{\frac{MTE}{m_e c^2}} \quad (2.9)$$

2.1.3.4 Typical Photocathode Properties

Table 2.1 below shows a variety of different photocathodes used in accelerators along with the typical quantum efficiency, number of electrons out compared to incident photons often shortened to QE, which can be expected from them, as well as the laser wavelength and typical lifetime of the photocathode.

As previously mentioned, metal photocathodes have very low quantum efficiency, however, they

last many months/years as their structure is not damaged by back travelling ions accelerated towards the cathode. Also, as a result of electron-electron scattering the electrons which are able to escape the material are those which originate close to the surface, as they were less likely to scatter due to a shorter distance to travel. This means metal photocathodes are prompt emitters, which is useful for bunching purposes. A further downside of metal photocathodes is that the low QE means a high power laser is required and furthermore due to a higher band gap the laser needs to be in the UV range which is more difficult to work with [66].

Semiconductor photocathodes have much higher QE (> 5%) but are far more fragile and susceptible to damage due to back bombardment [67] and so require more stringent vacuum requirements. The response time of semiconductors is good but not as fast as metal cathodes and largely depends on photon energy due to different penetration depths, emission time can be from 1 picosecond to over 100 picoseconds. Laser requirements of semiconductor photocathodes are less stringent than metal photocathodes due to smaller band gaps between the conduction and valence band. The laser wavelength required is typically in the visible spectrum which is easier to work with. An exception is alkali telluride cathodes which require UV to near UV laser wavelengths [68].

Only approximate values of cathode lifetimes can be given. Cathode performance will decrease over time due to contamination. It is usual to quote lifetimes in terms of reduction in QE by a factor of 1/e. Cathode lifetimes depend on the charge with which it is operated and the quality of the vacuum.

Table 2.1: Commonly used photocathodes covering both metal and semiconductor varieties

Material	Type	QE (%)	λ (nm)	Approximate Lifetime	References
Mg	Metal	0.06	266	Months	[69]
Cu	Metal	0.0014	250	Months	[70]
Cs ₂ Te	SC-PEA	4-20	211	Weeks	[71]
Cs ₃ Sb	SC-PEA	0.4-4	432	Weeks	[72]
K ₃ Sb	SC-PEA	7	400	Weeks	[73]
GaAs (Cs-O)	SC- NEA	0.2	532	Days	[74]

2.1.3.5 Gallium Arsenide

Gallium arsenide warrants its own mention firstly because it is the cathode material used in experiments covered later in this work and secondly for its unique application as a spin polarised source of electrons. GaAs is a direct band gap semiconductor which means that the momentum vector of the conduction band and valence band are aligned. Presently GaAs is the only cathode capable of producing a polarised electron beam. An electron's spin can either be up or down. Generally the ratio of each spin of electrons emitted from a photocathode is 50% with no spin state preferred. A polarised source is one in which the ratio between the two spin states is not equal. Polarised electron sources could have practical benefits in condensed matter physics [75] and also high energy particle physics [76].

In the 1970s it was first proposed [77] that GaAs may be a source of polarised electrons. Under illumination of circularly polarised light, electrons can transition from the $P_{\frac{3}{2}}$ or $P_{\frac{1}{2}}$ state to a positive or negative $S_{\frac{1}{2}}$ state. The sign of the initial transition state depends on the direction of polarisation, left or right. Upon mechanical straining, the stretching of the bonds further than their usual interatomic spacing causes a small shift in the valence band states such that the energy of the photon can realistically be adjusted to allow one transition type only. This is how a polarised electron beam is obtained with theoretically 100% polarisation. Experimentally 90% polarisation has been achieved with 85% achieved over a long time period [78].

As a result of this interesting property, GaAs has been extensively studied. Furthermore to its spin characteristics, its NEA activated state also offers beams with small energy spreads which has further increased interest in this material. Even though it has been studied in many different experiments, the results of emission characteristics are different from paper to paper. It is generally agreed that GaAs has a narrow cone of emission with an angle of $\sim 15^\circ$ [79], however, other groups report not seeing this phenomenon [80]. In the next half of this chapter an experiment is described which attempts to measure the properties of GaAs and other photocathodes under controlled conditions.

2.2 TESS Experiment

One such experiment investigating this is the Transverse Energy Spread Spectrometer (TESS) experiment located at Daresbury laboratory. TESS is an experiment designed and commissioned

by ASTeC with the aim of measuring basic properties, principally the emittance and, of cathode materials of both semiconductor and metal varieties. TESS is designed to measure the transverse energy of electrons emitted from a photocathode under conditions that will allow emittance to be measured without perturbing effects which can lead to emittance growth in an accelerator. The figure shows the basic working principle of TESS in which stimulated electrons are emitted from a cathode and accelerated to a detector system. TESS has been designed to be completely symmetric and block stray electric and magnetic fields which could affect electron trajectories. Figure 2.3 shows a schematic of how TESS works to measure electrons using a camera.

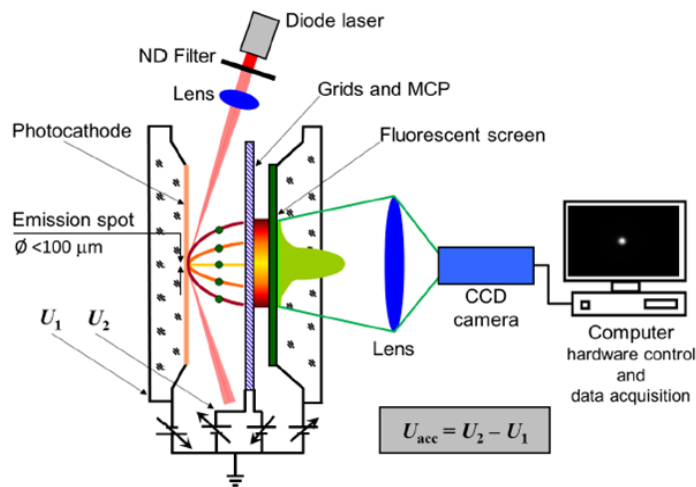


Figure 2.3: Working principle of the TESS experiment. Courtesy of Lee Jones, ASTeC, STFC.

Wire meshes are used to accelerate electrons away from a photocathode towards a detector system. By carefully selecting the potential of the wire meshes and analysing the electron distribution at the detector, the initial properties of the electrons at the point of emission can be studied. In the following sections the process in which a photocathode is prepared is outlined, the TESS apparatus is described, previous commissioning results of the transverse energy spread are presented before continuing with a discussion on how TESS can be used to measure the longitudinal energy spread of the initial energy distribution.

2.2.1 Photocathode Preparation

Photocathodes are prepared using the photocathode preparation facility (PPF). It was designed to allow cathodes to be prepared and transported to an accelerator without exposure to potential contaminants which could lead to poisoning and limit cathode performance. Figure 2.5 shows the PPF during the commissioning process. The PPF comprises of three chambers: the Loading Chamber, the Hydrogen Cleaning Chamber, and the Preparation Chamber which the cathode moves through, using a magnetic manipulator, in turn before transport to the final destination. A more detailed description of the PPF, operation and the commissioning is given in [81]. The GaAs has an active area of 9.5 mm and is bound to a 1.4 mm recess on the bottom of a upturned 2 mm molybdenum petri dish with height 6.5 mm and diameter of 19 mm [82], figure 2.4.

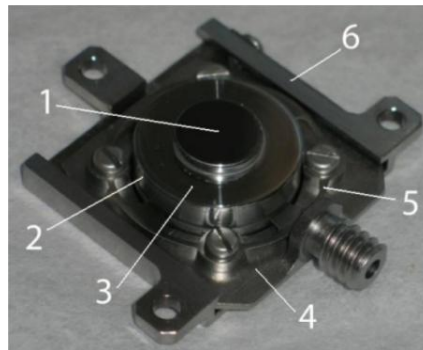


Figure 2.4 Cathode holder used in TESS and the PPF. (1) Cathode active area (2) Molybdenum petri dish (3) Polished surface flow (4) Transport holder (5) Spring (6) installation socket [82].

The polished surface surrounding the cathode improves heat flow generated by high powered lasers. The cathode is first chemically etched with hydrochloric acid to remove oxides which form on the surface. The photocathode is transported to the Loading Chamber on a z-translation stage in a nitrogen environment to prevent oxidation of the surface. The Loading Chamber is then pumped down using an ion pump to a pressure of 10^{-9} millibar and then heated to $\sim 150^{\circ}\text{C}$ in a process called 'bake out' in which water molecules are outgassed and extracted with a vacuum pump. The photocathode is then moved to the Hydrogen Cleaning Chamber for further cleaning to prepare it for activation. Atomic hydrogen, when heated to high temperatures, cleans the surface without large damage to the cathode material. The conventional technique without

hydrogen cleaning requires heating up to 600 °C to remove more difficult to remove oxide species. However, with hydrogen irradiation they are converted to more volatile molecules and only a further bake of 450 °C is required. This method has been shown to produce better results compared to the conventional technique [83]. In the Preparation Chamber the photocathodes are activated with alternating layers of caesium and pure oxygen or nitrogen trifluoride (NF₃) known as the 'Yo-Yo' process. With NF₃ it has been found that a consistently higher QE can be achieved compared to O₂ but it is inherently more dangerous to handle [84]. The caesium is deposited onto the photoemissive material by the sublimation of solid caesium dispensers whilst the O₂/NF₃ is introduced from an outer canister through a piezoelectric leak valve. During this process a 635 nm laser illuminates the photocathode and the photocurrent is measured. The yo-yo process is repeated until the photocurrent saturates. The final QE is established by the laser energy and the measured photocurrent. The photocathode plug is transported under a load lock mechanism thereby preserving the vacuum.

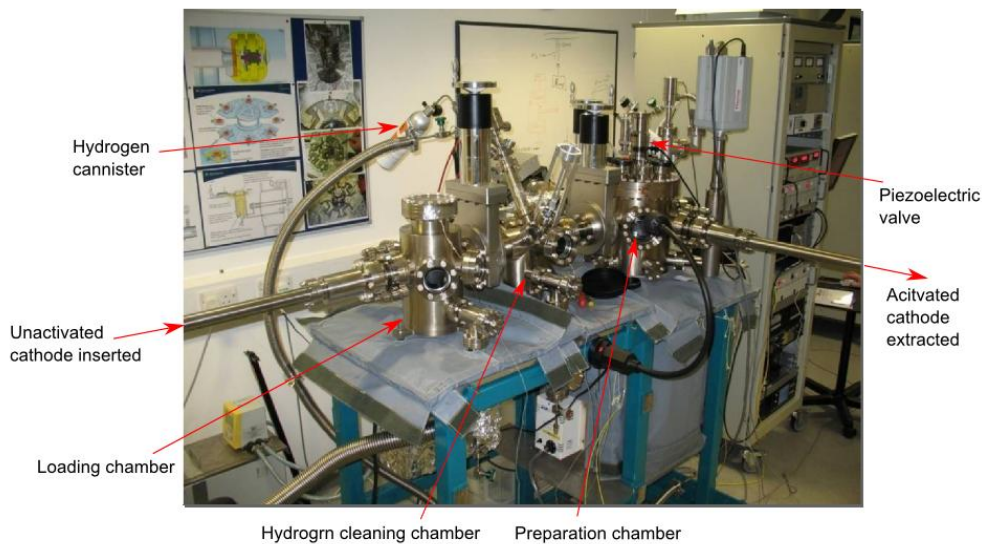


Figure 2.5 Photocathode preparation facility built to prepare GaAs to a high quantum efficiency.

Once the cathode is prepared it is passed to the TESS chamber. The main components of TESS are the cathode holder, three gold coated tungsten wire meshes, a detector system composing of a two stage multi channel plate (MCP) detector, Phosphor screen and a CCD cameras, a μ -metal shield and cryogenic pipes. When a prepared cathode is placed into TESS electrons are emitted from the cathode when prompted by an external laser source directed towards the cathode.

2.2.2 TESS Set-up

The laser is focused onto a small spot using lenses and hits the cathode at a grazing angle of about 17° . This angle occurs due to the fixed geometry of the system. This angle is defined by the geometry of the cathode position and the entry view port the laser enters the chamber. The laser spot size on the cathode surface is measured in a diagnostics section on a virtual cathode to be between $40\text{-}80\ \mu\text{m}$ FWHM, however, due to the grazing angle the spot on the cathode is more elliptical than circular. The set up allows several different diode lasers to be used in the set up at low power (sub mW) in CW mode. From equation 2.25 this means electrons will have different energies when emitted from the cathode and also different energy spread. Neutral density (ND) filters are used to attenuate the laser so only a low intensity beam is generated. The filters used have a combined maximum value of 7 corresponding to a minimum transmission of $10^{-5}\%$. Electrons from the cathode are accelerated away from the cathode towards the meshes due to the potential difference between them. The mesh is photoetched from a tungsten sheet and is $35\ \mu\text{m}$ thick. The cells in the mesh do not form a square but have a small bending radius. The thickness of the metallic wires is $50\ \mu\text{m}$ and the cell pitch is $500\ \mu\text{m}$. The meshes are coated with gold because the secondary electron yield is lower in gold than in tungsten for electron energies less than $1\ \text{kV}$ [85]. Figure 2.6 shows a schematic of the wire meshes. The distances between the first and second mesh is $1.3\ \text{mm}$ and between the second and third it is $1.4\ \text{mm}$. Four non-magnetic, electrically insulated supports keep the meshes in place. Figure 2.7 shows the layout of TESS from the cathode to the detection system front.

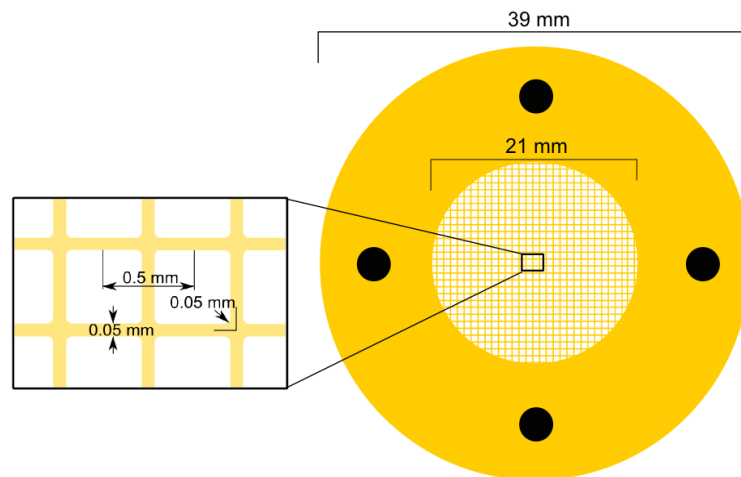


Figure 2.6: TESS mesh plate. The inset shows the finer structure of the mesh .

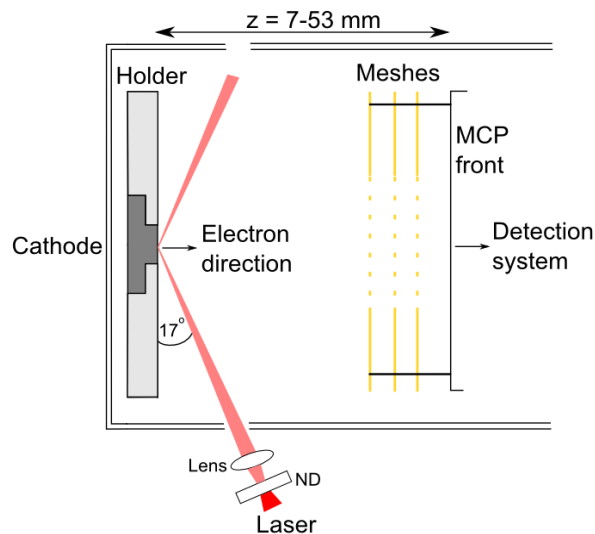


Figure 2.7: The first stage of the TESS experiment from the cathode to MCP front.

Once the electrons pass through the meshes they are detected by a combination of a two stage multichannel plate (Hamamatsu F1094-01), phosphor screen (P43 ITO type) and a 14 bit CCD camera (PCO.2000).

A multichannel plate (MCP) is a high resistive metal plate with a regular array of tubes, microchannels, running through it with a voltage difference between the front and back of the detector. The MCP works as an electron multiplier where an electron is accelerated and hits the wall of the microchannel generating further electrons. The high voltage then accelerates these electrons in a cascade effect where the final signal is much higher than the input signal. TESS uses a two stage MCP which has higher gain compared with a single stage MCP, about $10^4/10^7$. However, this leads to a worse position resolution with a spatial resolution quoted to be in the region of 80-100 μm for the two-stage MCP and between 40-50 μm for the single stage. The MCP channels are 12 μm on a 15 μm pitch which gives an open area ratio of 60% [86]. The distance between the third mesh and front face of the MCP is 2.3 mm.

The phosphor screen converts the electrons into photons which are then focused onto the CCD camera. The screen is composed of grains of $\text{Gd}_2\text{O}_2\text{S:Tb}$, 6 μm in thickness and a grain size of 2-3 μm , which emit light when energy is deposited. A phosphor screen will produce between 20-600 photons per incident electron depending on the kinetic energy of the electron [87]. An indium-titanium-oxygen (ITO) layer shields the screen due to electrostatic effects on the screen

caused by electrons and ions. P43 screens, the number refers to the composition, have higher quantum efficiencies compared to other screen types but is slower, however, timing is not important in this application and P43 is at peak emission wavelength at 543 nm. The phosphor screen and MCP combination result in a spatial resolution between 80 and 100 μm . [88]

A PC0.2000 [89] CCD camera collects the photons generated by the phosphor screen and converts them into electrons which are measured. The camera is cooled to -40° and has a 2048 x 2048 pixel array. The charge collected by each pixel is converted to a digital number with each count equal to 2.1 electrons [90]. Using this matrix the image can be analysed numerically and noise limits can be established. The quantum efficiency of the pixels is $\sim 50\%$ and peak wavelength detection efficiency at 543 nm which matches the phosphor screen emission peak. The camera and lens system is vibration free allowing long camera exposure times. A Tamron [91] f3.5 180 mm imaging lens is used to magnify the image onto the pixel array. The detector system set up is shown in figure 2.8.

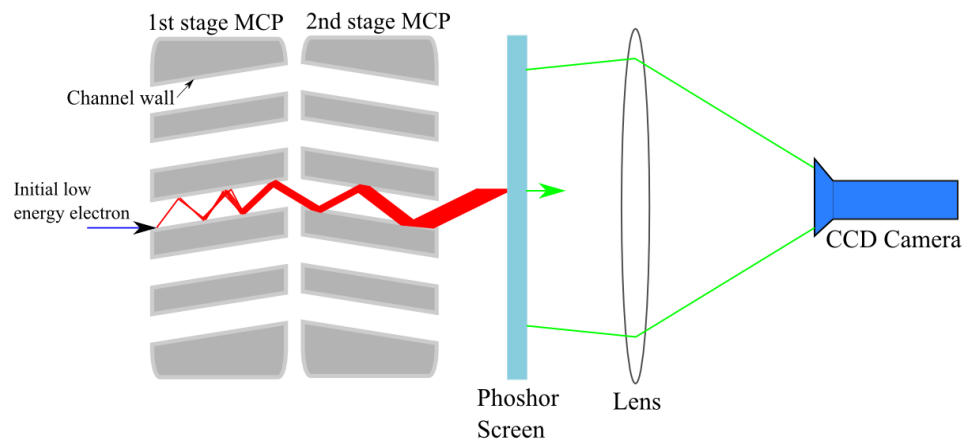


Figure 2.8: Second step of the TESS experiment in which an electron is detected. A two stage MCP amplifies the signal which then hits a phosphor screen generating photons. The light is then focused onto a CCD camera which is recording over a long exposure time

The detector head (meshes and MCP) is held in the chamber by the support shown in figure 2.9. The meshes and MCP are connected to external power supply units through metal high voltage conductors which are held in place around the steel supports and connected to the detector and flange feed through by safe high voltage 10 kV coaxial connectors. The meshes are limited to a maximum potential of 1kV and the first mesh and the detector front plate are electrically

common. The cathode holder and the shielding are at the same potential which produces a flat electric field in the drift region. The phosphor screen is operable up to 6 kV. The front back voltage of the MCP is limited to 2 kV which provides the high gain. The mesh-detector assembly is placed on a moveable stage so the distance from the photocathode to mesh 1 can be varied from 7.5 mm to 50 mm.

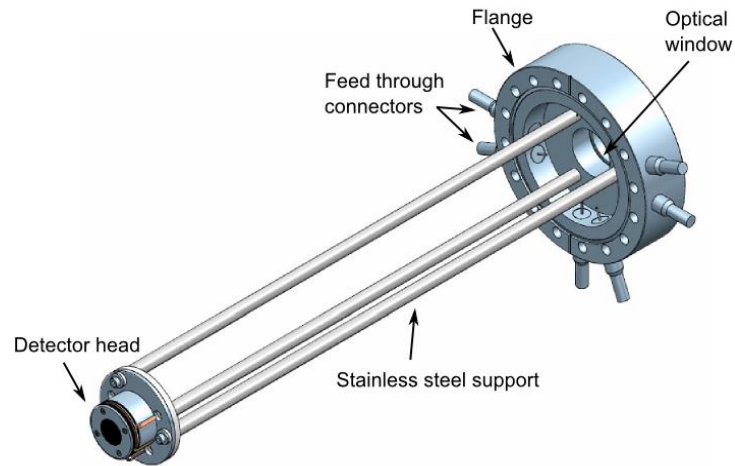


Figure 2.9: Support holding the meshes and detector to the flange. Connections are made through feed through connectors around the flange and transported to the detector head. Courtesy of STFC.

Installed around the inner elements of the detector system is a μ -metal shield to block external magnetic fields for example those generated by earth. However, the system is not blocked at the front and back i.e. only the curved section is covered. Additional installations include cryogenic cooling so liquid nitrogen temperatures can be reached and a piezo-electric valve which allows controlled degradation of the cathode and therefore control of the quantum efficiency

2.2.3 Transverse Measurements

Measurements of the transverse energy spread of electron emission were performed as part of the commissioning of TESS [88] and were performed outside of the work presented in this thesis. However, since the transverse properties will be required in later chapters the results are presented here as well as a brief summary of the analysis.

An electron emitted from a photocathode will have two velocity components, one in the

transverse plane and the other in the longitudinal plane, figure 2.10. The total energy, found by the sum in quadrature of the velocity components, is given as the sum of the transverse and longitudinal energy. This is further expanded upon in appendix A.

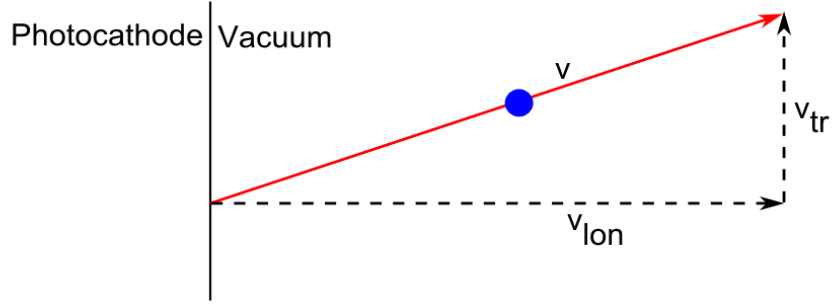


Figure 2.10: Electron emission from a photocathode to the vacuum. The initial velocity components can be described by a longitudinal and transverse component.

As a result of the transverse energy, electrons will move radially outwards the more transverse energy they have. The transit time, τ , from the photocathode to the MCP front face is a function of the distance d between the photocathode and MCP, the acceleration voltage U_{acc} and the longitudinal energy of the electron ϵ_{lon} and can be written as [92]:

$$\tau = d \cdot \sqrt{\frac{2m_e}{q_e U_{acc}}} \cdot \left(\sqrt{1 + \frac{\epsilon_{lon}}{q_e U_{acc}}} - \sqrt{\frac{\epsilon_{lon}}{q_e U_{acc}}} \right) \quad (2.10)$$

For high accelerating voltages, the energy gain due to the electrostatic field is much higher than the initial longitudinal energy i.e. $q_e U_{acc} \gg \epsilon_{lon}$. In this case equation 2.10 can be rewritten as:

$$\tau = d \cdot \sqrt{\frac{2m_e}{q_e U_{acc}}} \quad (2.11)$$

In the transverse plane the electron will move radially away from the point it was emitted. The point at which the electron hits the MCP is a radial distance r away from the point of emission

and is a function of the transit time and the transverse energy ϵ_{tr} of the electron:

$$r = \sqrt{\frac{\epsilon_{tr}}{2m_e}} \cdot \tau \quad (2.12)$$

The influence of the transit time which in turn is inversely proportional to the accelerating voltage means that for higher accelerating voltages the radial growth is smaller.

To establish the transverse energy distribution the centroid of the image recorded on the CCD is found (i.e. $r = 0$) by taking the peak value of the CCD matrix and deriving a radial distribution of intensity $I(r)$ around this. Using the relative intensity from the centroid, i.e. little or zero transverse energy, the spread of energies can be found. The derived radial intensity function represents the number of electrons incident in a ring with radius r and thickness δr . To convert the radial distribution to an energy distribution the displacement from the centroid is used and calibrated by normalising to the maximum value. From analysing images alone with suitable background correction the transverse energy distribution spread can be found. Further information on the transverse analysis procedure can be found in [88] and [92].

This was performed for two different wavelengths, 635 nm and 532 nm, and two different accelerating potentials. The results are shown in figure 2.11. The results are fit to a decaying exponential:

$$N(\epsilon_{tr}) = N_0 \cdot \exp\left(\frac{-\epsilon_{tr}}{MTE}\right) \quad (2.13)$$

Where N_0 is the peak intensity and MTE is the mean transverse energy at the 1/e value. The MTE of electrons emitted from the cathode for the 635 nm laser was $MTE = 45 \pm 7$ meV and for the 532 nm laser it was $MTE = 100 \pm 15$ meV. The results show that for the shorter wavelengths the MTE is larger which is to be expected as the electrons should have higher remaining kinetic energies after being emitted. The GaAs photocathode used was activated to 2 % quantum efficiency, making it a PEA cathode and the experiments were performed one after the other to avoid decrease in QE due to contamination. Further experiments have been performed to measure the response due to contamination using the piezoleak valve [93]. These experiments were performed at room temperature yielding a kT value of 25 meV and the MTE

measured in these experiments were greater than this value.

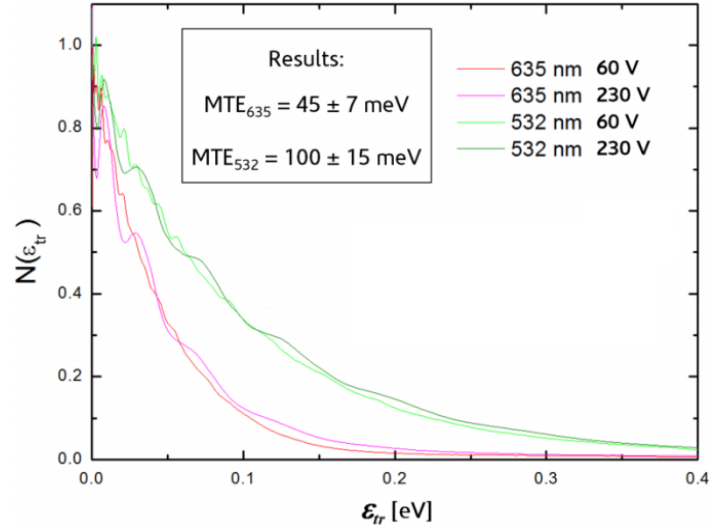


Figure 2.11: Experimentally obtained transverse energy distribution curves using TESS for two different wavelengths and two different accelerating potentials [88].

2.3 Longitudinal Experimental Technique

Whilst most studies on photocathode sources for accelerators are focussed on transverse emittance, less has been mentioned in literature about the initial longitudinal emittance. From the process of emission there is no doubt that there is a coupling of the two and greater understandings of both are required to fully understand electron generation. Two techniques will be addressed in which TESS can be used to measure the energy and the energy spread of an emitted electron beam:

1. Creating a retardation field using an electrostatic mesh
2. Modulation of the cathode potential

The first method uses a wire mesh to create a retarding field in the mesh region. This is a three stage technique shown in figure 2.12 which plots the potential versus longitudinal distance to explain the different stages that occur in the experiment. The electrons are accelerated away from the cathode, far left, due to a voltage difference between the cathode and first mesh. The energy of the electron after this stage is the kinetic energy gained during acceleration, left red

arrow, plus the initial energy component the electron had when emitted from the cathode. The second mesh is then biased with a potential lower than the first mesh, this decelerates the electron. If the second mesh potential is lower than the cathode potential, as in the figure 2.12, the electron loses all energy it has gained in the first step. If the energy remaining after deceleration is larger than the difference between the cathode and second mesh potential, smaller right arrow, then it continues to move forward, if not then it falls back towards the first mesh, which from this point will be called retardation. If the electron overcomes the potential barrier then a potential difference between the second mesh and MCP front plate accelerates the electrons. In this technique, in the simplest configuration, the third mesh is not used.

The second technique was proposed after the first technique had been tested and is only a two stage process. Instead of using a mesh to create a retarding field a potential difference exists between the cathode and MCP. The potential diagram is shown in figure 2.13. The electron is accelerated from the cathode to the first mesh where it is decelerated. The cathode potential is higher than the MCP potential which is held at 0 V. Detection occurs if the initial energy of the electron is larger than the red arrow in figure 2.13. The second and third meshes are sequentially lower in potential than the first mesh so deceleration still occurs. To measure the initial energy range of the electrons the cathode voltage is scanned, thereby increasing the energy barrier the electrons have to overcome.

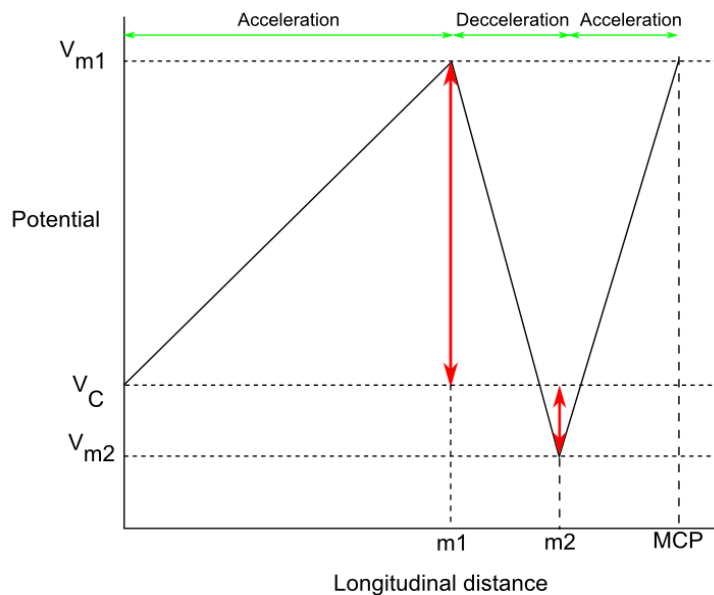


Figure 2.12: Potential diagram of the TESS system when using a mesh as a retardation filter.

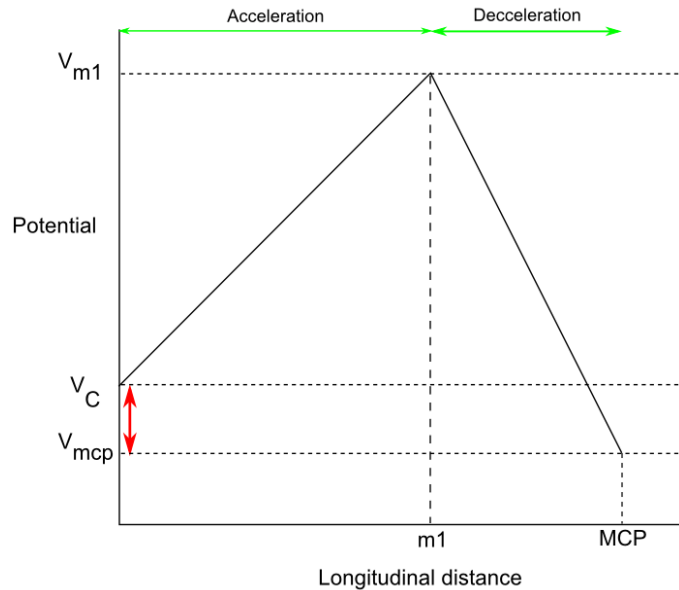


Figure 2.13: Potential diagram in the TESS system creating a potential difference between the cathode and MCP front plane.

2.4 Modelling Fields Around an Electrostatic Wire Mesh

2.4.1 Analytical Solution

An analytical expression of the potentials around a thin wire mesh will now be derived before moving on to more complex computer based methods.

2.4.1.1 Thin Wire Mesh Solution

Computational methods are slower to calculate and work as an approximation to the geometry, resolved only by the smallest finite element in that region. An analytical solution could make solutions faster to calculate and will offer some insight into the general solution of the system. A mesh structure can be analysed analytically but only when several assumptions are used because they make the problem more approachable. Once a solution was found the assumptions were assessed to see if the result may be used practically. The assumptions that were used were:

1. The mesh is infinitely large in two dimensions (x-y).
2. The mesh is comprised of wires which are infinitesimally thin.
3. A linear charge density is applied to the wires of the mesh.

It was found that the potential around a wire mesh arrangement can be found by using a complex potential analysis of a single wire above a ground plane and by superposition build up to the potential for the required geometry. The solution follows on from methods used for wire drift chamber particle detectors [94] [95].

For some two dimensional electrostatic problems it is sometimes easier to solve a system using a complex analysis where two spatial dimensions are treated in real and imaginary planes. A complex analysis only works in two dimensions and so for a three dimensional problem it is necessary to find a way to treat it in two dimensions. For the case of a thin wire suspended over a conducting plane, it is assumed the wire is infinitely long, so end effects can be ignored. In this case the system can be thought of as a two dimensional problem pictured in figure 2.14. By separating the two dimensions in this manner and not treating the distance as just a radius, the change in potential in both directions can be studied.

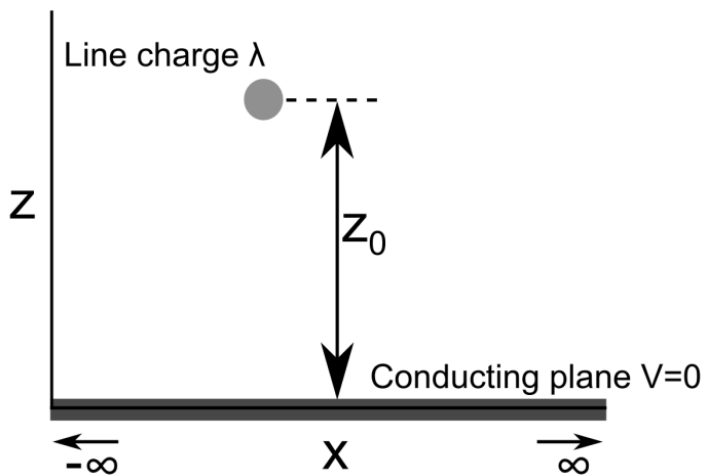


Figure 2.14: A charged wire, coming out of the page, above a conducting plane by distance z_0 . Defining the geometry like this allows a three dimension to be compressed into two dimensions.

The complex potential, ϕ , is written in the form [96]:

$$\phi(Z) = \psi(Z) + i\Omega(Z) \quad (2.14)$$

Z is the standard complex notation which contains the position co-ordinates x and z i.e. $Z = x + i \cdot z$. $\psi(Z)$ is the real potential term which describes equipotential curves. This is the standard expression for potential. The imaginary term $\Omega(Z)$, sometimes called the force term, describes the path a charge particle will move in a field. $\psi(Z)$ and $\Omega(Z)$ form an orthogonal pair. This is evident to understand in electrostatics as the force on a charged particle \vec{E} is found by the gradient of the potential U , i.e.: $\vec{E} = -\nabla U$. Thus in equation 2.14, $\psi(Z)$ is orthogonal to $\Omega(Z)$. Writing the potential in this manner is valid as long as the function is analytic. A function is analytic in a given region if the derivatives of the function are the same no matter what direction is taken, in this case the x or z directions. This is expressed mathematically by the Cauchy-Riemann equations. Using the same notation above [96]:

$$\frac{\delta\psi}{\delta x} = \frac{\delta\Omega}{\delta z} \quad (2.15)$$

$$\frac{\delta\Omega}{\delta x} = -\frac{\delta\psi}{\delta z} \quad (2.16)$$

Combining (3.1) and (3.2) by taking further derivatives it is found:

$$\frac{\delta^2 \phi}{\delta x^2} + \frac{\delta^2 \Omega}{\delta z^2} = 0 \quad (2.17)$$

$$\frac{\delta^2 \phi}{\delta z^2} + \frac{\delta^2 \Omega}{\delta x^2} = 0 \quad (2.18)$$

The relations above show a distinctive similarity with the Laplace equation:

$$\Delta V = \frac{\delta^2 V}{\delta x^2} + \frac{\delta^2 V}{\delta z^2} = 0 \quad (2.19)$$

From this it can then be said that if a complex potential function is analytic then it is also a solution to the Laplace equation. The Laplace equation is an important concept in electrostatics as it is related to Poisson's equation which describes solutions to charge free and charge occupied regions, respectively. The Laplace equation also has uniqueness about it so that if for a particular problem, if a solution is found then that solution is unique and no other solution exists. In summary, if the complex potential is analytic then it is a solution to the system of charges.

Returning to the line charge, it is a well-known result that, by applying a cylindrical Gaussian surface and using Gauss' law, the potential around a wire with constant line charge $-\lambda$ (C/m) is described in terms of the radius, r , as:

$$V = -\frac{\lambda}{2\pi\epsilon_0} \ln r \quad (2.20)$$

The real component of the complex potential for a line charge must be mathematically equivalent. The complex potential takes the simple form:

$$\phi(Z) = -\frac{\lambda}{2\pi\epsilon_0} \ln Z \quad (2.21)$$

If the complex term is in the form $Z = |Z|e^{i\theta}$ then it follows: $\ln Z = \ln|Z| + i \cdot \arg(Z)$. The complex potential is then written in the explicit form:

$$\phi(Z) = -\frac{\lambda}{2\pi\epsilon_0} \ln|Z| - i \cdot \frac{\lambda}{2\pi\epsilon_0} \arg(Z) \quad (2.22)$$

Looking at the real part the standard definition is recovered. It is also relatively straight forward to see, using equations 2.15 and 2.16 that this expression for the complex potential is analytic.

To account for the effects of the conducting plane the principle of image planes is used which states that to calculate the potential due to a boundary on a charge, an equal but opposite charge is placed on the other side of the conducting boundary an equal distance to the charge.

If the line charge is placed at $U' = x' + i \cdot z'$ then with a conducting plane at $z=0$, this is equivalent to a line charge of charge density $-\lambda$ placed at $U' = x' - i \cdot z'$ or using complex notation \bar{U}' . The potential of the system at a point $U = x + i \cdot z$ is then the superposition of the two line charges, the real line charge and the boundary induced potential, at that point.

$$\phi(U) = \frac{-\lambda}{2\pi\epsilon_0} \ln(U - U') + \frac{\lambda}{2\pi\epsilon_0} \ln(U - \bar{U}') = \frac{-\lambda}{2\pi\epsilon_0} \ln\left(\frac{U - U'}{U - \bar{U}'}\right) \quad (2.23)$$

To account for an infinite set of wires along the x plane, the potential at point U due to a wire at U_k needs to be included. For a set of k equally spaced wires a summation is performed:

$$\phi(U) = -\frac{\lambda}{2\pi\epsilon_0} \sum_{k=-\infty}^{k=\infty} \ln\left(\frac{U - U'_k}{U - \bar{U}'_k}\right) \quad (2.24)$$

Where U'_k is the position of the kth wire. If the wires are equi-spaced by a distance a , then:

$$U - U'_k = U - U'_0 - ka \quad (2.25)$$

Where U_0 is the position of the zeroth wire placed at $U'_0 = x_0 + z_0$. The summation can then be rewritten as:

$$\phi(U) = -\frac{\lambda}{2\pi\epsilon_0} \sum_{k=-\infty}^{k=\infty} \ln\left(\frac{U - U'_0 - ka}{U - \bar{U}'_0 - ka}\right) \quad (2.26)$$

Performing the summation and noting that at $U = ka$ it is required that the numerator and denominator must be zero then it follows that the solution is sinusoidal with a half period of π/a . The summation can then be rewritten:

$$\phi(U) = -\frac{\lambda}{2\pi\epsilon_0} \ln\left(\frac{\sin\left(\frac{\pi}{a}(U - U'_0)\right)}{\sin\left(\frac{\pi}{a}(U - \bar{U}'_0)\right)}\right) \quad (2.27)$$

To find the real potential of the parallel wires configuration the real part of equation 2.27 must be found, $V(x, z) = Re\{\Phi(U)\}$. The real part of a logarithm of a complex function is found from the modulus of that function i.e. $Re\{lnZ\} = ln|Z|$. Using multiple angle formula and hyperbolic identities it can be shown that the modulus of a sine term with a complex argument Z can be written: $|\sin Z| = \sqrt{\sin^2 x + \sinh^2 y}$. It follows then that the real potential can be written as:

$$V(x, z) = -\frac{\lambda}{2\pi\epsilon_0} \ln \left(\frac{\sin^2 \left(\left(\frac{\pi}{a} (x - x'_0) \right) \right) + \sinh^2 \left(\left(\frac{\pi}{a} (z - z'_0) \right) \right)}{\sin^2 \left(\left(\frac{\pi}{a} (x - x'_0) \right) \right) + \sinh^2 \left(\left(\frac{\pi}{a} (z + z'_0) \right) \right)} \right) \quad (2.28)$$

This is the solution for an infinite set of parallel wires [97]. To form a wire mesh with pitch size s , superposition is used by following the same procedure but now in the y - z plane. For two sets of parallel wires one along the y axis and the other along the x axis with equal charge density then the potential solution of the mesh can be written as:

$$V(x, y, z) = -\frac{\lambda_{wire}}{4\pi\epsilon_0} \ln \left[\left(\frac{\sin^2 \left(\left(\frac{\pi}{s} (x - x'_0) \right) \right) + \sinh^2 \left(\left(\frac{\pi}{s} (z - z'_0) \right) \right)}{\sin^2 \left(\left(\frac{\pi}{s} (x - x'_0) \right) \right) + \sinh^2 \left(\left(\frac{\pi}{s} (z + z'_0) \right) \right)} \right) \cdot \left(\frac{\sin^2 \left(\left(\frac{\pi}{s} (y - y'_0) \right) \right) + \sinh^2 \left(\left(\frac{\pi}{s} (z - z'_0) \right) \right)}{\sin^2 \left(\left(\frac{\pi}{s} (y - y'_0) \right) \right) + \sinh^2 \left(\left(\frac{\pi}{s} (z + z'_0) \right) \right)} \right) \right] \quad (2.29)$$

The electric field from this configuration can then be calculated as the gradient of the potential, but is not presented here.

The behaviour of equation 2.29 can now be studied in two cases a) through the centre of a cell i.e. $x = y = s/2$ and b) through a wire case i.e. $x = x_0$ or $y = y_0$. In both cases $x'_0 = y'_0 = 0$. The potential along the z direction is plotted for each case in figure 2.15 below. At distances comparable to half the cell pitch from the mesh the two solutions are nearly converged onto the same solution, and fully converged at distances equal to the cell pitch in each direction. At large z values away from the mesh both solutions converge to a constant value. From a distance the potential distribution looks like that from a thin charged sheet. It is only close to the meshes that the mesh structure effect becomes negligible. Taking z to be sufficiently large in equation 2.29 the potential reduces to $V = 2\lambda Z_0 / s\epsilon_0$. It can then be seen that from a distance the wire mesh looks like a sheet charge with charge density $\sigma = 2\lambda/s$.

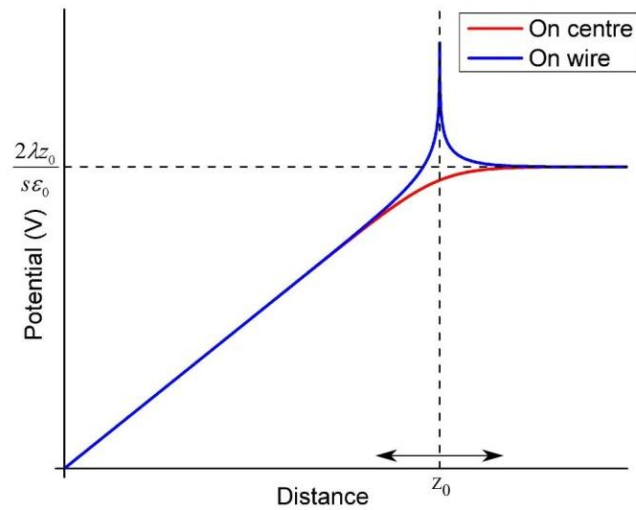


Figure 2.15: Potential along cut lines from points on a conducting plane with zero potential through the centre of a cell (red) and through the wire of a mesh (blue).

Figure 2.16 shows a comparison of values calculated from equation 2.29 with a computerised model using thin wires and a finite number of cells. The mesh has a cell size of 10 cm, placed 10 cm above a grounded plane and with line charge density equal to 0.5 nC. There is a good agreement between the values calculated from theory and those calculated on computer. Any small differences are located near the wires where the finite elements are difficult to resolve around infinitesimally thin wires. However, despite this there is good agreement even in the on wire case which shows that the steps made to derive the analytical model above are correct. No error bars are included in figure 2.16 as the computer derived values are difficult to associate with an error. To ensure that the computer model was as accurate as possible, a large number of cells were used, 14 x 14, and the steps in which the values were calculated were orders of magnitude less than the cell size. These settings show good agreement with analytical model.

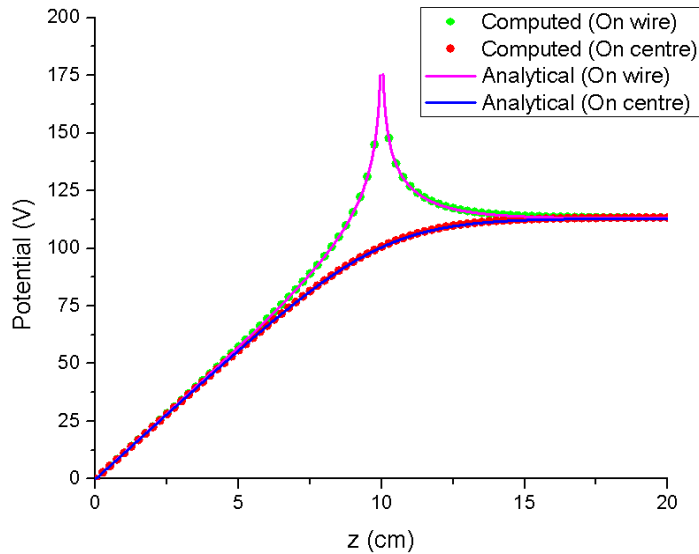


Figure 2.16 Comparison of analytical solution (solid lines) and values calculated using a finite element solver (points)

To include an even greater number of meshes, superposition can again be used. To calculate the electrostatic potential at any point of the system consisting of a conducting plate and multiple meshes, it is only required to calculate the potential at that point from each mesh in turn with the summation of the potentials giving the total potential at that point. For a set of n meshes the total potential is then:

$$V(x, y, z) = V_1(x, y, z) + V_2(x, y, z) + \dots + V_n(x, y, z) \quad (2.30)$$

So far only a simple configuration has been considered where one mesh is present. TESS has many electrostatic elements which need to be included in the solution. Let us now consider the matter of transparency. A mesh, unlike a sheet, has holes through which electric field lines may permeate. If the problem were now reversed with the mesh grounded and a source potential applied to the sheet, the situation resembles a Faraday cage where the electric field polarises the wire and the distribution of charges is such that the wires partially block field lines permeating through the mesh. In the simplest case of a single wire in the presence of an electric field, E , the total charge density is the sum of the contribution from the charge of the wire, λ , and the field induced from polarisation [95].

$$\sigma_{total} = \frac{\lambda}{4\pi\epsilon_0} + 2E\epsilon_0 \cos \theta \quad (2.31)$$

Where θ is the angle between the electric field and the radial vector of the wire. The inclusion of many wires complicates the matter and even though this effect has been known for centuries there is little mathematical discourse on the subject. In more recent literature on the matter [98] [99], the importance of the distance between the wire and the wire thickness has been studied. It was initially believed that the field beyond the cage decreases exponentially but it has been shown [99] that it is actually linear. Also the convergence is not to zero but to the solution of a homogenised problem. Convergence to zero in a circular cage only occurs when the number of wires in the cage approaches infinity which is not a physical cage.

2.4.1.2 Applicability of the analytical solution

With the analytical analysis taken as far without being overly complicated it is now time to consider the assumptions used to arrive at the result.

The first was that the wires of the mesh are infinite in length resulting in an infinite number of cells. When comparing the analytical values to simulated values a physical mesh with sufficiently large cell number converges to the solution of an infinite mesh. Therefore, for a large physical mesh with many cells the assumption is valid.

The second assumption was that the wires were given no thickness. This was done for simplicity in the solution. In the case of a single mesh when using the mesh just to accelerate the assumption may be tolerable. With a multi-mesh system with opposing charge meshes it is difficult to justify the assumption. The polarisation of wires due to external forces is a complicated matter and furthermore the non-basic shape of the TESS mesh would complicate it further. To accurately ascertain an approximate solution using a retarding mesh would be difficult without considering the mesh size and shape.

The third assumption was a linear charge density is applied to each wire. This is an obstacle when trying to find a solution to the system. To do so, for example, in a system containing a conducting plane, a mesh and sheet charge, all parallel to each other, a set of simultaneous equations needs to be established which relates the charges and the positions of each element to the voltage at that point. Taking the inverse of this matrix would mean the positions and intended voltages could be related to the necessary charges to apply. The problem is now in the

crossing of the wires. At the point the wires cross the region of charge contains more charge than in the regions where there is no crossing. Applying Gauss' law would reveal that the potential at the point of crossing is higher than elsewhere on the grid. Finding the potential close to the mesh then depends at what point it is being evaluated. For the purposes for which it is intended to be applied, applying constant potential to the mesh, this analytical model cannot be used. Furthermore, this critique also links to the second assumption as the polarisation of wires negates the notion of a linear charge density on the wires.

This attempt at a solution of a wire mesh has given insight into the electric potential and field due to such geometry but to account for complex mesh shape and non-uniform charge density, it is not possible to find accurate values, particularly close to the mesh wire themselves. For this reason to calculate electric fields for TESS, it was decided to use values calculated using finite element analysis software.

2.4.2 Finite Element Method Comsol Model

Since it is not possible to model a multi-mesh structure using physical sizes it was decided that finite element software will be used solely to calculate the fields. The software package that was extensively used was Comsol Multiphysics [100], but crosschecks were made with the Opera electrostatics package [101]. The geometry is built as a CAD model within the software and electric potentials are applied to surfaces. A finite element mesh is then constructed in the model with the finest elements applied to the thinnest regions. The geometry of a three and two dimensional model is shown in the right figure 2.17. The model consists of outer shielding, a cathode plate, an MCP plate and three mesh plates. For simplicity the MCP front plate is modelled as a flat surface. The inset on the far right is of a zoomed in part of the meshes. During calculation only a certain number of meshes were used that would be accurate to a full mesh. To model a full mesh with micrometer accuracy would require a large amount of computing power. A two dimensional axial symmetric model was used to calculate fields from the cathode to the first mesh, left of figure 2.17. This was to exploit the fact that far from the wire mesh it should appear as a potential surface.

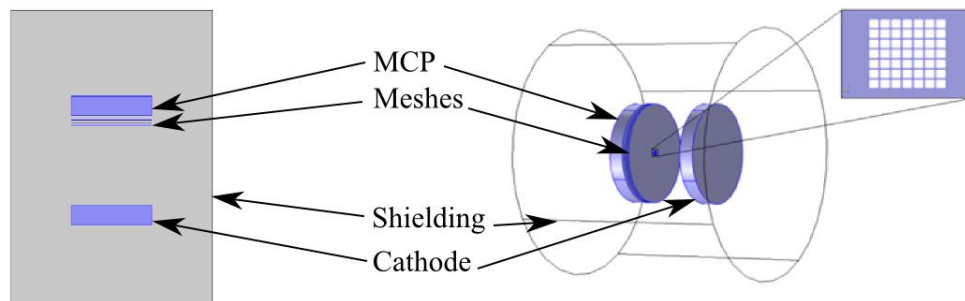


Figure 2.17: Three dimensional (right) and two dimensional (left) geometrical model of TESS built in Comsol Multiphysics. Inset on the three dimensional model shows the mesh structures.

In order to optimise the model the filter mesh technique is used as knowledge of the potential in this configuration is more crucial. Throughout the following sections the potential at the centre of the retarding mesh will be used as a measure of accuracy and will allow a way to view the effects of mechanical changes to the model. Another way the potentials are analysed is to calculate the potentials along a cut line from the centre of the cathode through the central mesh cell and on to the centre of the MCP front plate as this allows the potential to be analysed as a function of the longitudinal direction through the model. For consistency the same voltage configuration is used throughout with the cathode, shielding and retarding mesh set to -60V and the other elements at 0V .

Figure 2.18 shows the wire mesh built in Comsol. Using CAD software the bend radius, cell pitch and thickness can all be included so that an approximate solution can be attained which was not possible when attempting an analytical approach. Coloured boxes correspond to material covered shortly.

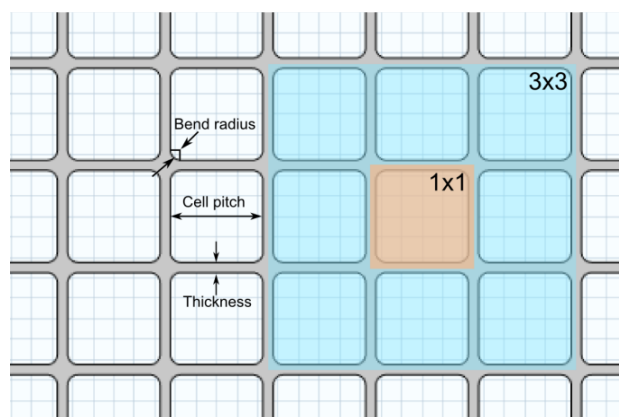


Figure 2.18: Wire mesh built in Comsol Multiphysics.

2.4.2.1 Numerical Methods

Numerical methods can be used to solve partial differential equations such as the Laplace equation. These methods often require dedicated software to calculate the solution. The methods which are used are the finite element method (FEM or sometimes FEA), finite difference method (FDM) and the finite volume method (FVM). All of these techniques do not calculate the exact solution but a reasonable approximation to the solution. FDM is a technique in which derivatives are approximated with a Taylor expansion, it is the easiest of the three to implement but restricted to simple structures. FVM works by splitting the geometry into small volumes and conservation laws applied within the volume are applied to the centre of the volume. FEM is the standard technique for physical problems such as structural calculations or electromagnetic as is the case here. A full description of FEM theory is beyond the scope of this work and only a brief summary of how it works is presented here, a more explicit discussion can be found in a large number of literature [102] [103] [104]. An object is split into primitive shapes with the same shape across the object. In 2D the shapes are either rectangular or triangular with the latter being more accurate. Curved triangular elements are possible so curves may be modelled. In 3D the shapes are hexahedral and tetrahedral with curved tetrahedral elements also possible. Curved structures are more complicated to generate but the best element shape for the TESS model. The FEM mesh built for a wire mesh built in 2D is shown in figure 2.19.

Once the structure is meshed the solution is calculated at each point, often called node. This is different compared to FVM in which the solution is averaged in the volume. The method in which the software will compute the solution is either to take a direct approach or iterative. Mathematically the solver is trying to calculate a solution to the linear equation $A \cdot x = b$ which represents the full system and calculates the potential at each node due to all other nodes. A direct solver finds an approximate solution in one step using factorisations to break the solution down whilst an iterative solver guesses at an initial solution and improves upon the solution over many steps until a tolerance is met. Direct solvers are more accurate, however, they take up a large amount of computer memory and for more intensive calculations the memory cost is too high.

Calculations of associated accuracies are difficult in FEM analyses. Validation can be achieved either through direct measurement, not possible in TESS, or through comparing with analytical expressions. This was shown in figure 2.16 where an analytical expression showed excellent agreement with calculated results of a simplified model. From this, it is assumed that more

complicated geometries are calculated accurately in Comsol assuming that a large enough number of cells are modelled, section 2.4.2.4. To be further confident in the calculated fields the results from Comsol are also compared to another solver, section 2.4.2.7. Uncertainties in potentials and fields calculated in Comsol are therefore not given as it may be reasonably assumed that they are correct. Several of the following sections will attempt to reinforce this claim.

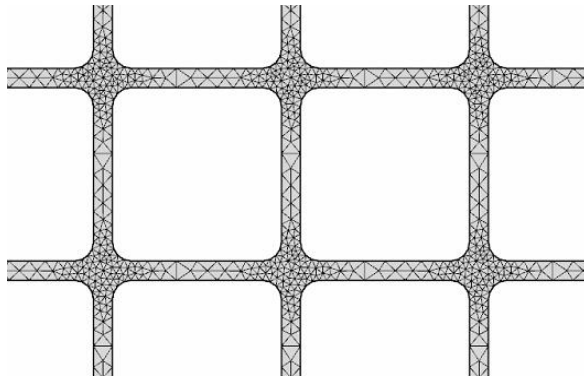


Figure 2.19: Front face of a wire with a FEM mesh built with triangular elements. More complicated regions are distributed with more elements.

What follows now is a look at the optimisation of the model, this includes:

1. The effect of the changing the thickness of the wires.
2. A study of the convergence of the finite element mesh.
3. Studying the number of mesh cells computed which will to simulate a full mesh.
4. The effect of the cell pitch size on the potentials calculated in the model.
5. The effect of adding deformations in to the model.
6. Benchmarking with another other code.

2.4.2.2 Wire Thickness

In the last section the equations of a mesh were derived for one dimensional wires. The effect of adding thickness is now considered. The TESS meshes are different in thickness on the face, 0.05 mm and in depth, 0.035 mm. Since they are thin and many of them need to be meshed, if it is possible to make any dimensions infinitely thin then this should be done as it would speed up

calculations. The potential distribution was calculated for the correct physical sizes, zero dimensional in widths and depths and the mixture of the two. These are shown in figure 2.20. The two intermediary cases are closer in absolute minimum potential, differing by 0.7 V. They are both off the physical size case by approximately 1.5 V and the difference between no thicknesses at all and a physical size is 6 V. The large differences in the potentials in each case means the model cannot be simplified in order to obtain realistic values of the potential surrounding the meshes.

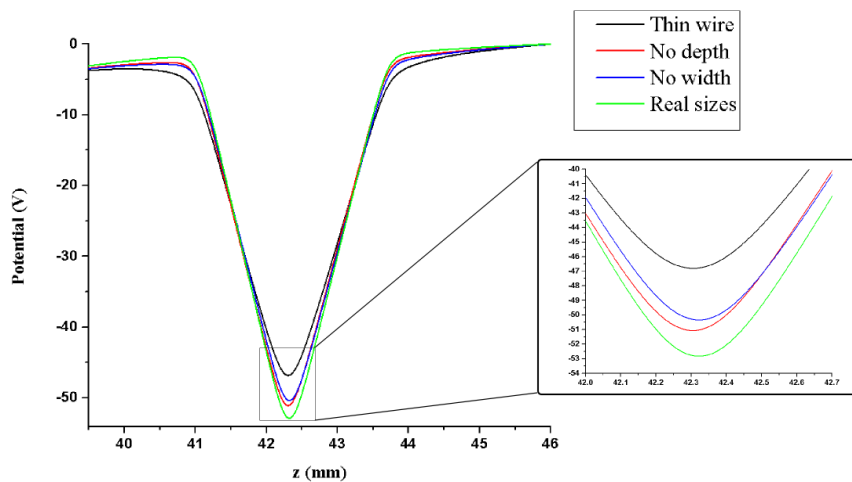


Figure 2.20: Potential through the centre of the three meshes with different dimensions applied to the mesh, the physical size case, wires infinitesimal in size and the intermediary cases with no width and no depth.

2.4.2.3 Finite Element Mesh Convergence Studies

When constructing the finite element mesh it is important to locate the finest elements in the thinnest regions of the geometry. It is also important to locate the fine elements where fields will be exported. The model shown in figure 2.17 was split into several mesh areas.

The first and most intense area was region around the three central mesh cells. It was decided that this mesh area should extend from the MCP face to a distance twice the cell pitch size from the first mesh. The FEM mesh was restricted to one 'channel' through the three central cells of the three meshes. A swept mesh approach, where a single face is meshed and dragged through a continuous structure, was attempted. It was found that even though the solution converged faster,

diagnostics within Comsol reported an excellent mesh was generated and the potential solutions were in large agreement compared to the standard meshing, implementing the swept mesh solution within the tracking code was unsuccessful with smaller steps required in exporting to produce similar results to the standard technique which meant computation time was far slower. The reason why the standard technique worked better is not clear however it was preferred method for meshing. The mesh converged with a minimum element size of 0.01 mm, reducing this value resulted in no improvement.

The second mesh region is a cylinder surrounding the remaining mesh cells. A cylinder was chosen because when using a cuboid the sharp edges created some problems when moving to a coarser outer mesh, a cylinder stopped errors of this nature. The field in this region is largely not exported from the model, the exception being a small gap between the ultra-fine region and the drift region, but the narrowness of the wires and small cell pitch still requires moderate accuracy in calculating fields and potentials due to these features of the mesh. The maximum element size in this region was allowed to be half the cell pitch size, any lower and there is a risk of inserting unnecessary finite elements. It was found by reducing the maximum element size in this region any more that this had a negligible effect in the field of the central cell. Increasing the maximum element size on the other hand led to problems tracking.

The last region covers the remaining geometry and has an element size small enough to resolve the edge of the mesh plates, in this case 0.035 mm, and big enough to not fill the drift space between cathode and meshes with unnecessary elements that will clog up the computation. The maximum element size in this region was set to 2 mm.

2.4.2.4 Cell Convergence Study

If the field due to a full mesh structure were to be calculated with a fine mesh then to obtain a good accuracy would require computing power beyond a desktop PC. For this reason it was necessary to perform a convergence test to include as many cells into the mesh plates so that the solution for one cell converges into the solution for a fully built mesh without modelling the whole structure. Electrostatic potentials were calculated for different number of cell configuration: 1x1, 3x3, 5x5, 7x7, 9x9 and 11x11, the first two are shown in figure 2.18. The results of this are shown in figure 2.21 where the absolute change from the proceeding configuration is plotted as a function of longitudinal distance, i.e. for the 7x7 curve this is the

difference in potential with the 5x5 solution. The inset shows the potential solution along a central cut line. The dashed purple lines show the longitudinal position of the three meshes. For each increase in the number of cells included there is a general improvement with the change approaching ever smaller values. The largest changes occur around each mesh with a local minimum at the centre of the mesh and local maxima just each side of the mesh. As the number of cells increases the transition becomes smoother.

Table 2.2 shows the minimum negative potential which occurs in the mesh region. For increasing numbers of cell number the potential increases. The largest difference is between the 1x1 geometry and the 3x3 geometry. The gap in potential between successive increases of cell numbers included in the geometry decreases for higher cell numbers. The gap between the 5x5 cell and 7x7 cells is 8 mV whilst from between 7x7 and 9x9 it is 3 mV.

Figure 2.22 shows the field along the direction of the mesh front face in the middle of the centre mesh. The dashed lines indicate the position of the edge of the wire mesh. The graph shows a parabolic shape with maximum potential found on the wire mesh which then drops away reaching a minimum negative potential at the centre. This figure is interesting to note as it will have significance in the dynamics of electrons passing through it. This will be talked about again in section 2.6.2.1.

Selecting what number of meshes to use then becomes a matter of choice. It was decided that a 7x7 cell design would be used. The difference between the 5x5 and the largest configuration 11x11 was 50 mV which was decided to be too large whilst it was decided not to use a 9x9 mesh cell because the time to calculate the solution was three times longer compared to the 7x7 solution and with only an 11 meV improvement on the result. It was found that in studies of a single mesh system, that the solution converged faster and at a lower cell number.

Table 2.2: Lowest potential achieved in the centre of the mesh cell for different configurations.

n x n	minimum mesh potential (V)	ΔV	% of applied
1 x 1	-54.021	-	90.04
3 x 3	-53.035	0.986	88.39
5 x 5	-52.875	0.160	88.13
7 x 7	-52.837	0.038	88.06
9 x 9	-52.826	0.011	88.04
11 x 11	-52.823	0.003	88.04

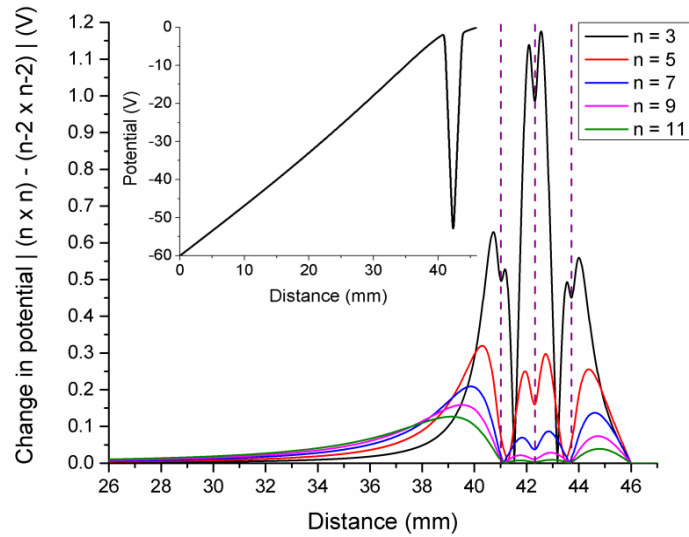


Figure 2.21: Convergence study of the number of cells included into the CAD model. The inset shows the potential along a cut line through the centre of the model. The main plot shows the difference in the potential for the point calculated between that configuration and the proceeding one.

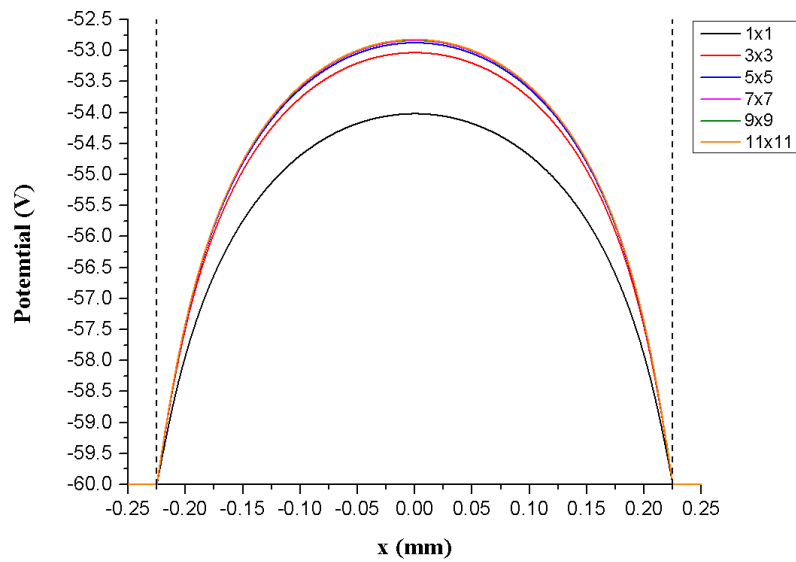


Figure 2.22: Field along the x axis of the centre mesh cell. Dashed vertical lines indicate the position of wires.

2.4.2.5 Cell Size Study

It has already been mentioned that the potential at the centre of the mesh cell is important. This is especially true in the case of using the meshes as an energy filter in longitudinal experiments. It was therefore decided to test the effect on the calculated potential for different pitch cell sizes. What was under study here was not the absolute value of the minimum potential calculated in the centre but the ratio of the potential at the centre of the mesh to the potential applied to the mesh. The reason why this was studied as well as the effects this can lead will be covered in the next chapter. Table 2.3 below shows the percentage of the potential at the centre compared to the applied potential. The wire thicknesses were kept constant throughout with only the cell pitch changed.

Table 2.3: Ratio between the potential at the centre of a mesh cell for various different cell pitches and the applied voltage expressed as a percentage.

Cell pitch (μm)	Centre/applied voltage (%)
250	96.03
500	88.06
750	81.63
1000	75.78
1500	65.72

2.4.2.6 Introducing Deformations

All cases so far have been calculated assuming that all the geometry is perfectly aligned with no deformations. In any real situation of course this is not true. To test this several deformations were introduced into the model to test for any change.

As the meshes and detector set up are on a z translational stage, the meshes and MCP plate were moved in the model from 40 mm to 10 mm and using the voltage configuration used previously only a small change, 2 meV, was observed at the minimum potential which is small enough that it may be assumed that any relation between the potential at the centre in this configuration is acceptable for the range of distances that the mesh-detector stage can be moved. The first deformation of the mesh set-up included into the model was to move the retarding

potential mesh, the second mesh, and small distances in the longitudinal away from the true position. The data points can be described well by a quadratic equation and it is seen that the minimum is at the position midway between the first and third mesh. It expected that the distances between the meshes will be too far the design specifications. What this study has shown is that even if the position of the second mesh is out by 0.1 mm then the calculated potential at the centre of the mesh is only off by a factor of 4 mV however larger drifts and the difference changes considerably.

The second deformation added to the model was to move the retarding mesh in the x-y plane. It is known that the TESS meshes are not perfectly aligned. In this test the second mesh was moved in equal steps of 0.05 mm in both x-y as this should be the most deformed case for each step. The results are shown in table 2.5 below. The steps were taken up to 0.25 mm which is half a cell pitch i.e. 0.25 mm would be completely misaligned. Even in this most extreme case the potential did not shift more than 2 mV away from the completely aligned case.

Table 2.4: Misaligning the x-y position of the retarding mesh and the potential at the centre.

X shift (mm)	Y shift (mm)	Difference with aligned solution (mV)
0.05	0.05	2
0.1	0.1	-2
0.15	0.15	0
0.2	0.2	2
0.25	0.25	1

Table 2.5: Difference in the minimum mesh potential when rotating the retarding mesh in the y plane.

Angle of rotation	Difference compared to 0° (mV)
1.5°	5
1°	0.5
0.5°	-0.5
-0.5°	-0.6

Other deformations considered are related to rotations of the meshes including of sagging of the meshes/MCP assembly and a small forward rotation of individual meshes. It was found that in both cases that the effect on the potential of the system is negligible, this is shown in table 2.5 for the case of rotating the retarding mesh in the y axis by small amounts, rotating any further results in touching plates.

2.4.2.7 Benchmarking with Opera

To be confident of the potentials which are being calculated for a mesh structure it is useful to compare potential values calculated with similar geometries in other codes. Opera was used because it too also allows electrostatic calculations to be made using CAD models. The CAD of the model built in Opera is shown in figure 2.23.

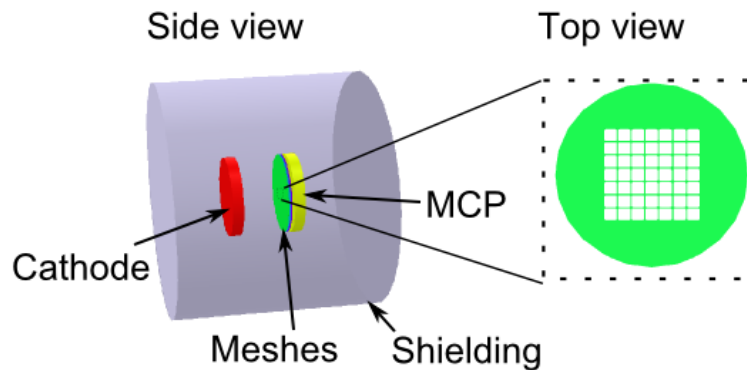


Figure 2.23: CAD model built in Opera. This figure only shows the surfaces with an applied potential surface. As in figure 2.17 the inset shows the mesh structure.

The FEM mesh controls in the version of Opera used, v15, were limited in that it had fewer options for the user to control the FEM mesh. This made it difficult to first of all successfully generate a mesh and secondly to control the resolution in the regions of interest, in the mesh area. To successfully build a mesh required careful placement of intermediary vacuum layers to allow the FEM mesh to grow between surface layers which were meshed first. Poor selection of volume mesh settings led to a failed FEM mesh generation. After several refinements of the Opera FEM mesh, reducing the maximum element size in the middle of the central mesh, the solutions after each refinement began to converge towards the Comsol solution at the point of minimum potential. On the last refinement the difference was approximately 15 mV.

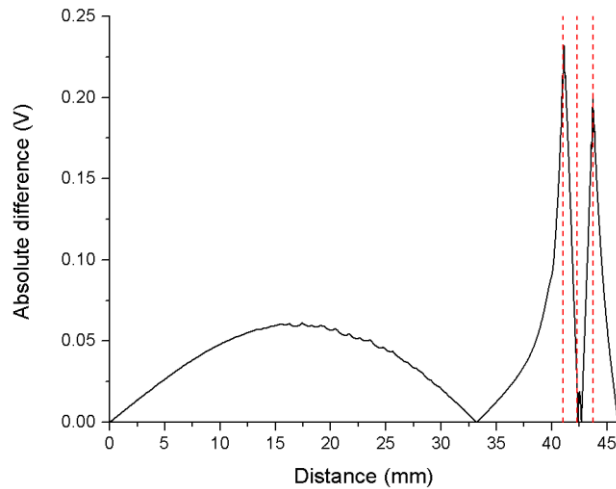


Figure 2.24: shows the absolute difference between Comsol and Opera for the potentials configuration discussed previously along the central cut line in steps of 10 μm . The red dashed lines represent the longitudinal position of the centre of the meshes.

Figure 2.24 shows the absolute difference between Comsol and Opera in potential along a central cut line. The biggest differences between the two solutions occurred in the drift region between the cathode and the meshes, but never more than 60 mV, and in the centre of the other outer two meshes. An advantage of Comsol is that it will use a smoothing algorithm so it can interpolate between points that are exported from the solution. As the FEM mesh is coarser in the drift region, larger than the exported step size this may explain the differences between the two solutions in this region. In the mesh region the large difference could potentially be explained by how the mesh was built in Opera. The finest mesh was restricted to the central cell of the middle mesh so a fine FEM mesh was not built in the centre of the two mesh cells than in the Comsol solution which may explain the sharp differences between the two models in this case.

The reason for performing this comparison study was to be confident in the values surrounding the filter mesh. Further refinement of the Opera solution was not performed because it became apparent that the solutions were slowly converging and a 15 mV difference between the two was enough to be confident that what Comsol was calculating is an accurate approximation to the solution.

2.5 Development of a Low Energy Tracking Code for Mesh Systems

A custom made tracking code was written in Matlab-Simulink in order to track particles through the electric field data calculated. There were three main reasons as to why this was done rather than using a commercially available code. The first is that accurate field data generated from finite element solvers must be used and so ease of importing large field maps is a requirement. The second is with dealing with cases in which an electron collides with a mesh. Having the flexibility to write algorithms for specific cases is beneficial. The third is that the initial velocity distributions should take any form so different distributions can be tested. Matlab Simulink offers a way to address all these requirements.

2.5.1 Code Structure

Matlab Simulink [105] is a data flow programming tool which has several benefits such as the ability to simply attach or disconnect aspects of the code befitting to the situation, an expansive range of premade Matlab functions are available such as a wide range of integration methods and look up tables as well as functionality with traditional script algorithms and also any initial profile or velocity profile may be implemented by the user. Figure 2.25 below shows the general layout of the tracking code in block diagram form developed for the mesh tracking code. The next section will describe each section in figure 2.25. A full layout of the code and further supplementary information is given in Appendix B.

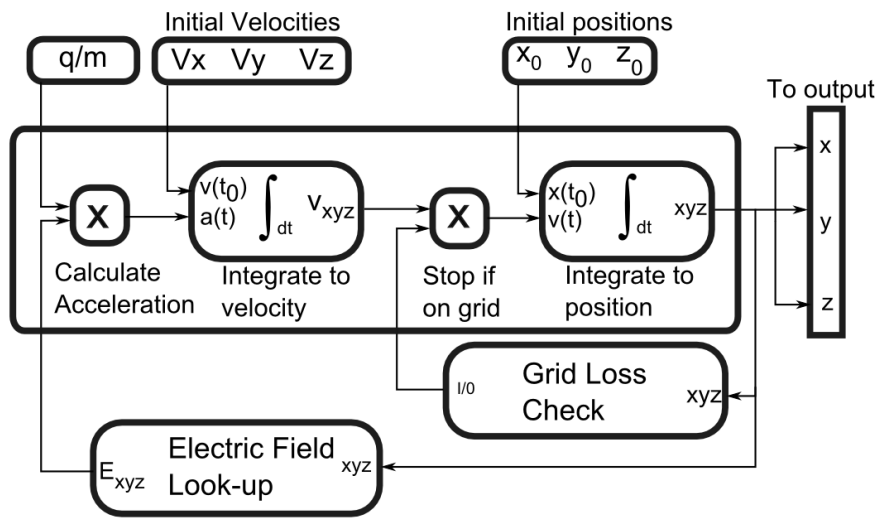


Figure 2.25: General layout of the tracking code developed for tracking particles through a wire mesh.

2.5.2 Operation of the Code

The electric field data from both the three dimensional and two dimensional CAD models are loaded into the workspace and sorted to establish the table break points and a three/two dimensional loop up table. The three dimensional lookup table is split into x,y and z the two dimensional table is split into r,z.

The end time is set before the simulation is started. Once the integration time has reached this value the program will exit. The duration is set to be long enough to allow particles to pass through the meshes and to be detected or retarded. Also before a simulation is started the integration method and integration step size is set. The step size needs to be chosen based on the speeds of electrons in the mesh system. The step size needs to be analysed before any simulation is run. This ensures particles do not overstep and only partially feel the electrostatic force.

Numerical integration methods work by taking small steps over a function to calculate the next step. The simplest technique is the Euler method which uses the derivative at the initial step and calculates the next value by linearly interpolating over a small step, h. The Euler method is a 1st order method. More complicated methods use higher order corrections to more accurately determine the next point. The most common technique is the Runge-Kutta 4th order method (ode4). The corresponding equations are shown below for an initial value problem specified by $\dot{y} = f(t, y)$ and $y(t_0) = y_0$ for a differential function f at an initial time and position t_0 and y_0 . The last term is the order of magnitude of the local truncation error, i.e. the difference between the calculated value and the actual value. The overall, global, truncation error over all steps is in the order of h^5 .

$$y_{n+1} = y_n + h \left(\frac{1}{6}k_1 + \frac{1}{3}k_2 + \frac{1}{3}k_3 + \frac{1}{6}k_4 \right) + O(h^5) \quad (2.32)$$

Where:

$$k_1 = f(x_n, y_n) \quad (2.33)$$

$$k_2 = f \left(x_n + \frac{1}{2}h, y_n + \frac{1}{2}k_1 \right) \quad (2.34)$$

$$k_3 = f \left(x_n + \frac{1}{2}h, y_n + \frac{1}{2}k_2 \right) \quad (2.35)$$

$$k_4 = f(x_n + h, y_n + k_3) \quad (2.36)$$

Using these equations the next point in a function can be calculated. Higher order solvers such as Dormand-Prince (ode5), as well as variable step solvers are available however comparing tracking paths using a fixed step RK4 solver and the DP5 solver shows little change and can increase computation time by several seconds per electron.

When the simulation is initiated the code looks up the electric field at that point. As the electric field map is defined by an array of finite points interpolation methods are required to evaluate the field values between these points. Two interpolation methods are available within the Simulink framework, linear and cubic spline. Linear as the name may suggest fits a straight line between points defined in the look up table to determine the electric field at that point. A cubic spline method fits a continuous piecewise function with continuous derivatives to then determine the field at that value. The choice between linear and cubic spline is a balance between time and accuracy. To linear interpolate between a non-linear field such as the field surrounding the meshes requires field maps with small spacing. Any small noises between points in the field map introduce errors into the calculation. Many finite element solvers however, smooth the data and interpolate data to be exported at points defined by the user. Cubic spline interpolation is a more accurate method and requires less points due to higher order fitting but computation time can be much many minutes per electron compared to one second. It's found that a linear solver is usually sufficient even in the meshes region as long as the data is smoothed and the step size in the transverse plane is enough to obtain at least 50/100 points in the mesh cell and in the longitudinal direction at least 3/5 points over the mesh thickness.

Particle tracking works by calculating the acceleration $\vec{a}(\ddot{x}, \ddot{y}, \ddot{z})$ due to a force on a particle with mass m and charge q whilst in an electric field $\vec{E}(E_x, E_y, E_z)$. This is written in the non-relativistic case as:

$$\vec{a}(\ddot{x}, \ddot{y}, \ddot{z}) = \frac{q}{m} \cdot \vec{E}(E_x, E_y, E_z) \quad (2.37)$$

To account further for the fact that the code is working in units of mm, mm/ns and V/mm it is necessary to define the electron charge and mass with suitable unit prefixes. Working through to arrive at acceleration in units of mm/ns² it is found that the value of q/m, top left figure 2.25, is just 1.6/9.1.

The new particle position is attained by the double time integral over a small time step using the

integration method and step size selected at the start of the simulation. On the first step the initial positions and velocities are used as initial conditions for the integration. A check is performed to test if the particle is in the position of the mesh. Checks are made in both the longitudinal and transverse position. If the longitudinal position is greater or equal to the MCP position or at the longitudinal position of a mesh and the transverse position of a wire then a false Boolean signal is sent to adjust the velocity to zero before the next position step is calculated keeping it at the same position until the simulation ends otherwise a true signal is sent and the code executes as normal. On each step of calculating the new position the output, and indeed any other calculated parameter, velocity for instance, can be sent to the Matlab workspace or saved to file or both. A condition is set within the code to switch from the 2D map to the 3D map at a predetermined point. From the analytical analysis mesh effects were only seen approximately a cell pitch spacing away from the mesh. However it was found in FEM studies that the effect of the mesh was still seen many cell pitch distances away from the mesh, figure 3.15.

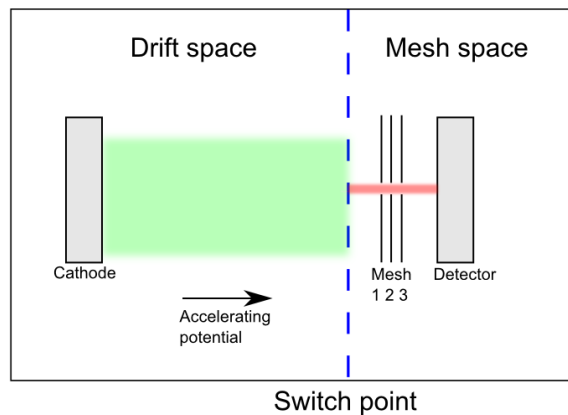


Figure 2.26: Layout of the different regions in the TESS geometry. The green region is the 2D drift region and red is the 3D mesh region. The blue dashed line is the point at which the code switches from one region to the other.

The switch condition was set to be 4/5 mm away from the first mesh. The reason why this distance was chosen was because plotting the potential at increasing distances away from the mesh on the transverse plane, figure 2.27, revealed at this distance the field was nearly completely flat. The closer to the mesh the more none flat the potential appears. Further away from the mesh the potential appears to be more constant and more parabolic closer to the mesh.

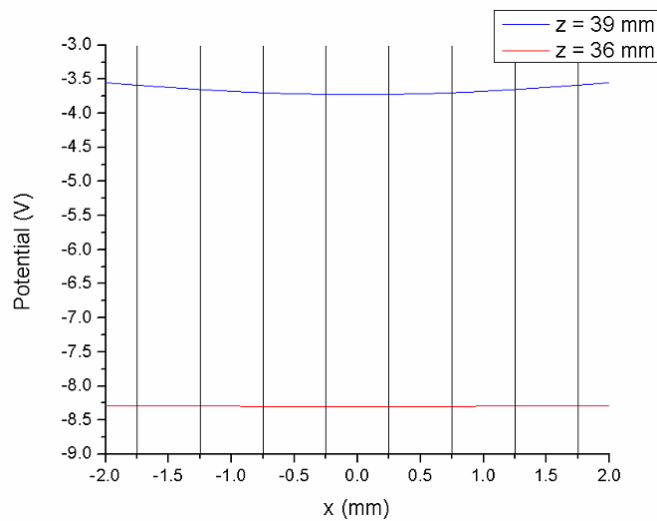


Figure 2.27: Potential along a transverse direction 2 distances away from the first mesh.

Within the drift region the code then makes a radius from the x and y co-ordinates and looks up the data from the two dimensional field map. In the mesh region it is necessary to account for the multi channels. An algorithm is implemented that scales the transverse position of the particle to the same point in the cell of the single cell mesh solution, figure 3.17. This works by calculating the position of the particle in relation to the centre of the cell which the particle is in then calculating the equivalent position in the solution channel, red box. The exact algorithm is given in Appendix B

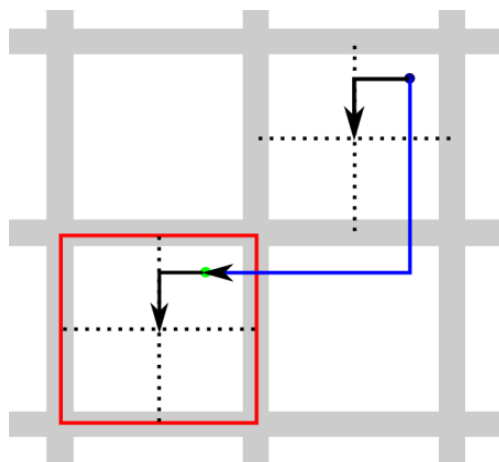


Figure 2.28: Scaling the particle position to the equivalent position in the central cell which has evaluated field values within the red box.

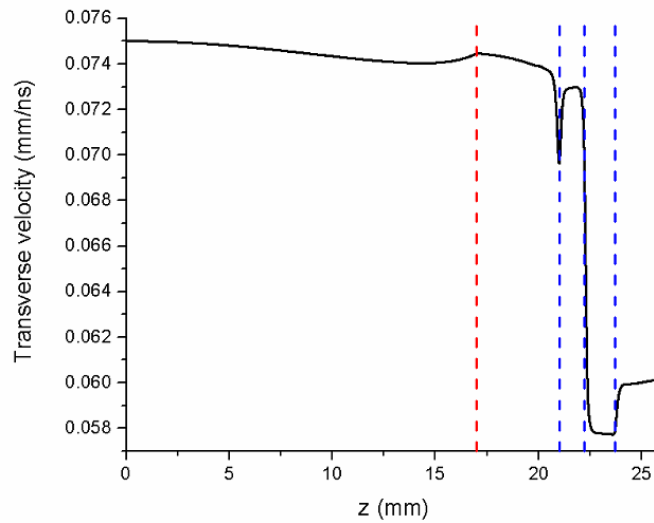


Figure 2.29: Transverse velocity plot of an electron. The red dashed line shows the point at which the field maps changed. The dashed blue lines show the longitudinal position of the three meshes.

This sudden shift can have a detrimental effect on the transverse energy if the transverse electric field is not flat in the drift region, as particle off the mesh centre will feel a discontinuity in force. This effect is seen in the transverse velocity graphs as a small discontinuity. However, in cases with a large potential difference the longitudinal velocity is much greater than the transverse and so only a small fraction of energy is lost due to this approximation. Figure 2.29 shows an example of the transverse velocity for a simulation of tracking a particle with some initial energy between the cathode and MCP held at zero potential and an accelerating potential between the cathode and meshes. The dashed red line represents the point in the tracking code in which the field maps were changed. A change can be seen when moving from one to the other but when calculated in terms of eV and taking the difference between each successive point calculated shows that the change in energy over the switching point is $2.5 \cdot 10^{-12}$ eV. This was done for an electron that crossed through a mesh cell 4 cells from the central one. For an electron which crossed the mesh 10 cells from the centre the results were similar.

2.5.3 Initial Parameters

Before the code is run the initial positions and velocities of the particles are set. Two different ways were used to assign velocities in this study. Initially the velocity distributions were made to follow experimental distributions closely in order that benchmarking could be attempted and to

gain a more physical picture of what was occurring in the experiment. The probability density function (PDF) distributions of energies take the form of equation 2.13. To sample from this distribution the cumulative density function (CDF) is calculated by the sum over positive and negative infinity, the inverse of the CDF allows the PDF to be sampled. It would be incorrect to sample the energy and finding the velocity from the energy because this involves taking the square root which drives velocities away from zero. The correct approach is to insert the term for velocity directly into equation 2.13 and sample from this. The PDF is written as:

$$N = N_0 \cdot e^{-\frac{m_e v^2}{2k_B T}} \quad (2.38)$$

This function is just a Gaussian function with well known techniques to sample from. Using a normally distributed random number between 0 and 1 the velocity is sampled by:

$$v = \sqrt{\frac{k_B T}{m_e}} \cdot \text{rand}(0,1) \quad (2.39)$$

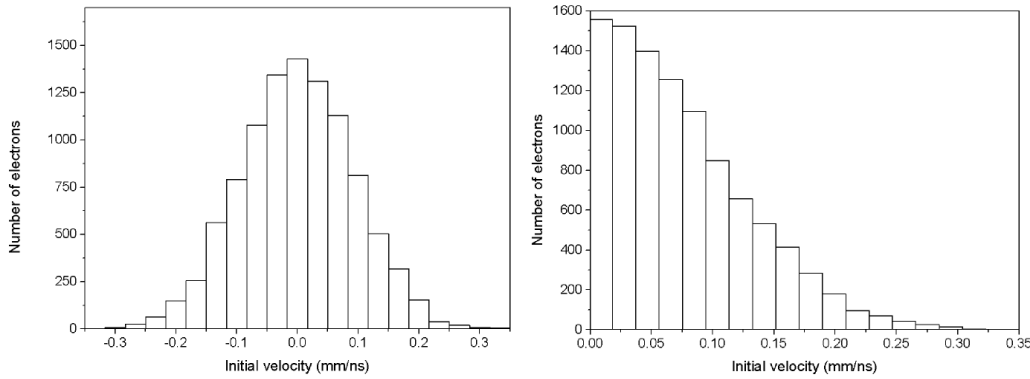


Figure 2.30: Initial velocity distributions based on experimental values. Left shows the transverse profile whilst right shows the longitudinal profile.

The second technique used was for debugging purposes. It became clear in certain situations, which will be discussed later in this chapter, that the total energy was not the only an important factor but also the relation between the longitudinal and transverse components. As a result, a second method for sampling initial velocities was used which couples the longitudinal and

transverse velocity to the total energy by an angle θ . Figure 2.31 shows how the velocities were defined in this case. The total initial energy in electron volts is converted to a velocity, v , and then distributed to the three orthogonal directions. To distribute between the transverse directions (x,y) a random angle ϕ is sampled between 0 and 2π .

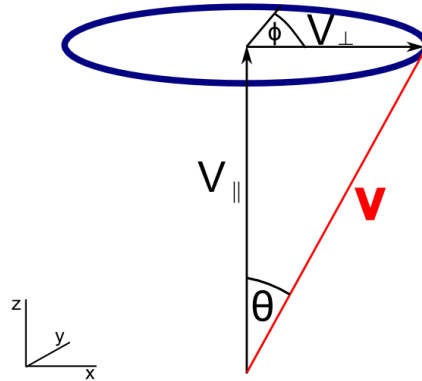


Figure 2.31: A technique for assigning the initial velocity distributions based on the velocity equivalent of the total initial energy, an angle θ and a random angle ϕ .

In both techniques of assigning velocity the total energy of the electron is given by the sum of the transverse parallel energies (See appendix A):

$$E = E_L + E_T \quad (2.40)$$

The initial transverse position on the cathode is sampled as a spot with FWHM of $40 \mu m$. In reality the spot on the TESS photocathode is elliptical but for these measurements the integrated signal is what is wanted so it was left as a circular profile. Figure 2.32 shows a histogram of the transverse profile in one direction.

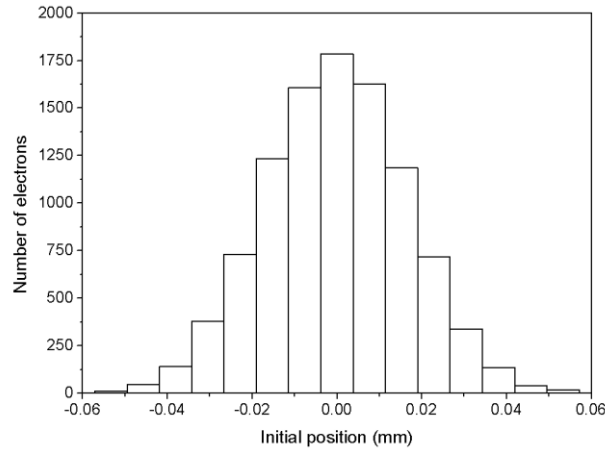


Figure 2.32: Histogram of initial transverse position in one plane.

2.6 Method One: Filter Mesh Technique

The first technique explained in section 2.3 will now be explored through both experimentation and simulation.

2.6.1 Experimental Results

The first technique attempted was to use a wire mesh to generate an energy filter to only allow electrons with sufficient energy to be detected. Experiments were performed shortly after transverse measurements were performed, so the experimentally found value of the transverse emittance was known for two laser wavelengths. The GaAs cathode was activated to NEA quantum efficiency levels and the cathode-mesh drift distance was approximately 40 mm. A laser wavelength of 635 nm was used to stimulate electrons from the cathode. The potential applied to the second mesh was decreased in steps of 0.5 V which was believed to be large at first, as this covers the entire range of energies that an electron should have at this laser wavelength, however, it allowed the technique to be understood.

Two sets of images were taken with the same potentials applied to the elements. The first was the main image during detection of stimulated electrons and the second with the laser shutter closed with no laser stimulated electrons, which was used as a background data set. The set-up is not completely light tight as a small aperture is required to allow the laser through which is mounted externally to the main chamber and so a background correction is required. The signal

collection time was 15 seconds which allowed a large signal to be collected without saturating the camera. A light and a dark image are shown in figure 2.33. From the camera pixel matrix (2048 x 2048) the background corrected data set is obtained from cell by cell subtraction of the dark data set from the light set. Figure 2.34 shows a projection and fitting of a Gaussian of a corrected image. A set of background corrected images for increasing retarding potential are shown in figure 2.35.

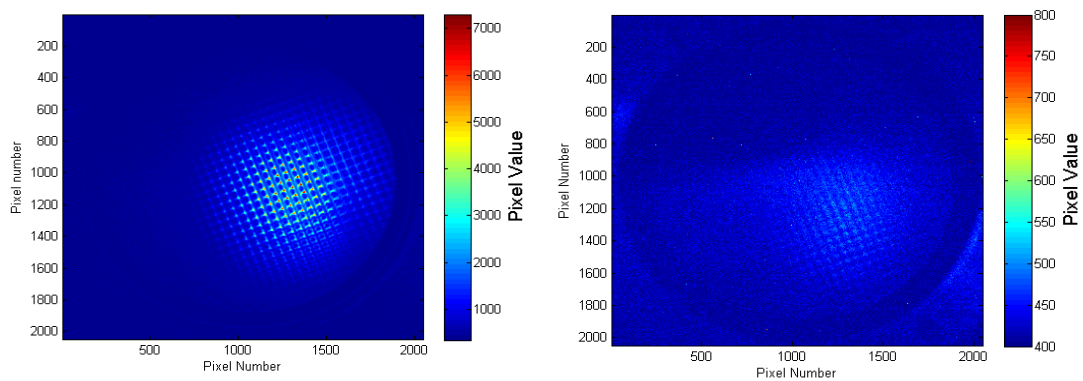


Figure 2.33: Camera pixel density when TESS is used for longitudinal measurements. The left image shows a live and the right image shows a dark image with the laser shutter closed.

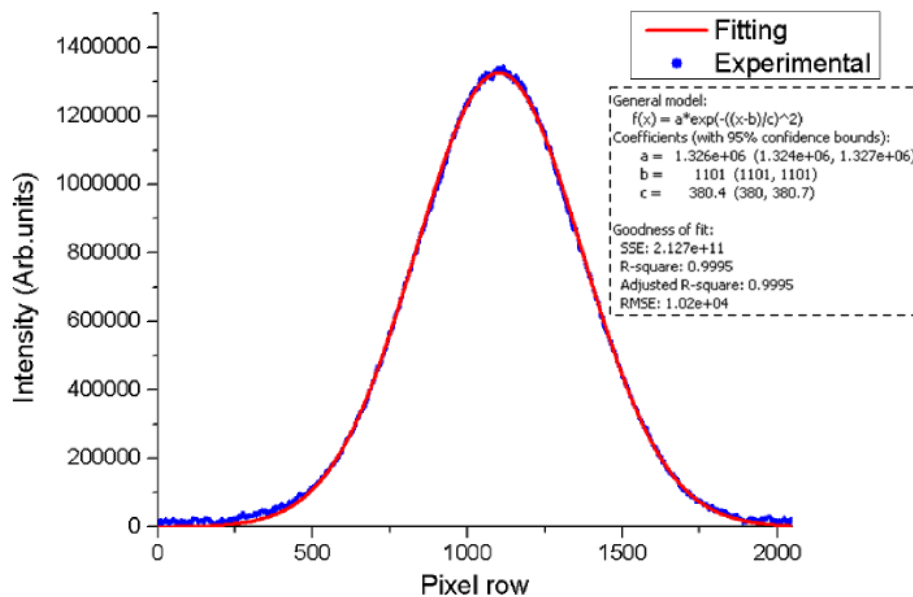


Figure 2.34: Fitting of the obtained pixel profile distribution. The fitting results are shown in the figure.

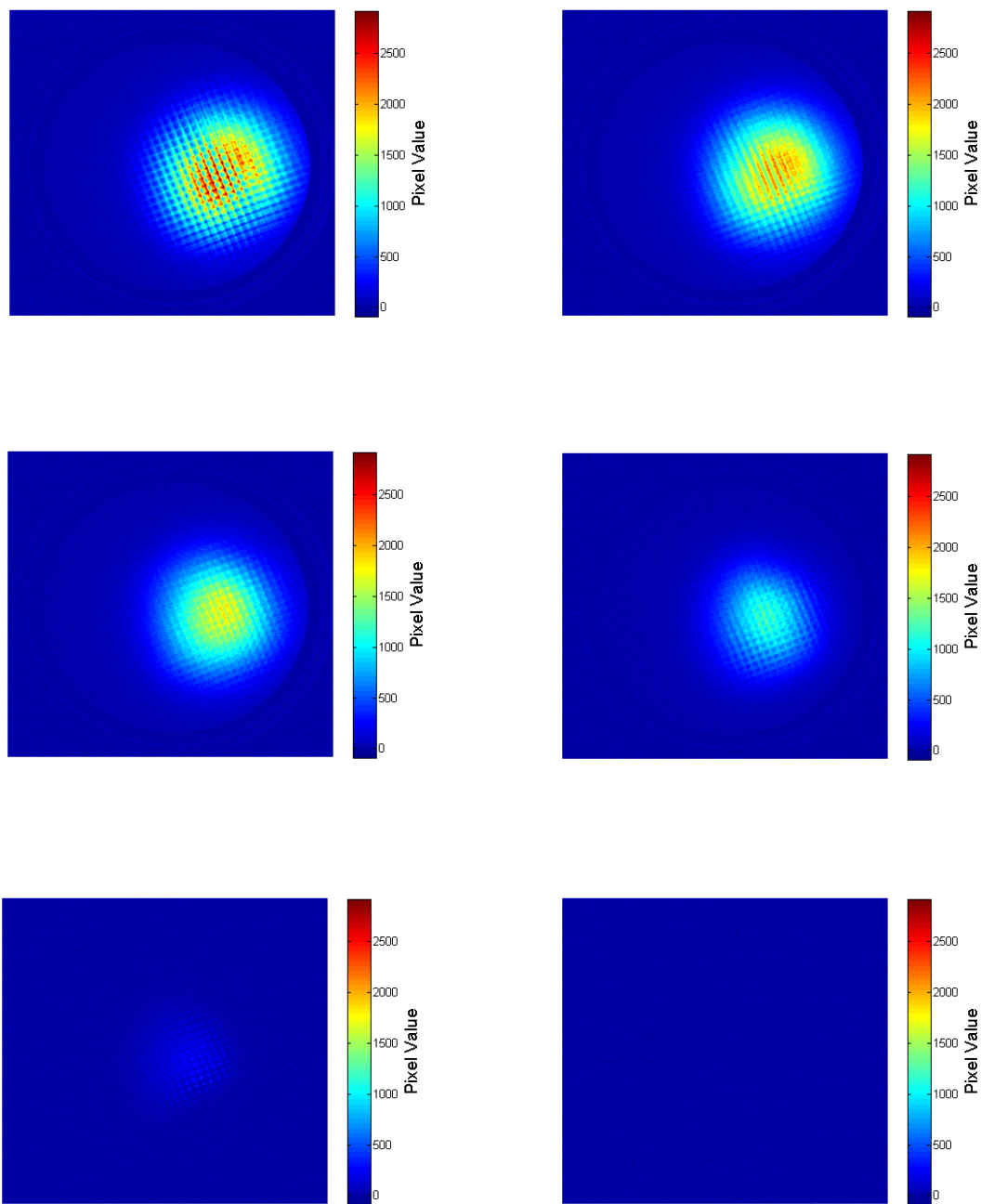


Figure 2.35: Background corrected pixel intensity values for increasing values of applied potential to the second mesh. The colour in each image is set to the same range so that they can be compared. From top left across and down: -56 V, -58 V, -60 V, -62 V and -64 V. Decreasing the second mesh potential reduces intensity.

After correcting the images for background, pixel values were summed for every value of the CCD matrix. Uncertainties of pixel values are attributed to noises in the camera due to thermal events e_{dark} and on chip noises e_{read} , which may be found from the datasheet [90], and the statistical nature of photon counting which is modelled by Poisson statistics with a standard deviation of the form \sqrt{signal} . The pixel uncertainty is found by the following equation [90]:

$$\Delta pixel = \frac{\sqrt{Pixel \cdot C + (e_{dark} \cdot n_{pix} \cdot t)^2 + (e_{read} \cdot n_{pix})^2}}{C} \quad (2.41)$$

Where C is the conversion of electrons per count, n_{pix} is the number of pixels and t is the integration time.

The results of this procedure versus the potential applied to the second mesh are shown in figure 2.36 where the intensity has been normalised to one. The intensity is approximately maximal for a potential greater than -58 V and falls to zero intensity at -64.5 V. The range in which the potential drops, from peak intensity to no detection, is 6.5 V. This is far higher than expected as the energy spread of electrons emitted from GaAs at this wavelength is expected to be less than 1 eV.

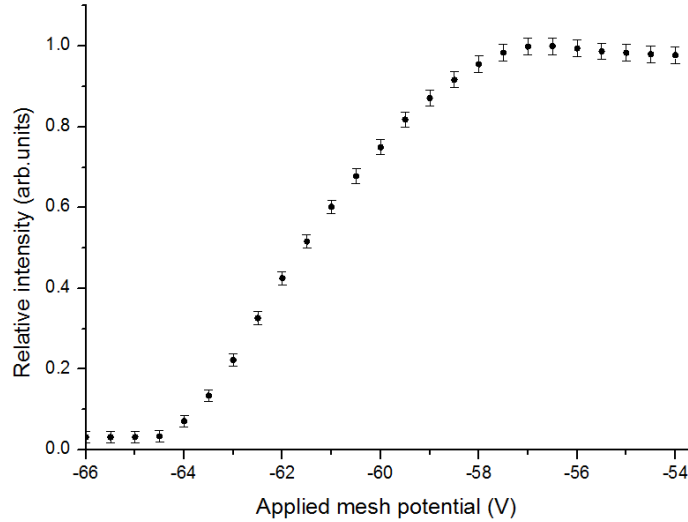


Figure 2.36: Signal from the camera obtained from the integral of fitted functions and normalised to the peak intensity. Both horizontal and vertical scans of the CCD matrix are shown and are consistent.

2.6.2 Simulation of the Filter Mesh Technique

To understand why the signal drops off over such a large range the tracking code was used to understand what is being seen in experiments.

2.6.2.1 Potential Surrounding the Mesh

When using the mesh as an energy filter the potential at the centre is the important value which needs to be known as it represents the lowest potential in which an electron can get through. It was shown in figure 2.22 that the potential around a mesh is such that the absolute potential minimum is found at the centre of the cell and increases parabolically to wires. When the first mesh, third mesh and MCP front potential are at zero potential the relation between the voltages applied to the second mesh and the potential at the centre of the mesh cell is found from Comsol by the relation:

$$V_{\text{centre}} = 0.8806 \cdot V_{\text{applied}} \pm 0.01 \quad (2.42)$$

This relation works over a wide range of voltage and does not depend on the longitudinal distance between the cathode and mesh/detector system.

2.6.2.2 Electron Motion in the Filter Mesh Technique

Figure 2.37 shows the path of an electron along the longitudinal and a transverse plane. The vertical lines show the longitudinal position of the three meshes, dashed, and MCP front, solid. The horizontal lines show the location of the wires onto the transverse plane axis.

Initially the electron travels a large distance in the transverse plane because at the beginning the velocities in both planes are equal. The electron is then accelerated towards the front mesh and as the longitudinal velocity is dominant at this point, the electron moves less in the transverse plane; this results in the curved path observed. The higher the initial transverse energy an electron has the further the transverse distance away from its point of emission in the drift space. As the electron passes the first mesh, the electron slightly moves towards a highly negatively charged wire. This may seem counterintuitive but can be explained. The potential in the mesh region between the first and second mesh is such that there is a lower potential, compared to the

potential of the wires, between the wires around the first mesh and a higher potential between the wires in the second mesh, compared to the wires potential applied to the second mesh. The electron is decelerated once it enters the mesh region and moves towards the region of higher potential, in this case the area surrounding the wires of the first mesh. However, closer to the second mesh the potential at the centre is at a higher potential, which means that the electron moves towards the centre of the second mesh. The turning point occurs just before the second mesh. After overcoming the potential barrier the electron is accelerated to the MCP.

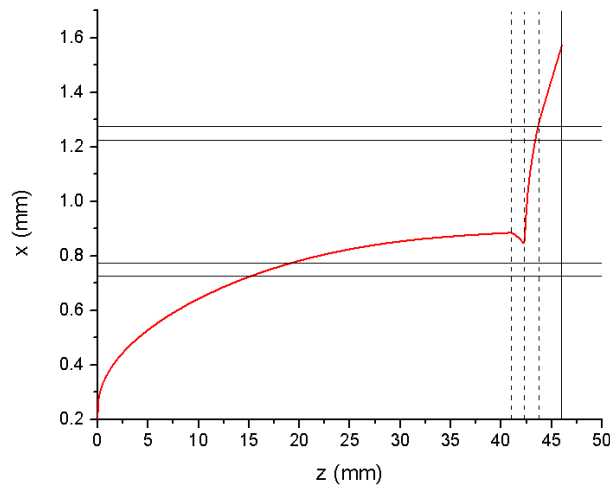


Figure 2.37: Electron path from emission at the photocathode towards the meshes, three dashed lines, onto the MCP face, solid vertical line. The horizontal lines indicated the positions of mesh wires.

Figure 2.38 shows the transverse energy of the electron in this example in units of electronvolts. The meshes have an effect of increasing the transverse energy of the electrons. As with the last case the vertical dashed lines indicate the position of the meshes. The transverse velocity drops slightly in the drift region but cannot be seen at this scale and occurs as result of a non-uniform transverse field. It then drops to near zero between the first and second mesh before sharply increasing to a plateau between the second and third mesh, then increasing to a second plateau after the third mesh. The last data point has been omitted since the velocity is forced to zero if the electron touches the MCP.

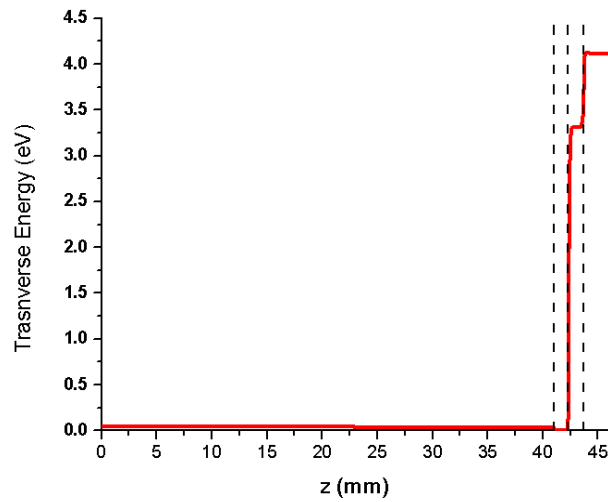


Figure 2.38: Transverse energy of an electron as a function of longitudinal distance in units of electronvolts. The dashed line again represents the three meshes

Tracking particles using the code it is possible to see why in the experimental images that the camera records the outline of the wire meshes. This may seem counterintuitive at first but can be explained by looking at the path of electrons. Figure 2.39 shows the image on the MCP from simulation, where it is possible to make out a mesh like structure.

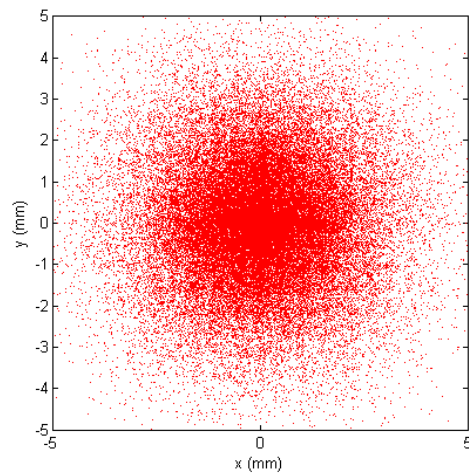


Figure 2.39: Simulated distribution of electrons on the MCP when the cathode and second mesh potential were both at -60 V. The points appear to make a mesh like pattern.

Figure 2.40 shows particle tracking, for one transverse direction, for many particles all with the same initial starting point and initial longitudinal velocity but with a random angle set between the two transverse directions so that they all follow unique paths. What is seen in this example is that all the electrons cross a common area, i.e just after the second mesh. The electrons which have not received a big kick in the x plane travel more in the y plane. The inset on the figure shows a zoomed in perspective of the crossing point.

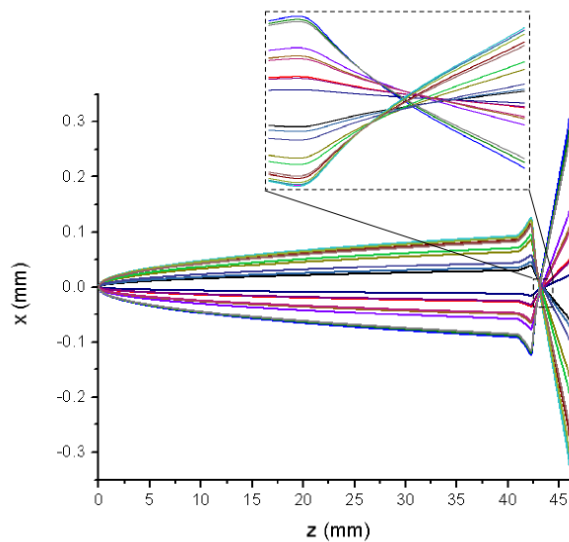


Figure 2.40: Electron paths of many electrons through the experiment. The inset shows a zoomed in look at the crossing point. The point of crossing occurs between the second and third mesh.

This can explain why in the experimental pictures the signal seems to follow the outline of the wires. Electrons which pass through the centre of the cell receive little perturbation in the transverse plane, whilst those which are travelling off centre are focussed in such a way that they are kicked further away from the centre. In this way the electrons position is transformed onto the resulting cross shape

In the figure just discussed, the initial transverse energy was small so the electrons passed through the same cell. If the transverse energy were to be increased but constant then, even though electrons have the same energy, the direction in which they enter the mesh region can lead to the appearance of interesting shapes on the MCP to appear.

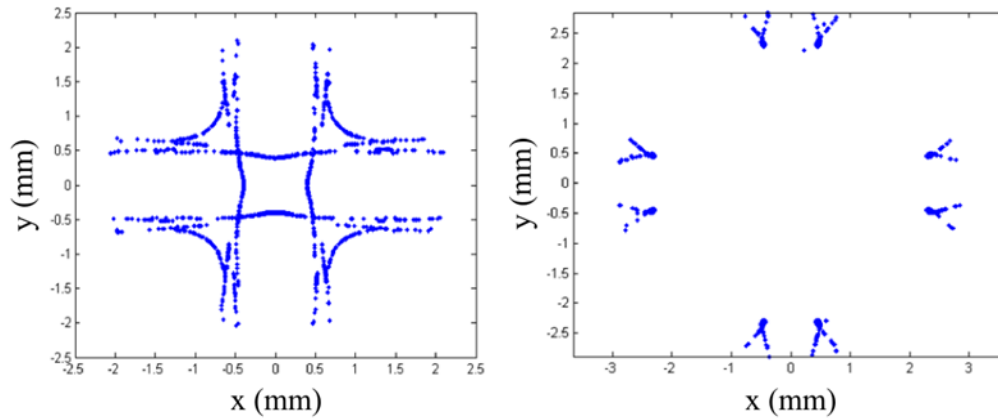


Figure 2.41: Patterns on the MCP for two cases. Left, cathode and retarding mesh at a similar potential and right with a high retarding mesh potential compared to cathode potential. In both cases the initial longitudinal and transverse energy are fixed.

Figure 2.41 shows the distribution of electrons on the MCP for two voltage configurations using an initial velocity distribution where the total initial energy and longitudinal velocity are fixed and a random angle is set in the transverse plane. Bearing in mind the initial transverse profile of electrons is circular, in both cases the recorded position is anything but a circular distribution. The left plot shows a case where the cathode potential and the retarding mesh potential are similar; in this case the mapping onto the MCP follows a mesh shape. The plot on the right shows a case where the retarding mesh potential is much higher than the cathode potential with a low initial energy of the electrons, i.e. only a small percentage are detected. As a result of the aperture window, discussed further in the next section, the point at which electrons can get through is small which leads to a different profile on the MCP. What is being demonstrated in this figure is that the focusing and defocusing effects on the meshes, along with deceleration, leads to complicated diffraction like patterns that would be hard to account for experimentally. Since experimentally it is clear that electrons are travelling through many cells, then from the distribution on the camera it is not possible to know the transverse energy of the detected particles. This is unlike transverse measurements where the transverse energy distribution is conserved. Furthermore, as the second mesh potential is increased, different shapes will appear on the MCP which is observed in experimentation. The code was then run using more realistic initial conditions to understand the experimentally obtained data.

2.6.2.3 Simulation Results using Realistic Initial Conditions

The code was used to simulate the experiment using initial conditions described in section 2.5.3, as in figure 2.31. The electric fields were calculated in steps of 0.5 V as in experiments, and the tracking code was run for each voltage setting for 50,000 particles. The percentages of particles recorded for each type of event are shown in figure 2.42 and figure 2.43.

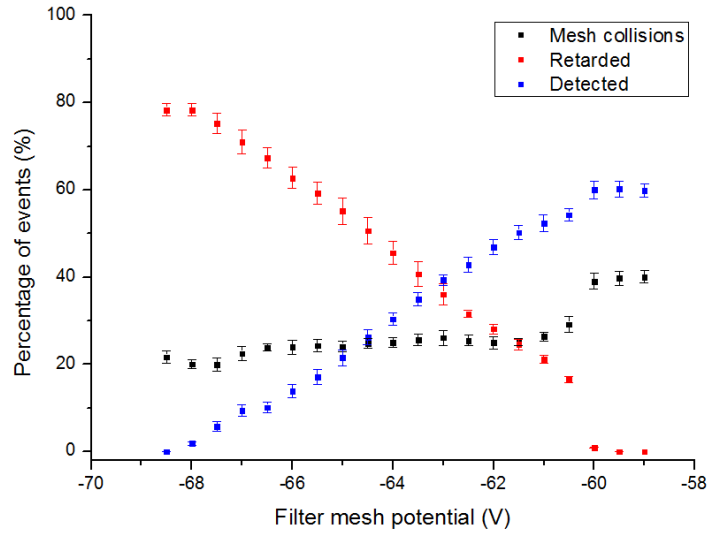


Figure 2.42: Simulated results of the percentage of events which were detected, retarded or collided with meshes for a range of voltages.

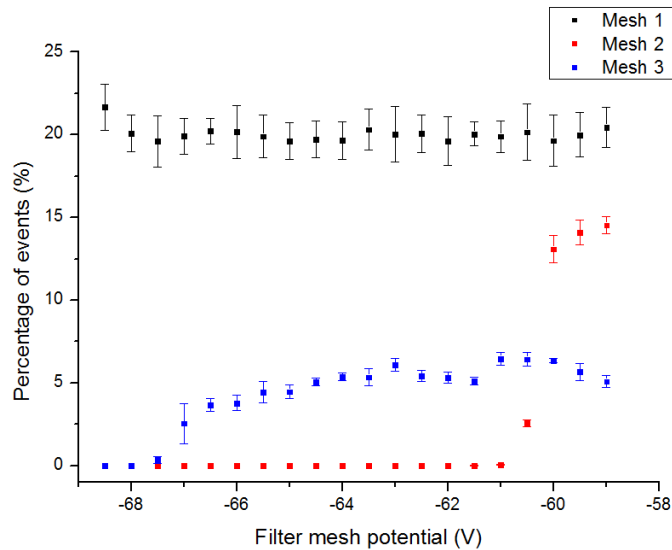


Figure 2.43: Breakdown of mesh events for each case for the simulated results.

The largest contribution to the uncertainty is the initial launch position on the cathode plate. A higher percentage of detected events usually occurred when the centroid of transverse distribution (which is a Gaussian, figure 2.32) is aligned with the centre of mesh cell. Errors were established by moving the centroid of the transverse position distribution from the centre to the cell corner and taking the mean and standard deviation of the number of events. Further contributions are due to the number of initial particles and also the MTE value used to sample the velocities. However, neither of these contributes as much to the uncertainty ($< 1\%$) as the initial position.

The results show several interesting features. The number of recorded events drops off after -60.5 V. This occurs due to an aperture window which is created around the wire with a minimum at the centre; this was seen in one dimension in figure 2.22. From equation 2.42 it is found that applying a potential of -60 V at the centre of the mesh means -68.135 V needs to be applied to the second mesh. This case is shown in figure 2.44 with each subsequent ring showing a decrease in potential of 1 V. As the potential applied to the second mesh is decreased this window becomes smaller and smaller. This means that even though the centre is at a potential which should allow all particles to pass through, if an electron attempts to pass through at areas closer to the wires then it may be retarded. This highlights a shortcoming of this technique. Only a small fraction of the electrons travelling with sufficient energy to overcome the barrier enter the region at the correct position to overcome the retarding potential. In this case the number of detected events falls to zero in the interval between -68 V and -68.5 V which is the region required to generate a -60 V potential at the centre. The simulation was run at the exact potential required to generate this value and no events were recorded.

It is found between -66.5 V and -67 V that the number of detected events stays constant. This was unexpected and was not due to lack of statistics or a poor field map and the number of retarded events follows trend. The number of collisions with the third mesh, however, falls sharply at this setting. Since electrons that pass the second mesh will be accelerated towards the MCP, regardless of energy loss with a mesh, they will now be counted as recorded events. By doing this the number of detected events follows a smooth curve

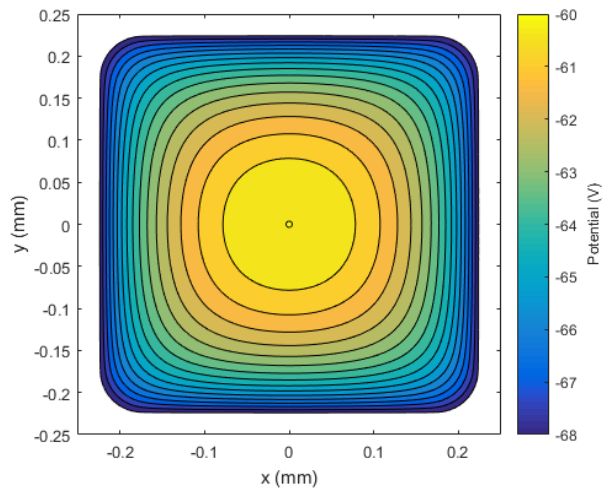


Figure 2.44: Contour plot of the potential in the mesh cell with -68.125 V applied to the second mesh. Each ring indicates a decrease in potential by 1 V.

The percentage of particles stopping at the first mesh is 19.1 ± 0.6 %. Assuming the open area of a mesh cell is a square with side $450 \mu\text{m}$ with the total area of the wires and space a square with side $500 \mu\text{m}$ then the open area ratio is 81 %. The value obtained from the simulation is consistent with a homogenous beam hitting the first mesh.

Below -60 V there are no collisions with the second mesh. This is a result of electrons near the second mesh wires being retarded. After -61 V there are no more recorded events. The initial velocity distribution favours a lower energy contribution which explains why the number of events fell suddenly after -60 V. The total energy distribution, i.e transverse plus longitudinal energy components can be greater than 1 eV when sampled and this explains why some of the events recorded at -61 V.

The number of third mesh collisions decreases with applied voltage which is to be expected as fewer particles make it through the energy filter.

2.6.3 Comparison between Simulation and Experimental Results

Figure 2.45 shows a plot of the relative intensity of both the experimental and simulated results as a function of applied voltage. The green dashed line indicates the point at which the potential at the centre of the mesh cell is -60 V.

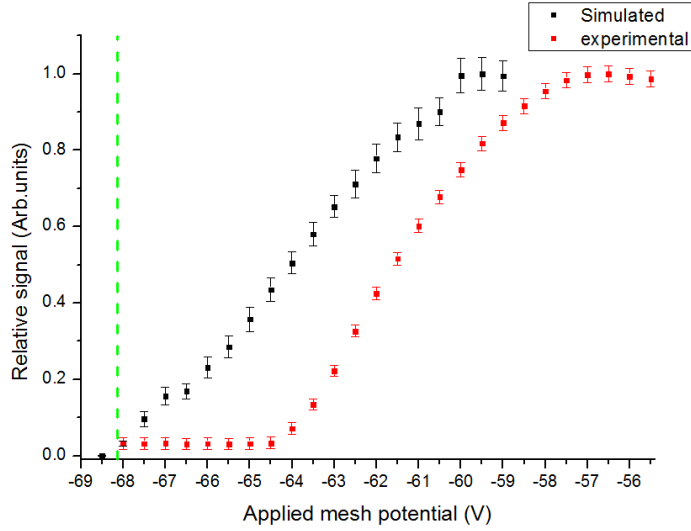


Figure 2.45: Experimental results and simulated points both plotted as a relative intensity to the maximum signal. The green dashed line shows the point at which -60 V is generated at the centre of the cell.

It is clear that even though the trend is similar, the simulated and experimental data decrease at different voltages. This is due to the Volta potential, sometimes called the contact potential. The Volta potential was observed by Volta in 1801 and occurs when the Fermi level of two electrically common materials re-adjusts to the same level [106]. This has an effect of creating a difference between the applied potential to a surface and the true potential difference between the two materials. In the simulated results this is not accounted for as applied and true potentials are assumed to be the same and is why there is a shift at which point the signal falls. The difference in work function ΔW between two materials with work functions ψ_A and ψ_B is equivalent to the contact potential V_c by:

$$\Delta W = (\psi_A - \psi_B)q_e = q_e V_c \quad (2.43)$$

For GaAs an estimation of the contact potential is difficult because the work function depends on the quantum efficiency which can widely change due to the vacuum conditions. An approximation can be found by taking the bandgap of GaAs as 1.42 eV [77] and the work function of tungsten as 4.52 eV [107]. This gives a contact potential of approximately 3 V which matches with experimental and simulated differences. This is only a very rough approximation as the Fermi level in GaAs can fluctuate depending on the surface state of the photocathode.

In both simulation and experiment the signal drops over several volts which would not be expected if signal reduce due to retardation of the initial energy spread only. As it has been explained previously the potential surrounding the wire mesh means that there are regions in which the electrons may pass through even if the applied potential is so high that electrons approaching the wires will be retarded. Increasing the second mesh potential means more and more electrons are retarded whilst the window in which electrons can pass gets smaller and smaller. At the point the second mesh potential produces a potential of sufficient magnitude so only particles with enough initial energy will pass through, it is such a small region that barely any electrons pass through. Therefore it was not possible to obtain an energy distribution curve from either the experimental data.

2.6.4 Review of the Filter Mesh Technique

This technique has many problems which have been found both through experiment and simulation. What has become apparent in these studies is the importance of the aperture window between the wire meshes.

The results obtained from simulations can be explained logically and they also demonstrate some consequences of the technique, namely the diffraction like effect of the wire meshes. Simulations also predict the reduction in detected signal due to the aperture window.

Lower voltages may work better in this scheme as the gradient in potential from the centre to the wire is smaller. However, even with optimised parameters, obtaining a useful signal is very difficult. Furthermore, as a result of the Volta potential it is not clear, even with good knowledge of the potential of the system, exactly at what point what is being detected by the camera is from electrons which overcome a barrier or due to their initial energy alone.

In these techniques, simulations have largely been focused on a perfectly aligned system. In section 2.4.2.6 distortions were considered and how they affect the potentials produced around wire meshes. Now the importance of the aperture window has been realised these effects would need to be considered in greater detail in terms of the detected signal. Even with optimised conditions the number of electrons at this point is small. Furthermore, simulations have shown that the initial point of emission has an effect on the number of detected particles. It was assumed in these simulations that the laser was incident directly at the centre of the cathode. By moving the mean of the Gaussian position profile, it was observed that off centre the number of

detected values drops for all voltage configurations with lower detected events moving further away from the centre. What this has shown is that not only the distortions of the mesh layout that could affect the result but also the emission point can affect how many electrons are detected.

Further ideas were considered in which the third mesh was not kept at 0 V but was used in order to work with the second mesh to create a flatter window close to the second mesh. This was found in simulations to increase the detected signal however geometrical errors would be more detrimental for potential calculations in this case and the signal was only fractionally better.

The relation between the voltage at the centre and the voltage applied was calculated as a function of mesh cell size. The reason for this study should now be apparent. The ideal case would be one where the voltage applied to the mesh and the minimum potential of the energy filter are similar. For the smaller cell sizes therefore the signal should be greatly improved compared to the case studied here however the problems just described will still be present somewhat. The other proposed technique will now be investigated which avoids many of the problems found from this technique.

2.7 Method Two: MCP/Cathode Gap Technique

The next technique attempted was not to use the wire meshes as an energy filter but to use a potential difference between the cathode and MCP front.

The MCP/Cathode gap technique avoids the need to know the exact field values surrounding the wire meshes. Whilst it is not necessary to study the fields using finite element solvers, this technique provides an opportunity to optimise the full package, and furthermore, the technique may be better understood and also the limitations can be explored.

In this technique electrons should be detected if they have sufficient energy greater than the potential difference between the cathode and MCP. Poor choice of step sizes chosen to export the field map can lead to erroneous results. As the outcome is known based on the initial energy of the electron, the correct step sizes could be found. This was not possible in the filter mesh technique since particles were retarded despite there being the opportunity for it to be detected

The camera and Phosphor screen are not utilised as a direct current measurement is taken from the front of the MCP. By doing this an accurate reading is obtained since the camera is not involved and fewer steps are taken to record data, however transverse information is lost and it is not known where exactly the electrons hit the MCP. This also makes the analyses slightly easier

as further complications with analysing camera data are avoided.

The current was read from the MCP front using a lock in amplifier, an SR830 [108]. The same device modulates the laser between off and on at a frequency between 1 mHz to 102.4 kHz. The SR830 records the current over the modulation of the on/off laser and records a photocurrent. By calculating the difference between the on/off laser state on the lock in amplifier a background subtraction is performed automatically with femto-Ampere precision. The device also takes into account the time of flight of electrons as well as timing effects from cables by locating the largest difference in maximum and minimum signal in a 90° phase shift.

The code is ran in the same way as previously discussed, however, this time individual two dimensional data maps are required for each case as unlike the previous method the field map in the drift region changes with each increase of the cathode potential.

2.7.1 Experimental Results

A dataset was obtained from TESS when a NEA GaAs cathode was inserted and a laser of 635 nm was used to stimulate electron emission. Three mesh potential configurations were used. In all three cases the MCP front voltage is 0 V. The cathode voltage was scanned between values of -10 V and +10 V. When it was found where the signal was decreasing due to retardation, smaller steps were used and the photocurrent measured from the MCP front. Figure 2.47 shows the photocurrent as a function of the cathode potential. The resolution of the voltage supplied to the cathode is 0.01 V and the noise of the measured current is $130 \text{ fA}/\sqrt{\text{Hz}}$ for the gain applied to the lock in amplifier and is related to the frequency of the system. The error bars are shown in figure 2.47 and it is clear how much more precise this technique is compared to using the camera system.

The range over which the signal drops is far smaller than with the filter mesh technique. As with the last technique the voltage is shifted due to the contact potential.

It is possible to obtain an understanding of the energy spread by differentiating the IV curve. This is shown in figure 2.48 where the experimental data set has been smoothed using a moving average smoothing filter. As a result of a non-flat plateau in all three cases in figure 2.46 there are regions before the Gaussian like curves where the calculation is less than zero which is not shown on the plot. Uncertainties are not presented of the LEDC curves as is the usual convention when presenting these curves in literature.

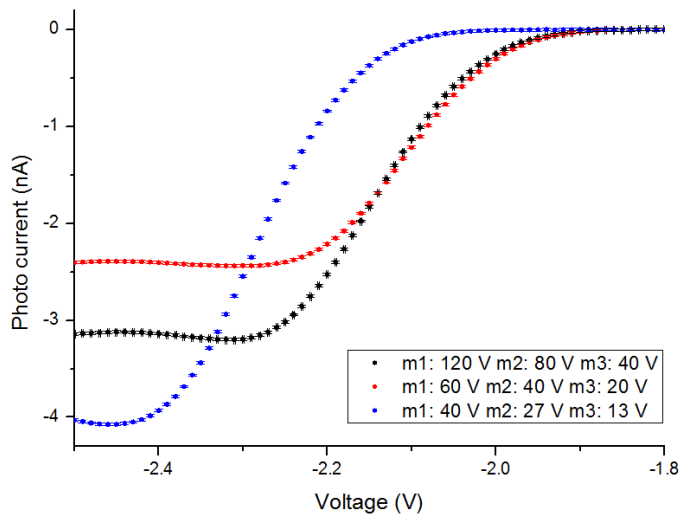


Figure 2.46: Measured current voltage (IV) curve with the cathode potential scanned in steps of 0.01 V and the current read from the front of the MCP.

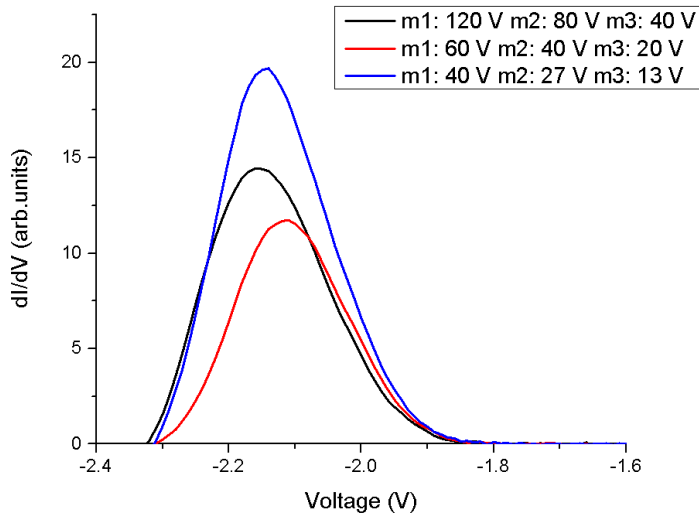


Figure 2.47: Differential of the IV curve in figure 2.46.

Figure 2.48 shows the same curves normalised to the peak height of each curve. Whilst the curves have a slight shift relative to each other their general shape is similar. Fitting a Gaussian to these curves yields values of standard deviations, and therefore the energy spread, of 83.5 mV, 83.3 mV and 89.0 mV for the black, red and blue lines respectively. This suggests that the potentials of the meshes are independent on the final result of energy spread. This should be expected since looking back to figure 2.13, the difference between the cathode and MCP is all

that matters and not the path of potential it takes to reach the detector.

The longitudinal energy distribution obtained is comparable to previous results of measuring GaAs at room temperatures [109]. This technique will now be studied using the simulation package to understand the technique further.

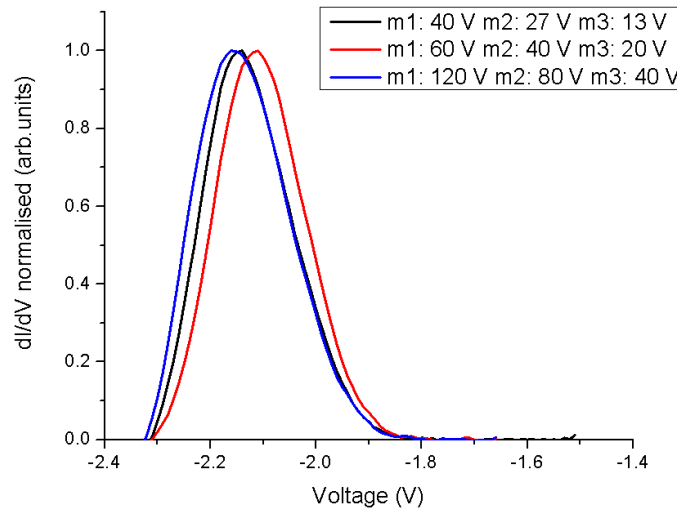


Figure 2.48: Longitudinal energy distribution curve derived from IV curve in figure 2.46.

2.7.2 Simulation

2.7.2.1 Electron Motion in the MCP/Cathode Gap Technique

The kinematics of electrons is different in this technique compared to the filter mesh technique; in fact it is simpler and avoids many of the complications described previously.

Figure 2.49 shows the path of several detected electrons using the voltage configuration described above, with the electrons given an initial energy sufficient to be detected. In this scheme electrons are accelerated in the drift region much in the same way as before. Deceleration occurs over a longer distance with retardation occurring between the third mesh and MCP front. The potential surrounding the wires is higher than the potential between the centre of the cell which causes the electrons to drift towards the wires.

It is found that the electrons do not follow the mesh like pattern shown in the previous method and the transverse distribution of electrons upon entering the mesh region is roughly conserved.

In the tracking code the MCP is treated as a flat surface which is not the case. Electrons can be

very short distances from detection and still be retarded. This is also the case with experimental data as local potential distortions from holes cannot be accounted for.

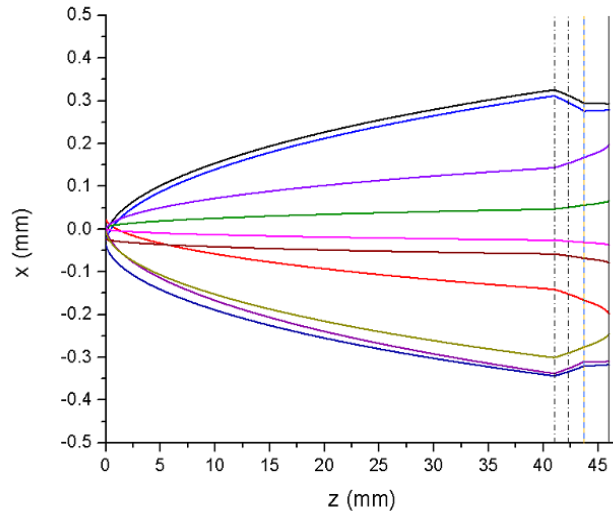


Figure 2.49: Electron paths for a couple of particles using the second technique. The dashed lines again represent the wire mesh locations and the solid vertical line the MCP front.

2.7.2.2 Potential Limitations of the Technique

When debugging the code some electrons were retarded even if they had sufficient energy to make it to the MCP. A large amount of these events occurred as a result of using poor parameters in the tracking code, coarse field maps and large steps in tracking etc. After these errors were fixed it was observed that some electrons were still being lost.

It was found that it did not necessarily matter if the initial longitudinal velocity was an equivalent energy to the potential gap i.e. if the initial longitudinal velocity component was not sufficient but there was some initial transverse velocity to put the total energy over the required value, then detection could occur. Further investigations found that retardation occurred as a function of the ratio of initial transverse velocity compared to longitudinal velocity. The following figures aim to demonstrate this and suggest reasons why it may occur.

It was found that all electrons were detected as long as their initial energy was put entirely in the longitudinal direction. Upon keeping the energy constant and increasing the amount of transverse velocity it was found that the number of detected events decreased and the number of retarded events increased. In figure 2.50 this is shown as the number of events which were

stopped on the MCP plate using the same voltage configuration used in experiments i.e. mesh values of 60 V, 40 V and 20 V and a potential difference between the cathode and MCP of 0.2 V. Within the script the total energy of electrons is fixed at 0.21eV which is then converted to a velocity. The initial velocity is then split between the transverse, v_{trans} , and longitudinal, v_{long} , directions through an angle θ , i.e:

$$v_{long} = V_{total} \cdot \cos(\theta) \quad (2.44)$$

$$v_{trans} = V_{total} \cdot \sin(\theta) \quad (2.45)$$

A total of 1800 particles are then simulated which are not chosen at random but are equally spread in the transverse plane so the distribution of electrons follows a circular distribution. Since there is no random selection process and completely systematic, performing the simulation any number of times would produce the same results and so no error bars are present.

The plot shows that there is a general trend of decreasing number of detected events when θ increases. At angle values of 6° and 18° the number of detected events fall dramatically, these coincide with a high number of mesh collision events. Taking this into account and ignoring these angles the number of detected events is still not decreasing linearly. This suggest that there may be a relation of particles being lost with the angle they enter the mesh region. This is not as was the case in when the mesh was used as a filter as the initial position of the electron does not affect the outcome, i.e. setting an angle of 0° and changing the initial position would only result in detection and mesh events. This was not the case for the other technique as particles would be retarded if they enter the mesh cell in particular errors.

What appears to be occurring is that the meshes are causing a transfer of longitudinal velocity to transverse velocity. When an electron is decelerated approaching the MCP front, it may occur that their longitudinal velocity is reduced to zero, whilst still having transverse velocity and is then retarded. The next two figures illustrate this further.

Figure 2.51 shows the transverse energy of electrons at the point close to the cathode in which they were sent back through the meshes. It is quite clear to see the relationship between the two. Electrons which have a high velocity in the transverse plane stop much sooner compared to those electrons which stop closer to the cathode. The electrons which make it closer to the cathode have more longitudinal velocity to make it this far but were ultimately not detected. The tracking code does not calculate the error in position or velocity and so none are given in the figures however a clear trend is observed.

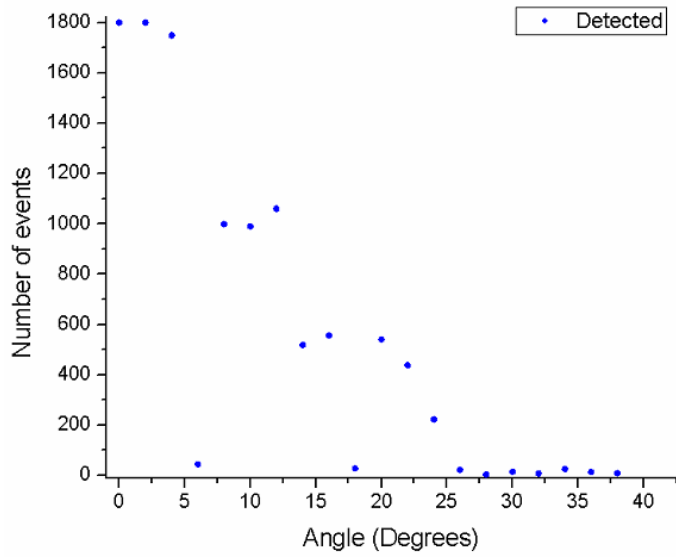


Figure 2.50: The percentage of events detected, retarded and collided with a mesh as a function of the angle between the transverse and longitudinal velocities

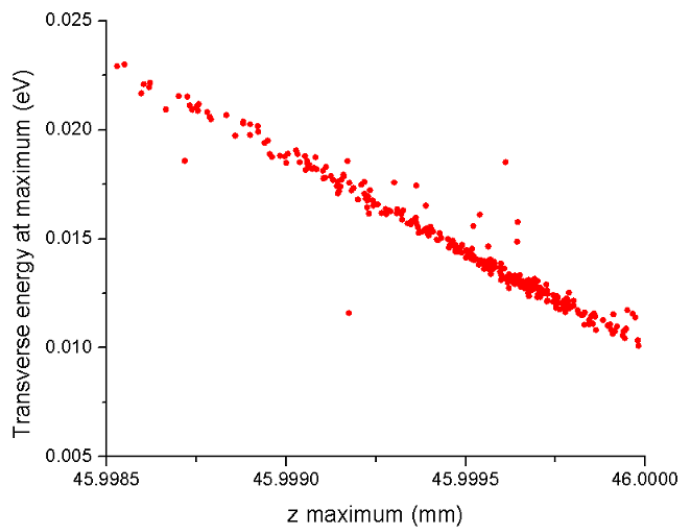


Figure 2.51: Electrons that were not detected as a function of the position at which it turned back and the transverse energy at that point.

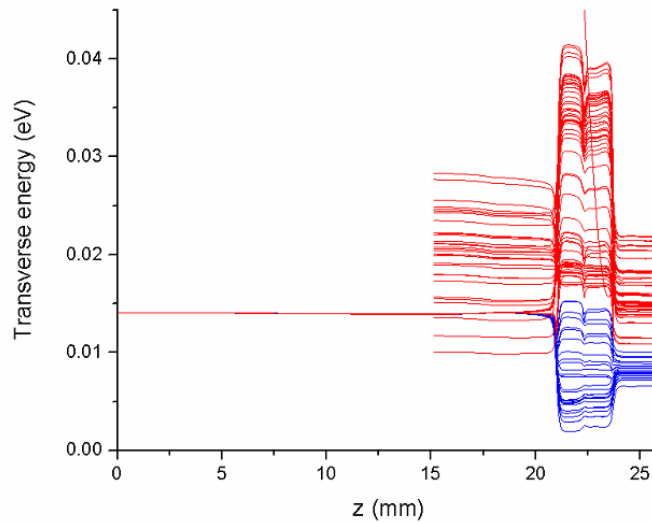


Figure 2.52: Transverse energy of electrons as they travel through the model. Red lines indicate lost electrons and blue lines were detected events.

Figure 2.52 shows the transverse energy of electrons detected, blue, and retarded, red, in units of electron volts as they are tracked through the model. What can be seen is that those electrons that were detected they experience a force which reduces the amount of transverse velocity whilst those that were retarded either gain transverse velocity or do not reduce transverse velocity as much as the detected events. Interestingly, the two colours can be seen to be distinct outcomes before the first mesh which further indicates that the point of entry into the mesh may also be a consideration. It is found that the higher the ratio of transverse to longitudinal velocity, that there is a higher transfer of velocity to the transverse plane.

What these studies have shown is that the cause as to why particles are not detected in certain situations goes beyond any numerical errors due to the code or technique. This effect may occur due to focusing effects from wire meshes as it appears to be that electrons require a certain amount of velocity pointing in the longitudinal direction so that they reach the MCP. The meshes cause a transfer of velocity between the transverse and longitudinal directions. This leads to electrons having too much transverse velocity whilst being decelerated in the longitudinal plane, and stops them reaching the detector.

This test was repeated for a single mesh, rather than the three mesh system TESS currently has to see if this has an effect. It was found the effect still occurs and also shows the behaviour at similar angles as with the three mesh system. This may be expected from the three mesh

examination as looking at figure 2.52, electrons appear to differentiate between detected and retarded after passing the first mesh.

2.7.3 Review of MCP/Cathode Potential Difference Technique

The MCP/Cathode gap technique has many advantages over the filter mesh technique. The most obvious advantage is the removal of the aperture window which meant only a small number of eligible particles were detected which had sufficient energy to be detected. Also the exact potentials surrounding the wire meshes do not need to be known which is difficult to know exactly when distortions are included in to the model. In this method there is no ambiguity at what point the signal is being recorded, unlike the filter mesh technique where the unknown contact potential made it impossible to know at what applied mesh voltage the potentials in the mesh cell were. The contact potential is still noticeable in the MCP/Cathode gap technique, however, it can be corrected for.

Using the tracking code it has been found that some electrons are retarded even though they have sufficient total energy to overcome the potential barrier. It has been found that this effect increases when more energy is given to the transversal energy component. This may suggest that the experimental result is an underestimation of the true value.

2.8 Chapter Summary

In this chapter studies have been presented which aim to improve the understanding of electron emission by the better understanding and the modeling of the TESS experiment.

The chapter began by introducing concepts behind electron emission sources for particle accelerators with a particular attention on photoemission and some of the common materials used. The TESS experiment was described which is to be used to measure both the transverse and longitudinal energy spread of photocathodes with gallium arsenide being used to commission the experiment but other materials are being considered for future experiments.

Measuring the longitudinal energy component was the main focus of this chapter. To fully the methods it was required to understand the electric fields generated around a wire mesh and to develop a tracking code so the TESS experiment can be modeled from electron emission to detection.

The tracking code was written in Matlab Simulink and was specifically developed for the

purposes of studying the motion of low energy electrons through electrostatic meshes. The code makes use of field maps calculated in finite element software. Existing packages such as SIMION [110] could have been used, however, the modelling of complex shapes and very detailed geometries is not possible. Understanding the fields from electrostatic elements is essential to track particles with good confidence. An analytical expression was first derived which gave insight into the approximate field around a mesh. More complex computer-based solvers were then used to find more accurate solutions.

In this chapter two methods of measuring the longitudinal energy distribution of electrons emitted from GaAs and were explored both through experimentation and simulation.

The first technique considered used TESS' wire meshes to generate an energy filter which the electron must overcome to be detected. This method was found to be ill-suited for the task due to several reasons. The first is that even with sufficient modelling tools, it is not possible to know the exact fields surrounding the wire meshes in any given configuration due to the contact potential which is an unknown value. Furthermore, and perhaps the main limiting factor, the potential distribution surrounding a mesh meant that applying a certain potential to a mesh produced a smaller potential at the centre of the cell. The particles which are allowed through are those which have potential greater than the centre potential. As a result of the cell size, a large cell pitch means the potential falls rapidly from the wires to the centre meaning that there was only a very small area that electrons could pass through. The effect of this was seen in both simulations and experiments in which signal reduced over many volts, the decrease is not attributed to particles having sufficient initial energy but due to the potential configuration. Operating the experiment at conditions in which electrons are retarded from having insufficient energy leads to a very small signal. This is true in simulations were everything was perfectly aligned. It was further found that the initial starting point of electron emission on the cathode in relation to the wire mesh also affects the outcome. For these reasons this technique should not be used to reconstruct an energy distribution curve of emitted electrons.

The second technique created a potential difference between the cathode and MCP. In this technique the detector set-up was changed, a current was measured rather than to taking images. Using this technique avoids complications with the wire mentioned above. It was possible to obtain a longitudinal energy distribution curve using this technique. It should principally be used to measure the longitudinal energy distribution curve of electrons in TESS. However, from using the simulation package that has been developed, it has been observed that in certain situations

electrons are not detected due to a transfer of velocity from the longitudinal direction to the transverse plane. This effect has not been considered before and should be the focus of any future work as it can lead to an underestimation of detected events close to the potential barrier. The outcome of this work has been the development of a new tracking code based on finite element analysis which can be used to accurately model the TESS experiment. The code has been benchmarked with experiments and there was a good agreement between the two. Through simulations TESS is now better understood in terms of what techniques work and what doesn't, and can be used to explain results obtained in experiments not previously considered. Furthermore, the simulations allow the resolution of TESS to be found. The code could also be used in understanding results in transverse measurements. In experiments similar to TESS [111], the analysis uses electrostatic lens theory [15] rather than more advanced simulation methods like the one developed here. Using this code may allow deeper analysis to be performed to understand how the system works in greater detail.

Chapter 3

Beam Loss Monitoring study for the Compact Linear Collider

The previous chapter focussed on the study of low energy electrons and studying ways into how they are generated. The next chapter focuses on how higher energy electron beam losses can be efficiently detected. This includes a review of technology commonly used at accelerator facilities to detect beam losses as well as a new type of beam loss detection technology utilising fibre optics currently under development for the Compact Linear Collider.

The chapter begins with an introduction of the causes of beam losses in an accelerator. To detect beam losses, Beam Loss Monitors (BLMs) are installed along the beamline. Signals are generated in BLMs by radiation being detected. For this reason a short summary of matter and light interaction with materials are first discussed.

Typical examples of beam loss monitors are then discussed with the drawbacks and benefits of each given. This work is incorporated within the CLIC project where the sheer size of the facility means a high number of detectors are required. Different CLIC loss scenarios are also presented.

The chapter then moves on to the development of a new beam loss monitor based on fibre optic technology coupled to photodetectors which may be a solution to the large number of detectors required for CLIC.

The photodetectors at the end of the optical fibre BLM are an integral component in the detection process of losses. The timing resolution of a detector can have a big influence on the limit with which a loss may be reconstructed longitudinally. Furthermore, the dynamic range of

the photo sensor may limit what type of pulses can be measured. Dead time is also a factor which is important to beam loss monitoring. A detector should ideally always be ready to detect the next loss. SiPMs are then formally introduced with their architecture and operation described along with some characterisation experiments that were performed with beam loss monitoring in mind. SiPM performance is then tested in conditions which they have never been tested before with emphasis on performance in beam loss monitoring applications

The chapter then moves on to experiments undertaken to test the optical fibre BLM at the CLIC test facility CTF3 which allows beam loss monitors to be tested using a CLIC-like beam. A short introduction is given to the CTF3 layout and the beam properties which are delivered by the accelerator. A summary is then given of simulation results of losses expected at CTF3. Multiple fibres and detectors have been installed at CTF3. The layout of the fibres within the CLEX hall is discussed. Experimental results of the signals obtained are then presented for all the detectors installed and a detailed data analysis is performed to understand the loss structure obtained from the fibres and also the performance of the localised detectors to distinguish inter-bunch train losses.

3.1 Machine Protection for Particle Accelerators

3.1.1 Beam Loss Monitoring

Machine protection is an important system to consider for maintaining an accelerator. It is important for both machine operation and for the health of people working on the machine.

High energy particle losses may collide with machine parts and turn them radioactive, making them hazardous for technicians to work around. If a beam loss is too high then this also might stop operation of the accelerator. For example the LHC uses superconducting magnets and if a beam loss was to occur and interact with the superconducting material this may cause the magnet to heat then quench and lose its superconductivity [112]. This would stop the magnet from working properly and operation of the accelerator would suffer. It is mandatory therefore to place instrumentation along the beamline where beam losses are expected to occur so that adjustments can be made to reduce the impact on the machine by either dumping the beam or changing machine settings.

A beam loss in an accelerator can be due to many different reasons and different protection systems are designed to limit the damage from these losses. Losses range from ultra-fast events,

which occur in the range of microseconds to steady state losses that occur over hundreds of seconds, particularly important for storage rings [113]. In between these two extremes are losses that occur in the region of milli to tens of seconds. BLMs are designed to detect these losses.

A BLM needs to satisfy many requirements and no one BLM will satisfy all of them. In order to be practical, a BLM must first be radiation hard to survive the high radiation environments in which they will be exposed and not require frequent replacing due to radiation induced damage. They must operate quickly so that changes can be made in order to prevent beam loss and to distinguish between beam loss events. In earlier years BLMs were not online tools but for modern accelerators they are indispensable tools for improving accelerator performance. Of increasing importance is the ability to have a high dynamic range, the range between the lowest and highest detectable signal. BLMs are also increasingly being used not only for machine protection purposes but also for online beam diagnostics such as for beam alignment and as such detection over a wide dynamic range would be beneficial. The total cost of a BLM network also needs to be taken into account. With increasingly larger machines thousands of localised monitors on a single beam line may be required. With the cost of machines often being a big factor in the approval for their construction, it may be more ideal to move away from localised detectors and move towards long BLMs which can span large distances but still provide the same loss coverage as localised detectors. Beam Loss Monitors cover two classes of losses:

- 1) Fast losses (also known as irregular losses): This class of losses contains losses which are avoidable. Examples of these include misaligned beams or faulty accelerator elements such as a trip occurring in the RF supplies. These losses are distributed throughout the machine. These types of losses can be captured by a good collimator system. A threshold value can be set so the beam is dumped if losses become too high [114].
- 2) Slow losses (also known as regular losses): This class of losses are avoidable. Slow losses are more prevalent to circulator machines due to the long storage time.

3.1.2 Parameters for Discussing BLMs.

Before discussing the various types of detectors it is necessary to define some parameters so that they can be compared. Radiation is detected because it deposits all or some of its energy into a

material. In this section the interaction between radiation and matter will be discussed as well as some common terms used to compare different BLMs. By radiation, this is inferred to mean either particles or electromagnetic radiation which deposit energy when passing through matter. The mechanism in which this occurs depends on the type of radiation as well as its mass and energy and the material it is passing through. Discussion will mostly be focused on mechanisms used in particle detection.

3.1.2.1 Charged Particle Interaction with Matter

Charged particle interaction can be broken down into three categories:

1. Inelastic scattering
2. Radiative losses
3. Elastic scattering

The amount of energy deposited per unit length by a particle into a material is called the stopping power, dE/dx . Relativistic heavy charged particles lose their energy mainly by inelastic scattering with electrons leading to ionisation and are the mechanism behind many particle detectors. The mean rate in which energy, E , is lost along a distance x in a bulk material is described by the Bethe formula [115]:

$$\frac{dE}{dx} = \frac{4\pi}{m_e c^2} \cdot \frac{nZ^2}{\beta^2} \cdot \left(\frac{q_e^2}{4\pi\epsilon_0} \right) \cdot \left[\ln \left(\frac{2m_e c^2 \beta^2}{I(1 - \beta^2)} \right) - \beta^2 \right] \quad (3.1)$$

Where Z is the atomic number of the bulk material, β is the ratio of the particle velocity and the speed of light, n is the electron density of the material, I is the mean excitation energy. This equation is an approximation and numerous corrections need to be made to fit specific cases. An example of this is concerning the velocity of the particle. The Bethe formula is derived assuming the electrons are motionless compared to the speed of the passing particle, this means that as different orbitals move with different speeds then the Bethe formula over calculates the stopping power and so must be corrected for. Similar corrections need to be taken at higher velocities. Equation 3.1 is the Bethe formula, when shell corrections are taken into account it is called the

Bethe-Bloch formula. A review of corrections and when they need to be applied is given in [116].

With electrons and positrons the situation is a little more complicated. As a result of their smaller mass, they are less penetrative because inelastic scattering causes a large energy loss. This means they have shorter range in matter than heavier particles with the same energy. They also have their own Bethe formula which is slightly different to equation 3.1. The discrepancy with the standard Bethe formula occurs because the mass of the incident particle and the target is the same. In this case the target and incident particle cannot be distinguished. The Bethe formula for electrons can be written as [117]:

$$-\frac{dE}{dx} = 4\pi \cdot N_A \cdot r_e^2 \cdot m_e \cdot c^2 \cdot \frac{Z}{A} \cdot \frac{1}{\beta^2} \cdot \left[\ln \left(\frac{\gamma m_e c^2 \beta \sqrt{\gamma - 1}}{\sqrt{2I}} \right) - (1 - \beta^2) - \frac{2\gamma - 1}{2\gamma^2} \cdot \ln 2 + \frac{1}{16} \left(\frac{\gamma - 1}{\gamma} \right)^2 \right] \quad (3.2)$$

It is important to stress that values calculated from the Bethe formula are mean values. Particle interaction is a statistical process and Monte Carlo codes, such as Fluka [118] or Geant4 [119], are required to simulate theoretical interactions rather than calculate them from a table.

At higher energies heavy particles also lose energy by emitting radiation. One type of radiative loss is Bremsstrahlung and occurs when a charged particle is decelerated in a Coulomb field, similar to synchrotron radiation mentioned in chapter 1. The effect is more pronounced for electrons; typically Bremsstrahlung for heavy particles does not become a factor until they are relativistic. Other radiative effects include Cherenkov radiation, covered later in this chapter and transition radiation, sometimes called Optical Transition Radiation (OTR), which is the effect in which a charged particle emits radiation when passing across a boundary with a change in the refractive index. OTR is used extensively in beam diagnostics to measure beam size, energy and emittance [120] [121].

Elastic scattering can also occur, where collisions between electrons and nuclei can cause many large deflections due to the large mass difference. However, as elastic scattering does not lead to the deposition of energy in a material it will not be discussed further.

Figure 3.1 shows the stopping power of a muon in copper as a function of particle energy. The stopping power reaches a minimum point in the Bethe-Bloch section of the plot. Particles travelling at this energy are called minimum ionising particles (MIPs). The stopping power then

increases again due to radiative effects. MIPs are a useful measure as it provides a measure on the least energy required to trigger a signal in a detector. A good approximation for many materials is that $MIP \approx 1\text{-}2 \text{ MeV/g/cm}^2$. Any particle above this energy can be considered a MIP. The number of detected particles should be proportional to the number of lost particles with the proportionality depending on the efficiency of the BLM. The efficiency depends on the sensitivity which depends on its dimensions, the particles being detected and the energy required to generate a signal etc. The energy deposited in a detector can either be written in terms of rad or in terms of MIP flux i.e. MIP/cm^2 by using some dimensional analysis and using the relation $1 \text{ rad} = 100 \text{ ergs/g}$ and $1 \text{ MeV} = 1.6 \cdot 10^{-6} \text{ ergs}$:

$$1 \text{ rad} = 100 \frac{\text{ergs}}{\text{g}} \cdot \frac{\text{MeV}}{1.6 \cdot 10^{-6} \text{ ergs}} \cdot \frac{\text{MIP g}}{2 \text{ MeV cm}^2} = 3.1 \cdot 10^7 \frac{\text{MIP}}{\text{cm}^2} \quad (3.3)$$

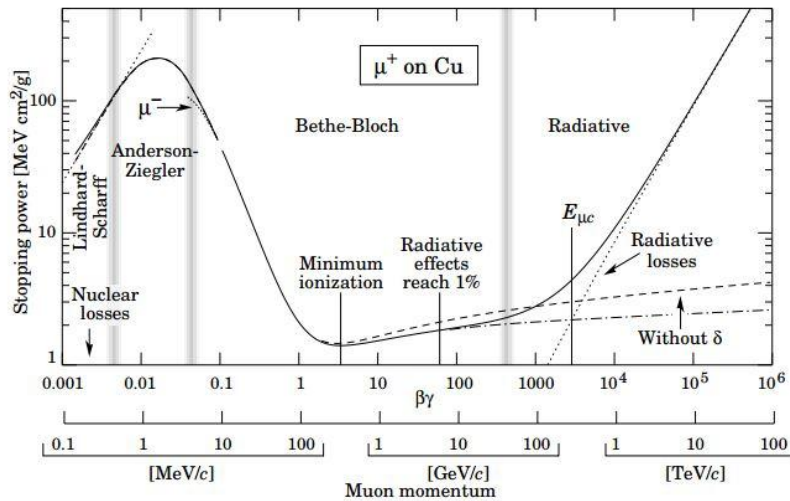


Figure 3.1: Stopping power of a muon travelling through copper as a function of energy [122] .

3.1.2.2 Photon Interaction with Matter

Light also interacts with materials with the most common mechanisms being:

- 1) Photoelectric effect
- 2) Compton scattering
- 3) Pair production

The photoelectric effect was already covered extensively in Chapter 2 and leads to ionisation. It is the dominant process at low energies and is useful for light detection, for example, generating electron/hole pairs in a semiconductor. Compton scattering is dominant at mid-level energies and is the process in which a photon elastically scatters off a particle. Compton scattering can lead to ionisation if enough energy is exchanged in the scattering process. Pair production is the formation of a particle/anti-particle pair by a highly energetic photon. The energy of the photon must be greater than the sum of the mass of the two created products. As a result of the conservation of momentum, pair production cannot occur in free space and requires a nearby nucleus or electron to absorb the recoil momentum.

The most common particle production is the formation of an electron/positron pair as the energy is smaller than that of heavier products, for example a 1.022 MeV photon is the threshold to create an electron/positron pair whilst to create a muon/anti-muon pair a photon with energy greater than 211 MeV is required. Even though electron/positron production is the most common, higher mass particle production must always be considered for machine protection/particle detection purposes as they have longer ranges in matter and can lead to more damage.

Other interactions of photons can occur such as photon-photon scattering and photonuclear scattering however they have low cross sections and are not considered in photon detection.

3.2 Classical Beam Loss Monitoring Technology

BLM detectors have been used at accelerators for many years. This means that the technology has matured and it has been well established what each detector can deliver. However as particle accelerators become more intense with increasingly complicated pulse structures the demands for BLM detectors are growing in terms of detecting a large dynamic range of losses and to resolve losses within a bunch. The type of accelerator can itself dictate what BLM can and cannot be used, for instance it would be useless to have a BLM highly sensitive to light to be placed in an area known for a high amount of synchrotron radiation. Classical BLM technology will now be presented as well as newer options currently in use.

3.2.1 Short ionisation chambers

Ionisation chambers (IC) are perhaps, along with scintillating screens, the most commonly used

BLM. The short ionisation chamber, figure 3.2 left, works by ionising radiation travelling through a volume of argon gas (nitrogen and air may also be used) between an anode and a cathode. Upon ionisation with the gas, electron-ion pairs are produced and drift to an anode/cathode, respectively, generating a current.

Operation of the IC requires high voltages, typically in the kV range, however, output is linear over a wide range of operating voltages so calibration does not change much with voltage drift [123]. Dynamic range is limited by an increased combination rate of ions and electrons at high doses and dark current limits the performance to measure lower signals. The dynamic range of an ionisation chamber can be as high as 10^9 [124].

The drift velocities of charge carriers are an important factor to consider as it defines how fast a detector can relay a signal. Typically, electron drift in gases like argon/nitrogen is in the order of $1 \text{ cm}/\mu\text{s}$ at close to atmospheric pressures [125] with ion drift times being longer. A small gap distance between the anode and cathode as well as a large applied voltage improves the response time of the detector. In the LHC IC which uses N_2 with a gap of 0.5 cm at a 1.5 kV potential, the ion and electron response times are $80 \mu\text{s}$ and 300 ns respectively [124].

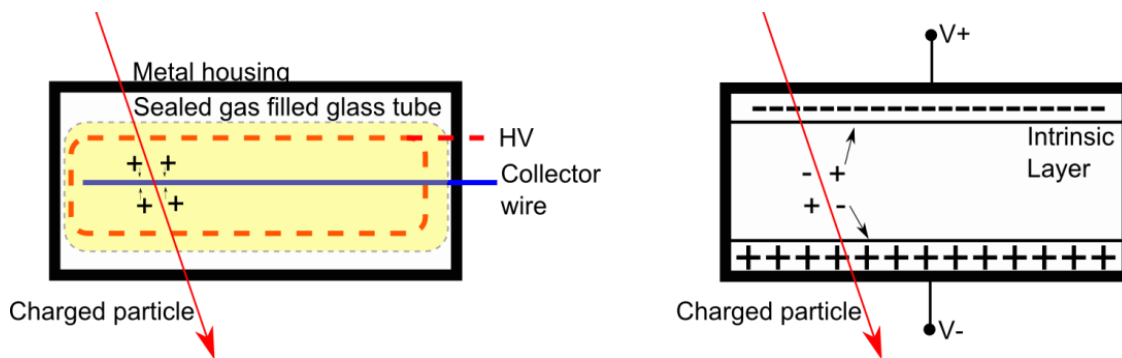


Figure 3.2: Schematic of two types of BLM. Left) Short ionisation chamber. Right) PIN diode.

3.2.2 PIN Diodes

A PIN diode is a detector where an intrinsic (undoped) semiconductor is sandwiched between a p-n junction. Placing semiconductor materials in this order a PIN diode is made where P, I and N stand for p type (hole majority charge carrier), intrinsic and n type respectively (electron majority charge carrier). A PIN diode works as a diode in that it only allows current to flow in one direction. When reverse-biased the device does not conduct current, apart from a small

leakage current. However, upon a particle passing with sufficient energy through the depleted region created in the intrinsic semiconductor, electron-hole pairs are created which are pulled by the reverse potential and generate a measurable current, figure 3.2 right. A problem which could be encountered with PIN diodes is that not only charged particles are detected but photons also, which can be troublesome in regions with a high level of background photons. For this reason a configuration of two PIN diodes could be used in coincidence. This was successfully utilised at the HERA ring at DESY [126] [127].

PIN diodes are very fast devices, as they are small, there is less distance for charge carriers to travel and they have high voltages applied to them. The typical rise time of a PIN diode is in the region of nanoseconds [128]. As with all silicon based detectors, PIN diodes are not very radiation hard and their quality to produce signals degrades after being subjected to high doses of radiation. However, the HERA PIN system was used over many years at radiation levels up to 10^8 rad with little damage observed [129] [114].

3.2.3 Long Ionisation Chambers

A long ionisation chamber (LION), sometimes referred to as a Panofsky Long Ion Chamber, works on the same principle to its short counterpart but uses a hollow axial cable filled with a gas of 95% Argon and 5% Carbon Dioxide [130]. Electrons that hit the copper coating of the cable shower and ionise the gas. The ions then drift to the electrode at the centre of the chamber. The signal that is created is sent in both directions along the accelerator. Position sensitivity is calculated from the time delay Δt between the pulse and the reflected pulse so a loss can be localised at a position x , from the delay in the signal and the length of the detector L .

$$\Delta t = \frac{2(L - x)}{\beta c} \quad (3.4)$$

Position resolution of losses using LIONs depend on the length of the chamber but at the Stanford Linear Collider a resolution of 1.5 m is reported [131]. However for longer chambers the resolution is much larger and is limited by broadening of the pulses along the co-axial line and electron collection time [128]. The long ionisation chamber method is cheap and offers uniform sensitivity however it is not very fast as the drift time of ions can be slow [132]. This

method has been used in accelerators such as the 3 km linear accelerator at Stanford in the 1980s [133].

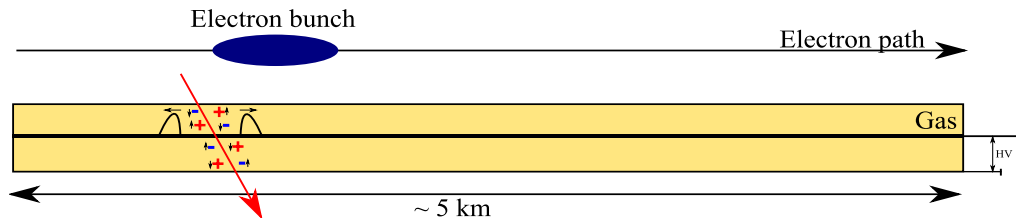


Figure 3.3: A long ionisation chamber is a small coaxial cable filled with an inert gas.

3.2.4 Scintillating Screens

Scintillation is an effect which occurs in organic transparent materials during inelastic scattering. An elevated electron from energy deposited in the material falls to a lower state and emits a flash of light in the optical wavelength range, the light is then transported in a light guide to a fast photodetector, typically a photomultiplier tube (PMT) [134].

Photomultiplier tubes are standard devices for detecting photons. Their operating principle is shown in figure 3.4. An electron is emitted when an incident photon hits a photocathode. The electron is then accelerated towards a charged dynode which stimulates the emission of multiple electrons. These are then accelerated to a second dynode at a higher potential where they collide and stimulate even more electrons. This process then repeats until they strike a signal collecting anode where the signal is read out [135]. After multiple stages of charge multiplication, the gain in a PMT is high and is usually in the region of $10^4/10^6$ [123]. Noise contributions originate from thermally generate electrons from the photocathode. Since electrons are in a vacuum travelling at low velocities, PMTs are very sensitive to magnetic fields. This means they require shielding, particularly if they are in regions of stray magnetic fields, which is particularly true in an accelerator environment. Choice of the photocathode dictates the spectral sensitivity of the device. PMTs are available suitable for the detection of infrared to extreme ultraviolet photons. Long wavelength detection is limited by the low absorption in the photocathode whilst for shorter wavelengths the device is limited by the window material covering the photocathode which is opaque at shorter wavelengths [123]. A more comprehensive overview of PMT technology and operational properties may be found in [123], [135] and [136].

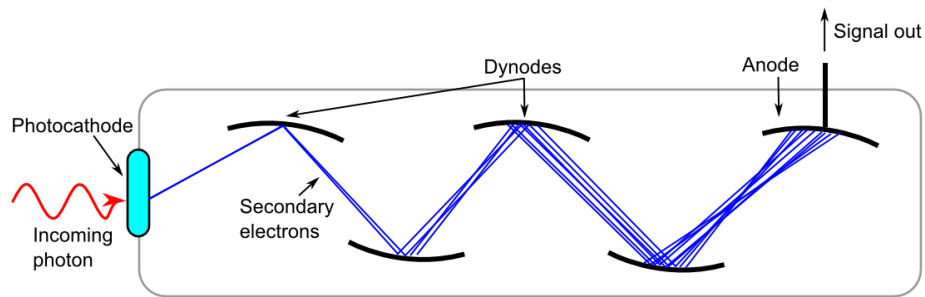


Figure 3.4 Operating principle of a photomultiplier tube.

A large number of materials exhibit scintillation but only a few are applicable to beam loss monitoring. Organic crystals like anthracene and stilbene can be used and have very high scintillation efficiencies but they are very expensive, can only be produced in small quantities and deteriorate quickly [128]. Liquid scintillators produced by dissolving organic crystals in an organic solvent are one solution of incorporating organic crystals. They are radiation hard but less efficient in generating light and are often not used as they are highly flammable and toxic [123]. Inorganic scintillating crystals such as NaI and CsI are more sensitive than organic based scintillators but they are less resilient to radiation damage however they may have some applicability in low energy anti proton rings [137].

The most popular method is to dissolve organic scintillators into a polymer base. The benefits of a plastic scintillator is that it can be cut into any shape, meaning they can be fit in around an existing set-up without much further regard for space requirements [138]. They are also cheaper than the other methods mentioned. The emission of photons is also relatively fast, typically a few nanoseconds [134]. As with the previous variations mentioned, plastic scintillators suffer from the fact that light transmission degrades over time due to radiation damage [139]. For these reasons organic based plastic scintillating screens are the most viable option for multiple installations, however, they should not be used in high radiation environments.

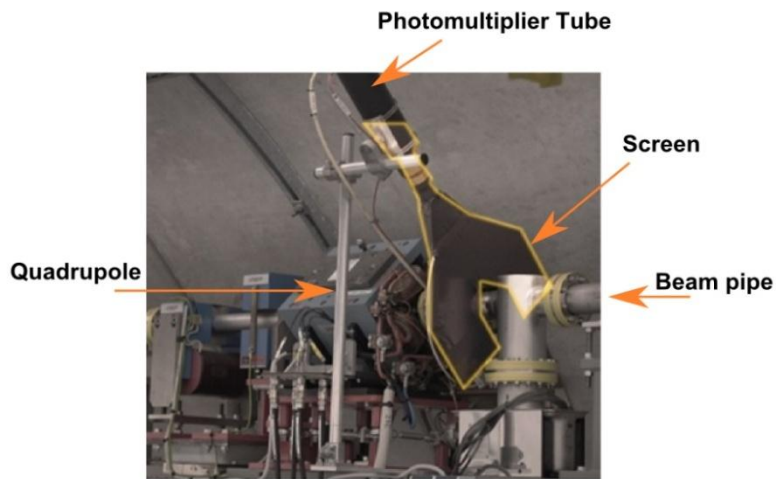


Figure 3.5: A plastic scintillator BLM, outlined in yellow, around a beam pipe [140].

3.2.5 Secondary Emission Monitors

In some situations beam losses are so high that saturation and radiation damage to the detectors themselves becomes a factor. In areas where this may occur such as near collimating systems and beam dumps a more resilient detector is required. A detector often used is a secondary emission monitor (SEM) [141]. These detectors work when secondary electrons are emitted from a surface due to the impact of charged particles. The choice of secondary emission surface should have a low yield to avoid false detection. For this reason the SEM has a low efficiency and typically used in high radiation areas [142].

One example is the ACEM detector which stands for aluminium cathode electron multiplier. An ACEM works like a photomultiplier tube with the photosensitive element removed and replaced with an aluminium foil. The secondary electrons are guided and accelerated to a series of anodes where the signal is amplified as much as 10^6 [143] the same as a PMT.

3.2.6 Diamond Detectors

Diamond detectors are not classical BLM detectors, as they have only fairly recently been used for beam loss monitoring, but their rapid increase in use warrants their mention. Working on a similar principle to PIN diodes, diamond detectors work as solid state semiconductor detectors. Diamond has a chemically strong structure and has a large bandgap 5.5 eV [144]. This makes

them very radiation hard. Diamond is grown by chemical vapour deposition (CVD) in which a gas, typically a mixture of hydrogen and methane, is deposited onto a substrate to form a synthetic diamond [145]. The speed in which they grow changes the crystal structure. Slow deposition allows a single crystal to form (sCVD) however they are expensive; the cheaper alternative is polycrystalline diamond (pCVD) which can be grown to larger sizes and the better candidate for BLM purposes. Previously used for collision detectors, diamond based BLM detectors have been tested at the LHC [146] where as a result of the fast speed of the detectors sub nanosecond pulse structures were observed.

3.2.7 Neutron Beam Loss Monitors

To make this general discussion of standard BLM techniques complete it may also be required to detect neutral particles such as neutrons. Neutrons do not carry charge and so do not interact through the Coulomb force. This means they do not directly lead to ionisation and so other methods must be used to detect them. This is usually though inducing them to trigger nuclear reactions in which the by-products are detected or by inelastic scattering, often referred to as a proton recoil process, where high energy neutrons collide with a nucleus transferring energy producing an ion which is detected. Several examples of neutron BLM detectors exist in existing facilities where proportional gas tubes are used. In these detectors a container is filled with nuclei such as B, He₃, Li₆ U₂₃₅ as they have high cross sections with thermal neutrons [123]. A recently developed ³He proportional counter, called Lupin [147], has been designed for the detection of pulsed neutron fields and may be an ideal candidate for BLM applications [148]. At the LHC tubes of boron tetrafluoride ,BF₃, are used, pure boron is not gaseous at room temperatures, which work by inducing neutron capture between incoming thermal neutrons and boron: $^{10}\text{B} + n \rightarrow ^7\text{Li} + \alpha$. The alpha particle which is created is heavily ionising and is detected. The tube is surrounded by polyethylene to slow down incoming neutrons to thermalise them and facilitate the reaction [149].

3.2.8 Choice of BLM Detector

It is clear that there is no perfect detector and the choice depends on the demands of each accelerator, as well as the space requirements and even the radiation doses that may be expected. For example the LION on paper may be a poor choice for machines which require knowledge of

losses over a wide dynamic range but for the SLC with its size it was used successfully for many years. Ionisation chambers and scintillating screens are perhaps the most popular detectors. Scintillating screens utilise fast photon detector technology, however, they are not suitable for high radiation areas. Ionisation chambers on the other hand are slower due to charge collection times but more radiation hard. Diamond detectors are fast and radiation hard, however, they are also expensive which makes installing thousands of detectors along a beamline unfeasible. Attention will now be turned to a specific BLM requirement for the CLIC facility.

3.3 CLIC BLM Study

Machine protection in CLIC is of high importance because of the high beam energy and the large energy spread from the novel acceleration scheme. For this reason, not only is the detection of beam losses important, but also using BLMs to understand beam propagation along the main accelerating beamline.

In CLIC, several scenarios have been identified [150] that may cause beam loss. For fast losses these include RF breakdown, a kicker misfiring or a klystron trip. An RF breakdown could produce enough of a transversal kick to send the main beam or drive beam into part of the accelerator. If a kicker were to misfire this can send the beam off trajectory and cause loss. A trip in the klystron could affect the beam enough to cause substantial losses. Slower losses that need to be considered are from drifts in temperature, alignment or beam feedback saturations. The effect and possible damage of kicks in the beam regardless of their origin have already been investigated [15]. In the MB, if different kicks are applied to one location at a time then the beam begins to grow and become unstable due to transverse wakefields and chromatic effects.

The lower detection limit required for a CLIC BLM is the detection of a loss of 10^{-3} of the full intensity of either beam along each DB decelerator or MB linac which would lead to luminosity losses due to beam loading variations. An upper detection limit is due to destructive beam losses when 10^{-4} of a main bunch train or 10^{-2} of a drive beam bunch train hits a single aperture restriction.

Table 3.1 shows the different requirements for the BLMs for each accelerator sub system of the MB and DB. What is clear to see, is that each subsystem has different requirements with regards to how sensitive they have to be and the dynamic range they must cover. Apart from the pre-damping and damping rings the response times of a CLIC BLM are at or below 8 ms. The reason

for this is due to the machine protection strategy for CLIC which is based on a next cycle permit system; where after each cycle the permit to continue is revoked and only re-established once the beam and equipment checks have been passed [39], this will lead to safe operation of the CLIC acceleration. The 8 ms comes from the highest envisaged repetition rate of 100 Hz for most CLIC sub-systems.

BLs used at the LHC, primarily ionisation chambers, have already been considered for use in CLIC. In table 3.1 the quantity refers to the number of detectors required for each sub-system. It is believed that these systems can be adapted for the requirement of CLIC BLMs [39]. However, as it can be seen, due to the size of CLIC this would mean the use of tens of thousands of ionisation chambers. Considering the analysis of the detectors just mentioned, ionisation chambers seem the best choice since they are fast enough to work within the machine protection system, radiation hard and has a high dynamic range. However, the large number detectors required will be costly.

One possible alternative detector under investigation involves placing optical fibres along the beamline. The method proposed is to induce Cherenkov radiation from lost particles. Similar to the long ionisation chamber, the signal is read out and the light signal analysed. Unlike the LION chamber, this detector is not limited by ion drift times. Before being used it is necessary to understand the properties of the detector so that its limitations and behavior in an accelerator environment may be understood.

Table 3.1 Beam loss requirements for CLIC for each accelerator subsystem [39]

Sub System	Dynamic Range	Sensitivity (Gy/Pulse)	Response time (ms)	Quantity
<u>Main Beam</u>				
e ⁻ , e ⁺ injector complex	10 ⁴	10 ⁻⁷	< 8	95
Damping rings	10 ⁴	10 ⁻⁷ (Gy/ms)	1	1396
Ring to main linac (RTML)	10 ⁴	10	< 8	1443
Main Linac	10 ⁶	10 ⁻⁹	< 8	4196
Beam Delivery system (Energy collimators)	10 ⁶	10 ⁻³	< 8	4
Beam Delivery system (Betatron collimators)	10 ⁵	10 ⁻³	< 8	32
Beam Delivery system (minus collimators)	>10 ⁵	<10 ⁻⁵	< 8	588
Post collision line	10 ⁶	10 ⁻⁷	< 8	56
<u>Drive Beam</u>				
Injector Complex	5x10 ⁴	5x10 ⁻⁶	8	4370
Decelerator	5x10 ⁶	5x10 ⁻⁸	8	41484
Dump lines	5x10 ⁶	5x10 ⁻⁸	8	96

3.4 Fibre Optics for Beam Loss Monitors

The basic working principle of a fibre optic BLM is shown in figure 3.6. A charged particle, in this case an electron, crosses a fibre and generating Cherenkov radiation. Light is then transported down the fibre core to the fibre end face where it exits. The photon will then be detected with an appropriate photodetector. The next several sections will cover the physics of optical fibres, the Cherenkov effect and factors which need to be considered to use this technology as an effective BLM.

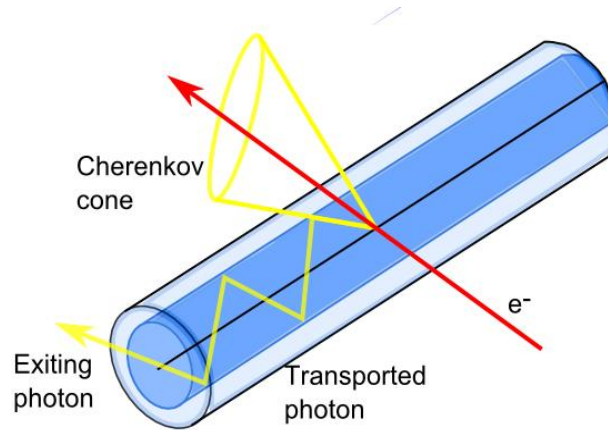


Figure 3.6: Operating principle of a fibre optic based BLM. A photon is generated by a charged particle which is then transported to the fibre end.

3.4.1 Optical Fibres

Optical fibres are widely used in the telecommunications industry because signals can be sent over a long distance with minimal losses. Mode optical fibres are made of fused quartz silica (SiO_2) with areas of different refractive index, surrounded by an opaque jacket to block ambient lighting, and can be bent without stopping a signal being reached at the end. The simplest picture to describe signal transmission is shown in figure 3.7. The process in which light travels down a fibre is total internal reflection. An optical fibre consists of two regions, core and cladding, with different refractive indices, n_{core} and n_{clad} . If light travelling towards the boundary between the two regions is above a critical angle, normal to the boundary surface, the light will be totally internally reflected. The equation for the critical angle is found from Snell's law:

$$\theta_c = \arcsin\left(\frac{n_{\text{clad}}}{n_{\text{core}}}\right) \quad (3.5)$$

For light to first enter into the fibre it must be within the 'nominal acceptance cone', otherwise the light will not be trapped. A quantity used to describe the range of angles that are accepted is the numerical aperture (NA). The NA is related to the angle of the acceptance cone, θ_a , and is defined as [151]:

$$NA = \sqrt{n_{core}^2 - n_{cladding}^2} = n \cdot \sin \theta_a \quad (3.6)$$

Where n is the refractive index of the outer medium, i.e for air $n \sim 1$. The NA is only used as an approximation in most cases because the refractive indices are not always constant values.

Similar to electromagnetic modes in an enclosed cavity, fibre optics have modes which describe how light propagates through them. Depending on what modes are allowed in a structure, it may be more useful, or appropriate, to describe light propagation with geometrical optics, as in figure 3.7, or solutions to Maxwell's equations, previously stated in equations 1.2 - 1.5.

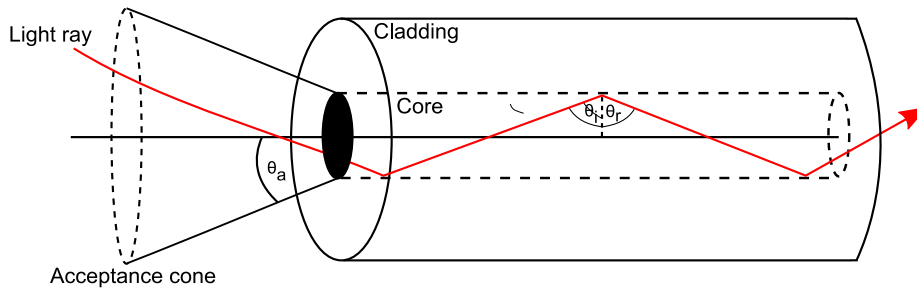


Figure 3.7: Light entering and transported down a fibre optic cable.

3.4.2 Multi-Mode Fibres

Multi-mode fibres are used typically in short distance telecommunications due to signal dispersion over long distances (to be discussed) and have a large core diameter compared to their single mode counterparts, typically 50-100 μm .

In terms of geometrical ray optics the way light propagates they are either bound, in which case the signal is locked in and does not leave the fibre, or they are tunnelling/leaky rays which travel a short distance before being lost. Bound rays are further classified as Meridional and skew rays. These are shown in figure 3.8 when looking at the fibre end face on with the path of meridional and skew rays shown relative to the fibre axis, also shown.

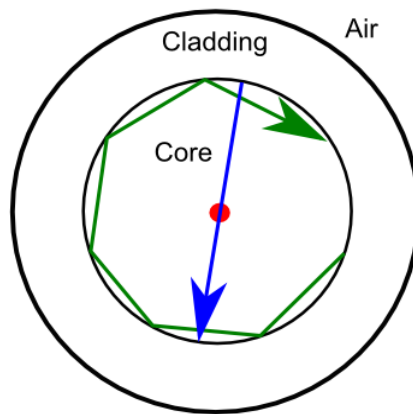


Figure 3.8: Meridional (Blue) and skew (green) rays propagating down a fibre as seen looking down the fibre end. Meridional rays pass through the fibre axis (red dot) on each reflection whilst skew ray spiral around the fibre axis as they propagate down the fibre.

Meridional rays (blue) travel by passing through the fibre axis, the axis which runs down the centre of a fibre and is orthogonal to the fibre end, on every reflection at the boundary. These rays are defined by a single angle, the longitudinal propagation angle, which is similar to the critical angle for TIR defined above and as such the condition for them to be accepted is the same as in equation 3.5. Skew rays (green) spiral down the fibre from the reflection at the core cladding boundary but never crossing the fibre axis. The angle of acceptance of a skew angle is larger than that of meridional rays.

Not all rays that travel within the core make it to the end. Those that do are called bound rays. Another class of rays travel a short distance before being lost, these are known as tunnelling and refracting rays. Refracting rays are lost from the fibre on their first interaction at the core cladding boundary and can be both meridional and skew rays with an angle beneath the critical angle for them to be bound. Tunnelling rays do not refract out at the first opportunity but propagate for a short distance down the fibre and are attenuated because they extend into the cladding and partly refract and partly reflect. They then lose power on each meeting of the core/cladding. For this reason they are sometimes called leaky rays. Tunnelling rays can contribute to the signal detected at the end of the fibre assuming attenuation is low.

3.4.2.1 Refractive Index Profile

The refractive index profile of a multi-mode fibre is either step index or graded index, figure 3.9.

Step index fibres (a) have two distinct levels of refractive index between the core and the cladding whilst graded index fibres (b) have a core where the refractive index slopes off, nearly parabolically, to the same value as the cladding. The profile shape impacts how the particles propagate in the fibre. For step index fibres the bouncing between core and cladding is a sharp transition in direction, as in figure 3.7, however, for graded index fibres the change in trajectory is slow as if they are being focused with stronger focusing at core/cladding boundary.

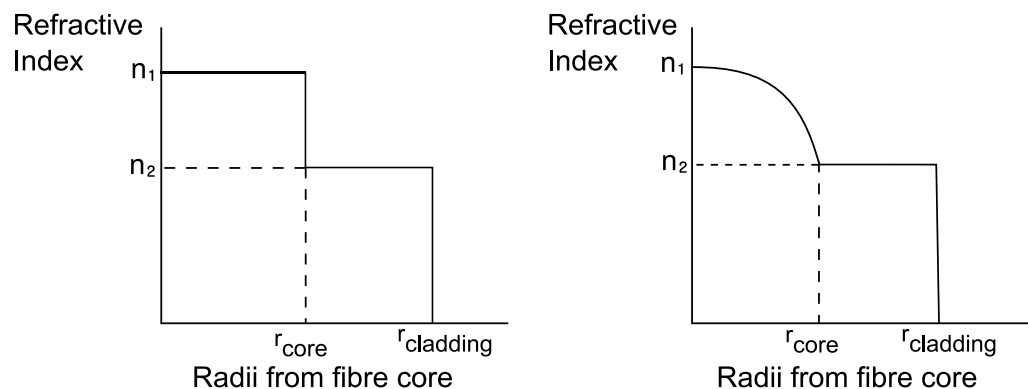


Figure 3.9: Refractive index profiles for step index (SI) and graded index (GI) fibres as against radius.

3.4.2.2 Intermodal Dispersion

As multi-mode fibres allow many modes, light can take many paths to reach the end of the fibre. The broadening of path lengths leads to a temporal broadening which increases as a function of distance. Graded index fibres with a high NA will allow more modes to be coupled in to the fibre however with more modes the dispersion will be greater. For a graded index multi-mode fibre the spread due to intermodal dispersion travelling over a distance L , the increase in pulse width is given by $\Delta t = L\Delta/2c$ where Δ is the normalised index difference. Intermodal dispersion also occurs in step index fibres but the temporal spread is a factor $\Delta/2$ greater therefore graded index fibres are advantageous over step index fibres as they suffer less intermodal dispersion.

3.4.2.3 Chromatic Dispersion

Chromatic dispersion can also occur in fibres which encompasses both material and waveguide dispersion. Glass is a dispersive medium which means the refractive index is a function of the

wavelength. For a wave packet containing a spread of wavelengths they will each see a different refractive index and each travel at different group velocities and will spread when travelling over a distance. Ignoring the wavelength dependence on the refractive index, the group velocity is a function of the wavelength in its own right and so leads to dispersion in this manner, this is known as waveguide dispersion.

3.4.3 Single Mode Fibres

Single mode fibres are much smaller in size, typically core diameters are in the region of 10 μm , and the physics of transmission cannot be explained in terms of geometric optics and can only be explained through a modal analysis [151]. Propagation in single mode fibres will only occur if the wavelength is above a critical value with respect to the core radius, a . This is given by:

$$\lambda_c = 2\pi a \cdot NA / 2.405$$

Single mode fibres are typically used for long distance communications due to higher achievable bandwidths and less signal dispersion as a result of transmission over a distance, i.e. no intermodal dispersion. Chromatic and waveguide dispersion are both present in single mode fibres but largely cancel each other out at wavelengths around 1.3 μm . [152]

It will be seen, or should already be clear, that due to the nature in which fibres will be used for a BLM, that only multi-mode fibres have been considered in order to increase the signal at the output.

3.4.4 Attenuation

A signal will reduce in intensity as it travels a distance, d , down a fibre due to attenuation effects. The optical power, P_1 , as a result of on an initial optical power P_0 is found from an attenuation coefficient α (dB/km) and is given by:

$$P_1 = P_0 e^{-\frac{\alpha d}{10}} \quad (3.7)$$

Attenuation in fibres occur mainly due to two processes of loss. 1) Scattering 2) Absorption.

1) Scattering losses/ Rayleigh scattering

Silica is an amorphous material, i.e. no repeating order in the lattice, and so suffers from structural disorder. This means there is a fluctuation in the refractive index through the material with each irregularity acting as a scattering point centre. The scale of the fluctuations is in the order of $\lambda/10$ and is characterised by an absorption coefficient that varies as λ^{-4} which means as a result of this, that shorter wavelengths (visible blue to ultra violet) are considerably more affected by this loss mechanism. The attenuation coefficient for Rayleigh scattering is given by

$$\alpha(m^{-1}) = \frac{8\pi^3}{3\lambda^4} n^8 p^2 K_B T_F \mu \quad (3.8)$$

Where p is the photoelastic coefficient, μ is a material coefficient, the isothermal compressibility at the fictive temperature, T_F , which is the temperature at which the glass disorder is frozen [153]. As a simple calculation, by using this equation along with the previous one, and using typical values for a fibre: $n = 1.46$, $p = 0.286$, $T_F = 1950$ K , $\mu = 7 \times 10^{-11} \text{ m}^2 \text{ N}^{-1}$ [154] and a short wavelength $\lambda = 0.45 \text{ }\mu\text{m}$ then for a fibre of length of 1km the power will fall in relation to the initial power by a factor 0.47 and for a 100 m fibre a factor 0.93. This will have a big impact when using optical fibres over long distances in an accelerator complex. For this reason an optical fibre based BLM should not be longer than 100 m to limit losses as a result of Rayleigh scattering.

2) Absorption losses

Absorptive losses can be classified into two subgroups, intrinsic and extrinsic. Intrinsic absorptive losses occur as a result of light interacting with the silica glass. Resonances occur in both the UV and infrared spectrum and are caused by electronic and molecular transition bands in the UV range and the generation of vibration modes causing stretching and contradiction of chemical bonds in the infrared range. Extrinsic absorptive losses occur due to interaction with molecules in the fibre which are not pure SiO_2 which are there purposefully or accidentally introduced in the manufacturing process. During manufacturing water vapour in the atmosphere can be absorbed leading to peaks of OH absorption which are large enough that the amount entering fibre needs to be tightly controlled usually to 0.5 parts per million [152]. Some fibres are purposefully doped with materials to increase their photosensitivity such as germanium [155]. The experimentally measured attenuation as a function of wavelength is shown in figure 3.10.

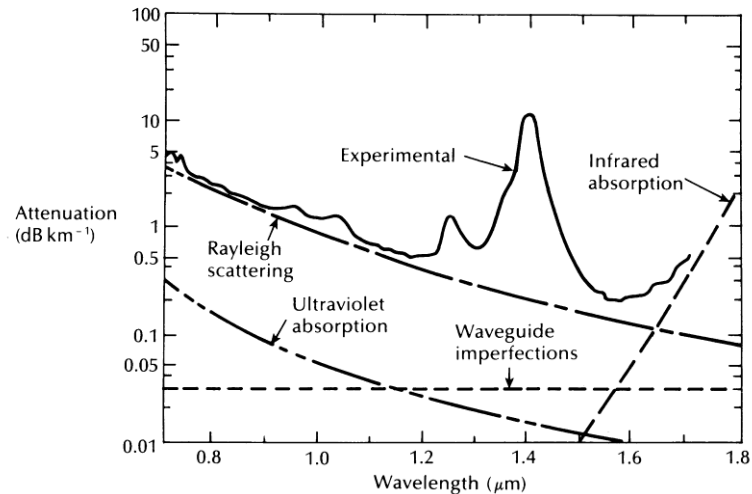


Figure 3.10: Measured loss spectrum for a germanium doped single mode fibre. Contributions to the attenuation are represented by dashed lines. [156]

3.4.5 Radiation Damage to Fibres

As fibres used in BLM will be kept in areas of high radiation it is prudent to briefly mention the effect of radiation on fibres.

Radiation can change every property of an optical fibre. The main problem to contend with is the increase of radiation induced attenuation (RIA). Other effects include the change of mechanical properties, such as tensile strength, change of bandwidth and change of the refractive index [157]. The increase in RIA can be attributed to ionising radiation creating free electron/hole pairs, breaking bonds in the silica. The electrons are then trapped at defect sites forming colour centres which create additional absorption bands absorbing guided photons [158].

There are many factors that influence the RIA and it is hard to predict the exact effects in any given application. The factors can be broken down into manufacturing influences, Designs parameters and environmental conditions. The design factors which can affect the RIA include: the fibre type, i.e. single mode, graded index, the core to cladding diameter ratio and the outer coating material. Manufacturing influences include the conditions in which the fibre was manufactured such as the temperature and speed with which it was formed, the dopants added to the core and cladding and the total OH content. Environmental factors include the total dose absorbed by the fibre, the rate at which the dose was absorbed, the ambient temperature in which

the fibre is kept and the lengths of time the allowed to anneal. Temperature is a factor because heat allows bonds to heal and reduces the amount of attenuation, it has been shown that at low temperatures the RIA significantly larger than at high temperatures and also sensitive to small temperature changes [159]. It is clear to see from this long list that it is difficult to control and compare values for the same product supplied by different vendors.

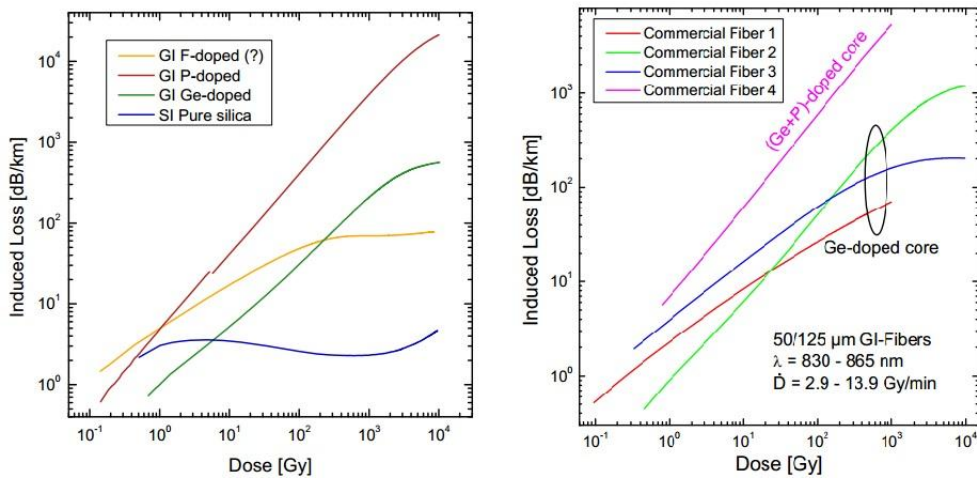


Figure 3.11: Left) The induced attenuation loss as a function of absorbed dose for a variety of different fibres doped with different molecules. Right) A comparison of the induced attenuation loss as a function of absorbed dose for fibres from different vendors, three of the fibres were marketed as germanium doped [157].

Figure 3.11 left shows the induced losses in dB/km as a function of delivered dose for fibres with different dopants. The tests were performed with a wavelength of 830 nm. The germanium doped fibre is the best performer at low levels of irradiation but as with the fluorine doped fibre the induced loss increases linearly in a logarithmic scale until they saturate at high doses. The worst performance is seen by the phosphorus doped fibre which does not appear to saturate even at high doses. The best performer is the pure silica step index fibre with a maximum no greater than 5 dB/km and appears to show an improvement during the irradiation process. Figure 3.11 right shows the performance under irradiation between four different commercial fibres available on the market from different vendors. Even though three of fibres are supposedly the same, no information is provided on the exact manufacturing processes, i.e drawing speed, and design parameters such as the coating material, the induced losses vary as much as a factor or

100 at a dose of 10^3 Gy. This highlights that small factors can affect the response of a fibre to radiation.

3.4.6 Cherenkov Radiation

A charged particle travelling through a medium faster than light can travel in that medium emits a cone of radiation called Cherenkov radiation. The physical cause of this phenomenon is attributed to a disturbance in the local electromagnetic field in a medium from a passing charged particle. Below the speed of light, a charged particle entering a medium locally polarises the surrounding molecules. After the charged particles has past the induced dipoles relax and emit radiation which destructively interferes and no light is observed. However, if the phase velocity of the charged particle is above the speed of light the wavelets of the emitted radiation are in phase on a wave front inclined in the direction of the moving particle. The light constructively interferes and coherent radiation is observed [160].

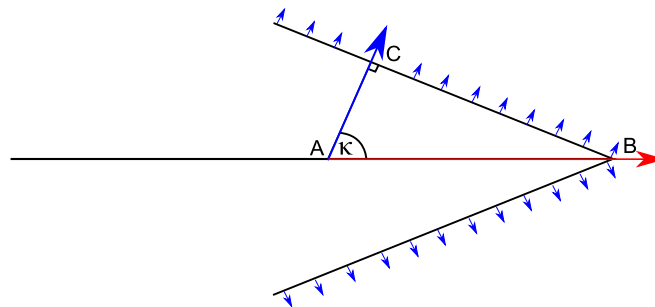


Figure 3.12: Cherenkov cone, with angle κ , generated by a charged particle travelling in a medium faster than light. The red arrow shows the direction of motion. The blue arrow shows the propagation of light

The angle of the Cherenkov cone κ , in figure 3.12, is directly related to the speed of the particle in a material with refractive index n . From figure 3.12 the red arrow is the direction of the velocity of the particle and the blue lines are the rays of emitted light. In a time t a particle travelling from point A to point B travels a distance βct , whereas a photon in the same time will travel a distance ct/n . It can be seen that the angle of the cone of light is a function of just the speed of the material and also the refractive index of the material and is given by:

$$\cos \kappa = \frac{1}{n \cdot \beta} \quad (3.9)$$

The light yield of Cherenkov radiation as a function of the length travelled through a medium L and the wavelength λ was derived by Ilya Frank and Igor Tamm and is given by [12]:

$$\frac{d^2 N_{ph}}{dL d\lambda} = 2\pi\alpha z^2 \frac{\sin^2 \kappa}{\lambda^2} \quad (3.10)$$

Where α is the fine structure constant, κ is the Cherenkov angle as define above, λ is the wavelength and L the path of the particle with charge z through the medium.

3.4.7 Signal Generation in Optical Fibres

Much has been written on the generation of signals in optical fibres due to Cherenkov fibres [161] [162] [163]. Whilst the full derivation is not included here, as each source uses different methods to derivate the final result, the basic principles are given. There is a small discrepancy between the sources in one crucial regard but this will be mentioned thereafter. The number of detected photons N_{photo} exiting from a Cherenkov fibre and detected with a photodetector depends on many factors:

1. The number of photons generated by a charge particle crossing the fibre Y
2. The probability that a photon is trapped, i.e. within a critical angle, P_t
3. The effects of attenuation during signal transmission η_{atten}
4. The coupling efficiency between the fibre and photodetector η_{coup}
5. The detection efficiency of the photodetector η_{PDE}

The number of detected photons can then be expressed as [162]

$$N_{photo} = Y \cdot P_t \cdot \eta_{atten} \cdot \eta_{coup} \cdot \eta_{PDE} \quad (3.11)$$

The light yield is found by the integration of equation 3.11 over the path length of the electron in the fibre which depends on the fibre radius R , the incident primary angle α , the closest distance the primary travels to the centre of the fibre, b , and the wavelength range which is limited to the range 200-900 nm because of the detection range of the photon detector and the transmittance of the fibre [162].

$$Y \approx \frac{2\pi}{137} \cdot \frac{2\sqrt{R^2 - b^2}}{|\sin \alpha|} \left(1 - \frac{1}{\beta^2 n^2}\right) \frac{\lambda_2 - \lambda_1}{\lambda_2 \lambda_1} \quad (3.12)$$

The trapping probability takes two cases into account, the first is that photon is trapped and the second is that it is trapped and exits at the end of the fibre, i.e. it is not reflected. The photons are trapped as long as they are within the critical angle. Photons may be reflected back if they are within an angle at the end face. The trapping probability P_{trap} can then be expressed for a single photon [161] as a function speed, core refractive index and incident angle:

$$P_{trap} = \frac{1}{\pi} \arccos \left(\frac{\beta \sqrt{n_{core}^2 - NA} - \cos \alpha}{\sin \alpha \sqrt{\beta^2 n_{core}^2 - 1}} \right) \quad (3.13)$$

Discrepancies are found within two sources [161] [162] with the former claiming the final result scales with the square of the fibre diameter and the latter with the cube of the diameter. Tests were performed to test the fibre diameter dependency and it was found that the square was the more likely scaling term,

3.4.8 Current State of Fibre Optic BLMs

The purpose of this chapter was to introduce key ideas of BLMs, discuss current state of the art detectors and to introduce a new type of BLM based on optical fibres.

Current standard detectors are sufficient to measure beam loss structure, as highlighted in the CLIC CDR. However, the sheer size of CLIC means that a large amount of these localised detectors are required. The optical fibre detector is proposed as a way of reducing the number of detectors whilst still covering the entire beamline. This beam loss detection method has been

shown to work at other accelerator complexes such as light sources, [164] [165] [166]. However, these were applied for machines greatly different to CLIC in both beam intensity and pulse structure. Furthermore, as this technology is not as mature as others, the true limitations of this detector are not fully understood and further testing is required with different types of beam bunch structures. It was shown within this chapter that one limitation of the detector is the allowable fibre length due to attenuation effects. Areas which have not been fully explored yet are position sensitivity to locate a loss location, optimal location to place the fibre and performance over time due to absorbed radiation dose.

3.5 Photodetector for Fibre Readout

3.5.1 The Silicon Photomultiplier

Silicon Photomultipliers were developed as an attempt to build the ‘ideal’ detector. An ideal detector would be one with a fast response, low noise and high gain in order to resolve individual input photons and in the instance of a large input signal the detector output should reflect the intensity profile of the light source. Over previous decades photomultiplier tubes have been the dominant technology. However, in the last ten years SiPMs are becoming more competitive as they are compact, robust, require lower operating voltages, cheaper and insensitive to magnetic fields. In the following sections the basic structure, operation and properties of SiPMs will be presented, along with associated drawbacks.

3.5.1.1 SiPM Structure and Properties

An SiPM is an array of avalanche photodiodes (APDs) connected in parallel to a common output. The output response from an SiPM is the total sum from each cell in the array, with each cell either being off (no detection) or on (detection occurred) and the output from each cell being approximately equal. Each APD is connected to a passive resistor which quenches the output back to zero upon detection. The equivalent circuit diagram of an SiPM is shown in figure 3.13.

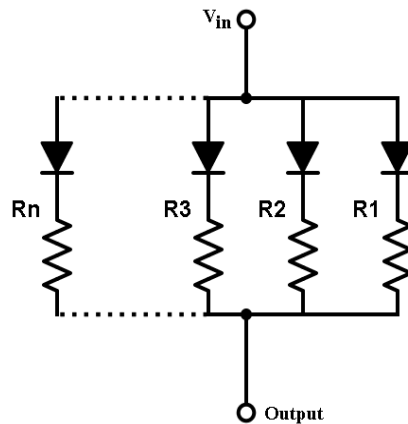


Figure 3.13: Equivalent circuit diagram of a Silicon photomultiplier. Each cell in the array can be modelled by a diode and resistor. The cells are connected in parallel to a common output.

An APD works in a similar manner to a standard semiconductor photon detector with the main difference being a large bias voltage is set across the active volume. When a photon enters the volume an initial electron and hole are produced in the depleted region however due to the large potential the electron is accelerated producing more electron hole pairs. This avalanche effect leads to a collected signal that is higher than the signal that started the process. This only occurs when the bias voltage supplied to the device is above a particular point called the breakdown voltage. In this operating regime the device is said to be operating in Geiger mode [123]. Typical gain above breakdown is of the order 10^6 and is independent on primary carrier number, i.e the resulting signal would be the same for a single photon as a massive highly charged particle, and is a function of bias voltage above the breakdown voltage.

To reduce reflections at the surface of the pixels, which could stop photons reaching the sensor, an antireflective coating is applied to the surface with an optically pure material such as Si_3N_4 , by doing this transmission of 90% is attainable [167].

The avalanche will be self sustaining unless it is quenched by a passive or active circuit. Re-firing of a pixel can occur mid recovery but the output is less than that of a fully recovered pixel. The passive approach is achieved by introducing a large resistor in series with a diode so that an avalanche current will lead to a voltage drop. The electric field then lowers and multiplication stops until the device has returned to its original state and is ready to start another avalanche. The quenching time is of the order of 10's of nanoseconds. An active quenching circuit approach requires sensing the rise of avalanche pulse and temporary reducing the applied voltage [168].

Active quenching circuits are limited to single APD devices only, called a single photon avalanche photodiode (SPAD). An individual active quenching circuit for every pixel is too much for SiPMs which can have many thousands of cells.

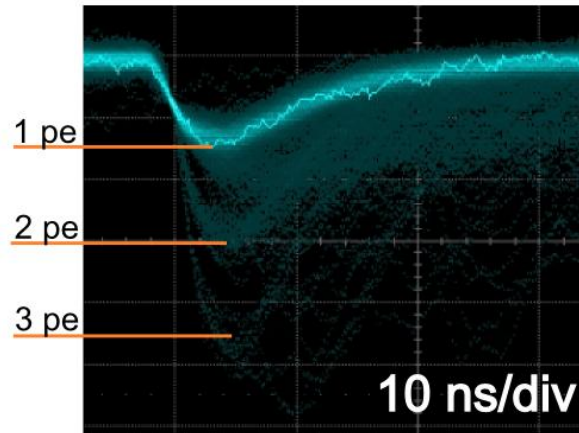


Figure 3.14: Persistence mode on oscilloscope observing an SiPM in dark mode connected to an amplifier with 200 gain. The 1, 2 and 3 cell outputs can be seen. Each vertical division is 20 mV.

Figure 3.14 shows a persistence plot of an SiPM working in dark mode, i.e. no input light signal. The heaviest trace is from a single pixel firing. The other fainter traces are from two and three cells firing. The two cells firing is approximately double the single firing height and treble the height for the three pixels etc. The output response is characterised by a short rise time, typically 500 ps to 2 ns, and a long fall time in the order of 20 ns. The response of an SiPM with one cell firing is called the single electron response (SER). The long recovery time of a pixel may be an obstacle for applying SiPMs in a BLM as light pulses exiting the fibre are in the same region as the pulse length which generated it. The non-instant recovery time of pixels will mean that during the recovery process the detector system is partially blind. This could be dangerous for machine protection purposes.

The photon detection efficiency (PDE) is defined as the percentage of photons that are finally detected to the total number of incident photons. The PDE is given as the product of: the quantum efficiency, the probability that a photon traversing the SiPM creates an electron hole pair which is a function of photon wavelength, the SiPM fill factor which is dependent on the geometry as only part of the pixel detector is sensitive to photon detection and the Geiger

efficiency which depends on the photon incidence position and on the applied voltage [123]. The PDE is given by [169]:

$$PDE = \epsilon_{QE} \cdot \epsilon_{geom} \cdot \epsilon_{geiger} \quad (3.14)$$

Where ϵ_{QE} is the quantum efficiency i.e. that an electron-hole pair is formed, ϵ_{geom} is the geometrical fill factor i.e. the ratio of the active area in which detection can occur to the total area and ϵ_{Geiger} is the probability for an avalanche to occur.

Some simple definitions can be defined. The first is the overvoltage, $\Delta V_{over\ voltage}$, which defines how far the bias voltage, V_{bias} is above the breakdown voltage, $V_{breakdown}$:

$$\Delta V_{over\ voltage} = V_{bias} - V_{breakdown} \quad (3.15)$$

The charge produced by a pixel, Q_{pixel} , is found from the over voltage and the pixel capacitance C_{pixel} .

$$Q_{pixel} = V_{bias} \cdot \Delta V_{over\ voltage} \quad (3.16)$$

The gain from the avalanche process is simply the total charge produced divided by the electron charge:

$$Gain = \frac{Q_{pixel}}{q_e} \quad (3.17)$$

The pixel recovery time is found by the characteristic time of an RC circuit i.e.:

$$\tau_{rec} = R_{quench} \cdot C_{pixel} \quad (3.18)$$

Where R_{quench} is the resistance used to quench the avalanche signal.

3.5.1.2 Dark Noise, Afterpulsing and Crosstalk

SiPMs are not perfect detectors and have drawbacks as a result of how they work. These effects include thermal noise, cross talk, and afterpulsing.

Whilst the SiPM allows the detection of single photons, in theory, the internal gain means even false signals such as from thermal excitation or quantum mechanical tunneling are also multiplied into an avalanche and becomes part of the final signal. Thus if the SiPM is being used to detect a handful of photons then dark counts from thermal excitation are a percentage of the final signal. Dark noise from thermal excitation can be reduced by two methods firstly by cooling the device down to reduce the probability of thermal excitation and secondly in situations where the number of incoming photons is high to discriminate against events of the firing of single cell to only events where there are multiple firing of cells [123]. Investigations into cooling down an SiPM to reduce thermal noise have already been carried out [170]. This was done for an SiPM used in liquid argon neutrino physics experiments where the device was tested from room temperature down to -196°C . It was found that for the SiPM used, a SensL i000 series, the single photoelectron rate at 25°C was 1 MHz but upon cooling to -196°C this had reduced to 40 Hz. It was also noted in this study that cross talk was independent of temperature.

Afterpulsing is a phenomenon which is caused by impurities in the SiPM. It is possible that electrons become trapped by the impurities and are released after a delayed time, typically in the region of 100 ns. If this delayed time is longer than the recovery time of the SiPM then another avalanche is released [171]. It has been shown that afterpulsing increases parabolically with the applied voltage [172] this means to operate SiPMs with minimum afterpulsing it is necessary to produce SiPMs which are “cleaner”, a longer recovery time and a smaller gain. [173]. However, these latter two points may not be beneficial to detecting certain types of pulses since as it will be seen long recovery times can lead to saturation effects.

Another phenomenon which can occur is optical crosstalk. This is the process in which photons caused by the avalanche migrate to neighbouring cells and cause an avalanche in this cell also. This optical cross talk can be reduced by introducing trenches between cells or by reducing the internal gain to the lowest possible value and still being in Geiger mode [174]. These latter two causes of noise, afterpulsing and crosstalk, can be reduced by manufacturing processes and the SiPM board architecture. Both have been reduced in recent years with improving designs [175].

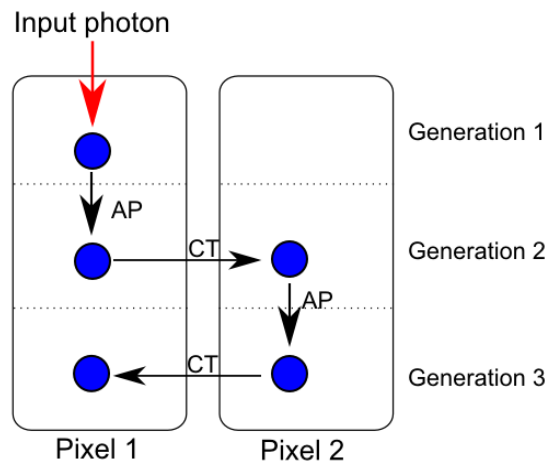


Figure 3.15: Branching process across three generations in which a single photon can generate 5 detected events

Figure 3.15 highlights how afterpulsing and crosstalk can complicate the detection process. A single photon triggers an avalanche in pixel 1 where afterpulsing occurs creating a second avalanche. Within this avalanche a photon migrates to a neighbouring cell, pixel 2, which is in a state ready to be triggered and a third avalanche occurs. Again afterpulsing occurs triggering a fourth avalanche and again cross talk occurs and triggers a fifth and final signal in pixel 1 which has since recovered from the second recorded avalanche. In this example a single photon leads to five avalanches and highlights the impact that cross talk and afterpulsing can have on signal detection. The likelihood of cross talk and afterpulsing occurs with some probability dictated by branching processes so eventually the branch will diminish [176].

3.5.2 Experimental Characterisation

Several experiments [177] were performed in order to experimentally characterise a sample of SiPMs. These experiments back up statements claimed above and give some early insight into their performance as part of a BLM. Experiments were carried out with a novel SiPM design by the company STMicroelectronics [178], henceforth referred to as ST, and a sample from Hamamatsu [179]. Furthermore an algorithm was developed to search for minima or peaks amongst noisy data sets to collect SER type peaks so they can be averaged.

3.5.2.1 SER Finding Algorithm.

During the course of this work it was necessary to develop an algorithm for finding SER peaks amongst output measured on the scope. Averaging on the scope meant double and treble pixel firings were included in the output along with signals which were triggered mid recovery. This algorithm allowed SER candidates to be found and averaged to obtain a true SER average.

Figure 3.16 shows the raw output from the oscilloscope with a trigger level set on the scope to catch the lowest pulse. Detector responses before the triggered pulse as well as further developed pulses are observed. Within this 9 pulses can be made out with height corresponding to a single electron response can be made out along with 2 double pulses about twice the height of a SER and 1 four fired pixel event. Many of the events are close in time which makes it difficult to obtain a true average of SER.

The algorithm works by locating local minima below a threshold voltage, thereby allowing only one minimum assigned even if the data is noisy. They are then separated based on the value of their height to distinguish between single, double, triple events and a check is made to only record minima which are sufficient distance apart. Running this algorithm over many files allows many SER type of events to be recorded. They are then averaged to obtain an SER pulse shape. Figure 3.17 shows the average pulse obtained using this algorithm. This pulse could then be used as an experimentally obtained SER for analysis. The rise and fall time of the average pulse is longer than expected but affected by limited bandwidth of the amplifier. An amplifier is required since SERs cannot be seen on a scope without it.

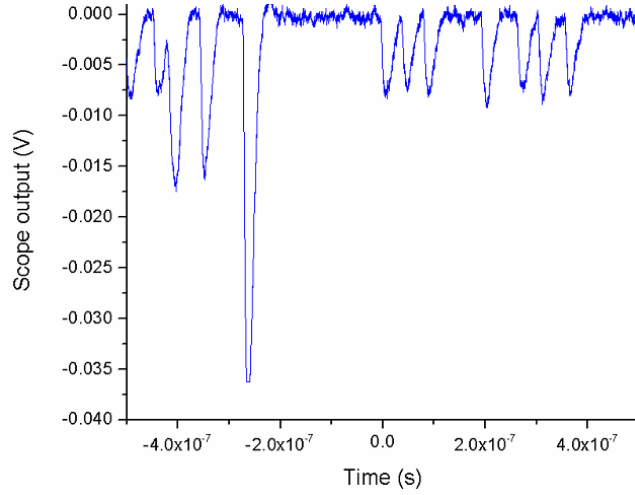


Figure 3.16: Raw scope output from the oscilloscope in dark mode.

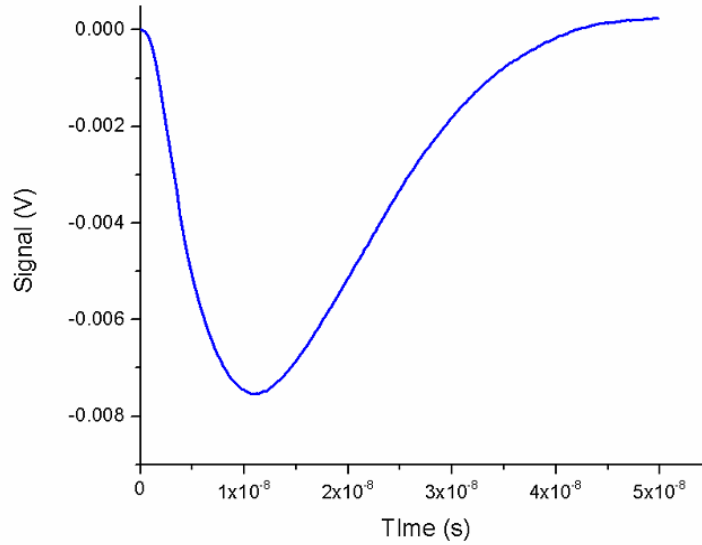


Figure 3.17: Averaged SER pulsed found using the algorithm.

The detector response of an SiPM as a function of time, $SiPM(t)$, can be modelled by a bi-exponential model based on two parameters: the rise time, τ_{rise} and fall time τ_{fall} :

$$SiPM(t) = \frac{1}{(\tau_{rise} - \tau_{fall})} \cdot \left(e^{\frac{-t}{\tau_{rise}}} - e^{\frac{-t}{\tau_{fall}}} \right) \quad (3.19)$$

3.5.2.2 Experimental Characterisation Set-up

A characterisation of two of the SiPMs was carried out using NIM modules housed in a crate which supplies the modules with power and a fan to cool the modules down for optimal performance. The modules were connected together with wires of varying length and in most cases labeled with the amount of time it takes for a signal to travel through the wire, typically 1 ns per 20 cm of cable. A digital oscilloscope was used to monitor the signals and to take some measurements. Another housing module was used for a digital counting unit which counts the digital signals from the NIM. SiPMs were pulsed by an LED operating at 375 nm at room temperature (24°C). The SiPM and LED were kept in two boxes to minimise the amount of light reaching the detector, surrounded by aluminum foil which was grounded to protect the sensor from the electromagnetic noise.

Table 3.2: Specifications for two different SiPMs.

	ST-Microelectronics (Model H)	Hamamatsu S10362-11-100C
Chip Size	4.37 x 4.37 mm	-
Array Size	1 x 1 mm	1 x 1 mm
Cells array	17 x 17	10 x 10
Cells Pitch	54 μ m	100 μ m
fill factor	44%	78.50%

The two samples used in this characterisation were one from ST and one from Hamamatsu. The specifications of the two devices are shown in table 3.2. The ST device is a multi-architecture device with different configurations of pixels on one board. The terminals are connected to only one array of pixels. The large difference in fill factor is a result in design. The ST SiPM is filled with a metal oxide between the trenches of the pixels to reduce the optical crosstalk, and this is true of all SiPMs produced by ST compared to other manufacturers [180]. The ST device has a bias voltage of close to 30 V and the Hamamatsu SiPM has a bias voltage of close to 70 V.

3.5.2.3 Dark Noise Measurement

Thermally generated electrons are a big source of dark noise and become part of the final signal. Dark events are produced even when the SiPM is activated but with no incident light source. The different levels from multiple triggered cells can be observed using a pulse discriminator and a counter to count the number of detected pulses. The discriminator was used to increase the threshold value of allowed pulse voltages. The SiPM was biased and the signal amplified with a gain of 200 before passing through the discriminator. The number of counts after 100s was measured, then the threshold voltage was increased and the number of counts recorded again, this was repeated in steps of 9 mV starting at 20 mV to the maximal threshold voltage attainable 191 mV. This was done for three separate activation voltages of the SiPM, for the ST SiPM these were 30 V, 30.5 V and 31 V.

There are two sources of errors from this experiment the first is from the fact that this is a Poisson counting experiment and so the error is the square root of the count. The second source of error is from the operator error from the fact the counter had to be stopped on 100 seconds and this was done with a stop watch and so the error is given by the reactions of the operator to stop the counter accordingly, for this an error of ± 0.4 s was assigned. The error associated with Poisson statistics contributes more than operator error than the timing error.

Figure 3.18 shows the number of counts on a logarithmic scale as a function of discriminator voltage. In all three bias voltages steps can be observed. Each pixel generates a certain amount of charge, multiple cells lead to multiple amounts of this charge being produced which are blocked by the discriminator, hence the steps observed. The first represents a single pixel output being stopped from recorded and the second step two pixels firing and so on. Higher bias voltages produce higher counts as it means an avalanche is more likely to form. Furthermore, the steps occur at different discriminator levels for each bias voltage because as from equations 3.15 and 3.16, a high overvoltage will produce more charge when an avalanche is formed. This means the height of the response peak is higher and so a higher discriminating voltage is required.

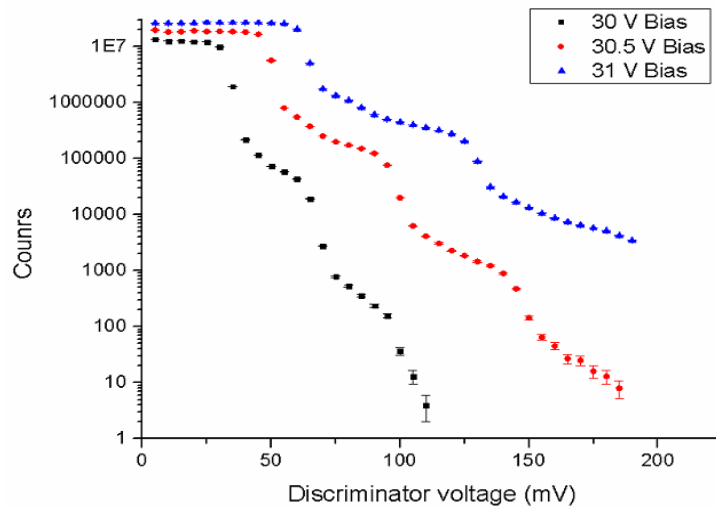


Figure 3.18: Number of recorded events as a function of discriminator voltage when operating the SiPM in dark mode for three different bias voltages.

3.5.2.4 Spectrum Measurement

The firing of pixels can also be measured as a charge distribution. A pulse generator was used to power the LED incident on the SiPM and also to set up a gate with which to set a window an analog to digital converter (ADC) to work. The output signal from the SiPM was amplified and integrated before being sent to the ADC so that the signal was within the window set up by the gate. This signal is sent to a computer which counts the number of events as a function of charge. Figure 3.19 shows the data and fitted results for the ST SiPM with 13 peaks observed in this case. Each peak corresponds to a pixel firing and the charge released for that number of fired pixels. The first peak at zero charge is a pedestal value and the peak after is the one cell firing case. The ideal charge output of an SiPM should approximately be an integer multiple of the output of one cells such that each peak represents a number of pixels being fired with each peak equally separated. This is only an approximation due to several reasons [181]:

1. Variation in gain from pixel to pixel.
2. Electrical noise, uncorrelated dark counts, afterpulses and crosstalk can distort the output shape for lower photon peaks.
3. A photon interacting with a cell mid recovery producing a second smaller charge output

4. A photon interacting in a boundary region between cells or at the wrong depth may give rise to a smaller or delayed signal.

Due to these reasons the single peaks are smeared into Gaussians. The distribution of the peaks is itself a Poisson distribution which can be seen from the envelope that covers all peaks, the bottom envelope below the peaks is due to the merging of the Gaussian distributions of the single peaks and is well represented as a Gaussian convolution. These reasons explain what can be seen in figure 3.19.

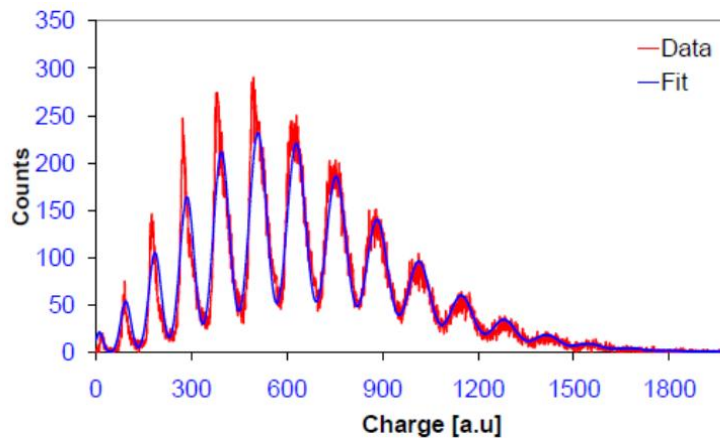


Figure 3.19 Charge distribution of SiPM output whilst illuminated with an LED [177].

The ability to resolve events and therefore single photons like this is what has caused a lot of interest in SiPM technology in position emission tomography [182], Cherenkov telescopes [183] and neutrino physics [184]. However, it is important to note that as a result of dark noise, cross talk and afterpulsing that the distribution below is not a fair representation of photon resolution of an incident pulse and statistical models [176] are required to fully understand the incident pulse on to a device. In the optical fibre beam loss monitor the lower level of the dynamic range is not limited to the photon detector. As it can be seen a single peaks can be resolved. The fibre is the source of lower dynamic range. Upper dynamic range is limited by the photo sensor, since there is only a finite number of pixels to fire on the detector array.

3.5.2.5 Time Resolution Measurement

For detecting losses in a particle accelerator understanding the timing resolution of the SiPM is of great significance as to locate a loss spatially requires understanding how long the SiPM took to trigger and using this information to know where the loss occurred.

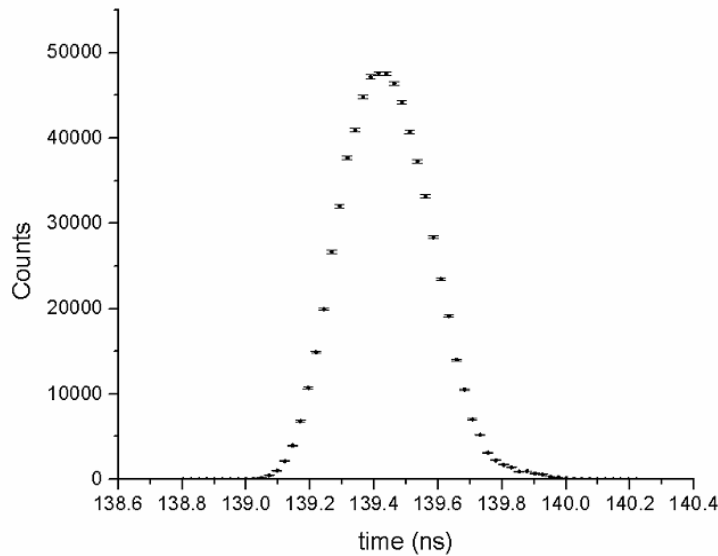


Figure 3.20: Distribution of the durations it took signals to be detected.

A start/stop approach was used where a start signal is sent to a time to digital converter (TDC) from the power generator used to power the LED and the stop signal is the SiPM pulse itself once it reaches the TDC. The counts as a function of time taken from the LED trigger to reaching the TDC is sent to a computer and allowed to collect a large number of counts. The total number of channels available in the TDC is 8191 over 200 ns. However, the final channel is used for the start/stop signal so the total number of used channels is 8190 which means that each channel one channel represents 0.0244 ns. The data, figure 3.20, follows a Gaussian distribution where the mean and standard deviation can be calculated.

The exact time in which the signal took to be recorded is not important as different electronics and wires will contribute to a delay in the signal. The spread of times however is what is of concern. The experiment was repeated this time with the optical signal passing through 100 m of optical fibre. This fibre has a numerical aperture of 0.46 with a core thickness of 400 μm , a cladding thickness of 430 μm .

Table 3.3: Spread in timing resolution for the ST and Hamamatsu SiPMs with and without a fibre attached and the equivalent error in distance along a fibre.

SiPM	σ_t no fibre (ps)	σ_t with fibre (ps)	σ_d (cm)
ST	264	1230	$7.9 < d < 37$
Hamamastu	143	903	$4.3 < d < 27$

Table 3.3 shows the deviation of the Gaussian pulse for the ST and the Hamamatsu SiPM with and without the fibre. The fibre increases the spread of time as a result of intermodal dispersions. The values of variation of distance are found from these two and can be taken as the associated error of a loss being generated at the start of a fibre and at the end. Even in the worst case with the worst performer, the ST device, the resolution is better than half a metre which is sufficient to separate losses between two successive quadrupoles at CTF3/CLIC.

3.5.3 SiPM Application to Optical Fibre BLM

The areas in which SiPMs have been well suited require the detection of fast low load, low intensity and short duration pulses and good SiPM photon number resolutions. Application of SiPMs to high intensity long pulses, however, has not been studied in great detail. Light signals from an optical fibre are arbitrary in shape depending on the loss which generated the signal. Furthermore, the light exiting the fibre is of varying intensity which could occur from large and small losses as well as variation in intensity along the loss structure itself. Detection of these types of light signals may be affected by SiPM operation.

In the case of a destructive beam loss along the CLIC DB, the number of photons exiting the fibre is calculated to be in the order of $10^7/10^8$ per pulse train [162] for the CLIC pulse train with a 365 μm diameter fibre. This equates to an incoming photon rate of 10^6 photons/ns.. This is far higher than the number of pixels available to fire on the device every nanosecond. Therefore behavior of SiPM performance under high intensities of light is required to be understood in response to high intensities of light.

In the case of short pulses of light saturation can occur from a limited number of pixels available.

The probability of a single pixel firing from a total number of pixels N_{pix} with an average number of Poissonian distributed photons N_{photo} can be found from the Bernoulli distribution with probability of detection P_1 and probability of no detection P_0

$$P_0 = e^{\left(\frac{-N_{photo} \cdot PDE}{N_{pix}}\right)} \quad (3.20)$$

$$P_1 = 1 - e^{\left(\frac{-N_{photo} \cdot PDE}{N_{pix}}\right)} \quad (3.21)$$

The average number of fired pixels can then be written as :

$$N_{fired} = N_{pix} \cdot \left[1 - e^{\left(\frac{-N_{photo} \cdot PDE}{N_{pix}}\right)} \right] \quad (3.22)$$

The PDE for a Hamamatsu S203632-33 SiPM is ~25% [185]. Figure 3.21 shows the above equation as a function of number of photons using. The number of fired pixels is approximately linear for a lower number of photons. However, as the number of photons increases the number of fired photons is asymptotic to the total number of fireable pixels represented as the dashed line.

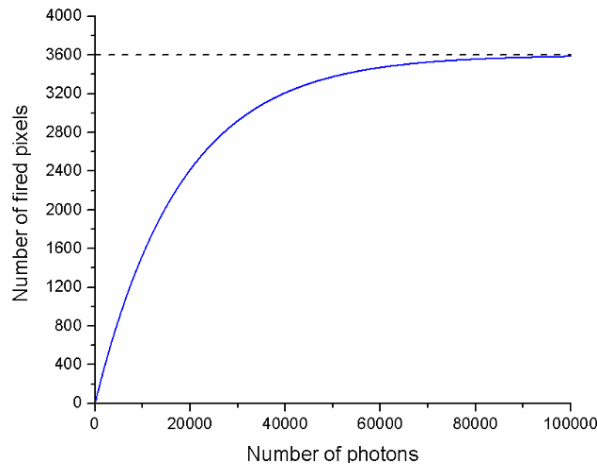


Figure 3.21: Number of fired pixels as a function of incident photons. The dashed black line is the total number of pixels available.

This is true for short pulses. It becomes more complicated for longer pulses because as well as the limited number of pixels, the long recovery time of pixels means that during recovery of a

pixel it won't retrigger to a full output pulse.

This is a problem that cannot be tackled directly but needs to be understood for different case scenarios. For this reason the sensors have been tested for two different input signals:

1. Response to long and intense pulses
2. Response to short double pulses

3.5.3.1 SiPM Response under a High Load

3.5.3.1.1 Experimental Results

A series of experiments were conducted to observe the response of an SiPM under the illumination of long intense pulses of light. The length of the light pulse was selected to be longer than the pixel recovery time.

The SiPM was biased using a Keithley 2450 source measuring unit (SMU) which allowed the current to be measured during the experiment and the output connected to an oscilloscope, Lecroy Wavesurfer 104 MXs-B with analogue bandwidth of DC to 1 GHz and terminated with a 50 Ω resistor which matched the resistor on the acquisition box. A blue LED was pulsed using a pulse generator, Agilent 81150A, which generated rectangular pulse with some small rise time, 2.5 ns. The LED was measured with a PMT to make sure the pulse shape was rectangular. No preamplifier was used in these experiments to avoid non-linearities and saturation at high light input. The second output of the pulse generator was connected to the scope for a trigger.

Optical density filters with OD values from 0.1 to 3.0 were placed between the LED and SiPM to vary the light intensity reaching the detector whilst keeping the peak voltage supplied to the LED constant. OD filters were sandwiched together to obtain intermediary intensities. The LED, SiPM and readout electronics were housed in a black metallic container to stop stray photons being detected. As a result of the OD filters there was a small gap that stray light may leak through. For this reason an additional black box was placed around the set up and lights turned off to ensure that background signals were reduced as much as possible.

This set up allows the SiPM response to be measured to long intense pulses. Figure 3.23 shows the scope output from an SiPM, green trace, when illuminated by a long 100 μ s, low intensity pulse, blue trace, Figure 3.24 shows a more intense light pulse, green trace, onto the same SiPM, blue trace.

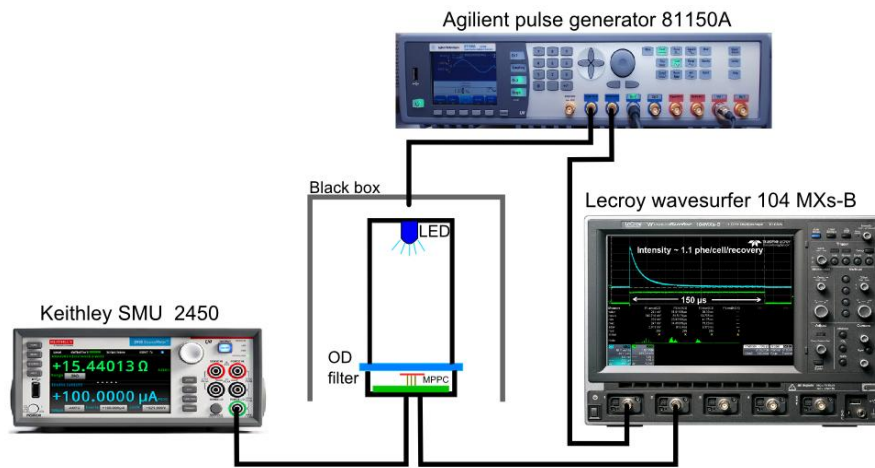


Figure 3.22: Experimental set-up to measure the output response of an SiPM subjected to a long intense light pulse from an LED. Optical density filters were used to vary the light intensity reaching the detector

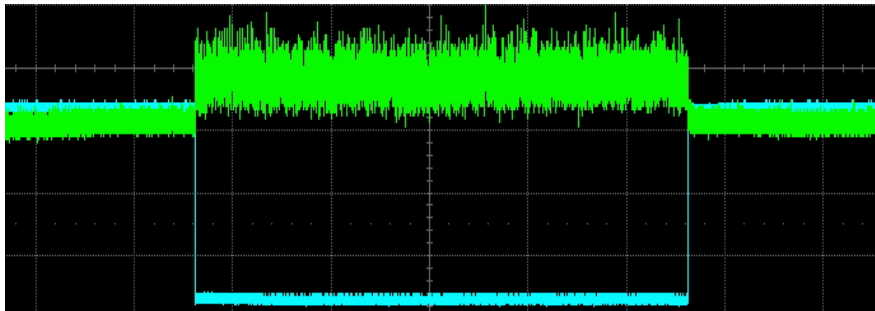


Figure 3.23: SiPM response to relatively low load. Blue trace indicates the LED pulse and the green trace is the SiPM response. Each vertical division is 2 mV.

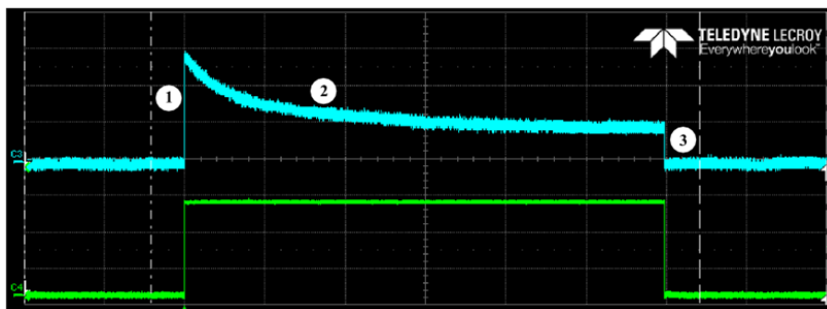


Figure 3.24: Scope output of SiPM output, blue trace, due to a long intensity of light, green trace. The output response can be identified by three distinct sections. 1) Initial rise 2) Decay to a plateau level. 3) Decay to zero when light is off. Each vertical division is 2 mV.

In figure 3.23 the output response approximately follows a rectangular pulse, albeit with some fluctuations on the plateau. In this case rise and fall time of the detector response is limited to the recovery time of pixels as it is a convolution of the near rectangular response of the LED pulse, assuming a rise time of a couple of nanoseconds when measured with a standard PMT , and the long recovery tail in the tens of nanoseconds.

The output response shown in figure 3.24 however does not resemble a rectangular pulse. The output shape can be characterised by three states:

1. Initial peak
2. Decay of initial peak to a plateau level
3. Final decay after light has been turned off

The initial peak, between $t = 0$ and $t = \tau_{fall}$, occurs due to the sudden illumination triggering all, or most, of the cells. Some cells are not available for triggering due to thermal noise and are in the recovering state however for the most pixels are fired. At this stage the number of fired pixels follows a Binomial distribution as in equation 3.22 and the mean count rate I_{bin} is given by [186]:

$$I_{bin}(t) = \frac{dN_{fired}}{dt} = I_{ini} \cdot e^{\left(\frac{I_{ini} \cdot t}{N_{pix}}\right)} \quad (3.23)$$

Where I_{ini} is the potential count rate of electrons capable to fire a pixel which can be written in terms of PDE, N_{photo} and mean number of crosstalk events n_{ct} as:

$$I_{ini} = N_{photo} \cdot PDE \cdot (1 + n_{ct}) \quad (3.24)$$

In this section the firing process is an exponential with characteristic time N_{pix}/I_{ini} . In the region of time $t \sim \tau_{fall}$ the number of fired cells is a mixture of those just fired during the first stage and those in the process of almost recovering. This results in a decrease of signal from the peak in the first stage.

At times $t \gg \tau_{fall}$, a plateau is reached due to the constant firing and recovering of cells at different rates. This can be described by a non-paralisable dead time model [187] which predicts an approximately Gaussian distribution of detection events with a constant mean count rate I_{steady} [186]:

$$I_{steady} = \frac{I_{inist}}{1 + \frac{I_{inist} \cdot \tau_{fall}}{N_{pix}}} = I_{ini} \cdot (1 + n_{ap}) \quad (3.25)$$

where I_{inist} is a steady state potential count rate taking into account the mean number of afterpulses n_{ap} per primary event. The light is then switched off. Within the signal output at this point is charge within the recovery process and afterpulsing events which eventually fall off to zero. Afterpulsing is present in figure 3.24 but cannot be seen at this scale.

The experiments shown in the previous figure were controlled in intensity by varying the voltage supplied to the LED to turn it on. The LED was a cheap commercial device which changed shape in terms of rise and fall time as a function of applied voltage when measured with the PMT. Furthermore, there is considerable doubt to assume that spectral output behaves linearly to applied voltage. For this reason the OD filters were used. This allowed the pulse generator settings to be optimised for one setting and the intensity of light reaching the SiPM was varied by changing the OD filters between the LED and detector.

The transmission of light through an OD filter is given by the equation [188]:

$$T = 10^{-OD} \quad (3.26)$$

When combined in a sequence the transmission of light through a stack of filters is simply the result of multiplying the transmission value of each OD value used. The OD filters used and the associated errors [189] are give in table 3.4 with the transmission of light as a percentage calculated from equation 3.26 along with the error in that calculation. The transmission for each filter is quoted by the manufacturer for red light. However, further observation shows that in most cases red and blue values are similar.

Table 3.4: OD values with errors and the calculated transmission and error.

OD	Error	Transmission (%)	Error (%)
0.1	± 0.01	79.43	0.79
0.2	± 0.01	63.10	0.63
0.3	± 0.01	50.12	0.50
0.4	± 0.02	39.81	0.80
0.5	± 0.03	31.62	0.95
0.6	± 0.04	25.12	1.00
1	± 0.06	10.00	0.60
2	± 0.1	1.00	0.10
3	± 0.15	0.10	0.02
4	± 0.2	0.010	0.002

The signals were recorded on the scope which measured the peak value of the waveform as well as the rise and fall times and also the integral of the waveform. Furthermore, the SMU allows the current drawn from the SiPM to be measured. The Keithley unit is a high precision device and so was considered a more accurate method of measurement. The LED was manually aligned with the SiPM so that maximum current was read from the SMU. Whilst the utmost care was taken that the LED was always aligned with the SiPM a 5% error is attributed to the current measured along with a round off error from recording the measured current.

Figure 3.25 shows the recorded current as a function of the transmitted intensity of light. The plot on the left shows the full scale of all recorded points whilst the plot on right shows the same plot but only from 0 to 10 % of transmitted light. The plot shows a clear saturation curve where the current is saturating to a value just above 3 μA and this saturation begins to occur about 3-4% of the transmitted light. There a jump in current this can be seen in the plot on the right. Repeated values were taken in this region with the same result.

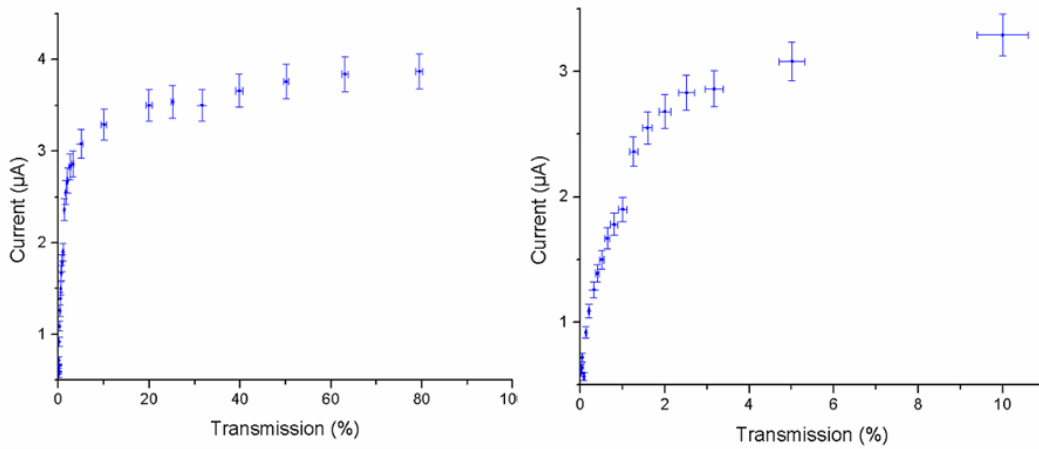


Figure 3.25: Left) Current measured on the SMU against the transmission of light from the LED calculated from the OD values. Right) Closer view of the curve from 0 to 10% of transmission.

It was observed during experiments that the rise time of the detector output was affected by the amount of light which reached the device. Figure 3.26 shows the results of measuring the rise time in this experiment. The left plot shows the rise time as a function of the OD transmission and the plot on the right shows the rise time plotted against the peak value. There is a clear linear trend between the rise time and pulse height. As with the previous figure a 5% error is attributed to potential misalignment.

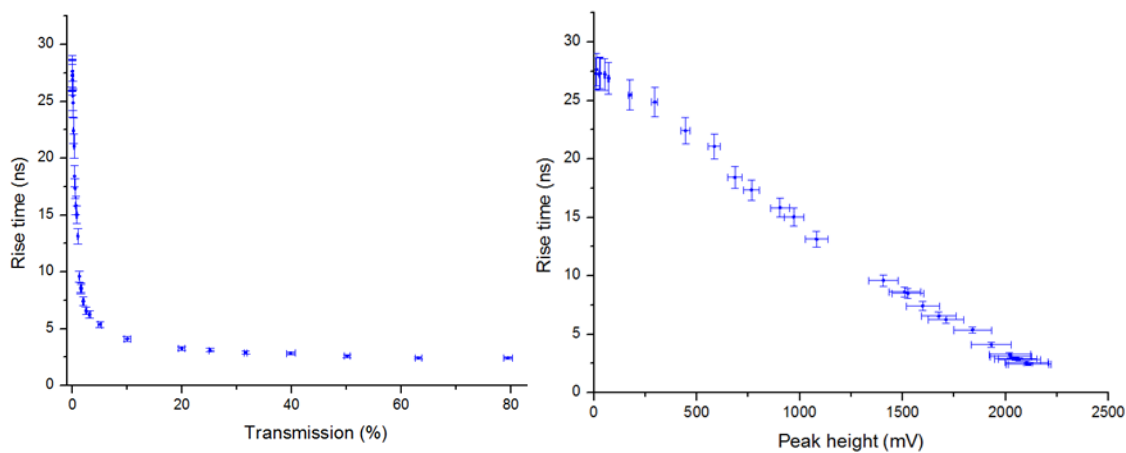


Figure 3.26: Left) Rise time of SiPM response against the transmission of light reaching the detector. Right) Rise time plotted against peak height.

3.5.3.1.2 Analytical Model of SiPM Initial Response to High Intensities

To understand the dynamics of an SiPM in the initial stages an analytical approach was taken. An analytical model of the output response of an SiPM under high load can be established by the convolution of the detector response and the light input. This is performed by taking the inverse Laplace transform, \mathcal{L}^{-1} , of the multiplication of the Laplace transform, \mathcal{L} , of both the detector response and the light intensity input, $light(t)$, i.e:

$$output(t) = \mathcal{L}^{-1}\{\mathcal{L}(SiPM(t)) \cdot \mathcal{L}(light(t))\} \quad (3.27)$$

The input response, I_{light} , of the light source can be modelled as a quasi-step function with some finite rise time T_{LED} and initial intensity rate I_0 :

$$I_{light}(t) = I_0 \cdot \left(1 - e^{\frac{-t}{T_{LED}}}\right) \quad (3.28)$$

Taking the Laplace transform of equation 3.19 and equation 3.28, multiplying them and simplifying as much as possible the output function takes the form of the complicated expression (solved with computer solver Mathcad [190]):

$$output(t, T_{LED}, \tau_{rise}, \tau_{fall}) = \frac{A - B + C}{(T_{LED} - \tau_{fall})(T_{LED} - \tau_{rise})(\tau_{fall} - \tau_{rise})} \quad (3.29)$$

Where:

$$A = 2T_{LED}^2 \cdot e^{\frac{-t}{2T_{LED}}} \cdot \sinh\left(\frac{t}{2T_{LED}}\right) \cdot I_0 \cdot (\tau_{fall} - \tau_{rise}) \quad (3.30)$$

$$B = 2\tau_{fall}^2 \cdot e^{\frac{-t}{2\tau_{fall}}} \cdot \sinh\left(\frac{t}{2\tau_{fall}}\right) \cdot I_0 \cdot (T_{LED} - \tau_{rise}) \quad (3.31)$$

$$C = 2\tau_{rise}^2 \cdot e^{\frac{-t}{2\tau_{rise}}} \cdot \sinh\left(\frac{t}{2\tau_{rise}}\right) \cdot I_0 \cdot (T_{LED} - \tau_{fall}) \quad (3.32)$$

This would be true if there were an infinite number of pixels which could be fired however the

limited number of pixels available to fire needs to be taken into account. The mean number of fired pixels in this case can be written by using the binomial based equation 3.22 and for the number of photons using the light intensity described in equation 3.28 and integrating over time for a total number of photons. The intensity rate, I_{fired} , of the mean number of fired pixels is then found from the differential of the mean number of photons as a function the number of photons from the LED.

The intensity of fired photons is found from the convolution of the bi-exponential model and the mean rate of fired pixels. Convolving this using Laplace transforms does not result in a simple expression and so must be convolved numerically using the standard convolution integral:

$$I = \int_0^t SiPM(t) \cdot I_{fired}(\tau - t) d\tau \quad (3.33)$$

The intensity is a function of LED intensity. This is plotted in figure 3.27 for different intensities. The number of fired pixels rate reaches a peak for all three intensities shown. This is a result of a limited number of pixels available to fire. The lowest intensity does not show a sharp peak as the intensity of light is so low. As a result of this there are still many pixels available to trigger unlike the high intensity case where the rate is so high that very soon there are limited pixels to fire and so the rate fall off. Furthermore, this may explain why for different intensities the rise time changed. Since the rate is higher, the SiPM will saturate faster and peak achievable output will be reached in a shorter time.

What these studies have shown is that as expected SiPM performance under high loads are limited by finite pixel numbers. Furthermore, a long recovery time can lead to dead time effects and distort the true pulse shape of a light source.

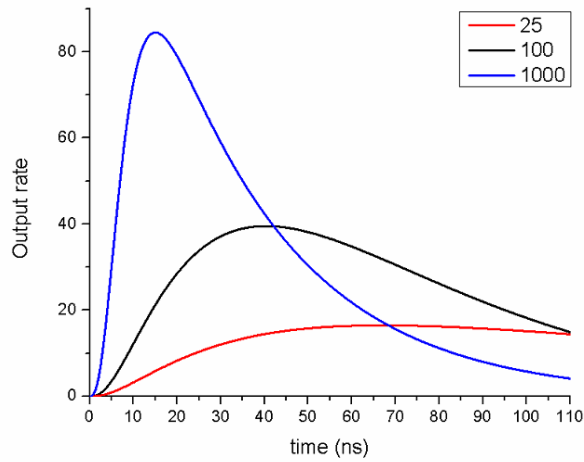


Figure 3.27: Output from the convolution of bi-exponential SER pulse and the mean firing rate as a function of photons emitted from an LED with a finite rise time.

3.5.3.2 SiPM response to Double pulses

A study [191] was performed into assessing an SiPMs ability to recover in time to detect a second input pulse. To do this an experiment was conducted as the set up in figure 3.28. A signal generator was used to pulse two laser drivers which controlled two lasers which pointed onto an SiPM. The SiPM in this case was a. An optical density filter was used so the laser did not saturate the detector and a diffuser was used to produce homogenous coverage of light over the photosensitive area. The experimental area was covered and performed in dark conditions to block ambient lighting.

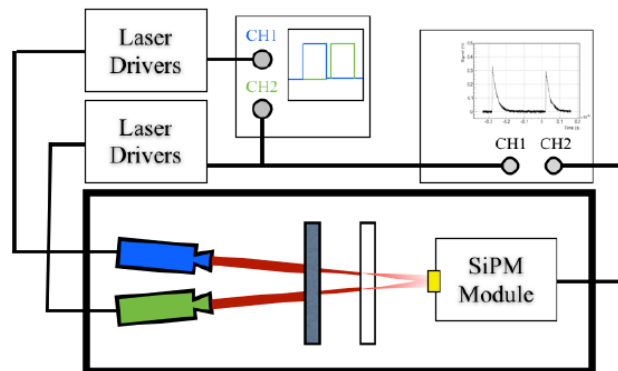


Figure 3.28: Experimental layout to measure an SiPM response to double pulses [191].

The signal generator produced a square pulse and a signal delay was introduced between the two laser pulses and varied from 1 to 300 ns. The output of the SiPM was read out with a Lecroy Waverunner 104-MXi-A scope with a bandwidth DC to to 1 GHz and was used to numerically integrate the output response to calculate charge. The charge from the device as a result of the second laser pulse was found from the difference between the total charge produced and the charge of the first pulse.

An analytical model was established within this study which as a starting point uses equation 3.28 however these do not take into account crosstalk. Figure 3.29 shows the comparison between experimentally obtained normalised charge from the second pulse and those predicted by the model for four intensities of light as a function of delay between the two laser pulses. The solid markers are those from experiment and the lines are predicted by theory. The analytical and experimental results do not match up quantitatively but the general trends are in agreement.

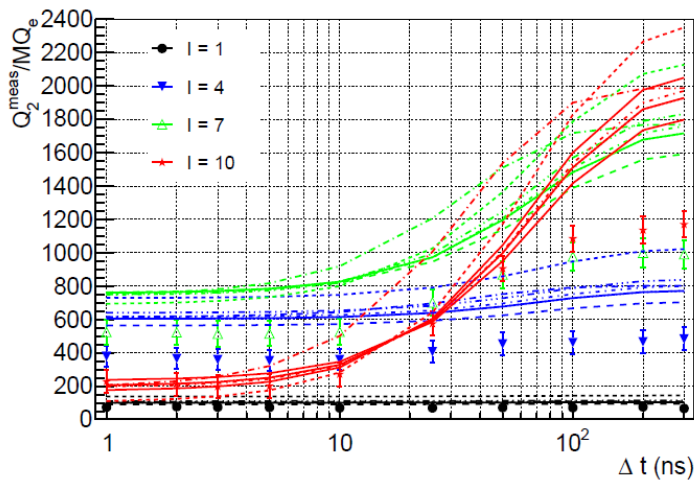


Figure 3.29: Measured and analytical model results of the charge of the second pulse for four different intensities [191].

It was found in this analysis that for low light intensity signals that the number of fired pixels or recovery time had a significant impact on the response of the detector. When the intensity of light is enough to trigger 20% of the pixels on the board however this breaks down. The response of detector to second pulse after this though decreases when the delay between the two pulses is comparable to the pixel recovery time. This work has shown that again higher pixel densities on the SiPM can improve the situation. Furthermore, better models of SiPM characteristics may be used to extrapolate data.

3.6 Measurements at CTF3

3.6.1 CTF3

The CLIC Test Facility at CERN, CTF3, was built to test the novel two beam acceleration method, figure 3.30. To achieve a high gradient from the transfer of power requires a DB with sufficient current and energy. It is not possible to generate the required parameters of the DB from a standard electron source. A short length, small current beam needs to be manipulated to create a long high current beam required for high energy transfer. The first part of CTF3 is dedicated to producing this type of beam and uses a delay loop and combiner ring to do so. The second part of CTF3 is dedicated to testing the power transfer structures to a test beam line which runs parallel located within the CLEX hall.



Figure 3.30: Layout of CTF3 [192].

A delay loop and combiner ring are used to increase the initial current from 3.5 A to 28 A. The DB is generated from a Cs_2Te photocathode and is accelerated through a linear accelerator structure up to 150 MeV. The initial beam is a long train (1.4 μs) of 2928 bunches of electrons [39]. An RF deflector is then used to split buckets of bunches up. The deflector kicks every other bucket of bunches around a delay loop. The length of the delay loop is such that by the time the bucket makes one rotation around the loop the bucket is interleaved with a bucket that is not kicked into the loop by the RF deflector, thus doubling the total charge of the incoming buckets.

The size of the delay loop allows this interleaving to occur however the loop also includes a wiggler half way around the loop such that the total path length around the loop can be controlled for better precision [193]. Electrons exiting the delay loop are ordered in 140 ns long pulses separated by 140 ns. The beam is then transferred to a combiner ring. The combiner ring has two RF deflectors that compensate each other so a new train can be injected when it arrives. After one turn, bunches of the next train are interleaved between the first injected train and so on for 4 turns. The beam exiting the combiner ring is still 140 ns in length but the total train current has increased by a factor of four. Figure 3.31 shows the pulse structure before and after the delay loop and combiner ring combination.

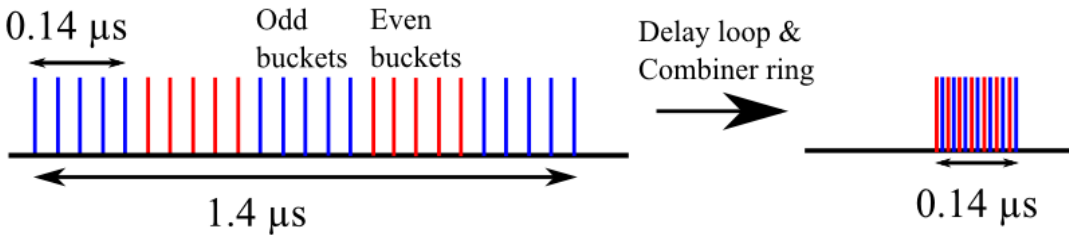


Figure 3.31: Pulse structure before and after manipulation. Beam current increases from 3.5 A to 28 A.

Table 3.5: Comparison of selected parameters between CTF3 and CLIC [39].

Parameter	TBL	CLIC
Number of PETS	16	1492
Length of PETS (m)	0.80	0.21
Initial average current (A)	28	101
Initial Energy (MeV)	150	2400
Mean energy extracted (%)	~54	84
Number of FODO cells	8	524
Pulse length (ns)	140	240
Bunch Spacing (GHz)	12	12

The beam is transferred to the CLEX hall where it is directed down one of two beam lines. The

first is the two beam test stand, TBTS, where a PETS tank transfers RF power to accelerate a probe beam in the CALIFES linear accelerator and the second is the test beam line, TBL, which is used to measure the stability of a decelerated beam. The TBL consists of 16 modules each containing a quadrupole, a beam position monitor and a PETS tank. Table 3.5 shows a comparison of TBL at CTF3 with the proposed CLIC drive beam.

The long pulse structure will be a challenge for the optical fibre to locate losses. This is due to cross-talk [162] between pulses in which one pulse train can cause multiple losses along the accelerator and there is ambiguity in which light pulse exiting the fibre originated from where.

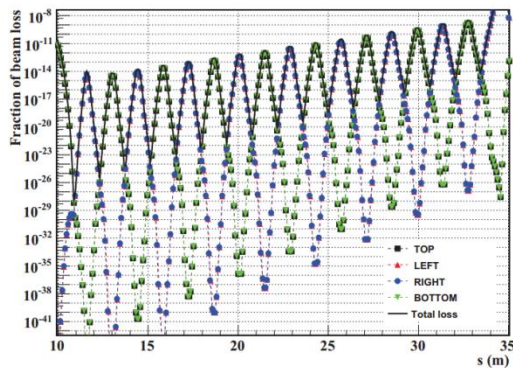
3.6.2 Simulations of Losses

Many simulations of beam losses along the TBL have been performed [194] [195] [196] for various loss scenarios and also arbitrary beam loss. Here, a description is given of a simple model of beam loss along the TBL [194]. Assuming that the beam can be modelled transversely as a two dimensional Gaussian. The parameters of this Gaussian when entering the TBL are found from a diagnostic section and matched to the FODO lattice. The energy loss in each PET is assumed to be equal from each structure. The amount of beam loss is found from the integral of transverse profiles with a limit greater than the beam pipe radius.

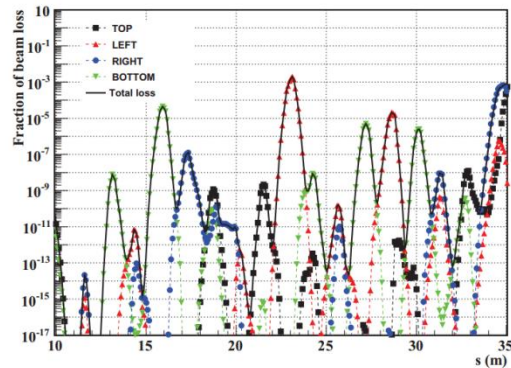
$$P_{LOSS} = \int_{\phi=\phi_i}^{\phi=\phi_e} \int_{r=r_o}^{\infty} f(s, r, \phi) \cdot r \cdot dr \cdot d\phi \quad (3.34)$$

Where f relates to the Gaussian profile and is a function of radial distance r , longitudinal position s and angle ϕ which is used as a way to estimate the direction of beam losses in a transverse plane. Four azimuthal regions were studied corresponding of ϕ_e and ϕ_i pairs. These are $(-45^\circ, 45^\circ)$, $(45^\circ, 135^\circ)$, $(135^\circ, 225^\circ)$ and $(225^\circ, 315^\circ)$ and referred to as right, top, left and bottom respectively in the following plots.

Figure 3.32 shows the calculated fractional beam loss for a) a centred beam and b) a misaligned beam. In the centred case a clear periodicity can be seen, with each peak corresponding to a quadrupole position. For the misaligned beam periodicity can be seen but distorted.



(a) Centered beam



(b) Misaligned beam

Figure 3.32: Fraction of beam loss for a) a perfectly centred beam and b) a misaligned beam [4].

Additional simulations have been performed using FLUKA [197], a Monte Carlo based programme which can be used to model the geometrical structure of the accelerator and components and measure fluence of radiation lost from a beam. To simulate a generic detector a region of air is modelled in various positions around the beam pipe and the fluence through this area recorded. The ideal position for a beam loss monitor can then be established from the simulation results.

From these studies [195] it was found that losses will mostly be generated at quadrupoles. In this scenario most radiation is absorbed in the beam pipe and magnet elements. The radiation that is created in the shower mostly comprises of electrons, 64 %, with the rest being made up of photons, neutrons and positrons. The impact angle of beam loss was varied from 0° to 10° with maximum energy deposition directed towards the detector in the case of 10° . Placing the detector closer to the beam line leads to a higher signal through the detector but placement is a trade off between detecting a high signal and avoiding saturation in the case of high losses.

3.6.3 Detector Layout

A multimode fibre has been installed along the 22.5 m long TBL at CTF3 to test this technology under multi bunch beam conditions. Along with the fibre, three localised detectors are installed, namely: ACEMs and diamond detectors, discussed in some detail earlier in this chapter, and also Cherenkov crystal PEP-II radiator detectors. These localised detectors are used as an independent measure of beam losses detected by the fibre BLM. The location of all the fibres and localised detectors along the TBL are shown in figure 3.36 which also shows the location of

the PETS and quadrupoles. The specifics of each detector are now discussed in turn. As well as the BLM data taken, data from the BPMs was also available so beam loss can be seen from each BPM as it travels down the TBL.

3.6.3.1 Fibre Layout

The fibres installed at CTF3 are made from Heraeus preform and have a core and cladding thickness of 200 μm and 220 μm respectively. For the measurements presented here a 28 m fibre was installed parallel to TBL attached to a rope 28 cm above the beam line. A fibre of 25 m is attached to the downstream end of the fibre and a 75 m fibre attached to the upstream end of the fibre using fibre couplers, measured to give approximately 80% transmission. These fibres are used to take the signal produced in the fibre parallel to the TBL to the photon detectors located outside the accelerator hall, where they are situated to protect them from potential radiation damage. Furthermore, placing the detectors outside of the main hall allowed them to be accessed without entering the hazardous CLEX hall during operation. Two additional fibres run alongside the downstream and upstream read-out fibres to subtract the background signals. Background signals are attributed to any signals created in the fibre which cannot be matched to a loss along the TBL, these may be from losses from other accelerator components (crosstalk) or losses from TBL which reach the fibre placed closer to the klystron gallery i.e. the fibre above the dotted line in figure 3.36. The downstream correction fibre was damaged shortly after installation and no signals were detected. However, as it will be seen upstream signals are better for analysis.

3.6.3.2 Silicon Photomultipliers

The photon detectors were Silicon PhotoMultipliers (SiPMs). The model of SiPM used in these experiments was a Hamamatsu S10362-33-050C [198]. Each was biased with a voltage of 71.6 V and is housed in a light tight box, figure 3.33, to protect the device from ambient lighting. The charge produced by the SiPM is converted to a voltage before exiting the box and sent to a LeCroy 104MXi-A 10 Gs/s oscilloscope with 1 GHz bandwidth.

The distance between the fibre end and SiPM is 1 cm. This allows full coverage of light onto the detector. Photons that hit the detector are meridional rays. Skew rays have a larger exit cone which means fewer skew rays are detected. This is intentional as skew rays arrive later than meridional rays as a result of travelling a longer distance and lead to temporal broadening [162].

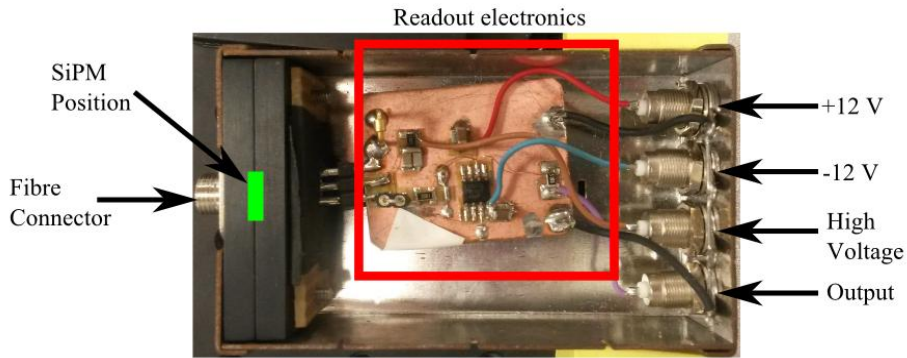


Figure 3.33: Light tight box containing SiPM photodetector and readout electronics.

The charge produced by the photodetector was amplified by a custom made transimpedance amplifier, figure 3.34. A transimpedance amplifier's gain is determined by the closed loop resistor and is an inverting current to voltage converter. In this case the gain is a factor of 500. Capacitive elements in the circuit serve to reduce any ripple in the supplied voltages. The scope was terminated with a 50Ω resistor which means the voltage is split between the load resistor and scope so gain measured by the scope is 250.

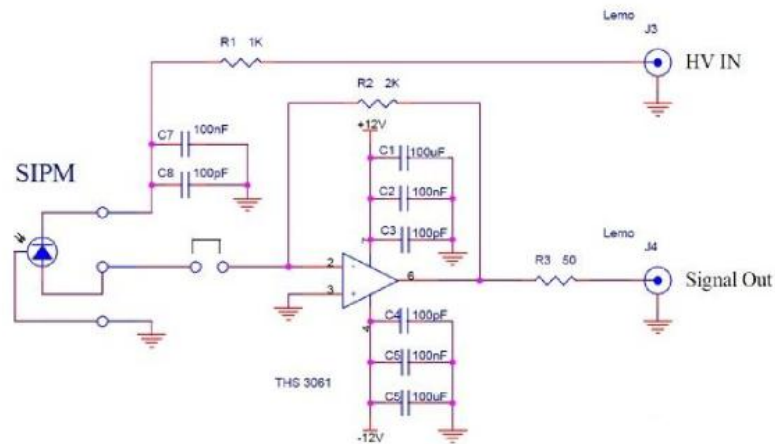


Figure 3.34: Circuit diagram of readout electronics. Courtesy of E Effinger CERN.

3.6.3.3 Localised Detectors

Three detectors, ACEM, PEP-II and diamond pCVD, were installed downstream of the 8th quadrupole of the TBL, located 10.2 m down from the first quadrupole, in order to perform direct comparison of their response. Furthermore, six extra ACEM detectors were installed

immediately after the 3rd, 4th, 7th, 11th, 12th, 15th and 16th quadrupoles in the FODO lattice. A configuration with one localised detectors in consecutive quadrupoles was chosen to potentially study the fraction of beam losses on the horizontal/vertical plane. To avoid saturation the detectors were placed 40 cm below the beam line.

PEP-II detectors are small Cherenkov detectors made from fused silica, 8 mm diameter and 10 mm long, coupled to a photomultiplier tube. These detectors were borrowed from the PEP-II experiment in Stanford [199]. PEP-II detectors, like the ACEM detectors, require shielding for the PMT tube. The diamond detector used in these experiments was a polycrystalline diamond detector bought from CIVIDEC [200]. These detectors are powered by a high voltage power source. The ACEMs and PEP-II are biased negatively with operational voltages between -600 to -700 V and -500 to -600 V respectively. The diamond detector is positively biased with an operational voltage in the range of 500 to 600 V. All three localised detectors were read out with a 250 MHz ADC. Figure 3.35 shows the layout of localised detectors located beneath the beam line after the eighth quadrupole.

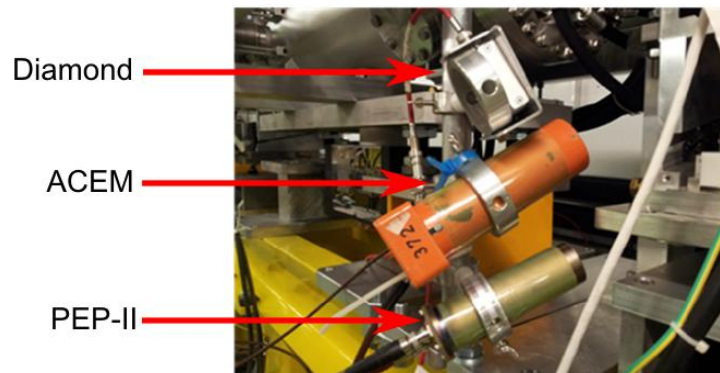


Figure 3.35: Localised detector located after the eighth quadrupole.++

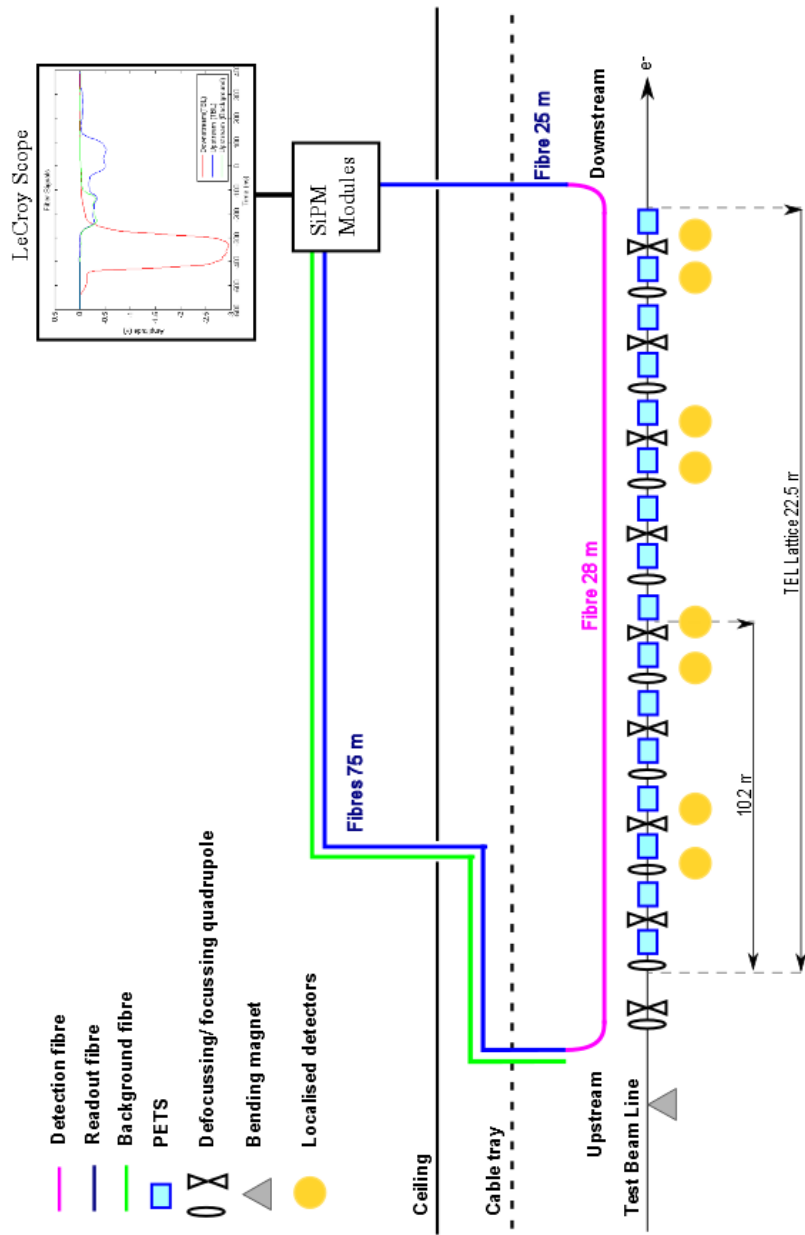


Figure 3.36: Layout of fibres and localised detectors in the CLEX hall.

3.6.4 Measurements

Various data samples were taken using the detector set-up described above during stable beam operation of TBL on the 15th May 2013. The beam conditions during data acquisition were a beam current of 16 A and a pulse length of 150 ns. The fibre used for downstream background subtraction was damaged before measurements had taken place; hence no measurement of this signal was possible. The experiments were performed parasitically, i.e they were performed when other experiments were on going.

Figure 3.37 represents an average of 25 pulse samples for the three localised detectors situated downstream of the eighth quadrupole in the lattice. The diamond detector produces a positive output since it was biased by a positive voltage and likewise the ACEM and PEP-II detectors were biased negatively which show a negative signal output. A clear difference in the time response between the detectors is observed. The PEP-II and the diamond detector are fast enough to follow the 150 ns beam pulse, providing also some information of the substructure of the beam losses within the bunch train. However, a small delay and widening of the signal is observed for the ACEM detector, which somewhat averages the structures observed in the other two detectors. Note also the presence of a small pre-pulse starting at -400 ns below the base line for the ACEM detector. This effect is still under investigation.

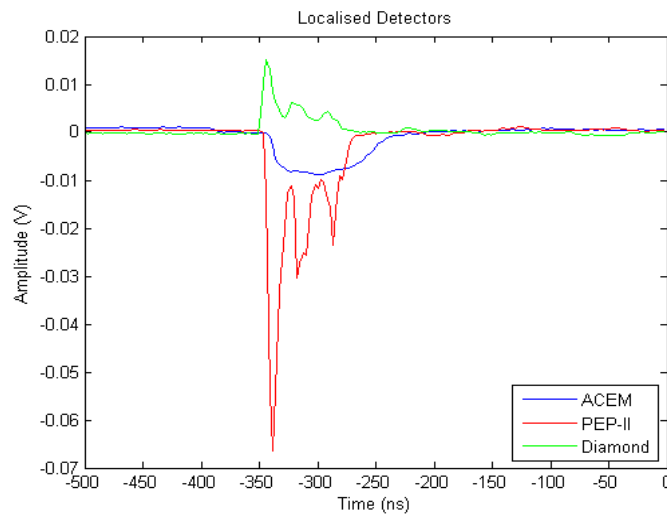


Figure 3.37: Average of 25 samples from the localised detectors.

Figure 3.38 shows the average for the same 25 samples on the signals observed by the working optical fibres. The blue (green) line corresponds to the upstream TBL signal (background) fibre. The signal observed between -250 ns and -150 ns is a background contribution, as both the TBL signal and background fibre detect an identical pulse. The plateau observed immediately after is attributed to the positioning of the fibre at certain points along TBL. Due to space limitations with the support system used, the ends of the 28 m fibre were not parallel to the beam line. As a result of the angular dependent response of the fibre and the fact that the ends were orientated at a more sensitive angle to the loss shower, a higher signal is detected in these regions which generate a higher signal than other angles. Furthermore, the duration of the plateau is comparable to the beam pulse which means that this data is consistent with losses from single locations.

The red line corresponds to the signal downstream fibre, which shows significantly higher amplitude compared to the upstream fibres. This is due to the fact that more particles are produced from losses in the downstream direction producing more photons and a higher signal. Moreover, the read out fibre connected to the downstream end of the TBL fibre is 50 m shorter than the corresponding upstream fibre; hence the signals travelling towards the downstream end are less affected by attenuation.

The upstream and downstream response show different pulse shapes as a result of signal bunching. The beam propagates in the direction of the downstream photons which means that when losses occur in two locations, the photons generated from the first loss will propagate in the fibre in the time it takes the electron bunch to generate photons from the second loss event. This results in signals bunching together which are difficult to resolve, as seen in figure 3.38. For upstream signals the situation is improved as photons propagate away from further loss events. For this reason, it is easier to analyse upstream signals.

There is a small rising edge and plateau observed between -530 ns and -430 ns in the downstream fibre, this is attributed to the background contribution. The time shift between the start of the upstream and downstream signals comes from the different time of flight of photons travelling to opposite ends of the fibre.

A plot of the background corrected signal after an average of 25 waveforms is shown in figure 3.39. It can be seen that there is a positive signal between -250 ns and -150 ns. This occurs where the background signal fibre is larger than the TBL fibre. The fibres are installed side by side, however, this does not mean that every signal generated in the TBL fibre is also generated

in the background fibre and vice versa.

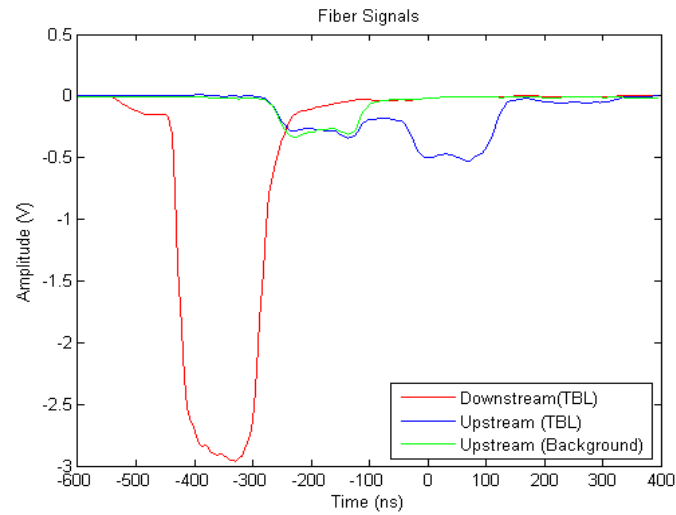


Figure 3.38: Average of 25 samples from the optical fibres.

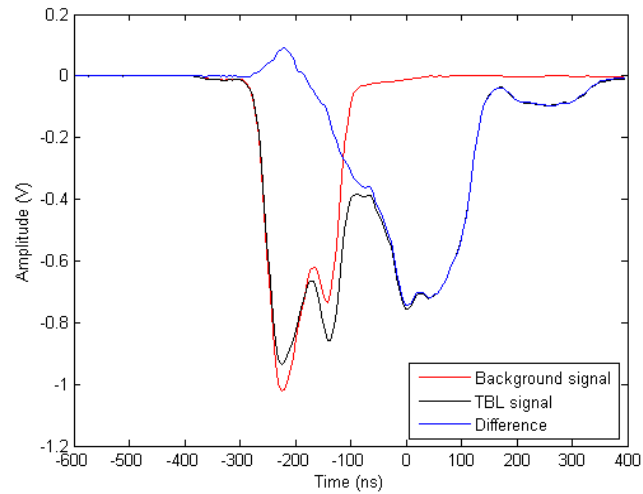


Figure 3.39: Signals from the TBL fibre (black) and background fibre (red) and the difference between them (blue).

3.6.5 Dose Calculations

The approximate dose of the detectors can be calculated by using parameters discussed earlier in the chapter. To do so several approximations need to be made. All radiation hitting the detector

are assumed to be MIPs. The output charge from the detectors is found by integrating the voltage signals and calculating charge based on the fact the detectors were terminated with a 50 Ω resistor. The number of MIPs generated per Gray per unit area can be found from the minimum ionising energy and the relation given in equation 3.3. This approach was adopted from [201] and uses an error analysis suggest by [202]

For the ACEM detector it is assumed that 5% of incident radiation produces secondary electrons [114], the PMT gain is approximately in the region of 10^4 . The output charge per gray then given by:

$$S_{Acem} = 3.56 \frac{\mu\text{C}}{\text{Gy}} \quad (3.35)$$

For the PEP-II detector many more assumptions are required. Firstly it is assumed that the number of generated photons per MIP per cm is the region of 227 photons/(MIP.cm) [114]. Of the photons that are generated, 80% make it to the PMT photosensitive layer and 30% of them are detected. The number of detected photons per total photons produced is then 24% The PEP-II active volume is 2.01 cm^3 and like the ACEM detector the PMT gain is in the order of 10^4 . The corresponding sensitivity is:

$$S_{PEP} = 0.64 \frac{\text{mC}}{\text{Gy}} \quad (3.36)$$

For the diamond semiconductor detector the active area is 0.64 mm^2 . An MIP travelling through diamond will produce $2.34 \cdot 10^4$ electron hole pairs and a charge collection efficiency of 30% [203]. A factor of a third is introduced as this is a poly crystalline diamond and so the total charge is approximately a third less compared to a defect free diamond [204]. Equation 3.37 shows the approximate output charge for incident radiation, the factor 2 is attributed to an electron hole pair having twice the elementary charge. For the diamond detector the output charge per gray is:

$$S_{\text{diamond}} = 1.73 \frac{\mu\text{C}}{\text{Gy}} \quad (3.37)$$

Table 3.6 below shows the approximate dose recorded from each detector. The PEP-II detector estimated dose does not match with the other detectors. The signal generation in PEP-II is more complicated and the assumptions stated may not be sufficient. The ACEM and diamond detector, however, are in good agreement.

Table 3.6: The charge produced by each detector found from the scope output and an estimate of dose detected from each.

Detector	Charge (C)	Dose (Gy)
ACEM	$4.96 \cdot 10^{-10}$	$(1.39 \pm 0.24) \cdot 10^{-4}$
PEP-II	$7.87 \cdot 10^{-10}$	$(1.31 \pm 0.29) \cdot 10^{-6}$
Diamond	$2.08 \cdot 10^{-10}$	$(1.20 \pm 0.24) \cdot 10^{-4}$

3.6.6 Signal Deconvolution

The pulse from the fibre readout is complicated. For this reason two methods of signal deconvolution were attempted. The first was a deconvolution with the single electron response of the SiPM and the second was with localised detector information. The reason for performing these techniques was to try and understand what is occurring along the beamline in terms of losses in the accelerator.

3.6.6.1 SiPM Single Electron Response Deconvolution

The output response from the SiPM is a convolution of the input into the SiPM from the fibre and the single electron response of the detector. The output response S_{out} from the detector is found by the convolution integral of the input into the detector, S_{in} and the detector response h_{sipm} . The detector response in this case is simply the single electron response of the SiPM. The convolution is written as

$$S_{out} = S_{in}(t) * h_{sipm}(t) = \int_{-\infty}^{\infty} S_{in}(\tau) h_{sipm}(t - \tau) d\tau \quad (3.38)$$

Here, the input response and the detector response is given in the time domain. It is more convenient to work in the frequency domain in this case as a convolution in the time domain is

simply a multiplication in the frequency domain, which is more straight forward to calculate compared to equation 3.38. By using the Fast Fourier Transform (FFT), it is possible to split a signal in time into its frequency components. Equation 3.38 can then be written as the following.

$$FFT(S_{out}) = FFT(S_{in}) \cdot FFT(h_{sipm}) \quad (3.39)$$

By taking the FFT of the SiPM detector response and fibre signals, dividing them and inverting the FFT, S_{out} can be retrieved. This technique is called deconvolution.

This was performed for the two upstream fibres and the corrected waveform. A problem arose however, when trying to use the SiPM detector response. As a result of the limited bandwidth of the oscilloscope each data point is separated in time by approximately 2 ns which is in the order of the SiPM rise time. Thus when calculating the deconvolution, the SiPM pulse required that the length of the vector was the same length as the fibre signal. Information is then lost on timing and the number of detector responses that created the output pulse is approximate. Figures 3.40, 3.41 and 3.42 show the upstream background signal, TBL signal and background corrected signal respectively. A smoothing algorithm was used to remove ringing oscillations, which often occurs in deconvolutions. No error analysis was performed for the deconvolution signal as the absolute number of units at any point in time is not under consideration but the pulse shape. Any uncertainties would be small ($< 1\%$) compared to the large number of units which are present in the signal.

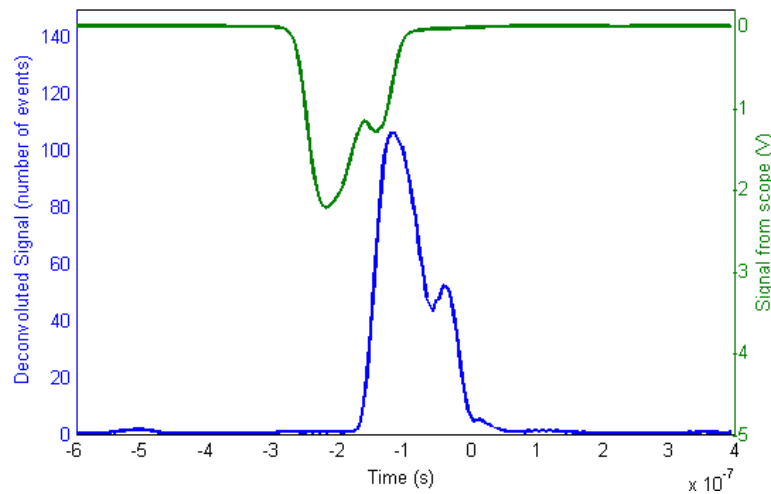


Figure 3.40: Background signal and deconvoluted signal.

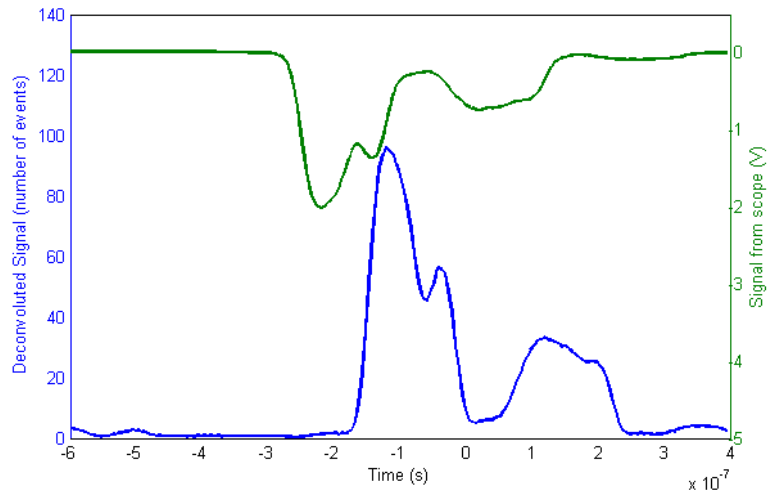


Figure 3.41: TBL signal and deconvoluted signal.

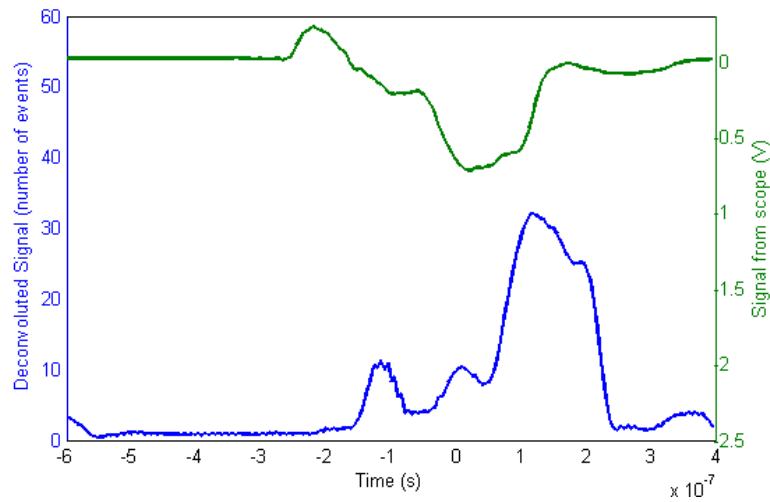


Figure 3.42: Difference between TBL fibre and background fibre signal and deconvoluted signal.

The purpose of performing deconvolutions with the detector response is to remove the smearing effect the SiPM response has on the output signal which may hide loss structure. From figures 3.40, 3.41 and 3.42 it can be seen that the deconvoluted signal is only different from the output signal (green) in only amplitude and sign, i.e. the deconvolution does not improve the understanding of the particle loss distribution as no further structure is resolved. The amplitude of the deconvoluted signal here suggests that the detectors were not under high loads in this case

due to the low number of units obtained in the deconvolution. However, it appears that long pulses with low sampling frequency means no further information can be established. Furthermore, looking at figure 3.42 the positive signal from the subtraction of the TBL fibre and background fibre leads to an additional contribution in the deconvoluted signal which is not attributed to any loss along the beam line. This further shows that the signal correction using a background fibre is not suitable for any advanced analysis. This method of background correction is not ideal and other methods, discussed in the chapter summary and conclusion, are being pursued.

3.6.6.2 Localised Detector Deconvolution

A second deconvolution technique uses the localised detector signals and based on a method proposed in [196]. The signals observed from a fibre can be expressed as the convolution:

$$S_{fibre} = \int S_{bunch}(t) \cdot f(t - \tau) d\tau \quad (3.40)$$

S_{bunch} represents the contribution from losses produced by a single bunch to the total signal observed in the fibre, S_{fibre} . The time evolution of beam losses throughout the beam pulse, $f(t-\tau)$, is assumed to be provided by the signal response in the installed PEP-II and diamond detectors. The ACEM detector was not selected as it is slow and did not show the same pulse structure like the other two detectors. As with the SiPM deconvolution, transforming equation 3.40 to the frequency domain, the single bunch contribution can be found.

The frequency domain does not contain any information about the origin of the loss; however it may provide an insight on the periodicity of beam losses. Beam losses are expected to occur at every quadrupole. Assuming that the signal is produced in the fibre at the same location and simultaneously with the beam loss it is easy to obtain, using the speed of light in the fibre as $2/3 c$ and a beam travelling at c , that S_{bunch} should have a significant contribution around 425 MHz. Equivalently, if losses happen only on alternate quadrupoles the frequency contribution should be 213 MHz. This second case is interesting as the beam size in the TBL is significantly higher in the horizontal plane. Hence, losses at every defocusing quadrupole are more likely to occur [194].

Figure 3.43 shows the resulting power spectrum for S_{bunch} for a single data sample. The signal of

the upstream fibre, with a correction using the corresponding background signal, is used for the calculation of $S_{fibre}(\omega)$ via FFT. Two other FFTs are applied to calculate $f(w)$ as seen by the Diamond and PEP-II detectors. There are large differences in the spectrums obtained for the two localised detectors, as two clear peaks are observed around 300 and 420 MHz only in the case of the diamond detector. The 420 MHz pulse may be a repeat of the 200 MHz pulse. The common feature to the two power spectrums is a peak at 200 MHz. For an analysis over 20 pulses, a common peak at a frequency ranging from 200 to 230 MHz was observed. A peak on the spectrum on this range may indicate the detection of losses in non-consecutive quadrupoles. Furthermore, the signal from ACEM detectors is greatly reduced for consecutive detectors which may also indicate this. Several factors, such as the effect of noise and the systematic differences encountered between the two localised detectors have not been taken into account and would require further investigation in future experiments.

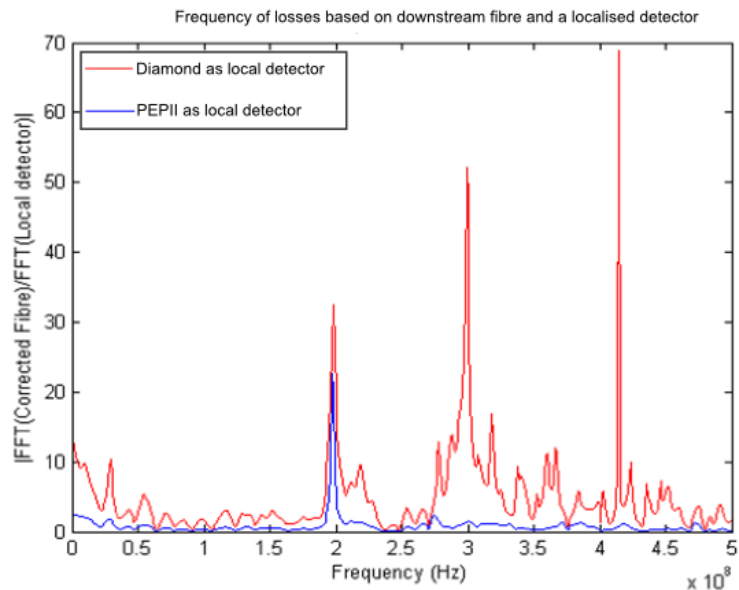


Figure 3.43: Estimate of bunch loss frequency using the fibre and localised signal detectors.

3.6.7 Further Experiments

More recent experiments [205] have been performed with an optical fibre BLM at CTF3 and at the Australian synchrotron light source. The experiments presented in this chapter were performed parasitically, with little control over the beam parameters, which made it difficult to

assess the system's full performance as a BLM.

It has been shown at the Australian synchrotron that locating losses with long electron beam pulses may be possible using an optical fibre coupled to an SiPM. In these experiments the pulse length of the electron beam was increased so the performance of the detector could be observed; this was not possible with the experiments performed at CTF3.

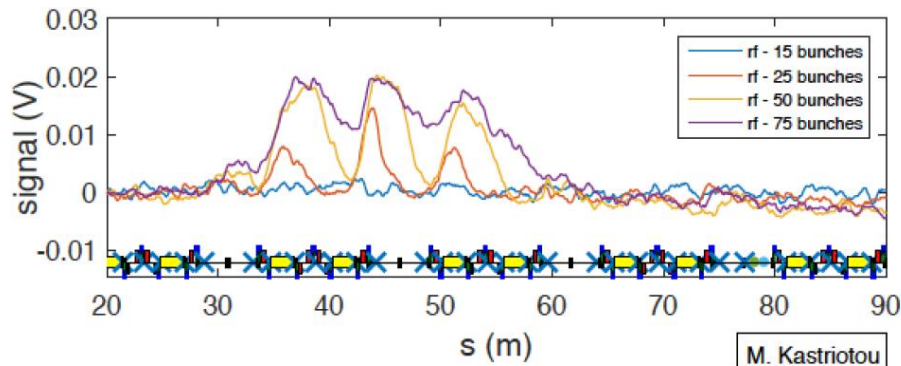


Figure 3.44: Loss signal measured from an optical fibre and the associated distance along the accelerator. Pulse shapes for longer trains are averaged out and it is difficult to locate the loss [205].

Figure 3.44 shows the detected losses, peaks, for pulse trains with bunches of 15, 25, 50 and 75 bunches which corresponds to pulses of lengths 30 ns, 50 ns, 100 ns and 150 ns, respectively. Determining loss location at longer pulse lengths is difficult as the pulse structure average out, however with correct analysis techniques like deconvolutions it may be possible to understand loss position. Experiments such as this will allow the performance of an optical fibre beam loss monitor to be tested to greater detail.

3.7 Chapter Summary

In this chapter a new type of beam loss monitor was presented which may be advantageous particularly in large accelerator facilities such as the Compact Linear Collider . This new BLM is based on optical fibres with photodetector readout, this chapter presented experiments conducted at the CLIC test facility as an early study to assess its applicability as a CLIC BLM.

The chapter began by introducing the reasons behind beam losses and to cover some of the standard techniques in which they are usually measured. A full strategy is already in place for the CLIC BLM system based on ionisation chambers, however, to cover the full length of the

accelerator a great many number of detectors would be required and therefore expensive. To this end, a new type of BLM based on fibres is being considered which could cover whole sections of beam line just using one detector. The basic principle of the operation of this technology in this context was described in this chapter with additional discussions about fibres themselves. It was necessary to cover this as the choice in fibre type and length will have far reaching consequences on its applicability as a beam loss monitor.

For the photodetector readout SiPMs are currently under investigation as they offer many advantages to commonly used PMT technology. However, it is not a simple matter of replacing PMTs with SiPMs. The chapter continued by discussing the operation of SiPMs along with detailed characterisation of the expected performance in beam loss monitoring applications. Several experiments were conducted to characterise two devices and it was seen that SiPMs are potentially ideal detectors as BLM as they offer excellent timing resolution with which a loss may be detected. However, when considering SiPM performance under high intensities of light and also pulses close in time at high intensities it was found that SiPMs begin to saturate due to a limited number of pixels and also from dead time due to long pixel recoveries. In both of the experiments mentioned it is clear that the pixel number plays a big role when considering implementing them into a BLM system. Devices with high pixels densities, as high as 90,000 [206], are currently under development and will likely solve saturation effects which may occur in beam loss monitoring from big losses. Furthermore, improvements in the design and the understanding of the avalanche process means that devices are now being made with improved characteristics with regards to crosstalk and after-pulsing. Both of these improvements will see SiPMs being introduced into many more areas of science.

The chapter concluded with experimental data recorded at the CLIC test facility during the timeframe of this project. The layout of test facility was discussed and the location of the detectors and signal processing were also covered. Data sets were obtained for fibre data along the main accelerating structure along with background correction fibres and also detector signals from localised detectors. All signals were collected with a time stamp so losses detected from the fibres and also the localised detectors could be cross examined. The signals from each detector were discussed in turn before moving onto more advanced signal analysis.

Deconvolution methods were discussed as part of signal analysis. The first method using the SiPM detector response and the second based on localised detector response. The latter was performed as an attempt to understand frequency of losses based on two detectors, the long fibre

and localised detectors. The former is the preferred technique for deconvolution since the latter required localised detectors and the benefit of the long optical fibre is the requirement for fewer detectors. In this analysis the localised detector deconvolution worked better as it gives a hint that losses are occurring at every other quadrupole. This has also been suggested through simulations. The straight deconvolution is limited as a result of fibre layout within CTF3. The background correction fibre idea is only a loose approximation of the signal generated along the fibre not placed along the TBL. From the waveforms shown in figure 3.38 it is clear that using the background fibre the contribution from signals not generated along the TBL can be identified. However, when trying to perform an analysis quantitatively the subtraction is insufficient. Placing the fibres side by side does not mean the same signal is generated in each.

One idea currently under development on the basis of the results from the here-presented studies is to redesign the fibre layout at CTF3. The background fibre would be removed and replaced by a hollow core fibre. This will allow light signal to be carried to the external photodetectors, however, since they are hollow no signal will be generated which means a background correcting fibre would not be required. This idea is still in the early stages of development and issues such as coupling to the standard TBL fibre still needs to be addressed, however, it appears to be an interesting and innovative solution to improving experiments at CTF3.

An issue that is currently under question is the ability to distinguish losses from the DB and MB and avoid cross-talk of losses between the two beamlines. A recent study [207] has shown that this might be a main limitation of the system and is another factor that needs to be considered. The studies presented here shown an initial attempt to understand their applicability as a CLIC BLM, however, many more are needed.

Chapter 4:

Conclusions and outlook

The concepts and work developed within this PhD project helped improve the generation, diagnostics and control of electron beams.

The first chapter began with a short summary of the history of electron accelerators leading on to over-arching concepts of electron beams including accelerating gradients, the so-called TWISS parameters, and beam emittance. Two applications of electron beams were then presented: Free electron lasers and electron/positron colliders. Both of these applications despite being used for different reasons rely on excellent beam quality which was to be the underlying focus of all following chapters. The first half of the thesis aimed at trying to understand electron emission properties to optimise beam quality whilst the second half targeted studies into beam quality control via loss detection.

4.1 Electron Beam Generation

The second chapter focussed on the low energy regime of electron beams. This took the form of introducing concepts behind electron sources and introducing the TESS experiment at the Cockcroft Institute which aims to understand electron emission from photocathodes finding the longitudinal energy distribution of emitted electrons.

The chapter began by explaining the physics behind different electron sources with a presentation of the state-of-the-art in field emission, thermionic emission and photoemission sources. The TESS experiment is designed to measure both the transverse and longitudinal energy distribution of photoemitted electrons. An overview of the experimental set up was presented and two proposed techniques to measure the longitudinal energy distribution of

electrons emitted from gallium arsenide, the material of choice during TESS commissioning. The first was to use TESS' wire meshes to create an energy window between the wires and the second to generate a gap in potential between the electron source and detector plate. In both cases electrons must overcome a potential generated by the system with detection of a signal occurring as a result of the initial energy distribution of the emitted electrons.

In order to understand these two methods it was necessary to investigate into the dynamics within the experiment. To this end a particle tracking code was developed which could perform this task. Furthermore, to understand the mesh filter technique the exact field surrounding the wire mesh needed to be understood. An analytical study was performed to see whether an expression could be derived which explained the fields accurately. Starting from several simplifications an analytical expression was found, however, it was concluded that no exact solution can be found even for the simple case of a single mesh. It was at this point that finite element analysis software was used to calculate field maps surrounding a mesh structure. Several studies were performed to optimise the model and to better understand the electrostatic fields surrounding a multi mesh system. Results were crossed checked with another finite element multi-physics package. The tracking code was then introduced with the structure of the code and operation procedure carefully described.

The chapter then returned to the underlying questions on the physics of the emission process with the union of both experimental and simulated data. Experimental results were obtained for both techniques. For the mesh filter technique it was found that the signal reduced over a large potential gap. By simulating this technique it was found that an aperture window created in the wire mesh region was the source of the reduction of signal over a wide range. Furthermore, it was shown from simulations that a position on the micro channel plate could not be correlated to the transverse distribution of electrons, with complicated diffraction-like patterns being observed using controlled initial conditions. The parameters used in the first set of experiments showed that using this technique it was not possible to obtain a longitudinal energy distribution curve of emitted electrons due to two reasons:

1. A low signal when the centre mesh potential is equal to the cathode potential.
2. Ambiguity into the true potential of the system due to the Volta potential.

For an electron to be detected as a result of the initial energy alone and not due to the energy

gain within the system the potential at the centre of the wire mesh needs to be equal to the cathode potential. At high voltages the aperture window in the wire mesh drops several volts in a short distance which effectively meant there was a very small window which the electrons to enter and be detected. This was understood through finite element analysis calculations and further demonstrated in tracking simulations. These studies suggested that lower voltages may be better and in simulations it was possible to obtain a signal, albeit a very small one, on the MCP. Even with this information it is difficult to obtain meaningful results. The Volta potential means that there is an unknown shift in potential in the system. From the intensity of the signal it is therefore impossible to know at what potential the system is completely stopping electrons based on initial conditions alone. This is before even more complications are considered such as geometrical distortions, which were shown to influence the fields of the system, and emission spot position in relation to mesh spacing. For this reason it was concluded that this technique not be used to calculate longitudinal energy distribution curves. The MCP/Cathode potential gap technique was more successful in obtaining a longitudinal energy distribution curve. Even though it was not necessary to simulate this experiment it offered an excellent opportunity to test the code in a configuration in which it is known it should work. It was found that there were certain situations in which simulations were suggesting that particles were lost despite the initial belief that they should be detected. After a thorough study of the code it was concluded that particles were being lost due to a transfer of velocity from the longitudinal to the transverse component. This shift in velocity left electrons with insufficient longitudinal velocity to reach the MCP and be detected. It was found that this effect was observed regardless of the applied potential to the wire mesh and even if a single mesh were used. This effect was unpredicted and was only found by utilising the tracking code.

The output of this work was a significant improvement in the understanding of the TESS experiment in both techniques which were explored. This could not have been achieved without the tracking code which was developed. The work also identified several additional areas which may be pursued at a later time.

- Incorporation of electrons lost due to velocity transfer:

This effect was only identified after assuring that it was not a software error and has not yet been included in the model.

- Effects from the MCP detector:

Currently, electrons in the code could reach extremely short distances away from the MCP and still not be detected. In the FEA software the MCP was modelled as a flat plate. In actuality the MCP has many small channels which would distort the electric field somewhat. This may have an effect on the final measured distribution. The experimental analysis does not take this effect into account either but understanding the overall contribution from these effects would be of interest.

- Transverse experiments:

The code developed has been entirely dedicated to longitudinal studies and has not yet been applied to enhance the understanding of transverse measurements. Even though transverse measurements can be described through electric lenses alone it would be interesting to compare the code with established analytical equations. Furthermore, detailed tracking studies may highlight unknown effects which may not have been considered correctly previously. An unmentioned example of this was when the code was used to explain a lensing effect observed when a high MCP front potential was applied.

4.2 Beam Loss Detection

Chapter three began with an introduction to this work and contained concepts related to beam loss monitoring and charged particle detectors. The chapter began by introducing several parameters which are used to describe a detector. Several commonly used detectors were described along with their individual advantages, limitations and approximate sensitivities. The proposed beam loss monitoring system for the CLIC accelerator was presented along with the requirements on the CLIC machine protection system. It is clear from the sheer size of CLIC that many thousands of local detectors would be required to cover the entire accelerator complex. For this reason a new type of beam loss monitor is under investigation based on optical fibre technology. This detector relies on a signal generated by charged particles inducing Cherenkov radiation which is then transported down the fibre and detected by a photosensor. The technology behind optical fibres was described with the aim of applying them for a beam loss monitor. The expected signal as a function of geometrical and material properties such as size and refractive indices was presented and some general considerations such as the restriction in

length due to attenuation and radiation effects were also discussed.

The chapter then proceeded with investigations into silicon photomultipliers which were the light sensors used at the fibre ends and the detectors used in the experiments presented later in the chapter. Experiments had shown that detector performance can improve or hinder what is understood about the beam from the optical fibre beam loss monitor. The principle operation of the detector was introduced with their operation and structure described along with unique operation effects which can limit their performance, namely afterpulsing and crosstalk. Their performance was tested in experiments to better understand their characteristics. Results were compared to analytical models that have been developed in the frame of this work. The outlook of this side of work is linked to the development of the detector technology itself. Currently it is difficult to understand the SiPM output signal from an arbitrary signal input. However, SiPM technology is a rapidly expanding area with applications in many areas beyond accelerator physics and many of the challenges highlighted in this thesis are being addressed. General trends of design performance are driven towards more pixels on the board, which means a greater dynamic range can be measured, faster rise and fall times, lower crosstalk and afterpulsing, as well as a better understanding of the performance from a statistical point of view. All of these improvements will benefit an SiPM-based optical fibre beam loss monitoring system.

The chapter finished with a presentation of the results from experiments conducted at the CLIC Test Facility. Previous simulation studies were presented which studied various loss scenarios using analytical methods and Monte Carlo codes. Several detectors were installed at CTF3 which included a main detection fibre placed above the test beam lines, fibres to take the signals to the klystron gallery where the photodetectors were located, as well as background fibres which were placed alongside the readout fibres. The latter allowed a signal subtraction to be carried out to account for signals generated not along the test beam line. In addition to the optical fibres three types of localised beam loss monitors were also installed for parallel measurements and cross-comparison of data. These included an aluminium based secondary emission monitor, ACEM, a small Cherenkov crystal coupled to a photomultiplier tube, borrowed from the PEP-II experiment, and a diamond based semiconductor detector as it is currently used in the Large Hadron Collider. The beam pulse used for the experiment had a beam current of 16 A with a 150 ns long pulse length, much longer than previous experiments using this technology. From the signal of the localised detectors it was seen that they all recorded a similar length pulse, however, the ACEM detector was slower than both the diamond and PEP-II detectors which showed sub

pulse structure with similar shapes appearing in both. Using analytical considerations the approximate dose of each localised detector was calculated. The diamond and ACEM detector were found to be generally consistent, however, the PEP-II was some way off the other two detectors. The background fibre for the upstream fibre was unfortunately damaged before measurements were taken. It was shown, however, that upstream signals were far better suited for studying loss structures due to signal bunching for upstream photons. Deconvolution techniques were then performed based on the photodetector response and also using the localised detectors to understand the frequency of losses. The latter was performed using the PEP-II and diamond detectors. It was found that the frequency of losses appeared to be consistent with losses at every other quadrupole with spectrum peaks observed in one location common when using either detector. This is in agreement with simulations. The second deconvolution method applied a more conventional approach, however, it was found that the bandwidth of the scope was insufficient to fully reconstruct the rise time of the detector response. Therefore, the fine structure of rise and fall time was lost. Based on the work carried out within this project several additional studies are being considered. These include the following:

- Removal of background correction fibres and change of readout fibres:
Hollow core fibres are now being considered as readout fibres for CTF3. The work presented in this thesis showed that the background correction, whilst showing a similar pulse shape, was not always correct after background subtraction and led to inverse signs. This was due to the fact that not the exact same signals were generated in each fibre. Removing the background fibres entirely and replacing the readout fibres with hollow core fibres could help overcoming this problem. Signals would be transported to the photodetectors whilst not allowing any further signals to be generated.
- Improvements to the readout electronics design.
Signal amplification as part of the here-presented studies was realised using a rather simple transimpedance amplifier. Its design has subsequently been improved to allow more stable operation of the voltage readout. The revised design is now being used in all beam loss measurements.

- **Dark Current Measurements**

Larger core fibres might be more sensitive and have the potential to generate larger signals. This could allow a direct route for measuring dark current. Studies are ongoing and initial results look promising.

- **Investigations at other facilities**

Multiple experiments have recently been performed at another electron accelerator facility, the Australian Synchrotron in Melbourne. This allows a better control of the stored electron beam and loss generation. The aim of these studies is to identify the true position resolution of an optical fibre-based beam loss monitoring system.

Appendix A: Velocity Distribution Relations

Figure A1 shows a velocity system of a blue particle described in spherical co-ordinates of velocity magnitude v and angles ϕ and θ .

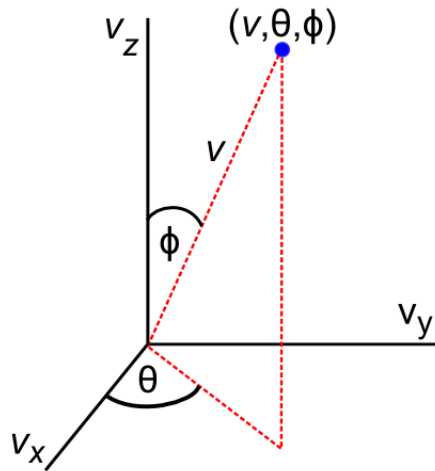


Figure A1: Description of velocity coordinates of a particle

The equivalent Cartesian coordinates can be written as:

$$v_x = v \cos(\theta) \sin(\phi) \quad (\text{A.1})$$

$$v_y = v \sin(\theta) \sin(\phi) \quad (\text{A.2})$$

$$v_z = v \cos(\phi) \quad (\text{A.3})$$

The kinetic energy of an electron of mass m is given by:

$$E = \frac{1}{2} m v^2 \quad (\text{A.4})$$

If the transverse velocity v_T is defined as the magnitude of the velocity in the v_x and v_y plane then:

$$v_T^2 = v_x^2 + v_y^2 \quad (\text{A.5})$$

$$v_T^2 = v^2 \cos^2(\theta) \sin^2(\phi) + v^2 \sin^2(\theta) \sin^2(\phi) \quad (\text{A.6})$$

$$v_T^2 = v^2 \sin^2(\phi) (\cos^2(\theta) + \sin^2(\theta)) \quad (\text{A.7})$$

$$v_T^2 = v^2 \sin^2(\phi) \quad (\text{A.8})$$

Similarly, taking v_z to be in the longitudinal direction it follows for the longitudinal velocity v_L :

$$v_L^2 = v^2 \cos^2(\phi) \quad (\text{A.9})$$

The equivalent transverse, E_T , and longitudinal, E_L , energy can be written as:

$$E_T = \frac{1}{2} m v_T^2 = \frac{1}{2} m v^2 \sin^2(\phi) \quad (\text{A.10})$$

$$E_L = \frac{1}{2} m v_L^2 = \frac{1}{2} m v^2 \cos^2(\phi) \quad (\text{A.11})$$

The total velocity is the sum in quadrature of the longitudinal and transverse velocity, i.e.:

$$v^2 = v_L^2 + v_T^2 = v^2 \cos^2(\phi) + v^2 \sin^2(\phi) \quad (\text{A.12})$$

Multiplying both sides of by $\frac{1}{2}m$

:

$$\frac{1}{2} m v^2 = \frac{1}{2} m v^2 \cos^2(\phi) + \frac{1}{2} m v^2 \sin^2(\phi) \quad (\text{A.13})$$

Comparing Eq.(A13) with (A4), (A10) and (A11) it follows:

$$E = E_L + E_T \quad (\text{A.14})$$

Appendix B: Further Code Description

The following diagrams give the subsystems discussed in chapter 2. The first diagram is the umbrella which contains all aspects of the code. The legend shows what each box represents. This is for the simplest case, for example, velocity values can be sent to the Matlab workspace similarly to how x , y and z are here. However, in this figure, this is not shown.

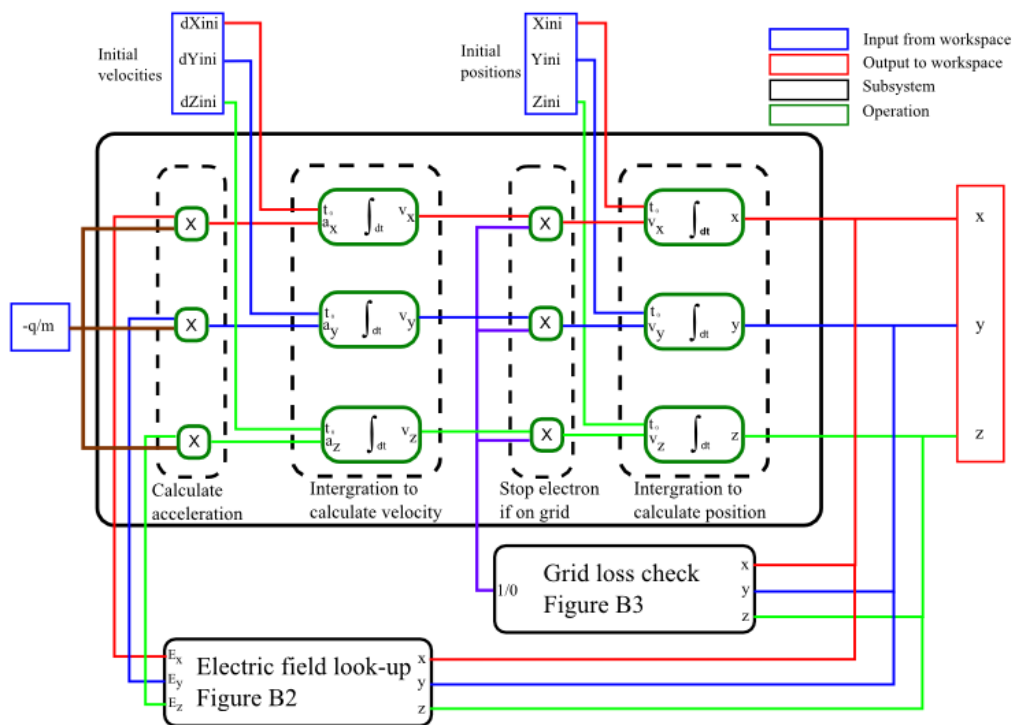


Figure B1: Overarching code layout

Lookup tables effectively look up values based on a table pre-loaded before the code is run. The field maps exported from finite element solvers are defined in tables corresponding to field data at positional co-ordinates which increases incrementally. Before the code is run, two operations need to be performed. First the Electric fields in term of radii and Cartesian co-ordinates need to be defined and secondly breakpoints need to be defined which tells the Simulink program at what point there are co-ordinates defined. The look up table then uses an interpolation method to define an electric field value. The algorithms used to organise the field maps so they can be used by the code for 2D and 3D field maps are written as:

2D Algorithm:

```

E2D(isnan(E2D))=0;
for j=1:n2dz
    for i=1:n2dr
        E2r(i,j)=E2D((i+(j-1)*n2dr),3);
        E2z(i,j)=E2D((i+(j-1)*n2dr),4);
    end
end
Br(1:n2dr)=E2D(1:n2dr,1);
Bz(1:n2dz)=E2D(1:n2dr:n2dz*n2dr,2);

Br=Br';
Bz=Bz';

```

3D Algorithm:

```

for k=1:n3dz
    for j=1:n3dy
        for i=1:n3dx
            Ex(i,j,k)=E3D((i+(j-1)*n3dx+(k-1)*n3dx*n3dy),4);
            Ey(i,j,k)=E3D((i+(j-1)*n3dx+(k-1)*n3dx*n3dy),5);
            Ez(i,j,k)=E3D((i+(j-1)*n3dx+(k-1)*n3dx*n3dy),6);
        end
    end
end
Ax(1:n3dx)=E3D(1:n3dx,1);
Ay(1:n3dy)=E3D(1:n3dx:n3dx*n3dy,2);
Az(1:n3dz)=E3D(1:n3dx*n3dy:n3dx*n3dy*n3dz,3);

Ax=Ax';
Ay=Ay';
Az=Az';

```

The following diagram shows how the look up tables are used within the Simulink code. For the two dimensional sub-system, it is necessary to make a radius. Once the electric field is returned it is necessary to split this into the x and y directions. This is done by multiplying the field value by the x/y co-ordinate and then dividing by the radius. It is possible to run the drift region in 3D also, in this case it is identical to the mesh region box with the exception that the Ncell function is removed and similarly the above algorithms are defined in the same way for both.

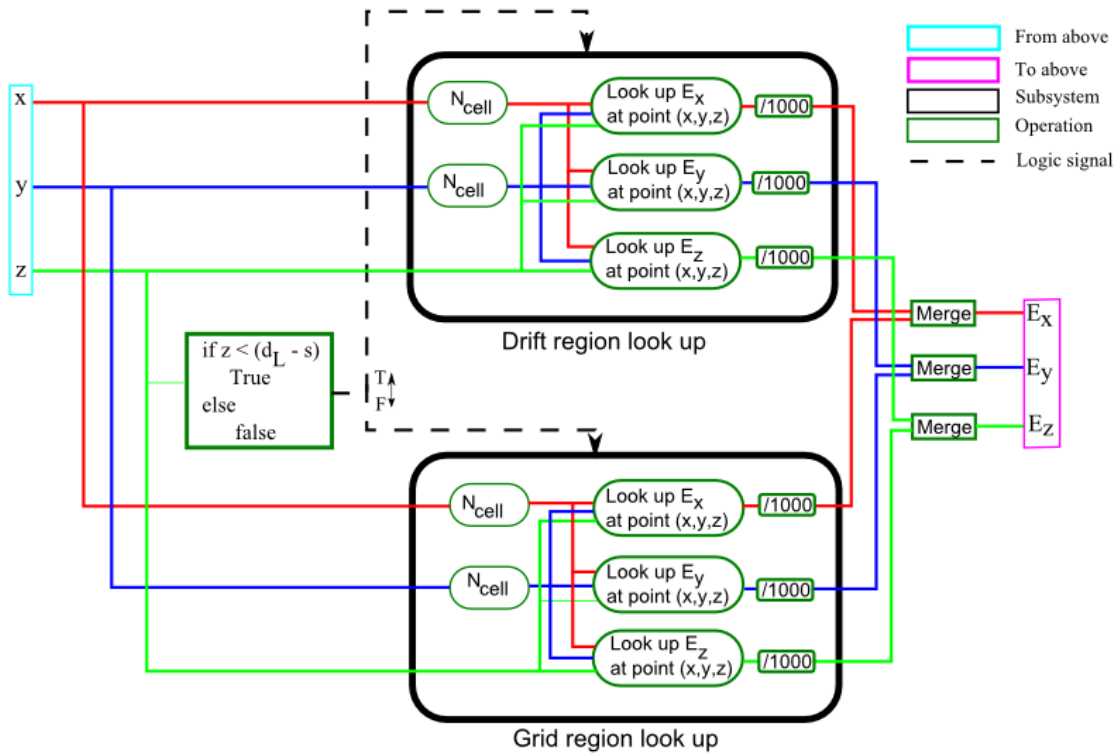


Figure B2: Electric field lookup block.

The following figure shows the Simulink function which checks if the position co-ordinate is on a wire or the MCP. The lookup tables are loaded similarly to the electric field values before the code is run. The XY loss table defines the transverse position of the wires of the mesh and the z loss table contains information on the longitudinal location of the wires and the MCP. The values contained in the XY and Z loss tables are so that if the electron needs to be stopped the result of the addition of both branches must equal two. In this case a 0 is sent to figure A1, if not then a 1 is sent and the tracking proceeds as normal with no freezing of the velocity. The XY loss table is defined as a square. This is not true of the mesh cell which has a small bending radius. The amount of free space is small compared to the covered area so the assumption is reasonable. The multiplication factor of 1.9 allows the logic of the algorithm to work when the XY loss tables return values of 0 and 1.

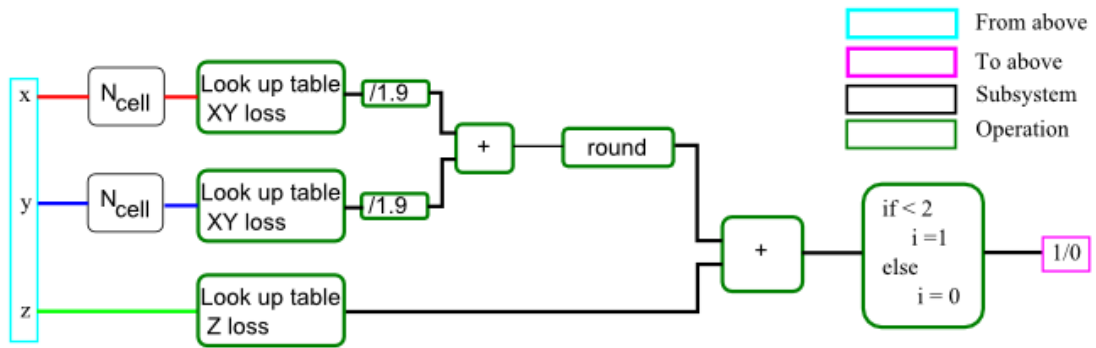


Figure B3: Grid loss check block.

The following figure is what is used to relocate the mesh space position to the position in the solved mesh cell.. If the sizes are different from 0.5 x 0.5 mm the multiplier (in the case below x2) within the code will require changing. The required change would require that for a pitch side length D mm that: D x multiplier = 1 mm.

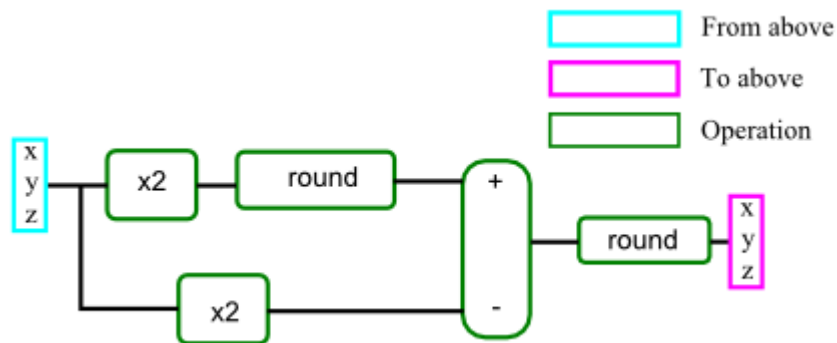


Figure B4: Algorithm to calculate position in the centre cell.

List of Figures

1. Chapter 1	
1.1. Cockcroft Walton voltage multiplier	13
1.2. Widerøe linac	15
1.3. Electromagnetic modes in a circular cavity	18
1.4. Quadrupole magnet	19
1.5. Transverse phase space ellipse	20
1.6. Spectral and temporal distribution of emitted photons	25
1.7. Oscillator type FEL	26
1.8. Free Evolution of brilliance per generation	27
1.9. CLIC layout	29
2. Chapter 2	
2.1. Three Step Model of Photoemission	39
2.2. Band structure of metals, NEA and PEA photocathodes	40
2.3. TESS experiment	44
2.4. Photocathode holder	45
2.5. Photocathode preparation facility	46
2.6. TESS mesh plate	47
2.7. First stage of TESS: Emission and acceleration	48
2.8. Second stage of TESS: Detection	49
2.9. Voltage connector mount	50
2.10. Emission velocity components	51
2.11. Transverse emission results	53
2.12. Filter Mesh technique scheme	54
2.13. MCP/Cathode Gap technique scheme	55
2.14. Line charge over a conducting surface	56
2.15. Potential along a curt line through/on wire from the analytical solution	61
2.16. Comparison of analytical and computer model	62
2.17. Comsol model of TESS	65

2.18. Comsol model of a mesh.....	65
2.19. FEM structure of a mesh	67
2.20. Effect of wire thickness on potential surrounding the mesh	68
2.21. Difference in potential from preceding configurations of cells.....	71
2.22. Potential along transverse profile across the central mesh cell	71
2.23. Opera model of TESS.....	74
2.24. Absolute potential difference between Opera and Comsol	75
2.25. Matlab Simulink code layout	76
2.26. Layout of field map areas.....	79
2.27. Potential at different switching points.....	80
2.28. Scaling mesh region co-ordinates to solved cell position	80
2.29. Transverse velocity as a function of longitudinal position.....	81
2.30. Initially experimentally derived velocity distributions.....	82
2.31. Assignment of velocities between longitudinal and transverse components	83
2.32. Initial transverse position distributions	84
2.33. Camera image of a live and dark data file.....	85
2.34. Fitting of summed data and fitting results.....	85
2.35. Corrected recorded pixel intensity with decreasing second mesh potential.....	86
2.36. Integrated intensity as a function of potential normalised to peak value	87
2.37. Electron motion through the mesh region for the filter mesh technique.....	89
2.38. Transverse energy as a function of longitudinal distance.....	90
2.39. Distribution on the MCP for simulated data.....	90
2.40. Path of many electron using the filter mesh technique.....	91
2.41. Distribution on the MCP showing diffraction like effects	92
2.42. Simulated results showing the percentage of the final outcomes of electrons .	93
2.43. Breakdown of mesh collisions	93
2.44. Contour plot of potential in the mesh cell	95
2.45. Comparison of simulated and experimental results.....	96
2.46. Experimental results from the MCP/Cathode gap technique	100
2.47. Longitudinal energy distribution curve	100
2.48. Normalised distribution curve	101
2.49. Path of electrons using the MCP/Cathode gap technique.....	102

2.50. Percentage of recorded events as a function of coupling angle	104
2.51. Transverse energy at point of retardation	104
2.52. Transfer of velocity from longitudinal to transverse	105
3. Chapter 5	
3.1. Stopping power of a muon travelling through copper	114
3.2. Ionisation chamber and PIN diode.....	116
3.3. Long ionisation chamber	118
3.4. Photomultiplier tube	119
3.5. Scintillator around a beam pipe	120
3.6. Principle of detection in fibre	125
3.7. Light propagation in a fibre	126
3.8. Meridional and skew rays	127
3.9. Refractive index profiles.....	128
3.10. Absorption attenuation.....	131
3.11. Attenuation for absorbed dose	132
3.12. Cherenkov cone	133
3.13. SiPM circuit equivalent diagram	137
3.14. Persistence plot of SiPM in dark mode.....	138
3.15. Branching process of SiPM	141
3.16. Raw SiPM signal	143
3.17. Averaged signal	143
3.18. Dark noise steps.....	146
3.19. Charge spectrum	147
3.20. Time resolution experiment.....	148
3.21. Saturation curve	150
3.22. Equipment layout.....	152
3.23. SiPM response under low light.....	152
3.24. SiPM response under intense light.....	152
3.25. Current against light intensity showing saturation.....	156
3.26. Rise time as a function of light intensity	156

3.27. Convolution of SER response with LED pulse for three intensities	159
3.28. Layout for double pulse measurements.....	159
3.29. Double pulse measurements with analytical model	160
3.30. Layout of CTF3.....	161
3.31. Pulse structure before and after delay & combiner ring.....	162
3.32. Simulated beam loss.....	164
3.33. Light tight box housing	166
3.34. Circuit board layout.....	166
3.35. Localised detectors	167
3.36. Detector layout	168
3.37. Averaged localised detector pulse.....	169
3.38. Averaged fibre pulse	171
3.39. Difference between signals	171
3.40. Deconvoluted upstream back ground signal.....	174
3.41. Deconvoluted upstream TBL signal.....	175
3.42. Deconvoluted corrected signal	175
3.43. Frequency of losses	177
3.44. Australian synchrotron results.....	178

List of Tables

1.1 Sample of CLIC beam parameters	30
2.1 Photocathode typical parameters and references	42
2.2 Cell convergence study results	70
2.3 Cell size study results	72
2.4 x-y misalignment	73
2.5 z angle misalignment	73
3.1 CLIC machine protection requirements	124
3.2 CLIC and CTF3 comparison	144
3.3 Localised detector dose results	149
3.4 SiPMs used in characterisation studies	155
3.5 Time resolution results	162
3.6 OD values with associated transmission and error	173

Bibliography

- [1] J. Cockcroft and E. Walton, "Experiments with high velocity positive ions -(I) Further developments in the method of obtaining high velocity positive ions," *Proceedings of the Royal Society of London*, vol. 136, pp. 619-630, 1932.
- [2] R. Hellborg and others, *Electrostatic accelerators: Fundamentals and applications*, R. Hellborg, Ed. Springer, 2005.
- [3] K. Wille, "Synchrotron radiation sources," *Report on Progress in Physics*, vol. 54, pp. 1005-1068, 1991.
- [4] G. Ising, "Prinzip einer Methode zur Herstellung von Kanalstrahlen hoher Voltzahl," *Arkiv för matematik, astronomi och fysik*, vol. 18, pp. 1-4, 1924.
- [5] R. Wildroe, "Über ein neues Prinzip zur Herstellung hoher Spannungen," *Archiv für Elektrotechnik*, 1928.
- [6] G. Caryotakis, "The Klystron: A Microwave source of surprising range and endurance" in *39th Annual Meeting of the Division of Plasma Physics of the American Physical Society (DPP 97) Pittsburgh, Pennsylvania, November 17-21*
- [7] A. Heil and O. Hell, "Eine neue Methode zur Erzeugung kurzer, ungedämpfter, elektromagnetischer Wellen großer Intensität," *Zeitschrift für Physik*, vol. 95, no. 11, pp. 752-762, 1935.
- [8] A. Hull, "The effect of a uniform magnetic field on the motion of electrons between coaxial cylinders," *Physical Review*, vol. 18, pp. 31-57, 1921.
- [9] E. Ginzton, W. Hansen, and W. Kennedy, "A linear electron accelerator," *Review of Scientific Instruments*, vol. 19, no. 2, pp. 89-108, 1948.
- [10] E. Wilson, *An introduction to particle accelerators*. Oxford University Press, 2000.
- [11] W. Hansen, "A type of electrical resonator," *Journal of Applied Physics*, no. 9, pp. 654-663, 1938.
- [12] J. Jackson, *Classical electrodynamics*. Wiley, 1998.
- [13] D. Pozar, *Microwave engineering*. Wiley, 2012.
- [14] H. Wiedemann, *Particle accelerator physics*. Springer, 2007.

- [15] M. Reiser, *Theory and design of charged particle beams*. Wiley, 2008.
- [16] J. Buon, "Beam phase space and emittance," in *Presented at the CERN Accelerator School 1990*, 1990.
- [17] M. Cornacchia and P. Emma, "Transverse to longitudinal emittance exchange," *Physical Review Special Topics- Accelerators and Beams*, vol. 5, 2002.
- [18] J. Lawson, *The physics of charged particle beams*. Oxford University Press, 1977.
- [19] C. Nguyen, et al., "Overions of the 100 mA average-current RF photoinjector," *Nuclear Instruments & Methods in Physics Research, Section A: Accelerators, Spectrometers, Detectors, and Associated Equipment*, 2004.
- [20] B. Carlsten and D. Palmer, "Enhanced emittance compensation in a high-frequency RF photoinjector using RF radial focusing," *Nuclear Instruments & Methods in Physics Research, Section A: Accelerators, Spectrometers, Detectors, and Associated Equipment*, 1999.
- [21] C. Limborg-Deprey and P. Bolton, "Optimum electron distributions for space charge dominated beams in photoinjectors," *Nuclear Instruments and Methods in Physics Research A*, vol. 557, pp. 106-116, 2006.
- [22] K. Kim, "RF and space-charge effects in laser-driven RF electron guns," *Nuclear Instruments and Methods in Physics Research A*, vol. 275.
- [23] T. Wangler, *RF linear accelerators*. Wiley-VCH, 2008.
- [24] A. R. t. comittee, "Clinical electron-beam dosimetry," *Medical Physics*, vol. 18, pp. 73-109, 1991.
- [25] C. Vieu, et al., "Electron beam lithography: resolution limits and applications," *Applied Surface Science*, 2000.
- [26] J. Nicholls, M. Deakin, and D. Rickerby, "A comparison between the erosion behaviour of thermal spray and electron beam physical vapour deposition thermal barrier coatings," *Wear*, 1999.
- [27] E. Zanazzi and F. Jona, "A reliability factor for surface structure determinations by low-energy electron diffraction," *Surface Science*, 1977.

- [28] P. Suortti and Thomlinson, "Medical applications of synchrotron radiation," *Physics in Medicine and Biology*, vol. 48, no. 3, 2003.
- [29] M. Rossmann, "Synchrotron radiation as a tool for investigating virus structures," *Journal of Synchrotron Radiation*, vol. 6, pp. 816-821, 1999.
- [30] R. Talman, *Accelerator x-ray sources*. Wiley, 2006.
- [31] G. Margaritondo, *Elements of synchrotron light*. Oxford university press, 2002.
- [32] G. Brown, K. Halbach, J. Harris, and H. Winick, "Wiggler and undulator magnets - a review," *Nuclear Instruments & Methods*, vol. 208, pp. 66-77, 1983.
- [33] S. a. B. F. Mobilio, *Synchrotron Radiation: Basic. Methods and Applications*, C. Meneghini, Ed. Springer, 2015.
- [34] Tokyo University of Science. (2015) FEL. [Online]. http://www.rs.noda.tus.ac.jp/fel-tus/pics/E-FEL_Scheme.gif
- [35] P. Schmusser, M. Dohlus, and Rossabach, *Ultraviolet and soft x-ray free electron lasers*. Springer, 2009.
- [36] N. Thompson, "Introduction to FELs," in *Cockcroft Institute lecture series*.
- [37] B. McNeil and Thompson, "X-ray free-electron lasers," *Nature Photonics*, vol. 4, 2010.
- [38] D. Dowell, et al., "Cathode R&D for future light sources," *Nuclear Instruments & Methods in Physics Research, Section A: Accelerators, Spectrometers, Detectors, and Associated Equipment*, vol. 622, no. 3, pp. 685-697, 2010.
- [39] CLIC collabotation, "CLIC Conceptual Design Report," CERN, Tech. rep., 2012.
- [40] A. Cappelletti, et al., "Demonstration of the high RF power production feasibility in the CLIC power extraction and transfer structure (PETS)," *Nuclear I*, vol. 657, pp. 78-81, 2011.
- [41] R. Ruber, et al., "The CTF3 two-beam test stand," *Nuclear Instruments & Methods in Physics Research, Section A: Accelerators, Spectrometers, Detectors, and Associated Equipment*, vol. 729, pp. 546-553, 2013.
- [42] M. Oivegård and V. Ziemann, "Effect of large momentum spread on emittance measurements," *Nuclear Instruments and Methods in Physics Research Section A: Accelerators, Spectrometers, Detectors and Associated Equipment*, vol. 707, pp. 114-119,

- 2013.
- [43] M. Wendt, et al., "Status of the CLIC/CTF beam instrumentation R&D," in *Proceedings of IPAC2014*, 2014.
 - [44] J. R. Towler, et al., "{Technologies and R&D for a High Resolution Cavity BPM for the CLIC Main Beam}," no. CERN-ACC-2013-0307, p. 4, Sep. 2013. [Online]. https://cds.cern.ch/record/1638353
 - [45] D. Walsh, S. Jamison, and W. Gillespie, "A femtosecond resolution electro-optical diagnostic using a nanosecond pulse laser," in *Proceedings of IBIC2013*, 2013.
 - [46] M. Micheeler, "Development of longitudinal diagnostics for electron beams based on coherent diffraction radiation," Ph.D. dissertation, Royal Holloway University London, 2010.
 - [47] T. Aumeyr, "Development of a laser-wire beam profile monitor for PEP-III and CLIC," Ph.D. dissertation, Royal Holloway University of London, 2013.
 - [48] K. Kruchinin, et al., "Sub-micrometer transverse beam size diagnostics using optical transition radiation," *Journal of Physics: Conference Series*, vol. 517, 2014.
 - [49] A. Jeff, et al., "A Quantum Gas Jet for Non-Invasive Beam Profile Measurement," in *Proceedings of IBIC2014*, 2014.
 - [50] M. Lezlinger and E. Snow, "Fowler–Nordheim tunneling into thermally grown SiO₂," *Journal of applied physics*, vol. 40, pp. 278-283, 1969.
 - [51] H. Padamsee, *RF Superconductivity*. Wiley, 2009.
 - [52] M. Dehler, "Design and modelling of field emitter arrays for a high brilliance electron source," in *Proceedings of ICAP 2006*, Chamonix, France, 2006.
 - [53] D. Temple, "Recent progress in field emitter array development for high performance applications," *Materials Science & Engineering R Reports*, vol. 24, no. 5, pp. 185-239, 1999.
 - [54] V. Guzenko, A. Mustonen, P. Helfenstein, E. Kirk, and S. Tsujino, "High-density large-scale field emitter arrays for X-ray free electron laser cathodes," *Microelectron. Eng.*, 2013.
 - [55] J. Lawson, *The physics of charged particle beams*. Oxford University Press, 1977.

- [56] P. Davis, "Comparison of thermionic cathode parameters of low index single crystal faces of LaB₆, CeB₆ and PrB₆," *Applied Surface Science*, 1989.
- [57] K. Togawa, et al., "Low emittance 500 kv thermionic electron gun," in *Proceedings of LINAC 2004*, Lubeck, Germany, 2004.
- [58] A. Einstein, "ijber einen die Erzeugung und Verwandlung des Lichtes betreffenden heuristischen Gesichtspunkt," *Ann. Physik*, vol. 17, 1905.
- [59] W. Spicer and A. Herrera-Gomez, "Modern Theory and Applications of Photocathodes," SLAC, Tech. rep., 1993.
- [60] H. Bonzel and C. Kleint, "On the history of photoemission," *Progress in surface science*, vol. 49, no. 2, pp. 107-153, 1995.
- [61] P. Feibelman and D. Eastman, "Photoemission spectroscopy—Correspondence between quantum theory and experimental phenomenology," *Physical Review B*, vol. 10, pp. 4932-4947, 1974.
- [62] Z. Shen and D. Dessau, "Electronic structure and photoemission studies of late transition-metal oxides - Mott insulators and high-temperature superconductors," *Physica Reports*, vol. 253, pp. 1-162, 1995.
- [63] K. Flottmann, "Note on the thermal emittance of electrons emitted by Cesium Telluride photocathodes," DESY, Tech. rep., 1995.
- [64] K. Flottmann, "Note on the thermal emittance of electrons emitted by Cesium Telluride photo cathodes," 1991.
- [65] L. Cultera, "Advances in photocathodes for accelerators," in *IPAC2014*, Dresden, 2015.
- [66] D. Dowell and J. Schmerge, "Quantum efficiency and thermal emittance of metal photocathodes," *Phys. Rev. ST Accel. Beams*, vol. 12, p. 074201, Jul. 2009.
- [67] B. M. Dunham, et al., "Advances in DC photocathode electron guns," *AIP Conference Proceedings*, vol. 472, no. 1, pp. 813-822, 1999.
- [68] C. Hernandez-Garcia, P. O'shea, and M. Stutzman, "Electron sources for accelerators," in *Physics Today*, 2008.
- [69] T. Nakajyo, J. Yang, F. Sakai, and Y. Aoki, "Quantum efficiencies of Mg photocathode under illumination with 3rd and 4th harmonics Nd: LiYF₄ laser light in RF gun,"

Japanese Journal of Applied Physics, vol. 42, pp. 1470-1474, 2003.

- [70] D. H. Dowell, "Advances in cathodes for high-current rf photoinjectors," in *Proceeding of SPIE 3614, Free electron laser challenges II*, 1999.
- [71] A. Fry, E. Hahn, W. Hartung, and M. Kuchnir, "Experience at Fermilab with high quantum efficiency photocathodes for RF electron guns," in *Proceedings of Linac98*, 1998.
- [72] C. Hessler, et al., "Recent results on the performance of Cs₃Sb photocathodes in the PHIN RF-gun," in *Proceedings of IPAC2015*, 2015.
- [73] S. Schubert, et al., "Influence of growth method on K₃Sb photocathode structure and performance," in *Proceedings of 2014*, 2014.
- [74] N. Chanlek, "Quantum efficiency lifetime studies using the photocathode preparation experimental facility developed for the ALIC accelerator," Ph.D. dissertation, The University of Manchester, 2012.
- [75] D. Pierce, R. Celotta, J. Unguris, and H. Siegmann, "Spin-dependent elastic scattering of electrons from a ferromagnetic glass, Ni₄₀Fe₄₀B₂₀," *Physical Review B*, 1982.
- [76] S. Mane, Y. Shatunov, and K. Yokoya, "Spin-polarized charged particle beams in high-energy accelerators," *Reports on Progress in Physics*, vol. 68, pp. 1997-2265, 2005.
- [77] D. Pierce and F. Meier, "Photoemission of spin polarized electron from GaAs," *Physical Review B*, vol. 13, no. 12, 1976.
- [78] J. Clendenin, "Polarized electron sources," in *IEEE Particle accelerator conference*, 1995.
- [79] Z. Liu, Y. Sun, P. Pianetta, and R. Pease, "Narrow cone emission from negative electron affinity photocathodes," *Journal of vacuum science & technology B*, vol. 23, pp. 2758-2762, 2005.
- [80] G. Vergara, A. Hernandez-Gomez, and Spi, "Escape probability for negative electron affinity photocathodes: calculations compared to experiments," in *SPIE proceedings 2550*, 1995.
- [81] B. Militsyn, et al., "High voltage DC photoinjector development at Daresbury Laboratory," *ICFA Beam Dynamics Newsletter*, 2010.

- [82] B. Militsyn, et al., "First results from the III-V photocathode preparation facility for the ALICE ERL photoinjector," in *Proceedings of IPAC'10*, Kyoto, Japan, 2010.
- [83] T. Maruyama, et al., "Atomic hydrofren cleaning of polarized GaAs photocathodes," *Applied Physics Letters*, 2003.
- [84] L. Jones, et al., "Gallium arsenide photocathode research at Darsbury laboratory," in *Proceedings of IPAC2011*, San Sebastian, Spain, 2011.
- [85] R. Petry, "Secondary electron emission from Tungsten, copper and gold," *Physical R*, vol. 28, 1926.
- [86] Hamamatsu. (2015) [Online].
http://www.hamamatsu.com/resources/pdf/etd/MCPassy_TMCP0001E.pdf
- [87] Stanford Computer Optics. (2015) [Online].
<http://www.stanfordcomputeroptics.com/technology/image-intensifier/phosphor-screen.html>
- [88] L. Jones, et al., "The commissioning of TESS: An experimental facility for measuring the electron energy distribution from photocathodes," in *Proceedings of FEL2013*, 2013.
- [89] PCO. (2015) [Online]. <http://www.pco.de/sensitive-cameras/pco2000/>
- [90] PCO. (2016, Mar.) [Online].
https://www.pco.de/fileadmin/user_upload/db/download/pco_cooKe_kb_snr_0504.pdf
- [91] Tamron. (2015) [Online]. <http://www.tamron.eu/uk/>
- [92] H. Schreiber, "First measurements of photoelectron transverse energy distribution curve using TESS," in *ERL2013*, 2013.
- [93] L. Jones, B. Militsyn, T. Noakes, H. Scheibler, and A. Terekhov, "The evolution of the transverse energy distribution of electron from GaAs photocathode as a function of its degradation state," in *Proceedings of IPAC2015*, 2015.
- [94] K. McDonald. (2003, Mar.) Notes on Electrostatic Wire Grids. [Online].
www.hep.princeton.edu/~mcdonald/examples/grids.pdf
- [95] W. Blum, W. Riegler, and L. Rolandi, *Particle Detection with Drift Chambers*. Springer-Verlag Berlin and Heidelberg GmbH & Co, 1993.

- [96] M. Ablowitz and A. Fokas, *Complex Variables: Introduction and applications*, D. Crighton, Ed. Cambridge University Press,, 1997.
- [97] L. R. W Blum, *Particle Detection with Drift Chambers*, Me, Ed. Springer-Verlag Berlin and Heidelberg GmbH & Co. K, 1993.
- [98] P. Martin, "On acoustic and electric Faraday cages," *Proceedings of the Royal society A*, vol. 470, no. 2171, Sep. 2014.
- [99] S. Chapman, D. Hewett, and L. Trefethen, "Mathematics of the faraday cage," The university of Oxford, Tech. rep., 2015.
- [100] (2015) Comsol Multiphysics. [Online]. <http://www.comsol.com>
- [101] (2015) Cobham. [Online]. <http://www.operafea.com>
- [102] D. Hutton, *Fundamentals of finite element analysis*. McGraw-Hill, 2003.
- [103] R. Cook, D. Malkus, M. Plesha, and R. Witt, *Concepts and applications of finite element analysis*, 4th ed. Wiley, 2001.
- [104] J. Jin, *The finite element method in electromagnetics*. Wiley, 2014.
- [105] (2015) Mathworks. [Online]. <http://www.mathworks.com>
- [106] L. Loeb, *Static Electrification*. Springer, 1958.
- [107] E. Lassner and W. Schubert, *Tungsten- Properties, Chemistry , technology of the elementm alloys and chemical compounds*. Springer, 1999.
- [108] Stanford Reasearch Systems. (2015) [Online]. <http://www.thinksrs.com/products/SR810830.htm>
- [109] L. Jones, et al., "Cooled Transmission–Mode NEA–Photocathode with a Band–Graded Active Layer for High Brightness Electron Source," in *Proceedings of the Workshop on polarized electron sources and polarimeters*, 2008.
- [110] (2015) SIMION. [Online]. <http://www.simion.com>
- [111] M. Schmeisser, A. Jankiwia, T. Kamps, and S. Schubert, "In-situ characterization of K2CsSb photocathodes," in *Proceedings of IPAC2014*, Dresden, 2014.
- [112] B. Auchmann, et al., "Testing beam-induced quench levels of LHC superconducting magnets," *Phys. Rev. ST Accel. Beams*, vol. 18, p. 061002, Jun. 2015.

- [113] B. Holzer, "Commissioning and operational scenarios of the LHC beam loss monitor system," in *Proceedings of HB2006*, 2006.
- [114] K. Wittenburg, "Beam loss monitors," in *CERN Accelerator School on beam diagnostics*, 2008.
- [115] P. Sigmund, *Particle penetration and radiation effects*, E. Cardona, Ed. Springer, 2006.
- [116] K. Olive, "Passage of particles through matter," *Chinese Physics C*, 2014.
- [117] C. Grupen and B. Shwartz, *Particle detectors*. Cambridge University Press, 2008.
- [118] FLUKA. [Online]. <http://www.fluka.org/fluka.php>
- [119] Geant4. [Online]. <https://geant4.web.cern.ch/geant4/>
- [120] M. Castellano and V. Verzilov, "Spatial resolution in optical transition radiation beam diagnostics," *Physical Review Special Topics- Accelerators and Beams*, vol. 1, no. 062801, 1998.
- [121] D. Rule, "Transition radiation diagnostics for intense charged particle beams," *Nuclear Instruments and Methods in Physics Research Section B: Beam Interactions with Materials and Atoms*, vol. 24-25, Part 2, no. 901-904, 1987.
- [122] D. Groom, N. Mokhov, and S. Striganov, "Stopping Power and Range Tables 10 MeV - 100 TeV," *Atomic Data, and Nuclear Data Tables*, vol. 76, no. 2, Jul. 2001.
- [123] G. Knoll, *Radiation detection and measurement*. Wiley, 2000.
- [124] B. Dehning, et al., "The LHC beam loss measurement system," in *Proceedings of PAC07*, 2007.
- [125] J. Bowe, "Drift Velocity of Electrons in Nitrogen, Helium, Neon, Argon, Krypton, and Xenon," *Physical Review*, vol. 117, no. 6, 1960.
- [126] K. Wittenburg, "The pin diode beam loss monitor system at HERA," in *AIP conference proceedings 2000*, 2000.
- [127] K. Wittenburg, "Preservation of beam loss induced quenches, beam lifetime and beam loss measurements with the HERAp beam-loss-monitor system," *Nuclear, Instruments and Methods in Nuclear Research A*, vol. 345, no. 2, pp. 226-229, 1994.
- [128] L. Frohlich, "Machine Protection for FLASH and the european XFEL," Ph.D. dissertation, 2009.

- [129] K. Wittenburg, "Radiation damage in PIN-photodiodes," *Nuclear Instruments and Methods in Nuclear Research A*, vol. 270, no. 1, pp. 56-61, 1988.
- [130] W. Panofsky, "The use of a long co-axial ion chamber along the accelerator," Slac, Technical Report Report SLAC-TN-63-57, 1963.
- [131] McCormick, "Fast ion Chambers for SLC," SLAC, Tech. rep., 1993.
- [132] P. Forck, "Lectures on Beam Instrumentation and Diagnostics," in *Proceedings of JUAS 2012*, 2012.
- [133] M. Fisherman and D. Reagan, "The SLAC long ion chamber system for machine protection," in *IEEE Transactions on nuclear science*, 1967.
- [134] K. Nakamura and P. D. Group, "Review of Particle Physics," *Journal of Physics G: Nuclear and Particle Physics*, vol. 37, no. 7A, p. 075021, 2010.
- [135] Hamamatsu. (2015) [Online].
https://www.hamamatsu.com/resources/pdf/etd/PMT_handbook_v3aE.pdf
- [136] IEEE, "IEEE Standard Test Procedures for photomultipliers for scintillation counting and glossary for scintillation counting field," IEEE 3415699, 2006.
- [137] J. Harasimowicz, L. Cosentino, P. Finocchiaro, A. Pappalarado, and C. Welsch, "Scintillating screens sensitivity and resolution studies for low energy, low intensity beam diagnostics," *Review of Scientific Instruments*, 2010.
- [138] S. Payne and W. S., "Fine spatial beam loss monitoring for the ISIS proton synchrotron," in *Proceedings of EPAC06*, 2006.
- [139] Z. Li, et al., "Properties of plastic scintillators after irradiation," *Nuclear Instruments and Methods in Physics Research Section A: Accelerators, Spectrometers, Detectors and Associated Equipment*, vol. 552, no. 3, pp. 449-455, 2005.
- [140] K. Wittenburg, "Beam Loss monitors," in *oPAC Topical Workshop on Beam Diagnostics*, Vienna, May 2014.
- [141] G. Tautfest and H. Fechter, "A nonsaturable high energy beam monitor," *The Review of Scientific Instruments*, vol. 26, no. 2, 1955.
- [142] D. Kramer, D. B., E. Holzer, G. Ferioli, and M. Stockner, "Simulations and measurements of secondary electron emissio beam loss monitors for LHC," *Nuclear Physics B (Proc.*

- Suppl*), vol. 172, pp. 246-249, 2007.
- [143] S. Gilardon, A. S. E. Effinger, J. Gil-Flores, and U. Wienands, "Beam loss monitors comparison at the CERN proton synchrotron," in *Proceeding of IPAC 2011*, 2011.
- [144] W. Saslow, T. K. Bergstresser, and M. L. Cohen, "Band Structure and Optical Properties of Diamond," *Phys. Rev. Lett.*, vol. 16, pp. 354-356, 1966.
- [145] P. W. May, "CVD diamond: a new technology for the future?," *Endeavour*, vol. 19, no. 3, pp. 101-106, 1995.
- [146] M. Hempel, "Bunch by bunch beam loss diagnostics with diamond detectors at the LHC," in *proceedings of HB2012*, 2012.
- [147] M. Caresana, M. Ferrarini, M. G. M. Silari, and V. Varoli, "LUPIN, a new instrument for pulsed neutron fields," *Nuclear Instruments and Methods in Physics Research A*, vol. 712, pp. 55-26, 2013.
- [148] G. Manessi, "Development of advanced radiation monitors for pulsed neutron fields," PhD Thesis, The University of Liverpool, 2015.
- [149] C. Birattari, A. Ferrari, C. Nuccetelli, M. Pelliccioni, and M. Silari, "An extended range neutron rem counter," *Nucl. Instrum. Methods Phys. Res., Sect. A*, 1990.
- [150] M. Jonker, "The CLIC machine protection," in *Proceedings of IPAC10*, 2010.
- [151] A. Ghatak and K. Thyagarajan, *Introduction to fiber optics*. Ca, 1998.
- [152] J. Buck, *Fundamentals of optical fibers*. Wiley, 2004.
- [153] J. Wilson and J. Hawkes, *Optoelectronics: An introduction*. Pearson Education, 1998.
- [154] J. Senior, *Optical fiber communications*. Prentice Hall, 1992.
- [155] K. Hill, "Photosensitivity in optical waveguides: application to reflection filter fabrication," *Applied Physics Letters*, 1978.
- [156] T. Li, "Structures parameters and transmission properties of optical fibers," in *Proceedings of IEEE Vol 68*, 1980.
- [157] J. Kuhnhenh, "Radiation issues in fibers," in *Ditanet workshop on beam loss monitoring*, Hamburg, Jun. 2012.
- [158] Berghmans, *An Introduction to radiation effects on optical components and fiber Optic sensors*, W. Gannot and I. Tanev, Eds. Springer, 2006.

- [159] C. Issever, "The radiation hardness of CErernt optical fibers for the LHC upgrades at - 25C," in *Topical workshop n electrons for particle physics*, 2009.
- [160] V. Jelley, "Cerenkov radiation and its applications," *British Journal of Applied Physics*, vol. 6, no. 7, 1955.
- [161] S. Law, "Optical fiber design and the trapping of Cherenkov radiation," *Applied Optics*, 2006.
- [162] J. Van Hoorne, "Cherenkov fibers for beam loss monitoring at the CLIC two beam module," Master's thesis, Technical University of Vienna, 2012.
- [163] O. Ganel and R. Wigmans, "Quartz fiber calorimetry for LHC experiments," *Nucl Instrum Methods Phys Res , Sect A*, 1995.
- [164] D. Di Giovenale, L. Catani, and L. Frolich, "A read-out system for online monitoring of intensity and position of beam losses in electron linacs," *Nuclear Instruments & Methods in Physics Research, Section A: Accelerators, Spectrometers, Detectors, and Associated Equipment*, 2011.
- [165] X. Marechel, "Fiber beam loss monitor for the spring-8 X-FEL: Test operation at the spring-8," in *Proceedings of IPAC10*, 2010.
- [166] F. Wulf, "Beam loss and beam profile monitors with optical fibers," in *Proceedings of DIPAC09*, 2009.
- [167] N. Otte, "The Silicon Photomultiplier - A new device for High Energy Physics, Astroparticle Physics, Industrial and Medical Applications," in *SNIC Symposium, Stanford, California*, 2006.
- [168] S. Cova, M. Ghioni, A. Lacaita, C. Samori, and F. Zappa, "Avalanche photodiodes and quenching circuits for single-photon detection," *Applied Optics*, vol. 35, no. 12, pp. 1956-1976, 1996.
- [169] P. Eckert, H.-C. Schultz-Coulon, W. Shen, R. Stamen, and A. Tadday, "Characterisation studies of silicon photomultipliers," *Nuclear Instruments and Methods in Physics Research A* , vol. 620, no. 2-3, pp. 217-226, Aug. 2010.
- [170] P. K. Lightfoot, G. J. Barker, K. Mavrokoridis, Y. A. Ramachers, and N. J. C. Spooner, "Characterisation of a silicon photomultiplier device for applications in liquid argon based neutrino physics and dark matter searches," *Journal of Instrumentation*, vol. 3, no. 10,

2008.

- [171] S. Jungmann, "Development of New Detector Technologies -Cerenkov Light Readout with Silicon Photomultipliers," Master's thesis, University of Heidelberg, 2011.
- [172] C. Piemonte, et al., "Characterization of the First Prototypes of Silicon Photomultiplier Fabricated at ITC-irst," *IEEE Transactions on Nuclear Science*, 2007.
- [173] Y. Musienko, "State of the art in SiPM's," in *Presented at 'SiPM workshop'*, CERN, Geneva, 2011.
- [174] A. Otte, B. Dolgoshein, H. Moser, R. Mirzoyan, and M. Teshima, "Status of Silicon Photomultiplier Developments as optical Sensors for MAGIC/EUSO-like Detectors," in *Proceedings of the 29th International cosmic ray conference*, 2005.
- [175] J. Rosado and S. Hidalgo, "{Characterization and modeling of crosstalk and afterpulsing in Hamamatsu silicon photomultipliers}," 2015.
- [176] S. Vinogradov, "{Analytical models of probability distribution and excess noise factor of solid state photomultiplier signals with crosstalk}," *Nuclear Instruments and Methods in Physics Research A*, vol. 695, pp. 247-251, Dec. 2012.
- [177] M. Panniello, L. Devlin, P. Finocchiaro, and C. Welsch, "Spectroscopic characterization of novel silicon photomultipliers," in *Proceedings of BIW2012*, 2012.
- [178] M. Mazzillo, et al., "Silicon photomultipliers development at STMicroelectronics," in *Proc. SPIE 8773, Photon Counting Applications IV; and Quantum Optics and Quantum Information Transfer and Processing*, vol. 8773, 2013, pp. 877302-877302-10. [Online].
http://dx.doi.org/10.1117/12.2014035
- [179] Hamamatsu. [Online]. <http://www.hamamatsu.com/eu/en/4004.html>
- [180] R. Verheyden, et al., "Performance study of Silicon Photomultipliers as photon detectors for PET," in *12th International Vienna Conference on Instrumentation*, 2012, pp. 381-284.
- [181] P. Finocchiaro, et al., "Characterization of a Novel 100-Channel Silicon Photomultiplier x2014;Part II: Charge and Time," *Electron Devices, IEEE Transactions on*, vol. 55, no. 10, pp. 2765-2773, Oct. 2008.

- [182] M. A. Tétrault, É. Desaulniers Lamy, A. Boisvert, J. F. Pratte, and R. Fontaine, "{Real-time discreet SPAD array readout architecture for time of flight PET}," 2014, [IEEE Trans. Nucl. Sci.62,1077(2015)].
- [183] M. Shayduk, et al., "Light sensors selection for the Cherenkov Telescope Array: PMT and SiPM," *Nuclear Instruments and Methods in Physics Research Section A: Accelerators, Spectrometers, Detectors and Associated Equipment*, vol. 695, pp. 109-112, 2012.
- [184] M. Iori, et al., "SiPM application for a detector for neutrinos tested at Sphinx station," *Nuclear Instruments and Methods in Physics Research Section A: Accelerators, Spectrometers, Detectors and Associated Equipment*, vol. 742, pp. 265-268, 2014, 4th Roma International Conference on Astroparticle Physics.
- [185] Hamamatsu. (2015) [Online]. https://halldweb.jlab.org/wiki/images/4/49/S10362-33_series_kapd1023e05.pdf
- [186] S. Vinogradov, A. Arodzero, R. C. Lanza, and C. P. Welsch, "SiPM response to long and intense light pulses," *Nuclear Instruments and Methods in Physics Research Section A: Accelerators, Spectrometers, Detectors and Associated Equipment*, vol. 787, pp. 148-152, 2015.
- [187] T. Gupta, *Radiation, ionization and, detection in nuclear Medicine*. Springer, 2013.
- [188] Z. M. Zhang, T. R. Gentile, A. L. Migdall, and R. U. Datla, "Transmittance measurements for filters of optical density between one and ten," *Appl. Opt.*, vol. 36, no. 34, pp. 8889-8895, Dec. 1997.
- [189] Thorlabs. (2015) [Online]. https://www.thorlabs.com/newgrouppage9.cfm?objectgroup_id=5011
- [190] PTC. (2015) [Online]. <http://www.ptc.com/engineering-math-software/mathcad>
- [191] E. Nebot del Busto, et al., "Studies of SiPM nonlinearities and transients at short light pulse detection.," in *Proceedings of the international conference on laser applications at accelerators, LA3NET 2015*, 2015.
- [192] R. Corsini, "Results on CLIC proof of principle from CTF3," in *Proceedings of PAC07*, 2007.
- [193] A. Ghigo, et al., "Status of the CTF3 frequency multipaction rings," in *Proceedings of APAC2007*, 2007.

- [194] E. Nebot Del Busto, et al., "Monte Carlo simulations of beam losses in the Test Beam Line of CTF3," in *Proceeding of IBIC13*, 2013.
- [195] E. Branger, "Development of a Beam Loss Monitoring system for CTF3 TBL," Master's thesis, Linkoping University, 2013.
- [196] M. Zingl, "Longitudinal Resolution of Cherenkov Fibers," CERN, Tech. rep., 2013.
- [197] Fluka. [Online]. <http://www.fluka.org/>
- [198] Hamamatsu. [Online]. <http://www.hamamatsu.com/>
- [199] A. Fisher, "Instrumentation and Diagnostics for PEP-II," Stanford university, Tech. rep., 1998.
- [200] Cividec. [Online]. <http://www.cividec.at>
- [201] R. E. Shafer, "{A tutorial on beam loss monitoring}," *AIP Conf. Proc.*, vol. 648, pp. 44-58, 2003, [,44(2003)].
- [202] E. Branger, "Development of a beam loss monitoring system for CTF3- TBL," Masters Thesis, Linkopings Universitet, 2013.
- [203] L. Fernandez-Hernando, et al., "Development of a beam condition monitor for use in experiments at the cern large hadron collider using synthetic diamond," in *Proceedings of the instrumentation and measurement technology conference*, 2004.
- [204] M. Pomorski, "Electronic Properties of Single Crystal CVD Diamond and its Suitability for Particle Detection in Hadron Physics Experiments," Ph.D. dissertation, University of Frankfurt am Main, 2008.
- [205] E. Nebot Del Busto, et al., "Position resolution of optical fibre based beam loss monitors using long electron pulses," in *IBIC 2015*, Melbourne, 2015.
- [206] Hamamatsu. (2015) [Online]. <http://www.hamamatsu.com/jp/en/S12572-010P.html>
- [207] M. Kastriotou, et al., "Cross talk studies at the CLIC two beam module," in *IBIC 2015*, Melbourne, 2015.
- [208] H. Padamsee, "The science and technology of superconducting cavities for accelerators," *Superconductor Science and Technology*, 2001.
- [209] S. Lee, *Accelerator Physics*. Wspsc, 2011.

- [210] E. Lawrence and M. Livingston, "The production of high speed protons without the use of high voltages," *Physical Review*, vol. 38, 1931.
- [211] P. data group, *Accelerator physics of colliders*.
- [212] P. Dahl, "Rolf Wideroe: Progenitor of Particle Accelerators," Superconducting super collider laboratory, Tech. rep., 1992.
- [213] Z. Huang and K. Kim, "A review of x-ray free electron laser theory," *Physical Review Special Topics- Accelerators and Beams*, vol. 10, no. 0344801, 2007.
- [214] I. Gradshteyn and I. M. Ryzhik, *Table of integrals, series, and products*, A. Jeffrey, Ed. Academic press, 2000.
- [215] W.-S. Sul, et al., "Guard-Ring Structures for Silicon Photomultipliers," *Electron Device Letters, IEEE*, vol. 31, no. 1, pp. 41-43, Jan. 2010.
- [216] T. Frach, "Optimization of the digital Silicon Photomultiplier for cherenkov light detection," in *Proceedings of the workshop on fast cherenkov detectors*, Apr. 2012.
- [217] H. Goldstein, C. Pool, and H. Saiko, *Classical Mechanics*, 3, Ed. Addison Wesley, 2002.
- [218] H. Scheibler. ERL2013. [Online]. http://epaper.kek.jp/ERL2013/talks/wg107_talk.pdf

Acknowledgements

I would first like to thank my supervisor Carsten Welsch for giving me the freedom to explore all areas of my research whilst still supporting me both on an academic and personal level.

The broad scope of this work would have never have been completed without the help and support from the following people. All the people involved in the BLM and SiPM project: Sophie Mallows, Marco Panniello, Eduardo Nebot del Busto, Maria Kastriotou and Sergey Vinogradov. Oleg Karamyshev for his assistance in code development. Lee Jones and Tim Noakes for allowing me to work on the TESS project, listening to my suggestions, data taking and filling in my vast lack of knowledge and also Heinrich Scheibler for suggesting the second TESS technique and experiments.

Thank you to Rob Ashworth for taking the time to help me in the initial stages of organising this thesis. Thank you to James Hunt for agreeing to review part of this thesis and all the members of my group not mentioned above who have come and gone over the past four years.

I would like to thank Alexandra Alexandrova for being my coffee buddy and putting up with me through many number of existential crises, Emilia Cruz-Alaniz for the drinking, climbing and the laughs and Tomasz Cybulski for looking after me from my first day until his last.

My cat Suki, whose antics make me happy even when I've had a bad day.

My parents, for making me the person I am today.

Finally thank you to Sophie. The past few years would be unimaginable without you. Without your love and support, I would have never completed this thesis and now we can finally plan the rest of our lives together.